

**FINITE ELEMENT MODELLING AND EXPERIMENTAL  
VALIDATION OF FRETTING WEAR IN THIN STEEL WIRES**

**AITOR CRUZADO GARCÍA**

Supervisor:  
Dr. Xabier Gómez



A thesis submitted for the degree of  
Doctor por Mondragon Unibertsitatea

Mechanical and Manufacturing Department  
Engineering Faculty  
Mondragon Unibertsitatea

November 2012



*To my family and my girlfriend*



---

# PREFACE

---

## Declaration

I hereby declare that this thesis is the result of my own work and that, to the best of my knowledge and belief, no part of this dissertation has previously been submitted for any similar qualification or degree.

*Aitor Cruzado*

(November 2012)

## Copyright and reproduction

This thesis is copyright Aitor Cruzado, 2012.

I authorize Mondragon Unibertsitatea to reproduce this thesis, in part or in whole, at the request of other institutions or individuals for the purpose of academic research.



---

# ACKNOWLEDGMENTS

---

Tras cuatro años de intenso trabajo que ha supuesto la realización de mi tesis doctoral y que ha contribuido a mi desarrollo tanto personal como profesional, he de agradecer a todas esas personas que han estado cerca de mí y que han contribuido a que todo esto sea posible.

Me gustaría agradecer en primer lugar a mi director de tesis Dr. Xabier Gómez, por su intachable dedicación en la dirección de esta tesis. Por su completa implicación, apoyo, motivación, por guiarme en este largo camino y porque siempre ha estado ahí, para ayudarme y para hacer esas correcciones que son tan necesarias, tanto en agosto como muchos fines de semana a lo largo de los años.

A la línea de superficies especialmente a Dr. Wilson Tato, por darme la oportunidad de poder trabajar en este grupo tan fructífero, por ser tan riguroso en la dirección de éste y porque su experiencia me ha aportado mucho profesionalmente. Dentro de esta línea también he de agradecer a Mikel Ezkurra por sus puntuales contribuciones y Andrea por su simpatía y compañerismo. A los proyectandos, Alaitz, Ion y Santi, porque su esfuerzo y colaboración han nutrido el desarrollo de este trabajo.

Al grupo de Ikerlan, especialmete a Felix Martínez y a Hodei Usabiaga por sus consejos y aportaciones.

A Orona EIC porque gracias ha ellos he podido realizar esta trabajo, sobre todo a Mikel Urchiegui por ser quien empezó este camino del estudio del *fretting* en los cables, y que ha seguido confiando siempre en esta vía.

Al Gobierno Vasco por la financiación aportada al proyecto SIVICA (Ref. UE2009-5) enmarcado dentro de esta tesis doctoral, bajo el programa Universidad Empresa.

A mis compañeros de doctorado, Luis, Joseba, Asier, Zubitu, Christian, Ion García, Haritz Zabala y demás por hacer ameno la estancia en la universidad durante este largo periodo. A

Pablo Puerto y Javier Trinidad, quienes cursaron la ingeniería superior conmigo y que también han empezado a navegar por el mundo de la investigación.

I would like to thank to my supervisor Prof. Sean Leen during my 4 months stage in the University of Galway. His enthusiasm and encouragement has made my short stage very valuable, interesting and positive experience. I learned a lot of with him and he was very friendly with me. To all the Ph. D. students that I met in the University of Galway, who made me to feel very comfortable. And also I would like to thanks to my housemates Tayyab, Xiao Wei and Siyuan Chen, because they did my stage very enjoyable.

Ich danke auch den Menschen der Bundesanstalt für Materialforschung und-prüfung (BAM) aus Berlin, für öffnete die Türen. Ich bedanke mich bei Rolf Wäesche und Manfred Hartelt, für das Vertrauen in mich vom ersten Tag gelegt und für was ich gelernt habe sie. Ich möchte auch Christine Neumann für die technische Unterstützung bedanken. Ich bedanke mich meine Deutschlehrer Dirk und Miren, für mein Deutsch verbessern und Ich bedanke mich auch Dirk Morenweiser für helfen mir mit dem technische Deutsch.

Quiero agradecer a toda mi familia. En primer lugar a mi madre y a mi padre, porque ellos siempre han confiado en mí y me han ayudado en todo lo que han podido. Porque sin ellos no podría haber llegado donde estoy ahora. A mi tío Luis por ser un gran apoyo y ejemplo a seguir, a mi primo Oskar por escucharme infinidad de veces y hacerme ver el lado más realista de las cosas, a mis abuelos allí donde estén y demás miembros de mi familia.

Y finalmente me gustaría agradecerle todo esto a Karen, porque a ella la conocí justo antes de empezar esta tesis (posiblemente fue el destino) y siempre ha estado ahí para lo bueno y para lo malo, aguantándome esos cambios de humor que viene en esos periodos en los que se te hace complicada la tesis y dándome esa fuerza y motivación para que todo esto halla sido posible. Porque ella siempre ha confiado en mí y con su apoyo incondicional todo esto ha resultado mucho más sencillo.



---

# ABSTRACT

---

Fretting wear is one of the main degradation mechanism produced in steel wire ropes. This phenomenon leads to produce wear scars between the contacting thin steel wires reducing considerably the fatigue life of these components. The complex assemblage of the wires in the wire rope systems make difficult the experimental characterization of this phenomenon, being economically costly and too much time consuming. With the aim to reduce these disadvantages and increases the knowledge of this phenomenon in complex components such as the wire rope systems, in this thesis a fretting wear simulation methodology for predicting wear scars in thin steel wires has been developed. The complex multicontact problem presented in wire rope systems, has been simplified with the development of an individual crossing cylinder model, in which the severity of the wear scars can be analysed under the range of the different geometrical and operational parameters appeared in each contact.

In order to define the frictional and wear behaviour of the thin steel wires, in terms of the coefficient of friction and the wear coefficient, fretting wear tests have been carried out under different conditions (loads, strokes and number of cycles). Firstly in a more common tribological system of  $90^\circ$  crossed cylinder arrangements and secondly with different crossing angles, which are a more realistic configuration to that one presented in wire ropes. This study has reported the influence of the contact pressure and the wear debris in the wear behaviour. Thus two wear mechanisms have been derived from this type of tests, a more aggressive wear mechanism in the beginning of the test and a stable wear mechanism in the remaining part of the test.

The developed wear simulation methodology is based on the Archard's wear law applied in a local perspective. So that the wear simulation is an iterative process in which the Archard's local equation is solved according to the contact pressures and slip distributions obtained by the finite element model, as many times as sliding increments needed to reach the desired sliding distance or, in the case of fretting wear, the desired number of cycles.

Nevertheless this process requires high computational time, which increases in the case of the 3D problem presented in the thin steel wires. Therefore an optimized methodology for modelling any tribological system has been proposed, based on the optimization of the main parameters involved in the wear modelling (mesh size, sliding increment and speed factor).

This methodology has been applied first in a cylinder on plane sliding wear 2D FE model and then was adapted to the 90° crossed cylinder 3D fretting wear FE model. Finally this approach has been implemented in the crossing angle 3D FE model, in which the parameterization of all the geometrical parameters and meshes that form the model has been introduced, in order to reduce the time required for modelling all the type of contacts presented in the wire rope systems. It has been demonstrated that following this methodology it can be defined the optimum parameters for modelling fretting wear of 3D problems in terms of the minimum computational time with the minimum difference in the final wear scar.

The optimized wear simulation methodology has been finally validated following an exhaustive validation methodology. To this end the specific wear coefficients obtained in the fretting wear thin steel wires tests have been used. The validation consisted of three steps: wear scar dimensions, wear scar depth (profile) and wear scar volume comparison. This procedure has shown the accurate validation of the entire wear scar shape in both top and bottom specimens.

The proposed methodology has been used then to study the severity of the wear scars under the different geometrical and operational parameters presented in the wire ropes contacts. The analysis of the severity of the wear scars has been done in terms of the percentage of resistant area loss and the stress concentration factor, concepts that are in relation with the catastrophic rupture of the wire and the fatigue life reduction of the wire, respectively. To develop this study the methodology of design of experiments (DOE) has been used. The great influence of the diameter and the crossing angle was derived from this study.

Finally the effect of fretting wear on the fatigue life reduction of thin steel wires has been analysed. For this purpose the frictionally-induced multiaxial contact stresses obtained from the 90° thin steel wires FE model have been used. The fatigue life prediction model uses a critical-plane SWT (Smith-Watson-Topper) approach in a 3D crossed cylinder problem. A new damage accumulation methodology for the adaptive mesh simulation in 3D problems, based on the cyclic material removal, has been developed. The effect of the contact pressure and stroke has been analysed and contrasted with the results obtained experimentally. Guidelines for developing a more robust methodology were proposed in the end of this research work.

---

# RESUMEN

---

El *fretting* es uno de los principales mecanismos de degradación presente en el interior de los cables metálicos. Este fenómeno conlleva la aparición de huellas de desgaste entre los hilos en contacto reduciendo considerablemente la vida a fatiga de estos componentes. El complejo ensamblaje de los hilos de acero en los cables metálicos dificulta la caracterización experimental de dicho fenómeno, resultando una tarea costosa tanto en tiempo como dinero. Con el fin de reducir estas desventajas y aumentar el conocimiento de este fenómeno en sistemas complejos como los cables metálicos, en esta tesis se ha desarrollado una metodología de simulación del desgaste para predecir las huellas de desgaste producidas por el fenómeno de *fretting*. El complejo problema de contacto múltiple presente en los cables, se ha simplificado por medio del desarrollo de un modelo individual de cilindros cruzados, en el cual se puede analizar la severidad de las huellas de desgaste bajo el rango de los parámetros, tanto operacionales como geométricos, presentes en cada uno de los contactos del cable metálico.

Con el fin de definir el comportamiento a rozamiento y desgaste de los hilos, en términos de coeficiente de rozamiento y desgaste, se han realizado ensayos tribológicos de *fretting* bajo diferentes condiciones (fuerza normal, carrera y número de ciclos). Primeramente con una configuración mas común de cilindros cruzados a 90° y a continuación con una configuración mas realista a la presente en los cables metálicos de ángulos cruzados. En dicho estudio se ha mostrado la influencia de la presión de contacto y las partículas de desgaste en el comportamiento ha desgaste de los hilos, observándose dos mecanismos principales de desgaste: un mecanismo de desgaste agresivo en el inicio del ensayo y un mecanismo de desgaste mas estable en la restante parte del ensayo.

La metodología de simulación de desgaste desarrollada en esta tesis, se basa en la ley de desgaste de Archard aplicada a nivel local. Por lo tanto la simulación del desgaste consiste en un proceso iterativo en el cual la ecuación de Archard local es resuelta por medio de las presiones de contacto y distribución de deslizamientos obtenidas por el modelo de elementos

finitos (EF), tantas veces como incrementos de deslizamientos sean necesarios para completar al deslizamiento requerido o, en el caso de *fretting*, para completar el número de ciclos. Sin embargo este proceso requiere un alto coste computacional, el cual es mayor en el caso del problema 3D presentado en los hilos. Por lo tanto se ha propuesto una metodología de simulación de desgaste optimizada para cualquier tribosistema, basada en la optimización de los principales parámetros involucrados en la simulación del desgaste (tamaño de la malla, incremento de deslizamiento y acelerador de desgaste).

Esta metodología se ha aplicado primeramente en un modelo 2D de EF, el cual representa un ensayo de deslizamiento continuo de cilindro-plano, y a continuación se ha adaptado al modelo 3D de EF de cilindros cruzados a 90° sometido a *fretting*. Finalmente dicha metodología se ha implementado en el modelo 3D de EF de cilindros cruzados, en el cual se ha incluido la parametrización de todos los parámetros tanto geométricos como de malla, con el fin de reducir el tiempo requerido para el modelado de todos los tipos de contactos presentes en los cables. Se ha demostrado que mediante la utilización de esta metodología se pueden identificar los parámetros óptimos para la simulación del desgaste en problemas 3D de *fretting* en términos de mínimo tiempo computacional y mínima diferencia en la huella de desgaste final obtenida.

La metodología de simulación de desgaste optimizada ha sido finalmente validada por medio de un exhaustivo procedimiento de validación. Para ello se han utilizado los coeficientes de desgaste específicos obtenidos tras los ensayos de *fretting* con hilos. Dicha validación se ha basado en tres aspectos relacionados con las huellas de desgaste: dimensiones de la huella, profundidad de la huella de desgaste (perfil central) y volumen de desgaste de la huella. Este procedimiento ha demostrado la precisa validación tanto de la huella del cuerpo superior como del inferior.

La metodología propuesta ha sido utilizada a continuación para el estudio de la severidad de las huellas de desgaste bajo los diferentes parámetros tanto operacionales como geométricos presentes en los cables. El estudio de la severidad se ha realizado en términos de porcentaje de área resistente perdida y factor de concentración de tensiones, conceptos que están relacionados con la rotura catastrófica del hilo y con la reducción de la vida a fatiga del mismo, respectivamente. Para su desarrollo se ha utilizado la metodología del diseño de experimentos (DOE). Dicho estudio ha demostrado la influencia tanto del diámetro como del ángulo de cruce en la reducción de vida de este tipo de componentes.

Finalmente se ha estudiado el efecto del *fretting* en la reducción de la vida a fatiga de los hilos. Para ello, a partir del modelo de simulación de desgaste de cilindros cruzados a 90°, se han utilizado las tensiones multiaxiales de contacto producidas por el rozamiento. El modelo de predicción de la vida a fatiga consiste en la implementación de la metodología del

plano crítico y el modelo de fatiga SWT (Smith-Watson-Topper) en el problema 3D de cilindros cruzados. La metodología propuesta incorpora además un nuevo modelo de acumulación de daño que tiene en cuenta el desgaste cíclico y consiguiente remallado adaptativo del material en problemas 3D. El efecto de la presión de contacto y la carrera han sido analizados y contrastados con los resultados obtenidos experimentalmente. Al final de esta tesis se han presentado las directrices para el desarrollo de una metodología más robusta para la predicción de la vida a fatiga debido al fenómeno de *fretting* en los hilos del cable.



---

# LABURPENA

---

Kable metalikoen barnean gertatzen den degradazio fenomeno garrantzitsuenetako bat da *fretting*-a. Gertaera honek dakar kablearen neke bizitza murriztea, hariz osatutako kableetan pitzadurak sortuaz. Altzairuzko harien muntai konplexuak fenomeno honen karakterizazio esperimentalak oztokatzen du, batez ere ikerkuntzaren luzapenean eta koste ekonomikoan. Desabantaila hauek ahal diren eina gutxitzeko batetik, eta kable metalikoa bezalako sistema konplexuetan fenomeno honi buruzko ezagutza handitzeko bestetik, *fretting* fenomenoaren sortutako pitzadurak iragartzeko higadura simulazio metodologia garatu da tesi honetan. Kableetan sortzen den harien arteko multi-kontaktu arazoa zaila suertatzen dela jakinda, bi zilindrok gurutzatzean sortzen duten kontaktu bakarreko modelo bat eraiki da. Modelo honek, kableetan agertzen diren kontaktu bakoitzeko pitzaduren larritasuna neurri geometriko edo funtzionamenduen ondorioz aztertze gaitasuna dauka.

*Fretting* saiakuntza tribologikoak baldintza ezberdinetan egin dira (indar normala, deslizamendu anplitudea eta ziklo-kopurua) marruskadura eta higadura portaerak ezagutzeko. Saiakuntzak hasieran, 90°ko angeluz gurutzatuta dauden zilindroen konfigurazio arrunt batean egin dira, ondoren, kableetan agertzen diren benetazko angelu ezberdinetan izan direlarik. Azterketa hauetan, harien arteko presioa eta higaduraren ondorioz sortzen diren partikulen eraginak aztertu dira, bi higadura mekanismo nagusi bereiztuz: higadura oldarkorra (saiakuntzaren hasieran) eta higadura egonkorra.

Tesi honetan garatu den higadura simulazioaren metodologia, Archard higaduraren legea maila lokalean aplikatzean datza. Higadura-simulazioa prozesu iteratiboa izanik, Archard-en ekuazioa lokala ebatzen da elementu mugatuen (FE) modelotik lortutako presio kontaktu eta deslizamendu erlatiboa erabiliz, behar diren deslizamendu erlatibo gehikuntza adina errepikatuz, distantzia osoa bete arte, *Fretting*-aren kasuan ziklo kopuru osoa bete arte. Tesi honetan aztertu den altzairuzko hariaren 3D simulazioak denbora konputazional handia eskatzen duela jakinik, edozein tribosisteman higadura simulatzeko metodologia

optimizatua proposatu da, higadura simulazioan parte hartzen duten parametro garrantzitsuen optimizazioan oinarrituta (sare tamaina, irrista gehikuntza eta higadura bizkorgailua).

Metodologia hau, zilindro-plano 2D FE modelo batean aplikatu da lehenik eta 90° zilindro gurutzatuta dauden 3D FE modelo batera egokitu da ondoren. Azkenik, metodologia hau angelu ezberdinez gurutzatzen diren zilindroen 3D FE modeloan inplementatu da. Modelo honek gainera parametro geometriko eta sarearen parametrizazioa dakar, kabletan agertzen diren kontaktu mota guztiak modelatzeko behar den denbora murrizteko. Metodologia honen erabilerarekin *fretting* higadura simulatzeko parametro optimoak identifikatu daitezkeela frogatu da, bai 2D modeloetan, baita 3D modeloetan, denbora konputazional txikiena eta pitzaduran diferentzia txikiena erabiliz.

Higadura simulatzeko metodologia optimizatua balioztatu da, balioztatzekeo prozesu zehatz bat jarraitu ondoren. Hau lortzeko hariekin egindako *fretting* saiakuntzen ondorioz lortutako higadura koefizienteak erabili dira. Balioztapen hau, pitzadurarekin erlazionatuta dauden hiru alderdietan oinarritu da: pitzaduraren dimentsioak, pitzaduraren sakonera (erdiko profila) eta bolumena.

Pitzaduren larritasuna aztertzekeo proposatu den higadura simulatzeko metodologia, kabletan agertzen diren parametro geometriko eta funtzionalen pean erabili da. Hariaren larritasunaren azterketa, azalera erresistentereen portzentai galera eta tentsio kontzentrazioa baliatuz aztertu da. Bi parametro hauek hariaren apurtzekeo ahalmenarekin eta nekearen bizitza murriztekeo ahalmenarekin loturik daude. Beraz, azterketa hau garatzeko esperimentu diseinuaren metodologia (DOE) erabili da. Azterketa honetan diametro eta angelu gurutzatuen bizitza murriztekeo ahalmena ikusi da.

Azkenik, *Fretting* fenomenoak altzairuzko harien neke bizitza murriztean duen efektua aztertu da, horretarako, 90°-ko higadura simulatzeko modelotik, marruskaduraren ondorioz agertzen diren kontaktuzko tentsio multiaxialak erabili dira. Neke-bizitza aurreikusteko metodologia, planu kritiko eta SWT (Smith-Watson-Topper) neke eredia 3D ko zilindro gurutzatu modeloaren inplementazioan datza. Horretaz gain, 3D modeloen higadura ziklikoa kontutan hartzekeo, kaltea pilatzeko modelo berri bat gehitu zaio. Azkenik, kontaktu presioaren eta deslizamendu anplitudearen eragina aztertu da, *fretting* saiakuntzan lortutako emaitzekin alderatuz. Tesi honen amaieran *fretting* fenomenoaren eraginez altzairuzko hariz osaturik dauden kable metalikoen neke bizitza aurreikusteko metodologia sendoagoa garatzeko jarraibideak proposatu dira.



---

# ZUSAMMENFASSUNG

---

Schwingungsverschleiß ist der wichtigste Abbaumechanismus der bei Drahtseilen auftaucht. Dieses Phänomen führt zu Verschleißnarben zwischen den sich berührenden dünnen Stahldrähten, was eine erhebliche Senkung der Lebensdauer dieser Komponenten erzeugt. Die komplexe Ansammlung von Leitungen in den Drahtseil-Systemen erschwert die experimentelle Charakterisierung dieses Phänomens, weil sie wirtschaftlich aufwendig ist und zu viel Zeit in Anspruch nimmt. Mit dem Ziel, diese Nachteile zu verringern und das Wissen über dieses Phänomen in komplexen Komponenten wie Seil-Systemen zu erhöhen, ist in dieser Arbeit eine Schwingungsverschleiß-Simulationsmethodik zur Vorhersage von Verschleißnarben bei dünnen Stahldrähten entwickelt worden. Das Problem des komplexen Mehrfachkontakts bei Drahtseilen wurde mittels eines entwickelten individuellen sich kreuzenden Zylinder-Modells vereinfacht. In diesem Modell kann das Ausmaß der Verschleißnarben im Bereich der verschiedenen geometrischen und betrieblichen Parameter bei jedem Kontakt analysiert werden.

Um das Reibungs- und Verschleißverhalten der dünnen Stahldrähte zu definieren, wurden Schwingungsverschleißtests in Bezug auf Reibungs- und Verschleißkoeffizient unter verschiedenen Bedingungen (Belastungen, Gleitamplitude und Anzahl der Zyklen) durchgeführt. Zuerst in einem allgemeinen tribologischen System von  $90^\circ$  gekreuzten Zylindern und dann mit unterschiedlichen Kreuzungswinkeln, was eine realistischere Konfiguration bei Drahtseilen darstellt. Diese Studie hat den Einfluss des Anpressdrucks und den Faserverschleiß auf das Verschleißverhalten untersucht. Zwei Verschleißmechanismen wurden beobachtet: ein aggressiverer Verschleißmechanismus am Anfang des Tests und ein stabilerer im weiteren Verlauf des Tests.

Die entwickelte Verschleiß-Simulationsmethodik basiert auf dem Archard Verschleißmodell, angewendet auf lokalem Niveau. Die Verschleiß-Simulation ist ein Iterationsverfahren, in dem die Archard Gleichung gemäß der Flächenpressung und Gleitverteilung durch die Finite-Element-Methoden gelöst wurde. Dennoch erfordert dieser Prozess eine hohe

Rechenzeit, die sich im Falle des 3D Problems bei den erwähnten dünnen Stahldrähten erhöht. Daher wurde eine optimierte Methodik zur Modellierung jedes tribologischen Systems vorgeschlagen. Sie basiert auf der Optimierung der Hauptparameter der Verschleißsimulation (Maschenweite, Gleiteinkrement und Beschleunigungverschleiß).

Diese Methodik wurde zunächst durch das 2D FE Modell auf Zylinder-Ebene angewandt. Anschließend wurde das 3D Schwingungverschleiß FE Modell, den 90° gekreuzten Zylindern angepasst. Schließlich wurde dieser Ansatz im Kreuzungswinkel-3D-FE-Modell implementiert. Es hat sich gezeigt, dass nach dieser Methode die optimalen Parameter für die Modellierung von 3D Schwingungverschleiß Problemen in Bezug auf die minimale Berechnungszeit mit der minimalen Differenz der endgültigen Verschleißnarbe definiert werden.

Die optimierte Verschleiß-Simulationsmethodik wurde schließlich nach einer genauen Validierungsmethodik für gültig erklärt. Dazu wurden die spezifischen Verschleiß-Koeffizienten, die in den Schwingungverschleißtests erhalten wurden, verwendet. Die Validierung basiert auf drei Aspekten der Verschleißnarben: Größe, Tiefe (Zentralprofil) und Ausmaß. Dieses Verfahren hat die genaue Validierung der oberen und unteren Verschleißnarbe gezeigt.

Die vorgeschlagene Methode wurde verwendet, um den Schweregrad der Verschleißnarben unter den verschiedenen geometrischen und betrieblichen Parameter in den Drahtseilen zu untersuchen. Es wurde eine Analyse des Schweregrads der Verschleißnarben hinsichtlich des Prozentsatzes von resistenten Flächenverlustdaten und den Kerbwirkungsfaktoren durchgeführt. Diese Faktoren stehen im Zusammenhang mit dem Bruch und der Verkürzung der Ermüdungslebensdauer des Drahtes. Für diese Studie wurde die Methodologie der Anordnung von Experimenten (DOE) verwendet. Der große Einfluß des Durchmessers und der Kreuzungswinkel wurde durch diese Studie deutlich.

Schließlich wurde die Wirkung von Schwingungverschleiß auf die Verkürzung der Ermüdungslebensdauer von dünnen Stahldrähten analysiert. Durch die Verwendung der 90° gekreuzten dünnen Stahldrähte des FE-Modells wurden induzierte multiaxiale Kontaktspannungen durch die Reibung beobachtet. Das Lebensdauer-Prognosemodell besteht aus der Anwendung der kritischen Ebene-Methode und dem SWT (Smith-Watson-Topper) Modell. Es wurde eine neue Schadensakkumulation-Methodik, die auf dem zyklischen Materialverschleiß in 3D Modellen basiert, entwickelt. Die Wirkung des Anpressdruckes und die Gleitamplitude wurde analysiert und mit den experimentell erhaltenen Ergebnissen kontrastiert. Am Ende dieser Forschungsarbeit werden Richtlinien für die Entwicklung einer robusten Methodik vorgeschlagen.

---

# PUBLICATIONS

---

## Journal Articles

A. Cruzado, M. A. Urchegui, X. Gómez, Finite element modeling and experimental validation of fretting wear scars in thin steel wires, *Wear* 289 (2012) 26-38.

A. Cruzado, A. Zabala, M. A. Urchegui, X. Gómez, Optimized methodology for the wear simulation of metallic materials, *Revista de metalurgia* 46 (2011) 106-114.

A. Cruzado, M. Hartelt, R. Wäsche, M.A. Urchegui, X. Gómez, Fretting wear of thin steel wires. Part 2: influence of crossing angle, *Wear* 273 (2011).60-69.

A. Cruzado, M. Hartelt, R. Wäsche, M.A. Urchegui, X. Gómez, Fretting wear of thin steel wires. Part 1: influence of contact pressure, *Wear* 268 (2010) 1409-1416.

### *Under Review:*

A. Cruzado, S. B. Leen, M. A. Urchegui, X. Gómez, Finite element analysis of fretting wear induced multiaxial stress state for fatigue life prediction in thin steel wires, *International Journal of fatigue* (Under Review).

A. Cruzado, M. A. Urchegui, X. Gómez, Finite element modeling of fretting wear scars in the thin steel wires used in wire rope systems with different crossing angles, *Wear* (Under Review).

## Conferences

A. Cruzado, I. Lizarralde, M. A. Urchegui, X. Gómez., Application of optimized methodology for wear simulation in 3D systems subjected to fretting, *XVIII Conferencia del grupo español de fractura*, 2011, Gijón, España.

A. Cruzado, A. Zabala, M. A. Urchegui, X. Gómez., Optimized methodology for the wear simulation of metallic materials, *XII Congreso nacional de propiedades mecánicas del solido*, 2010, Aránzazu, España.

A. Cruzado, M. Hartelt, R. Wäsche, M.A. Urchegui, X. Gomez., Fretting wear of thin steel wires: influence of crossing angle, *Nordtrib 2010*, 2010, Lulea, Sweden.

A. Cruzado, M. Hartelt, R. Wäsche, M.A. Urchegui, X. Gomez., Analysis of the influence of multistage cryogenic treatment in thin steel wires subjected to fretting wear, *XI Congreso nacional de materiales*, 2010, Zaragoza, España.

---

# CONTENTS

---

<b>Preface</b> .....	<b>v</b>
<b>Acknowledgments</b> .....	<b>vii</b>
<b>Abstract</b> .....	<b>ix</b>
<b>Resumen</b> .....	<b>xi</b>
<b>Laburpena</b> .....	<b>xv</b>
<b>Zusammenfassung</b> .....	<b>xvii</b>
<b>Publications</b> .....	<b>xix</b>
<b>Contents</b> .....	<b>xxi</b>
<b>List of tables</b> .....	<b>xxv</b>
<b>List of figures</b> .....	<b>xxvii</b>
<b>Glossary</b> .....	<b>xxxiii</b>
<b>1 Introduction</b> .....	<b>1</b>
1.1 Thesis framework .....	2
1.1.1 Wire ropes components .....	2
1.1.2 Steel wires damage mechanism.....	3
1.2 Motivation .....	5
1.3 Research objectives.....	6
1.4 Working methodology.....	6
1.4.1 Chapter II: Literature review .....	6
1.4.2 Chapter III: Fretting wear characterization in thin steel wires .....	7
1.4.3 Chapter IV: FEM modelling of fretting wear in thin steel wires .....	7
1.4.4 Chapter V: FEM analysis of the severity of the wear scars .....	8
1.4.5 Chapter VI: FEM-based fatigue life analysis due to fretting wear .....	8
1.4.6 Chapter VII: General conclusions, recommendations and further work.....	8
<b>2 Literature review</b> .....	<b>9</b>
2.1 Introduction .....	9
2.2 Contact mechanics.....	10
2.3 Fretting damage mechanism .....	15
2.3.1 Introduction.....	15
2.3.2 Fretting regimes.....	16
2.3.3 Experimental fretting tests parameters.....	21
2.3.4 Multiaxial fretting parameters.....	26

2.3.5	Fretting in steel wires .....	32
2.4	Fretting wear modelling .....	35
2.4.1	Wear models .....	35
2.4.2	Wear modelling .....	38
2.4.3	FE fretting wear modelling .....	42
2.5	Critical study of literature review .....	45
<b>3</b>	<b>Fretting wear characterization of thin steel wires in thin steel wires .....</b>	<b>49</b>
3.1	Introduction .....	49
3.2	Fretting test rig .....	50
3.2.1	Experimental details .....	50
3.2.2	Test program .....	52
3.2.3	Tribological quantities .....	57
3.2.3.1	Friction behaviour .....	58
3.2.3.2	Wear behaviour .....	58
3.3	Results and discussion .....	59
3.3.1	Fretting wear in 90° crossing angles thin steel wires .....	59
3.3.1.1	Friction behaviour .....	59
3.3.1.2	Wear behaviour .....	61
3.3.2	Fretting wear in thin steel wires with different crossing angles and the same normal force .....	69
3.3.2.1	Friction behaviour .....	69
3.3.2.2	Wear behaviour .....	70
3.3.3	Fretting wear in thin steel wires with different crossing angles and the same initial contact pressure .....	72
3.3.3.1	Friction behaviour .....	72
3.3.3.2	Wear behaviour .....	73
3.4	Conclusions .....	76
<b>4</b>	<b>FEM modelling of fretting wear in thin steel wires .....</b>	<b>79</b>
4.1	Introduction .....	79
4.2	FEM wear methodology of 2D block on ring model .....	80
4.2.1	Introduction .....	80
4.2.2	Block on ring experimental testing .....	81
4.2.2.1	Sliding wear test rig .....	81
4.2.2.2	Tribological quantities .....	82
4.2.2.3	Experimental tests results .....	83
4.2.3	FEM wear methodology .....	84
4.2.3.1	Cylinder on plane FE model .....	84
4.2.3.2	Wear local model .....	88
4.2.3.3	Wear simulation method .....	88
4.2.3.4	Optimized wear simulation methodology .....	90
4.2.4	Results and discussion .....	90

---

4.3	FEM methodology of fretting wear in thin steel wires .....	96
4.3.1	Introduction.....	96
4.3.2	FEM wear modelling.....	96
4.3.2.1	FEM model.....	96
4.3.2.2	Wear local model .....	101
4.3.2.3	Wear simulation method.....	102
4.3.3	Validation methodology .....	104
4.3.4	FEM wear simulation in 90° crossing angle arrangements .....	108
4.3.4.1	Introduction .....	108
4.3.4.2	Interpolation method study .....	108
4.3.4.3	FE wear parameters optimization.....	110
4.3.4.4	Wear modelling validation.....	114
4.3.5	FEM wear simulation in different crossing angle arrangements .....	119
4.3.5.1	Wear modelling optimization.....	119
4.3.5.2	Wear modelling validation.....	124
4.3.6	Conclusions.....	127
<b>5</b>	<b>FEM analysis of the severity of the wear scars.....</b>	<b>131</b>
5.1	Introduction .....	131
5.2	Methodology description .....	132
5.2.1	Geometrical parameters of the wire rope.....	132
5.2.2	Wear scar severity parameters description .....	134
5.2.3	Experimental design .....	137
5.3	Results and discussion .....	139
5.4	Conclusions .....	144
<b>6</b>	<b>FEM-based fatigue life analysis due to fretting wear.....</b>	<b>147</b>
6.1	Introduction .....	147
6.2	Experimental details.....	149
6.2.1	Introduction.....	149
6.2.2	Material .....	149
6.2.3	Tribological testing.....	150
6.3	FEM Methodology description.....	150
6.3.1	FEM model .....	150
6.3.2	Damage modelling.....	152
6.3.3	Material fatigue constants.....	158
6.4	Results and discussion .....	160
6.4.1	Introduction.....	160
6.4.2	Subsurfaces stress distribution analysis.....	161
6.4.3	Subsurface stress distribution in a pre-stressed wire .....	163
6.4.4	Fatigue crack nucleation analysis .....	165
6.4.5	Fretting wear life prediction methodology discussion.....	170
6.5	Conclusions .....	171

<b>7</b>	<b>General conclusions, recommendations and further work .....</b>	<b>173</b>
7.1	Introduction .....	173
7.2	Conclusions .....	173
7.3	Recommendation and further work.....	177
7.3.1	Fretting tests.....	177
7.3.2	Fretting wear modelling .....	178
7.3.3	Fretting wear-fatigue modelling.....	179
<b>8</b>	<b>References .....</b>	<b>181</b>



# LIST OF TABLES

Table 3-1. Fretting test conditions for different mean contact pressure and 90° crossing angle.....	54
Table 3-2. Fretting test conditions for different crossing angles and the same normal load.....	54
Table 3-3. Fretting test conditions for different crossing angles and the same mean contact pressure. .....	55
Table 3-4. Hertzian contact radius and wear scars contact radius limit for both 32.5 μm and 65 μm for the tests carried out with 90° crossing angle. ....	56
Table 3-5. Wear scars contact radius limit for the test carried out with different crossing angles the same load and 65 μm sliding amplitude. ....	57
Table 3-6. Wear scars contact radius limit for both 32.5 μm and 65 μm in the tests carried out with different crossing angles and the same initial mean contact pressure. ....	57
Table 3-7. Coefficients of wear for different tests for the running-in period and the stable period. ....	68
Table 4-1. Test specimens dimensions and roughness. ....	81
Table 4-2. Block on ring tests conditions values . ....	82
Table 4-3. FEM vs experimental wear scar dimension analysis for both top and bottom specimens. ....	115
Table 4-4. FEM vs experimental wear scar depth analysis for both top and bottom specimens.....	117
Table 4-5. FEM vs experimental wear scar volume analysis for both top and bottom specimens. ....	119
Table 4-6. FEM vs experimental wear scar dimension analysis for both top and bottom specimens. ....	125
Table 4-7. FEM vs experimental wear scar depth analysis for both top and bottom specimens.....	126
Table 4-8. FEM vs experimental wear scar volume analysis for both top and bottom specimens. ....	127
Table 5-1. Values corresponding to the geometrical values of nick type A and nick type B contacts in 7x19 stranded wire rope. ....	134
Table 5-2. Values obtained in the sensibility analysis of the optimum mesh size selection . ....	137
Table 5-3. Lower limit and upper limit of the different parameters used in the fractional factorial DOE for the analysis of the percentage of resistant area and the stress concentration factor <i>K<sub>t</sub></i> . ....	138
Table 5-4. Values of the different parameters used in the general full factorial DOE for the analysis of the percentage of resistant area and the stress concentration factor <i>K<sub>t</sub></i> . ....	139
Table 6-1. Mechanical properties of the 0.45 mm diameter wire. ....	150
Table 6-2. Fretting test conditions for the study of crack initiation process in 90° crossed cylinders steel wires.....	150
Table 6-3. Coefficients of wear obtained from fretting wear tests under different loads-stroke conditions.....	152
Table 6-4. Estimation methods of fatigue coefficients from monotonic tensile tests. [28-30]. ....	159

Table 6-5. Mechanical properties of Beretta's 1.97 mm diameter wire. [155] .....	159
Table 6-6. A summary of the fatigue coefficients obtained from the different methods. ....	160
Table 6-7. Comparison of measured and predicted lives and failure locations under different SWT coefficients fitting methods (x represents de location from the centre of the wear scar, D represent the damage after $50 \times 10^3$ number of cycles ).....	169

# LIST OF FIGURES

Fig. 1-1. Steel wire ropes application: (a) lifts [1], (b) cranes [2], (c) funicular [3].	2
Fig. 1-2. Schematic of a wire rope composed of different strands of wound steel wires [4].	3
Fig. 1-3. Wire rope-sheave system in a gearless elevator motor [7]: (a) photograph and (b) schematic of the wire rope-sheave system.	4
Fig. 1-4. Type of contacts detected in a wire rope system [4]: (a) linear contacts (b) punctual contacts; nick type B (between the outermost wires of adjacent strands) and nick type A between the outermost wires of strands and core .	4
Fig. 1-5. Wear scars produced by the different contact types [4]: (a) linear wear scar, (b) elliptical wear scar produced by nick type A, (c) elliptical wear scar produced by nick type B.	5
Fig. 2-1. Crossed cylinders contact types: (a) linear contact (both cylinders parallel to each axis), (b) elliptical point contact (both cylinders crossing at different angles), (c) circular point contact (both cylinders crossing at 90°).	11
Fig. 2-2. Distribution of pressure and stresses in on the contact surface according to Hertz: (a) Normalised contact pressure, (b) subsurface normalised stresses for $\nu = 0.3$	13
Fig. 2-3. Shear tractions distribution of the Midlind problem ( $Q/F_n=0.5, f=0.7$ ).	14
Fig. 2-4. Hysteresis loop friction force–relative displacement for the different fretting sliding conditions: (a) stick , (b) partial slip, (c) gross slip.	17
Fig. 2-5. Fretting maps: (top) running condition fretting map (RCFM): PSR: partial slip regime; MFR: mixed fretting regime; GSR: gross slip regime and (bottom) material response fretting map (MRFM): cracking (PSR); wear-cracking (MSR), wear (GSR) [27].	18
Fig. 2-6. Fretting regimes transition criteria: (a) Friction force–relative displacement hysteresis loop, (b). Evolution of A, f and %GS in running conditions tests [29].	19
Fig. 2-7. Friction force–relative displacement hysteresis loop.	21
Fig. 2-8. Hysteresis loop friction force–relative displacement in a fretting wear test: definition of stroke.	22
Fig. 2-9. Hysteresis loop friction force-displacement in a fretting wear test: definition of coefficient of friction.	23
Fig. 2-10. Evolution of friction force-displacement curves under different displacement amplitudes ( $F_n=9$ N): (a) Partial slip regime, (b) mixed slip regime, (c) gross slip regime.[80]	34
Fig. 2-11. Fretting cracks observed in dry sliding and water conditions: (a) wear scar in dry condition, (b) transversal perspective of the crack in dry conditions, (c) wear scar in immersed condition, (d) transversal perspective of the crack in immersed condition.[84]	35
Fig. 2-12. Wear particles formation FE model based on fracture mechanics [116].	40
Fig. 2-13. Wear simulation example using the movable cellular automata (MCA) method [119].	41
Fig. 3-1. SEM micrograph of Brass film cover in a longitudinal cut of the wire.	51

Fig. 3-2. Photograph of the fretting wear test rig .....	51
Fig. 3-3. Wire supporting holders: (a) bottom holder (left) and upper holder (right), (b) top view of the bottom wire supporting holder, (c) upper holder in the fixing arm (detailed image of the marks introduced in the holder for different crossing angles configurations.) .....	52
Fig. 3-4. Friction behaviour plots for 3 N-65 $\mu\text{m}$ and 2000000 numbers of cycles: (a) coefficient of friction evolution along the cycles and (b) $F_f$ - $\delta$ hysteresis loops during a fretting test and..	58
Fig. 3-5. Coefficient of friction for 90° crossed cylinder fretting tests with different normal loads, strokes and number of cycles.....	60
Fig. 3-6. Total dissipated energy for 90° crossed cylinder fretting tests with different normal loads, strokes and number of cycles.....	61
Fig. 3-7. Wear scar surface after the test: (a) wire specimen with wear scar and debris; (b) surface inside wear scar.....	61
Fig. 3-8. Oxide wear particles: (a) inside wear scar; (b) compacted wear particles; (c) outside wear scar and (d) shape of oxide wear particle.....	62
Fig. 3-9. Volumetric wear of both wear scars for 90° crossed cylinder fretting tests with different normal loads, number of cycles and a stroke of 65 $\mu\text{m}$ : (a) top specimen (b) bottom specimen. ....	63
Fig. 3-10. Wear scars in upper wire (cylinder 1: perpendicular to sliding cylinder: static): (a) $F_n=1$ N, $\Delta x=130$ $\mu\text{m}$ , $n = 20 \times 10^3$ cycles; (b) $F_n=1$ N, $\Delta x=130$ $\mu\text{m}$ , $n = 50 \times 10^3$ cycles; (c) $F_n=1$ N, $\Delta x=130$ $\mu\text{m}$ , $n = 100 \times 10^3$ cycles.....	63
Fig. 3-11. Wear scars in bottom wire (cylinder 2: parallel to the sliding displacement: moving): (a) $F_n=1$ N, $\Delta x=130$ $\mu\text{m}$ , $n = 20 \times 10^3$ cycles; (b) $F_n=1$ N, $\Delta x=130$ $\mu\text{m}$ , $n = 50 \times 10^3$ cycles; (c) $F_n=1$ N, $\Delta x=130$ $\mu\text{m}$ , $n = 100 \times 10^3$ cycles.....	63
Fig. 3-12. Total volumetric wear for 90° crossed cylinder fretting tests with different normal loads, strokes and number of cycles: (a) influence of normal load and (b) influence of stroke. ....	64
Fig. 3-13. Coefficient of wear for 90° crossed cylinder fretting tests with different normal loads, strokes and number of cycles: (a) influence of normal load and (b) influence of stroke. ....	65
Fig. 3-14. Energy-specific wear resistance for 90° crossed cylinder fretting tests with different normal loads, strokes and number of cycles: (a) influence of normal load and (b) influence of stroke. ....	65
Fig. 3-15. Square of on-line linear wear $W_{l,onl}^2$ for 20 x 10 <sup>3</sup> , 50 x 10 <sup>3</sup> , 100 x 10 <sup>3</sup> , 200 x 10 <sup>3</sup> , 1 N and 130 $\mu\text{m}$ . ....	66
Fig. 3-16. The on-line Volumetric wear $W_{v,onl}$ with respect to the Archard's loading factor for different tests: (a) the influence of load for 65 $\mu\text{m}$ stroke and (b) the influence of stroke for 1 N load.	67
Fig. 3-17. The total volumetric wear $W_{v,tot}$ with respect to the Archard's loading factor for different tests: (a) the influence of load for 65 $\mu\text{m}$ stroke and (b) the influence of stroke for 1N load.	68
Fig. 3-18. The on-line volumetric wear as function of Archard's loading factor $F_n \times s$ .....	69
Fig. 3-19. Coefficient of friction for different crossing angles 1 N-130 $\mu\text{m}$ and 50000 cycles.....	69
Fig. 3-20. Wear scars in upper wire (cylinder 1: perpendicular to sliding cylinder: static): (a) $F_n=1$ N, $\Delta x=130$ $\mu\text{m}$ , $n = 50 \times 10^3$ cycles, $\beta = 30^\circ$ ; (b) $F_n=1$ N, $\Delta x=130$ $\mu\text{m}$ , $n = 50 \times 10^3$ cycles, $\beta = 60^\circ$ ; (c) $F_n=1$ N, $\Delta x=130$ $\mu\text{m}$ , $n = 50 \times 10^3$ cycles, $\beta = 90^\circ$ .....	70
Fig. 3-21. Wear scars in bottom wire (cylinder 2: parallel to sliding cylinder: moving): (a) $F_n=1$ N, $\Delta x=130$ $\mu\text{m}$ , $n = 50 \times 10^3$ cycles, $\beta = 30^\circ$ ; (b) $F_n=1$ N, $\Delta x=130$ $\mu\text{m}$ , $n = 50 \times 10^3$ cycles, $\beta = 60^\circ$ ; (c) $F_n=1$ N, $\Delta x=130$ $\mu\text{m}$ , $n = 50 \times 10^3$ cycles, $\beta = 90^\circ$ .....	70
Fig. 3-22. Wear behaviour analysis results for different crossing angles 1 N-130 $\mu\text{m}$ and 50000 cycles: (a) total volumetric wear; (b) total linear wear; (c) energy-specific wear resistance and (d) coefficient of wear.....	72

Fig. 3-23. Coefficient of friction for different crossing angles and the same initial mean contact pressure. ....	73
Fig. 3-24. Wear scars in upper wire (cylinder 1: perpendicular to sliding cylinder: static): (a) $F_n=1.6$ N, $\Delta x=130 \mu\text{m}$ , $n = 50 \times 10^3$ cycles, $\beta = 45^\circ$ ; (b) $F_n=1.1$ N, $\Delta x=130 \mu\text{m}$ , $n = 50 \times 10^3$ cycles, $\beta = 75^\circ$ ; (c) $F_n=1$ N, $\Delta x=130 \mu\text{m}$ , $n = 50 \times 10^3$ cycles, $\beta = 90^\circ$ .....	73
Fig. 3-25. Wear scars in bottom wire (cylinder 2: parallel to sliding cylinder: moving): (a) $F_n=1.6$ N, $\Delta x=130 \mu\text{m}$ , $n = 50 \times 10^3$ cycles, $\beta = 45^\circ$ ; (b) $F_n=1.1$ N, $\Delta x=130 \mu\text{m}$ , $n = 50 \times 10^3$ cycles, $\beta = 75^\circ$ ; (c) $F_n=1$ N, $\Delta x=130 \mu\text{m}$ , $n = 50 \times 10^3$ cycles, $\beta = 90^\circ$ .....	74
Fig. 3-26. Wear behaviour analysis results for different crossing angles the same initial mean contact pressure and two strokes: (a) total volumetric wear, (b) total linear wear, (c) energy-specific wear resistance and (d) coefficient of wear. ....	75
Fig. 4-1. Photograph of the block on ring test rig: (a) tribometer and (b) testing specimens.....	82
Fig. 4-2. Volumetric wear calculation: (a) testing specimen with the wear scar and (b) wear scar profile.....	83
Fig. 4-3. Friction and wear behaviour results: (a) coefficient of friction and (b) Volumetric wear of the block vs. Archard's loading factor (coefficient of wear). ....	84
Fig. 4-4. Cylinder on plane FE model: (a) FE mesh, (b) partitions near the contact zone and (c) mesh in the contact zone. ....	85
Fig. 4-5. Boundary conditions in the block on ring FE model: (a) step 1 and (b) step2.....	85
Fig. 4-6. Surface stress distribution $\sigma_{xx}$ in the block: (a) FEM model and (b) surface stresses with and without sliding. ....	86
Fig. 4-7. Contact pressure and slip distribution study: (a) comparison of the contact pressure distribution with and without sliding (b) Deviation of the contact pressure with sliding and (c) slip distribution in the contact width. ....	87
Fig. 4-8. Wear simulation algorithm including UMESHMOTION subroutine for the sliding wear case. ....	89
Fig. 4-9. Contact pressure: (a) for different mesh sizes, (b) evolution of the contact pressure with the sliding distance. ....	91
Fig. 4-10. Mesh size analysis with respect to the contact pressure for two sliding distance: (a) 240m, (b) 1800 m (0.25m/s-2h) tribometer test.....	92
Fig. 4-11. Effect of the mesh size for a 0.25 m/s-2 h-65 N test: (a) evolution of the maximum contact in the first 20 m and (b) final wear scars for different meshes. ....	93
Fig. 4-12. Analysis of the maximum wear increment for a sliding distance of 480 mm: (a) influence of the sliding discretization in the contact pressure and (b) maximum wear increment vs maximum wear depth. ....	94
Fig. 4-13. Effect of the variable accelerator factor: (a) influence in the maximum contact pressure and (b) influence in the final wear scar.....	95
Fig. 4-14. Experimental wear scar vs FEM wear scar for the test conditions: 0.25 m/s-2 h-65 N.....	96
Fig. 4-15. FE model end mesh details of $90^\circ$ crossed cylinders: (a) full model, (b) contact region detail for top cylinder, (c) contact region detail for bottom cylinder. ....	97
Fig. 4-16. FE model and mesh details of $30^\circ$ crossed cylinders: (a) full model, (b) contact region detail for top cylinder, (c) contact region detail for bottom cylinder. ....	98
Fig. 4-17. Ramp amplitude graph for the application the reciprocating movement in step 2. ....	99
Fig. 4-18. Wear simulation algorithm including UMESHMOTION subroutine for fretting wear problems. ....	102
Fig. 4-19. Wear scars of top and bottom: (a) top wear scar obtained by SEM, (b) top longitudinal profile obtained by confocal microscopy, (c) bottom wear scar obtained by SEM, (d) bottom longitudinal profile obtained by confocal microscopy. ....	105
Fig. 4-20. Wear scars of top specimen: (a) top wear scar obtained by SEM in the direction of the major axis, (b) top longitudinal profile obtained in the direction of the major axis by confocal	

microscopy, (c) top wear scar obtained by SEM in the longitudinal direction of the wire axis, (d) top longitudinal profile obtained in the longitudinal direction of the wire by confocal microscopy. ....	106
Fig. 4-21. Wear scars of bottom specimen: (a) bottom wear scar obtained by SEM in the longitudinal direction of the wire axes, (b) bottom longitudinal profile obtained in the longitudinal direction of the wire by confocal microscopy. ....	106
Fig. 4-22. Confocal 3D image of the bottom wear scar: (a) 90° crossing angle and (b) 15° crossing angle. ....	107
Fig. 4-23. Planimetric wear of the centre profile of top wear scar obtained by FEM. ....	108
Fig. 4-24. Longitudinal wear scars comparison with different interpolation methods: (a) top wear scar, (b) magnification of (a), (c) bottom wear scar and (d) magnification of (c). ....	109
Fig. 4-25. Longitudinal wear scar with and without interpolation: (a) top and (b) bottom wear scar. ....	110
Fig. 4-26. Hertzian contact pressure vs FEM contact pressure for different mesh: (a) contact pressure distribution without wear and (b) maximum contact pressure evolution in the first 1000 wear cycles. ....	111
Fig. 4-27. Longitudinal wear scar in the bottom specimen for different mesh sizes: (a) 1000 number of cycles and (b) 20000 number of cycles. ....	112
Fig. 4-28. Longitudinal wear scar in the bottom specimen: (a) for different increments per cycle and 1000 number of cycles and (b) for different cycle jumps for 1000 and 20000 number of cycles. ....	113
Fig. 4-29. FEM wear scars for a 1 N-130 $\mu\text{m}$ -50000 cycles: (a) top wear scar, (b) bottom wear scar. ....	114
Fig. 4-30. Wear scars of top specimen for 1 N-130 $\mu\text{m}$ : (a) 20000 cycles SEM, (b) 50000 cycles SEM, (c) 200000 cycles SEM, (d) 20000 cycles FEM vs experimental, (e) 50000 cycles FEM vs experimental and (f) 200000 cycles FEM vs experimental. ....	116
Fig. 4-31. Wear scars of bottom specimen for 1 N-130 $\mu\text{m}$ : (a) 20000 cycles SEM, (b) 50000 cycles SEM, (c) 200000 cycles SEM, (d) 20000 cycles FEM vs experimental, (e) 50000 cycles FEM vs experimental and (f) 200000 cycles FEM; vs experimental. ....	116
Fig. 4-32. Longitudinal wear scar for different coefficient of friction: (a) top wear scar (b) bottom wear scar. ....	118
Fig. 4-33. Longitudinal wear scar for different coefficient of wear ratios: (a) top wear scar (b) bottom wear scar. ....	118
Fig. 4-34. Contact pressure distribution: (a) for 15° crossing angle and (b) for 60° crossing angle. ....	120
Fig. 4-35. Contact pressure distribution FEM vs HERTZ for 30° crossing angle: (a) major axis contact width, (b) minor axis contact width. ....	120
Fig. 4-36. Semi-axes ratio vs crossing angle for Hertzian contact ellipse and for 50000 cycles 1N and 130 $\mu\text{m}$ experimental top wear scar. ....	121
Fig. 4-37. FEM top wear scar profiles for 1 N-130 $\mu\text{m}$ -50000 cycles 30° crossing angles and different meshes: (a) longest axis position, (b) shortest axis position. ....	122
Fig. 4-38. FEM top wear scar profiles for 1 N-130 $\mu\text{m}$ -50000 cycles 30° crossing angles and different cycle jumps: (a) longest axis position, (b) shortest axis position. ....	123
Fig. 4-39. Wear scars of top specimen for 1 N-130 $\mu\text{m}$ -20000 cycles: (a) 15° experimental, (b) 45° experimental, (c) 60° experimental, (d) 15° FEM, (e) 45° FEM, (f) 60° FEM. ....	124
Fig. 4-40. Wear scars of top specimen for 1 N-130 $\mu\text{m}$ -20000 cycles: (a) 15° longest axis, (b) 45° longest axis (c) 60° longest axis, (d) 15° longitudinal direction of the specimen, (e) 45° longitudinal direction of the specimen, (f) 60° longitudinal direction of the specimen. ....	126
Fig. 5-1. Description of the contacts produced between the outermost wires of strands (Nick B) and the outermost wires of strands and core (Nick A) in a 7 x 19 stranded wire rope. ....	133
Fig. 5-2. Wear scars of top specimen for 1 N-130 $\mu\text{m}$ -20000cycles: (a) longitudinal perspective, (b) transversal cut. ....	135
Fig. 5-3. FE model and mesh for the Stress Concentration Factor calculation: a) FEM, b) S33 stress distribution. ....	136

Fig. 5-4. Main effects plot for the percentage of resistant area loss $A_{R, loss}[\%]$ under different factors: (a) diameter, (b) crossing angle, (c) normal force, (d) stroke, (e) curvature.....	140
Fig. 5-5. Main effects plot for Stress concentration factor $K_t$ under different factors: (a) diameter, (b) crossing angle, (c) normal force, (d) stroke, (e) curvature. ....	141
Fig. 5-6. Main effects plot for: the percentage of resistant area loss $A_{R, loss}[\%]$ under different factors: (a) diameter, (b) crossing angle; and for the stress concentration factor $K_t$ under different factors: (c) diameter, (d) crossing angle.....	142
Fig. 5-7. Interaction plots for: the percentage of resistant area loss $A_{R, loss}[\%]$ under different factors: (a) diameter, (b) crossing angle; and for the stress concentration factor $K_t$ under different factors: (c) diameter, (d) crossing angle .....	143
Fig. 6-1. Experimentally obtained engineering stress- strain curve for 0.45 mm diameter wire.....	149
Fig. 6-2. FE model and mesh details of the 90° crossed cylinder fretting wear test.....	151
Fig. 6-3. FE mesh in the adaptative meshing framework and each centroid points: (a) 3D FE mesh with a cut of one of the longitudinal plans, (b) FE mesh with the centroid points before and after the wear process.....	155
Fig. 6-4. Flow chart of the accumulative damage model due to the effect of the material removal. ....	157
Fig. 6-5. Damage accumulation process: (a) Damage of the first cycle (circle) in the first three layers and the two linear equations which represent the evolution of the damage between the layers, (b) damage in the second FE cycle due to wear (square), (c) damage of the first cycle interpolated back to the new centroid position of the second cycle (x), (d) accumulated damage in the second cycle (triangle) and the new linear equations (graphic b plus graphic c).....	158
Fig. 6-6. Fitting curve to obtain the Basquin's coefficients from the uniaxial fatigue tests data reported by Beretta and Mateazzi [155] according to the Goodman relationship. ....	160
Fig. 6-7. Subsurface stress distribution for 1 N-130 $\mu\text{m}$ , 20000 number of cycles and different amplitude displacement locations: a) stress distribution $\sigma_{11}$ , b) stress distribution $\sigma_{13}$ .....	161
Fig. 6-8. Multiaxial subsurface stress distribution in the bottom cylinder for 1 N-130 $\mu\text{m}$ and different number of cycles in the amplitude displacement position of 65 $\mu\text{m}$ : (a) stress distribution $\sigma_{11}$ , (b) stress distribution $\sigma_{22}$ , (c) shear stress distribution $\sigma_{13}$ and (d) shear stress distribution $\sigma_{12}$ .....	162
Fig. 6-9. The axial subsurface distribution for 1 N-130 $\mu\text{m}$ and different coefficient of friction: (a) stress distribution $\sigma_{11}$ , (b) shear stress distribution $\sigma_{13}$ .....	163
Fig. 6-10. Elastic-plastic finite element analysis of the wire fixation $\sigma_{11}$ axial stresses.....	164
Fig. 6-11. The axial subsurface stress distribution for 1 N-130 $\mu\text{m}$ , 50000 number of cycles and different pre-stresses in the amplitude displacement position of 65 $\mu\text{m}$ : (a) stress distribution $\sigma_{11}$ , (b) shear stress distribution $\sigma_{13}$ .....	165
Fig. 6-12. FE critical plane SWT plots for 1 N-130 $\mu\text{m}$ and 2000 MPa pre-stress: (a) longitudinal SWT value plot for different number of cycles, (b) evolution of SWT peak value, (c) 3D plot of the SWT value without wear, (d) 3D SWT value plot after 50000 number of cycles. ....	166
Fig. 6-13. FE critical plane SWT plots for 1 N-130 $\mu\text{m}$ with and without pre-stress: (a) SWT peak value evolution, (b) longitudinal plot of the maximum SWT value. ....	167
Fig. 6-14. Failure of the wire under different conditions fretting wear tests: (a) 4 N-65 $\mu\text{m}$ -2 x 10 <sup>4</sup> , (b) 2 N-130 $\mu\text{m}$ -2 x 10 <sup>4</sup> .....	167
Fig. 6-15. FEM simulated wear scars for: (a) 4 N-65 $\mu\text{m}$ -2 x 10 <sup>4</sup> , (b) 2 N -130 $\mu\text{m}$ -2 x 10 <sup>4</sup> . ....	168
Fig. 6-16. Predicted location of the failure according to Manson's universal slope coefficients: 4 N-65 $\mu\text{m}$ -5.5 x 10 <sup>3</sup> , (a) Top view, (b) longitudinal cut; 2 N-130 $\mu\text{m}$ -2.45 x 10 <sup>4</sup> , (c) Top view, (d) longitudinal cut.....	170





---

# GLOSSARY

---

$a$	Contact radius / semi contact width / contact ellipse major semi-axis
$A$	Energy ratio
$A_{R,loss}$	Percentage of resistant area loss
$b$	Contact ellipse minor semi-axis / Basquin's fatigue strength exponent
$c$	Midlin stick radius / Coffin-Manson fatigue ductility exponent
$d$	Diameter of the wire
$d_r$	Diameter of the wire rope
$D$	Diameter of the sheave
$D$	Cyclic damage
$e$	Relation between the sliding amplitude and the contact zone radius
$E$	Young modulus
$E_e$	Equivalent Young modulus
$E_d$	Frictional dissipated energy during one fretting cycle
$f$	Coefficient of friction
$f_r$	Frequency
$f$	Friction ratio
$F_f$	Friction force
$F_n$	Normal force
$h$	Gap between undeformed surfaces in Hertz contact
$H$	Hardness of the material
$k$	Coefficient of wear
$k_1$	Local coefficient of wear
$K$	Archard's coefficient of wear
$K_t$	Stress concentration factor
$l$	Width of the block
$n$	Number of cycles
$N_i$	Number of cycles for crack initiation
$p$	Contact pressure
$p_m$	Mean contact pressure
$p_{max}$	Maximum contact pressure
$q$	Tangential traction
$Q$	Tangential force
$r_c$	Radius of curvature
$r_e$	Energy specific wear resistance
$r_s$	Theoretic radius of the strand or the core
$R$	Radius of curvature

$R_a$	Surface average roughness
$R_e$	Reduced radius of curvature
$s$	Sliding distance
$T$	Temperature
$\nu$	Poisson coefficient
$w$	Damage
$W_l$	Linear wear
$W_{l,onl}$	On-line linear wear
$W_q$	Planimetric wear
$W_v$	Volumetric wear
$W_{v,onl}$	On-line volumetric wear
$x, y, z$	Cartesian coordinates
$\Delta\varepsilon_a$	Strain amplitude
$\Delta h$	Incremental wear depth
$\Delta n$	Cycle jump
$\Delta s$	Incremental slip / relative slip
$\Delta x$	Stroke
$\Delta x_{\text{peak-peak}}$	Peak-to-peak stroke
$\Delta x_{\text{sliding}}$	Sliding stroke
$\beta$	Crossing angle
$\varepsilon$	Strain
$\varepsilon'_f$	Coffin-Manson fatigue ductile coefficient
$\alpha$	Energetic wear coefficient
$\gamma$	Twisting angle
$\sigma$	Principal stress
$\sigma_a$	Alternating stress
$\sigma'_f$	Basquin's fatigue strength coefficient
$\sigma_m$	Mean stress
$\sigma_{\text{max}}$	Maximum stress
$\sigma_{\text{nom}}$	Stress in the net section
$\sigma_u$	Ultimate tensile strength
$\sigma_y$	Yield strength
$\tau$	Shear stress
$\delta(t)$	Relative displacement between two contacting surface at time t
$\delta_d$	Sliding amplitude

### Abbreviation

BEM	Boundary Element Method
DOE	Design of experiments
FC	Fibre core
FEA	Finite Element
FEA	Finite Element Analysis
FEM	Finite Element Method
FS	Fatemi Socie
GSR	Gross slip regime
IWRC	Independent wire rope core
MCA	Movable cellular automata

MPM	Material point mesh
MRFM	Material response fretting map
MSR	Mixed slip regime
NFC	Natural fibres core
PSR	Partial slip regime
RCFM	Running condition fretting map
RA	Reduction in area
RH	Relative humidity
SEM	Scanning electron microscopy
SFC	Synthetic fibres core
SWT	Smith Watson Topper
WC	Steel core
WSC	Wire strand core
X-FEM	Extended finite element method



---

## CHAPTER I

# INTRODUCTION

---

This document presents the thesis 'Finite Element Modelling and Experimental Validation of Fretting Wear in Thin Steel Wires' to obtain the Ph. D. degree. The research presented in this dissertation is focused in developing numerical tools for the simulation of fretting wear in the thin steel wires used in the wire rope systems.

Nowadays, the new tendencies in the elevator sector focus on gearless electric motors. These types of engines take up less space, so the main advantage is that the machine room is no longer needed, saving great space and reducing the construction costs. Nevertheless, these engines produce less torque with the disadvantage that the used sheaves have to be smaller. So the working conditions of the main traction system of the lifts 'Wire rope-sheave' are more aggressive, increasing one of the main damage mechanism of wire ropes 'Fretting'. The increased pressure in the last years to improve the main traction system used in the lifts and as a consequence the main component used in this system 'Wire rope', has motivated this research work.

Orona Elevator Innovation Center (EIC), in cooperation with Mondragon Unibertsitatea (MU) and Ikerlan-IK4, has promoted different research projects to design new generation of wire ropes for the new generation traction systems with gearless electric engines and small sheaves. Thus, the acquired knowledge will be used to improve the design of the new generation wire rope systems for the gearless electric motors.

This chapter is focused on describing the thesis framework, motivation, objectives and the methodology proposed to develop this research work. First of all, the framework of the thesis related to the following two aspects are presented:

- Wire ropes.
- Steel wires damage mechanism.

Based on fretting wear, which is the main damage mechanism produced in wire rope systems, and with the aim to understand better this phenomenon in thin steel wires with geometrical and loading conditions close to those presented in the wire ropes, the motivation of this research study is outlined.

From the previous two points the research objectives of the thesis are defined. The main objective of this thesis is the development of a numerical tool for the improvement the knowledge about fretting wear in wire rope components. This general purpose is also complimented with some specific objectives. Finally, the thesis scope is presented; describing the main stages needed to carry out both the general and the specific objectives and to structure this research work.

The current thesis has been carried out within the research group of ‘Surface Technologies’ and it has been developed within the Ph. D. program ‘Mechanical Behaviour and Materials’ at the University of Mondragon. This thesis has been financially supported by Orona EIC in the frame of the SIMCABLE-PREVI project and the Basque Government under the Universidad Empresa program in the frame of the SIVICA project.

## 1.1 Thesis framework

---

### 1.1.1 Wire ropes components

Steel wire ropes are the main mechanical components used as elements for transporting people, material or equipment, such as, drum hoists, cranes, residential or industrial lifts, funicular railway, sky lifts, etc. (Fig. 1-1). The main reason to use these components is because they combine two useful properties, indispensable in these types of mechanisms (wire rope-sheave or wire rope-drum): high axial strength and bending flexibility. These two properties are obtained due to the use of high strength steel wires which are hierarchically spirally twisted in complex configurations.



Fig. 1-1. Steel wire ropes application: (a) lifts [1], (b) cranes [2], (c) funicular [3].

As shown in Fig. 1-2 the wire ropes are composed of individual wires twisted spirally in various layers along a central wire to form strands, which are then wound into a central core to form the final rope. The mechanical properties of wire ropes mainly depend on their construction and the properties of the wires itself. Molkow and Wolfgang [5] reported that the properties of the rope depend on the number, size and arrangement of the wires in the strands, the number and arrangement of the strands and the core type. The core is usually made of fibre or steel. While the fibre core (FC) is made either from natural fibres (NFC) or synthetic fibres (SFC), steel core (WC) is made from steel wires arranged as a wire strand (WSC) or normally as an independent wire rope (IWRC). Feyrer [6] in his book about wire ropes presents numerous formulas about the life calculations of different types of wire ropes in both stationary or running conditions, analyzing the wire ropes under tensile loads and under bending and tensile stress loads respectively.

This research is focused on a problematic appeared in steel wire ropes formed by WC core in running conditions and used mainly in the elevator sector. This problematic will be analyzed in the following section.

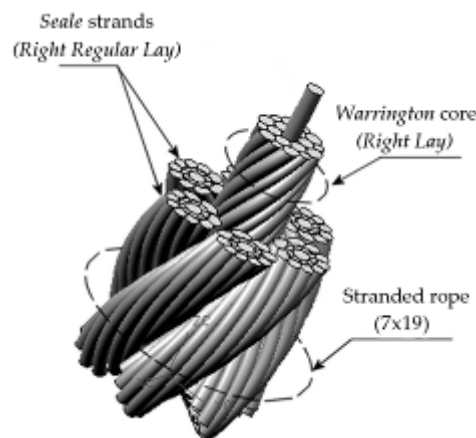
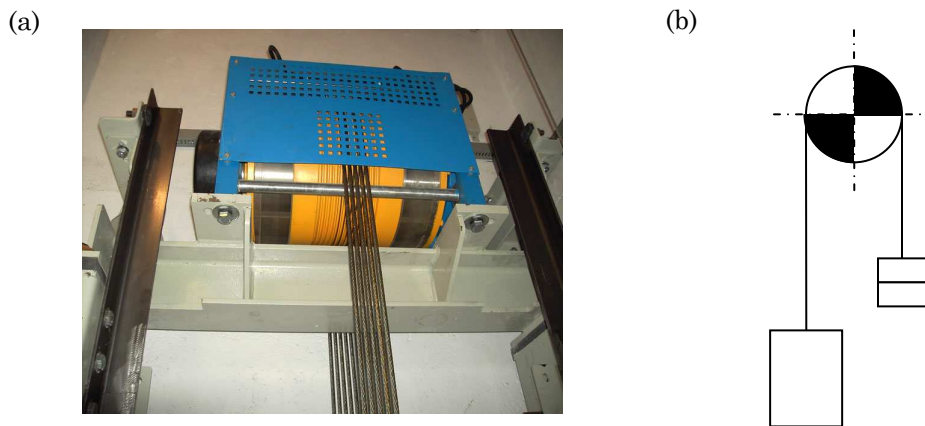


Fig. 1-2. Schematic of a wire rope composed of different strands of wound steel wires [4].

### 1.1.2 Steel wires damage mechanism

As has been mentioned previously the main mechanism, in which the wire ropes are used, is the wire rope-sheave or wire rope-drum system as it is shown in Fig. 1-3. Nevertheless when the wire ropes run over the sheaves, they are subjected to the combine axial tensile load and bending stretch load, which leads to an oscillatory motion between the neighboring contacting wires. This phenomena results in a fretting wear damage mechanism as reported by Schrems [8] and Waterhouse [9].



**Fig. 1-3. Wire rope-sheave system in a gearless elevator motor [7]: (a) photograph and (b) schematic of the wire rope-sheave system.**

Urchegui et al. [10] studied this effect into a 7x19 stranded rope. As shown in Fig. 1-4 the steel wire ropes are composed by different contact types between wires. While linear contacts appear between the neighboring wires of the same strands, point contacts appear between the outermost wires of adjacent strands (Nick type B) and between the outermost wires of strands and core (Nick type B). The wear scars produced as a consequence of point contacts are known as Nick or Trellis [8].

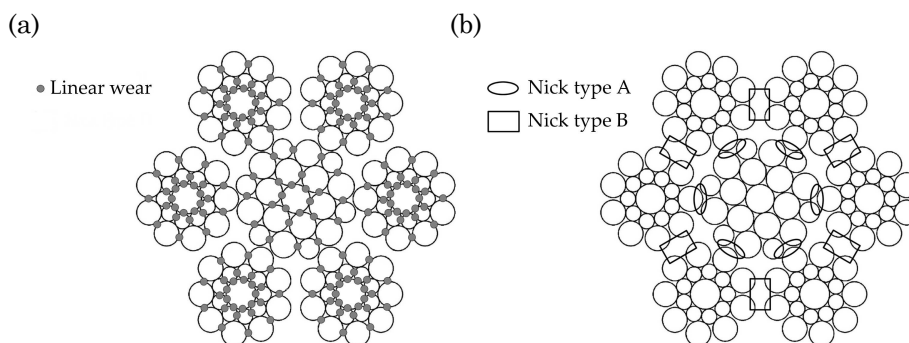


**Fig. 1-4. Type of contacts detected in a wire rope system [4]: (a) linear contacts (b) punctual contacts; nick type B (between the outermost wires of adjacent strands) and nick type A between the outermost wires of strands and core .**

These type of contacts leads into a different wear scars due to the fretting wear problem. While linear contacts produce linear wear scars (Fig. 1-5(a)), the point contacts produce elliptical wear scars as shown in (Fig. 1-5(b)) and (Fig. 1-5(c)). The most dangerous wear scars are the elliptical wear scars that produce high level of wear, causing a considerable reduction in the resistant area of the wire, which leads to an increase in the stresses on the worn cross section area and the failure of the wire.



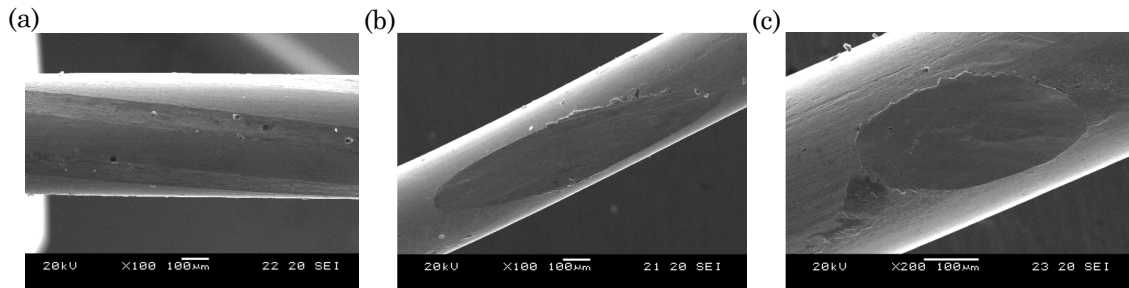


**Fig. 1-5. Wear scars produced by the different contact types [4]: (a) linear wear scar, (b) elliptical wear scar produced by nick type A, (c) elliptical wear scar produced by nick type B.**

Currently one of the most important trend taking place in the elevator sector focuses on gearless electric motors. These types of engines take up less space, so the main advantage is that the machine room is no longer needed, saving great space and reducing the construction costs. Nevertheless these types of engines produce less torque with the disadvantage that the used sheaves have to be smaller than the sheaves used with the geared engines. According to the standard UNE-EN 81-1 [11], the ratio between the sheave diameter  $D$  and the rope diameter  $d_r$  for traction elevators must be greater than or equal to forty ( $D/d_r \geq 40$ ). So the wire ropes used in the new elevator generation solutions should be smaller or in other case the proposed relation should be smaller. On the one hand the use of very small wire ropes implies to create new design solutions with very thin steel wires and the corresponding difficulty in the fabrication. On the other hand the use of greater diameter wire ropes implies to be out of the safety factor. In both cases the severity of the contact conditions between the wires increase, resulting in a more aggressive fretting damage mechanism and reducing considerably the life of the wire ropes.

## 1.2 Motivation

The approval of the new wire rope solutions for small sheaves gearless motors implies a greater knowledge of the influence of the parameters involved in the system and mainly in the parameters that increase the fretting damage, so that further experimental tests have to be carried out.

Nevertheless the experimental testing of thin steel wires with configurations and operational variables close to the ones presented in wire ropes systems requires high number of tests, with high time consuming and the cost associated to these tests. Furthermore the detection of fretting wear damage in wire rope systems is not perceptible by simple visual inspection, so that the wire rope has to be disassembled with the corresponding complexity. Taking into account the difficulties presented in the analysis of fretting in wire rope systems, in this research work it is proposed to increase the knowledge

about the fretting wear behaviour in thin steel wires developing a numerical tool for predicting this phenomenon. It requires the friction and the wear characterization of thin steel wires under fretting conditions; development and validation of simulation approaches for predicting fretting wear in 3D problems, where severe wear is produced; analysis of the predicted fretting wear scar severity under different operational and geometrical variables and study of the fretting frictionally induced fatigue life reduction in thin steel wire.

This tool will help the wire rope designers to find optimal solutions, reducing the fretting problem under different geometrical (diameter of wires, crossing angle, curvature...) and operational conditions (normal load, relative slips...) in the new generation wire ropes and reducing the cost associate to the experimental testing.

### **1.3 Research objectives**

---

The present work aims to develop a numerical tool for modelling fretting wear in thin steel wires and increase the knowledge about this problem in the wire rope systems. To accomplish that general purpose, the following specific objectives have been identified:

- Characterization of the tribological properties of thin steel wires in laboratory fretting wear tests.
- Development of a FEM simulation methodology for the prediction fretting wear in thin steel wires under different operational and geometrical conditions.
- Determination of the influence of the different geometrical and operational variables in the severity of the wear scars produced by fretting wear.
- Determination of the influence of the fretting wear induced multiaxial stress distribution in the fatigue life reduction of thin steel wires.

### **1.4 Working methodology**

---

The research exposed in this dissertation was divided into the following chapters with their corresponding tasks in order to achieve the above mentioned objectives:

#### **1.4.1 Chapter II: Literature review**

This chapter was carried out in order to identify the available knowledge about the main areas related to the problematic studied in this research work: the contact mechanics,

fretting damage mechanism and fretting wear modelling; as well as to understand the advantages and the limitations of those topics. Moreover their applications in the analysis of fretting in thin steel wires are discussed. From this analysis the different research opportunities were identified: analysis of the frictional and wear behaviour of thin steel wires under fretting wear conditions, implementation of FE wear modelling in crossing angles thin steel wires, study of the severity of the fretting wear produced wear scars under different geometrical and operational conditions and the analysis of the frictionally induced multiaxial contact stresses in the fatigue life reduction.

#### **1.4.2 Chapter III: Fretting wear characterization in thin steel wires**

This chapter describes the experimental tests carried out for the tribological characterization of fretting wear in thin steel wire. Two different tests have been carried out. The first one corresponds to the characterization of fretting wear in 90° crossed cylinders thin steel wires under different normal loads, strokes and number of cycles. The second one corresponds to the characterization of fretting wear in different crossing angles thin steel wires under different normal loads and strokes. These second type of tests presents more realistic configurations, close to those obtained in wire rope systems. In both cases the analysis of the frictional and wear behaviour has been carried out. Moreover an analysis of the wear debris, which plays an important role in the fretting process, is also included.

#### **1.4.3 Chapter IV: FEM modelling of fretting wear in thin steel wires**

This chapter shows the methodology proposed for the simulation fretting wear in thin steel. The complexity of developing a fretting wear simulation tool in a wire rope system because of the numerous contacts appeared in these components, leads to the simplification of the problem into a FE based wear simulation tool for the prediction wear scars under different geometrical and operational conditions between two wires in contact. This tool has been developed for the analysis of all the contact conditions appeared in a wire rope system.

Taking into account the complexity that implies the wear modelling of a 3D FE models (crossing angle cylinders), this chapter has been divided in three tasks. In the first one it is developed a FE method based on a modified version of Archard's equation, for the wear modelling in a simpler 2D block on ring model. This task also included the application of different optimization methods for the reduction the computational time and the validation of this methodology with the experimental tests carried out in the block on ring testing machine.

Based on the knowledge acquired in the first task a methodology for the simulation fretting wear in 90° 3D crossed cylinders arrangements has been carried. This methodology is based on the optimization of the FE wear simulation parameters and has been validated with the experimental data obtained in Chapter 3.

The last task includes the FE wear simulation methodology for thin steel wires configurations close to those presented in wire rope systems. This methodology is based on the methodology proposed for the 90° 3D crossed cylinders arrangements and has been adapted to the new 3D crossing angles cylinders FE model. Moreover the validation of all this methodology has been included.

#### **1.4.4 Chapter V: FEM analysis of the severity of the wear scars**

There are different damage mechanisms that cause the rupture of thin steel wires due to fretting wear in wire rope systems. One of these mechanisms could be the catastrophic rupture of the wire as a consequence of the increase of the stresses due to the excessive reduction of the cross section area produced by the wear scar. Another mechanism could be the so called notch effect caused by the wear scar, which leads to the reduction of the fatigue life of this component and the rupture of the wire. This chapter focuses on the analysis of these two phenomena, analyzing the severity of the wear scars obtained with the validated FEM wear simulation methodology developed in Chapter 4. To have a wider background about these aspects, a Design of Experiments (DOE) of the geometrical and operational parameters of the thin steel wires used in wire ropes has been analyzed.

#### **1.4.5 Chapter VI: FEM-based fatigue life analysis due to fretting wear.**

This chapter proposed the study of the fretting wear caused fatigue life reduction in the wires, using the frictionally induced multiaxial contact stresses obtained by the FEM wear methodology. The fatigue life prediction model has been carried out according to the SWT critical plane approach, to describe the crack initiation and it has been implemented in a 3D crossed cylinder problem. Moreover, a new approach in which the effects of the material removal in the accumulated damage as a consequence of the fretting wear has been developed. The results obtained in this methodology have been contrasted with the results obtained in the fretting wear tests under crack conditions. Moreover a discussion of the improvement of this methodology is included.

#### **1.4.6 Chapter VII: General conclusions, recommendations and further work**

This chapter outlines the main conclusions and contributions obtained from this thesis dissertation. Moreover it is included the main recommendations for future work.

---

## CHAPTER II

# LITERATURE REVIEW

---

### 2.1 Introduction

---

Fretting wear is the main damage mechanism presented in the thin steel wires used in wire rope systems. The study of this phenomenon in the wire ropes system is very complex, because the wires are wounded into other wires forming a complex hierarchical construction. This implies the appearance of hundreds of contacts, subjected to fretting which leads in the rupture of wires. The difficulty of study this problematic experimentally and the necessity of further understanding of this phenomenon, implies the development of a simulation tool for predicting fretting wear in configurations close to those presented in wire ropes. Thus a numerical tool could help to study in a more suitable way each of the contacts separately under the same conditions presented in wire ropes.

This chapter includes a review about the main topics of this thesis: fretting in thin steel wires and fretting wear modelling.

Firstly the analytical description of the contact problem presented in crossed cylinders is introduced.

Secondly a description of the fretting damage mechanism, the main experimental and damage parameters involved in this problematic and the main advances carried out around the experimental testing of fretting wear in thin steel wires is presented.

Finally the main advances presented around the fretting wear modelling which include an overview of the wear models, wear modelling and fretting damage modelling are reported.

## 2.2 Contact mechanics

---

In 1881 Hertz [12] presented the first analytical solution of the contact problem between two elastic bodies subjected to a normal load. This analysis is based on the following assumptions:

- The contact surfaces are smooth, continuous and non-conforming.
- The size of the contact area is small compared to the size of the body, so the strains are small.
- Each body is considered as an elastic half space in the vicinity of the contact.
- The surfaces are frictionless.

Moreover Hertz considered that the surface profiles were parabolic, so the gap  $h$  between the undeformed surfaces could be approximated by an expression of the form (Eq. 2-1)

$$h = Ax^2 + By^2 \quad (\text{Eq. 2-1})$$

The non-conforming contacts are produced between two surfaces with different curvature radius. This implies that depending on the contact area appeared after the elastic deformation three different types of contacts can be defined: linear contact, elliptical point contact and circular point contact. Thus, the resulting area for the different type of contact is used for the calculation of the contact pressure and subsurface stresses.

In the analysis of the contact produced between two thin steel wires, which represent a crossed cylinder contact, the three contacts types mentioned previously are presented, as shown in Fig. 2-1. When two wires contact itself with its axis parallel, a linear contact is produced. When the contact is given at  $90^\circ$  crossing angle a circular contact point appeared and if the contact is produced at different crossing angles an elliptical point contact appeared.

In this study the most severe case corresponding to the circular contact point produced by two crossed cylinders at  $90^\circ$  is discussed. An extended description of the other two contacts can be found in the book written by Johnson [13]. So in the next paragraphs the analytical equations that describe the contact pressure distribution in the surface and the stresses produced in the subsurface are presented.

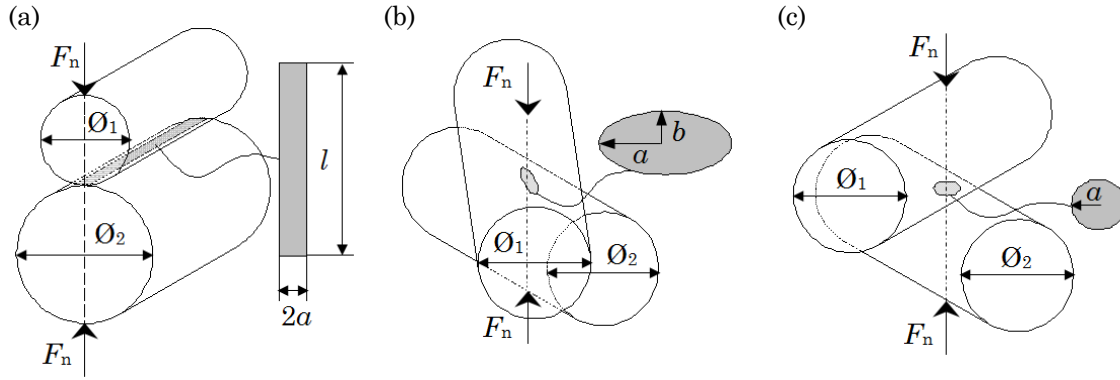


**Fig. 2-1. Crossed cylinders contact types: (a) linear contact (both cylinders parallel to each axis), (b) elliptical point contact (both cylinders crossing at different angles), (c) circular point contact (both cylinders crossing at 90°).**

When two elastic cylinders are pressed together with a normal force  $F_n$ , the contact radius  $a$  that describes the circular point contact is expressed by (Eq. 2-2):

$$a = \left( \frac{3 \cdot F_n \cdot R_e}{4 \cdot E_e} \right) \tag{Eq. 2-2}$$

Where  $R_e$  is the reduced radius of curvature, related with the two radius of curvature of both surfaces  $R_1$  and  $R_2$  as shown in (Eq. 2-3).

$$\frac{1}{R_e} = \frac{1}{R_1} + \frac{1}{R_2} \tag{Eq. 2-3}$$

And  $E_e$  is the equivalent contact modulus given by (Eq. 2-4), where  $E_1$  and  $E_2$  are the Young modulus of each body and  $\nu_1$  and  $\nu_2$  the Poisson coefficients.

$$E_e = \frac{1 - \nu_1^2}{E_1} + \frac{1 - \nu_2^2}{E_2} \tag{Eq. 2-4}$$

The resulting contact pressure distribution  $p(r)$  is described by (Eq. 2-5).

$$p(r) = p_{\max} \sqrt{1 - \frac{r^2}{a^2}} \rightarrow r^2 = x^2 + y^2 \tag{Eq. 2-5}$$

Where  $r$  is the radial coordinate from the centre of the circular contact. As shown in Fig. 2-2(a) the resulting normal distribution has a semielliptical form. The maximum contact pressure  $p_{\max}$ , which occurs on the axis of symmetry, and the mean contact pressure  $p_m$  are given by (Eq. 2-6):

$$p_{\max} = \frac{3}{2} p_m = \frac{3 \cdot F_n}{2 \cdot \pi \cdot a^2} \quad (\text{Eq. 2-6})$$

Now, the analyses of the subsurface stresses that have a critical role in the analysis of the severe stress location below the surface are presented. The different stresses presented along the axis of symmetry  $z$  ( $r = 0$ ) are given by (Eq. 2-7)-(Eq. 2-9):

$$\frac{\sigma_r}{p_{\max}} = -(1+\nu) \left\{ 1 - \left( \frac{z}{a} \right) \tan^{-1} \left( \frac{a}{z} \right) \right\} + \frac{1}{2} \left( 1 + \frac{z^2}{a^2} \right)^{-1} \quad (\text{Eq. 2-7})$$

$$\frac{\sigma_\theta}{p_{\max}} = -(1+\nu) \left\{ 1 - \left( \frac{z}{a} \right) \tan^{-1} \left( \frac{a}{z} \right) \right\} + \frac{1}{2} \left( 1 + \frac{z^2}{a^2} \right)^{-1} \quad (\text{Eq. 2-8})$$

$$\frac{\sigma_z}{p_{\max}} = - \left( 1 + \frac{z^2}{a^2} \right)^{-1} \quad (\text{Eq. 2-9})$$

This stress distribution for a half space with  $\nu = 0.3$  is shown in Fig. 2-2(b), where  $\sigma_r$ ,  $\sigma_\theta$  and  $\sigma_z$  are the principal stresses. On the other hand  $\tau_1$  represents the principal shear stress and is obtained according to the (Eq. 2-10). As shown in Fig. 2-2(b) the maximum shear stress  $\tau_1 = 0.31 p_{\max}$  is given at a depth  $z = 0.48a$ . Therefore, as this is the greatest shear stress in the material, its position is the likely site of the initiation of plasticity, so the failure will occur below the surface. From the previous equations can be deduced that the location and the maximum value of the shear stress will change depending on the material used and the Poisson's coefficient ratio [14].

$$\tau_1 = \frac{1}{2} \cdot |\sigma_z - \sigma_r| \quad (\text{Eq. 2-10})$$



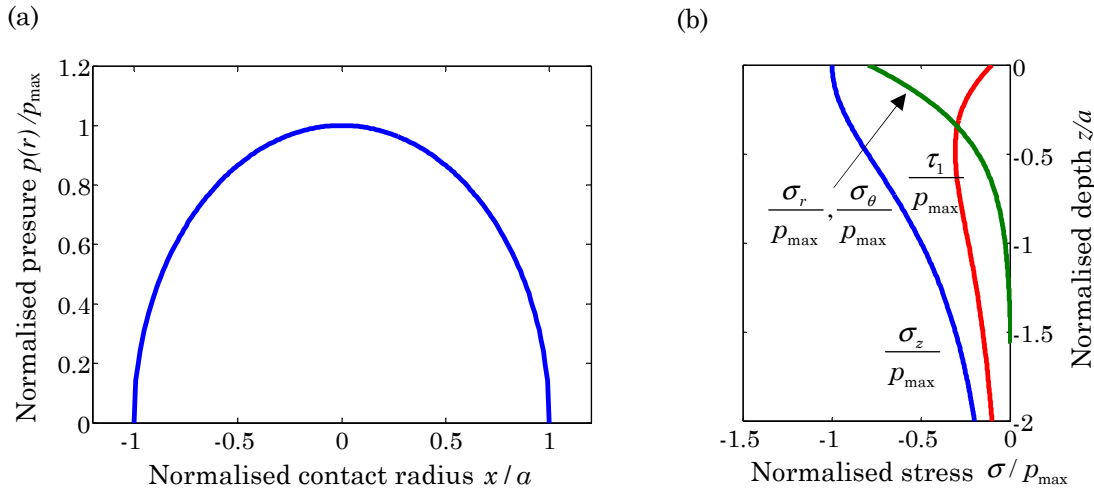


**Fig. 2-2. Distribution of pressure and stresses in on the contact surface according to Hertz: (a) Normalised contact pressure, (b) subsurface normalised stresses for  $\nu = 0.3$ .**

When studying the fretting problem, the contact experience a cyclic tangential force transmitted from one body to another. Considering a tangential force  $Q$  apart from the applied normal force  $F_n$ , a relative sliding movement is produced between the two bodies. Depending on the sliding conditions two different regimes are presented: gross sliding and partial sliding. If the Coulomb friction model is taken into account, the gross sliding regime is given when the tangential force is equal or greater than the frictional limiting value  $Q \geq f \cdot F_n$  and the partial slip regime is given when the tangential force is smaller than the frictional limiting value  $Q < f \cdot F_n$ . While in the gross sliding regime the full sliding conditions are given in the entire contact zone, in the partial sliding regime two contact zones are presented, the first one is located in the centre of the contact and corresponds to an adhesion zone named stick and the second one corresponds to the exterior zone of the contact and corresponds to a sliding zone.

In the gross sliding regime the local surface tangential stress  $q(r)$  is expressed according to the (Eq. 2-11), where  $f$  is the coefficient of friction and  $p(r)$  is given by the previously explained (Eq. 2-5).

$$q(r) = f \cdot p(r) = f \cdot p_{\max} \sqrt{1 - \frac{r^2}{a^2}} \quad (\text{Eq. 2-11})$$

On the other hand Cattaneo [15] in 1938 and Mindlin [16] in 1949 proposed an analytical solution for solving the problem of partial sliding regime between two sphere in contact, where a circular point contact is produced. In 1955 this analytical expression was corroborated with the experimental study carried out by Jonson[17]. Firstly Mindlin

considered, for the case of full stick, a surface shear traction that causes uniform tangential displacement in the surface. This shear traction becomes infinite around the contact edge, requiring unrealistic infinite friction coefficient to slip can not occur. To overcome this problem Midlin applied a local Coulomb friction, assuming that the shear traction at any point on the interface could never exceed the limiting friction there (the product of a certain friction coefficient  $f$  and the local contact pressure). Following this assumption the interface is divided into two distinct regions: a circular stick region ( $r \leq c$ ) and an annular slip region ( $c \leq r \leq a$ ). The surface shear traction is shown in Fig. 2-3.

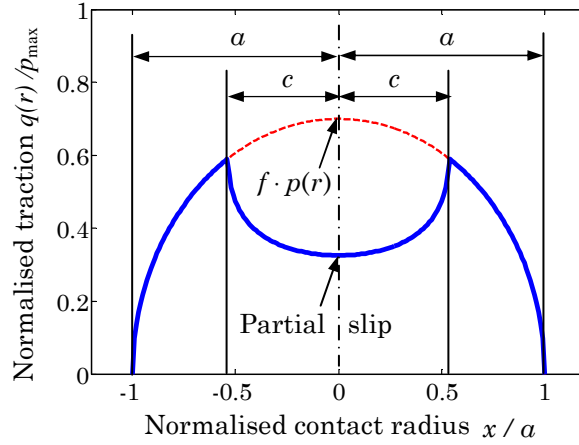


Fig. 2-3. Shear tractions distribution of the Midlin problem ( $Q/F_n=0.5$ ,  $f=0.7$ ).

The radius  $c$  corresponding to the stick region can be expressed according to (Eq. 2-12).

$$c/a = \left( 1 - \frac{Q}{f \times F_n} \right) \quad (\text{Eq. 2-12})$$

If  $c \leq r \leq a$  (slip zone) the shear traction is given by (Eq. 2-13).

$$q(r) = f \cdot p_{\max} \sqrt{1 - \frac{r^2}{a^2}} \quad (\text{Eq. 2-13})$$

If  $r \leq c$  (stick zone) the shear traction is given by (Eq. 2-14):

$$q(r) = f \cdot p_{\max} \left( \sqrt{1 - \frac{r^2}{a^2}} - \frac{c}{a} \cdot \sqrt{1 - \frac{r^2}{c^2}} \right) \quad (\text{Eq. 2-14})$$

---

## 2.3 Fretting damage mechanism

---

### 2.3.1 Introduction

Waterhouse [18] defined fretting as the small-amplitude oscillatory movement that may occur between contacting surfaces, which are usually at rest. Shaffer and Glaeser [19] defined this phenomenon as a special wear process that occurs at the contact area between two materials under load and subject to slight movement by vibration or some other forces. So fretting, can be considered as a surface degradation mechanism that is produced under small-amplitude oscillatory movement. This phenomenon is often presented as one of the most critical area of industrial applications. An example of this damage mechanism can be found in the following systems: contact between hubs, shrink and press fits, bearing housings on loaded rotating shafts or axles, flexible couplings and splines, jointed structures, wire ropes...., which concern to all type of industries: mechanical engineering, aeronautical, biomedical, nuclear industry, civil engineering...

In the fretting damage process it can be distinguished two degradation mechanisms: fretting wear and fretting fatigue.

When fretting wear is produced, one of the effects under atmospheric conditions is the formation of an oxidized debris layer between the bodies in contact, calling this phenomenon “fretting wear” or “fretting corrosion”. In the study carried out by Stachowiak and Batchelor [20] is concluded that this layer is formed from layers of oxide particles detached from the contacting surfaces which are then broke into smaller once. These oxides usually harder than the contact materials, accelerate the process of abrasive wear. However this abrasive wear mechanism is mitigated as the bodies are worn due to the formation of a compacted wear debris layer which acts as a protection of the contact surfaces.

Bertier et al. [21] argued that a change in the slip frequency could keep or remove the wear debris trapped between the two bodies increasing or mitigating the fretting wear damage. Waterhouse [18] reported that contacts consisting of geometrical surfaces such us sphere-on-flat, cylinder on flat and crossed cylinders increased the possibility for debris to escape. In the case of crossed cylinders arrangements Kuno and Waterhouse [22] found the great influence of the direction of motion in the wear debris escape.

On the other hand fretting fatigue is produced when one of the contacting bodies is subjected to a cyclic stress or fatigue and leads to the early initiation of fatigue cracks. The fatigue cracks are initiated in the contact points subjected to a heavy normal load or where there is a static tensile stress in one of the surfaces [18].

In the case of wire ropes, as has been mentioned previously, the phenomenon of fretting, is not produced as a consequence of the vibrations produced by the system, but occurs when the wire rope is subjected to an alternating tension or bending movement that results in a local small reciprocating movement of the numerous interwire contact.

There are many variables that affect in the behaviour of fretting. Dombrosky [23] classified these variables into primary variables which have a direct effect in fretting and secondary variables that affect indirectly by affecting the primary variables. The cited primary variables are the coefficient of friction, slip amplitude and the normal force. Depending on these variables the different fretting regimes can be described.

The characterization of the fretting phenomenon and the different regimes it is carried out by fretting laboratory tests. These tests are divided in two groups based on the loads conditions: fretting or fretting wear tests characterized by normal and tangential contact loadings without any applied bulk stress and fretting fatigue tests that combines the normal and tangential contact loadings with additionally introduced bulk fatigue stress. In both cases the different regimes involved in fretting are presented.

### **2.3.2 Fretting regimes**

There are several studies that characterize the different regimes produced as a consequence of fretting. In the fretting laboratory tests carried out by Vingsbo and Söderberg [24], they reported that fretting damage type is related to the sliding conditions. Taking into account this affirmation, they identify three sliding conditions:

- Stick condition: no slip occurs between the surfaces. The small displacement is accommodated by elastic deformation of the bodies. In this case there is a limited damage of the surface due to the corrosion and wear, producing multiple contacts between asperities with unaffected material between the individual contact points. In some case fatigue cracking is produced.
- Partial-slip condition: the contact zone presents a clear subdivision, while the central zone remains motionless or in adherence (stick), the annular zone or outer ring is in sliding. In this case the wear and oxidation produced in the contact area are small, but there is an accelerated crack growth accelerated reducing the fatigue life.
- Gross-slip condition: the whole contact area is subjected to sliding. The damage generated on the surface is essentially due to wear and oxidation, being limited the crack growth.

The transition between the different sliding conditions during fretting can be identified from the frictional force–relative displacement hysteresis loops. The different loops corresponding to the different sliding conditions are shown in Fig. 2-4: the closed cycle (Fig. 2-4(a)) corresponds to the stick condition; the elliptical cycle (Fig. 2-4(b)) corresponds to the stick-slip condition and the trapezoidal and dissipative cycle (Fig. 2-4(c)) corresponds to the gross slip condition.

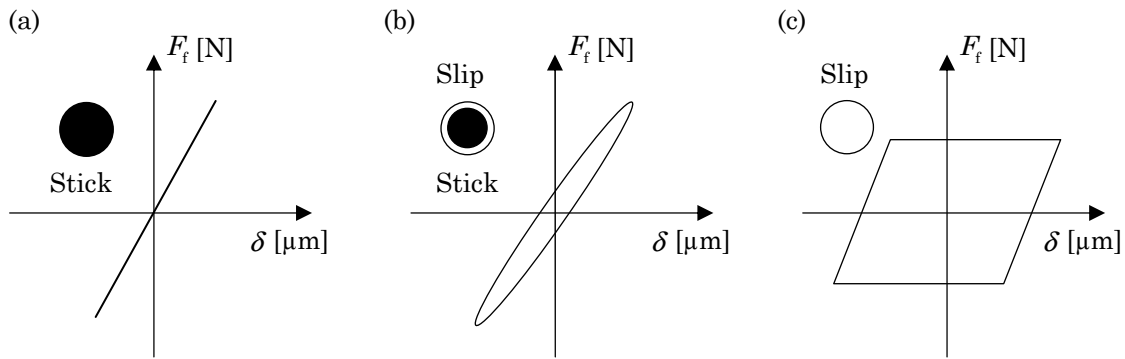


**Fig. 2-4. Hysteresis loop friction force–relative displacement for the different fretting sliding conditions: (a) stick , (b) partial slip, (c) gross slip.**

The different fretting conditions lead into different fretting regimes when the time evolution is considered. Vingsbo and Söderberg [24] based on the analysis carried out in crossed cylinder fretting tests introduce a diagram called ‘fretting maps’. The fretting maps are interesting to synthesize the influence of solicitations in the different damage types producing during fretting phenomenon. Most of the fretting maps that have been made by different authors are two-dimensional diagrams that depend on the factors that control fretting wear and fretting fatigue: normal force or contact pressure and displacement or relative sliding. The different fretting maps that characterise the different regimes in fretting wear and fretting fatigue are illustrated and compared by Zhou et al. [25].

Vincent et al. [26] proposed two kinds of fretting maps: the so called running condition fretting map (RCFM) that depends on the solicitation conditions, and the material response fretting map (MRFM), that depend on the response of the material. The two types of fretting maps are illustrated in Fig. 2-5 and as have been mentioned previously, both depend on the normal force and the amplitude of displacement.

The running condition fretting map includes three fretting regimes as described by Zhou et al. [25]:

- Partial-slip regime (PSR): associated with small displacement amplitudes. Partial slip and stick conditions are observed thorough the duration of the test. Midlin theory is valid in this regime.

- Gross slip regime (GSR): associated with big values of displacement amplitude. Gross slip conditions are observed thorough the duration of the test.
- Mixed slip regime (mixed stick-slip regime) (MFR): the sliding conditions change thorough the test. There is a transition from the gross slip regime to the partial slip regime. Midlin theory is no longer considered valid in this regime.

The material response fretting map (MRFM) relates the sliding regime with the evolution of the damage on the surface as shown in Fig. 2-5. While cracking is the main damage mechanism produced in the partial slip regime the wear and debris formation is the main damage mechanism produced in the gross sliding regime. On the other hand in the mixed slip regime both phenomena are produced: while in the beginning of the test high amount of wear is produced due to the gross sliding conditions, the formation of cracks was possible toward the partial slip regime at the higher number of cycles. So the mixed fretting regime is considered as the most critical regime for crack nucleation and propagation [25].

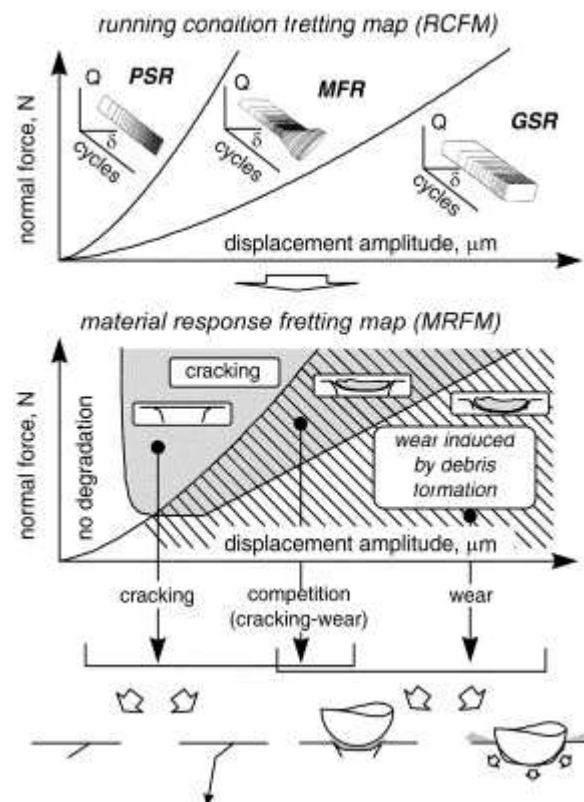


**Fig. 2-5. Fretting maps: (top) running condition fretting map (RCFM): PSR: partial slip regime; MFR: mixed fretting regime; GSR: gross slip regime and (bottom) material response fretting map (MRFM): cracking (PSR); wear-cracking (MSR), wear (GSR) [27].**

Fouvry et al. [28] proposed theoretical fretting maps based on analytical formulas developed for the analysis of the transition criteria from gross slip regime to partial slip regime in terms of energy ratio or sliding ratio. The theoretical results were compared with

fretting experimental tests based in two tribo systems which presented different coefficient of friction. The good correlation of the theoretical-experimental data was observed when the tangential compliance of the system was taken into account.

More recently Heredia and Fouvry [29] introduced a new criterion to identify the boundaries of the mixed fretting regime. This criterion was defined as the proportion of cycles in gross slip condition during a complete test  $\%GS = n_{GS} / n$ . Here  $n_{GS}$  is the number of cycles in gross slip condition and  $n$  is the total number of cycles during the test. In order to determine if a cycle is running in gross or partial slip condition, the energy ratio and the tangential force ratio proposed by Fouvry et al. [28] were used. The energy ratio  $A = E_d / E_t$ , is defined as the ratio between the dissipated energy ( $E_d$ ) and the total energy of the cycle ( $E_t$ ). The total energy is calculated in the following way  $E_t = 4 \cdot F_{f,max} \cdot \delta_d$ , where  $\delta_d$  is the maximum sliding amplitude and  $F_{f,max}$  is the maximal friction force associated with the hysteresis loop friction force-relative displacement as shown in Fig. 2-6(a). The friction ratio  $f = F_{f,max} / F_n$  is defined as the ratio between the maximum friction force ( $F_{f,max}$ ) and the applied normal force ( $F_n$ ). The analysis demonstrates that the sliding transition is associated to a discontinuity of both ratio, being this transition value  $A_t$  or  $f_t$ . So, if  $A > A_t$  or  $f > f_t$  the cycle is considered as gross slip and as partial slip if  $A < A_t$  or  $f < f_t$ . They proposed a transition ratio  $A_t = 0.2$  for cylinder plane and sphere plane configurations. Using the new criterion, both partial slip regime boundaries can be quantified, respectively, by  $\%GS = 0$  and  $\%GS = 1$ . The mixed fretting regime corresponds to the situation where  $0 < \%GS < 1$ . The transition of the different regimes using these three criteria is shown in Fig. 2-6(b).

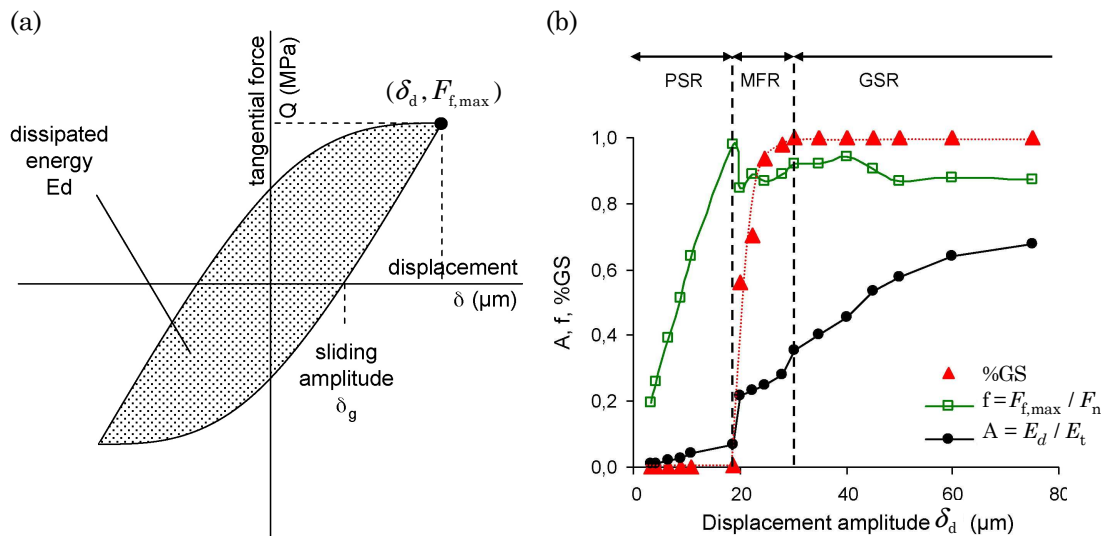


Fig. 2-6. Fretting regimes transition criteria: (a) Friction force–relative displacement hysteresis loop, (b). Evolution of A, f and %GS in running conditions tests [29].

There is another wear phenomenon called reciprocating sliding, whose difference from fretting is that it is produced at greater range of sliding amplitudes. In the literature different transition values corresponding to different strokes ( $\Delta x$ ) has been proposed. Vingsbo and Soderberg [24] as well as Ohmae and Tsukizoe [30] suggested that the transition from fretting to reciprocating sliding wear lies at 300  $\mu\text{m}$ , Lewis and Didsbury [31] suggested that the transition lies at 70  $\mu\text{m}$  and Toth [32] concluded that the transition lies at 50  $\mu\text{m}$ .

Warburton [33] and Chen and Zhou [34] reported that the main characteristic of the reciprocating sliding is that the wear volume for different sliding amplitudes remain constant for the same total sliding distance. So the sliding amplitude boundary conditions can be defined when both the wear mechanism and wear coefficients become approximately constant. This criterion is presented as the most appropriate to identify the transition between the two regimes.

Fouvry et al. [35] proposed another concept based on the contacting area and the sliding amplitude. He defined the relation between the sliding amplitude  $\delta_d$  and the radius of the contacting zone  $a$  ( $e = \delta_d / a$ ), as the main parameter to identify this transition: when the sliding amplitude is smaller than the contacting radius  $e < 1$  fretting happens and when the sliding amplitude is greater than the contacting radius  $e \geq 1$  reciprocating sliding happens.

Another concept to define the transition between fretting and reciprocating sliding was introduced by Varenberg et al. [36], who proposed a dimensionless parameter termed slip index. This index is calculated using the following expression  $s_i = \delta_d S_c / F_n$ , where  $\delta_d$  is the sliding amplitude,  $S_c$  is the slope of the hysteresis loop friction force- relative displacement and  $F_n$  is the normal force as shown in Fig. 2-7.

With this formula the transition between both regimes can be defined as: reciprocating sliding occurs when  $s_i > 10$  and fretting is restricted to  $s_i < 10$ . On the other hand Varenberg et al. [36] proposed the slip index as the method to replace the common fretting maps in identifying the different sliding regimes. Gross slip is characterized by  $0.8 < s_i < 10$  and partial slip by  $0.5 \leq s_i < 0.6$ . Based on this study they offered a new definition of fretting: ‘fretting is a relative cyclic motion between two surfaces, having a non-uniform distribution of local relative displacement at their contact’.



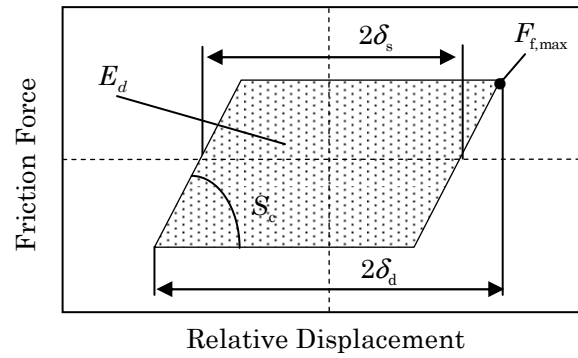


Fig. 2-7. Friction force–relative displacement hysteresis loop.

### 2.3.3 Experimental fretting tests parameters

The experimental study of the phenomenon of fretting, requires the knowledge of a number of parameters which describe both the frictional behaviour and the wear behaviour: stroke ( $\Delta x$ ), dissipated frictional energy ( $E_d$ ), coefficient of friction ( $f$ ), linear wear ( $W_l$ ), planimetric wear ( $W_q$ ), volumetric wear ( $W_v$ ), wear coefficient ( $k$ ) and energy specific wear resistance. These parameters were introduced first by Klaffke [37] to describe the behaviour of tribological fretting tests with a ball on disk configuration. Recently Urchegui [4] has used these parameters to describe the behaviour of thin steel wires under fretting wear tests. In the next paragraphs are briefly outlined the main parameters:

#### *Stroke*

The stroke ( $\Delta x$ ) represents twice the amplitude of motion ( $\delta_d$ ) and is given in ( $\mu\text{m}$ ). It can be determined in two ways: using the peak to peak distance of the motion ( $\Delta x_{\text{peak-peak}}$ ), or using the sliding part of motion ( $\Delta x_{\text{sliding}}$ ). The last one is determined by the width of the line in which the friction force ( $F_f$ ) is zero. Both values are shown in Fig. 2-8.

The difference between these two values is due to the rigidity of the test rig and increases when the stiffness of the system decreases. On the other hand this difference is independent of the stroke used but depends on the frictional force, so the sliding part of the motion decreases by increasing the frictional force. Taking into account this affirmation, Klafke [37] presents the stroke related to the sliding part of the motion ( $\Delta x_{\text{sliding}}$ ) as the realistic quantity which is connected with the amount of wear, so this parameter is used for the calculation of the coefficient of wear.

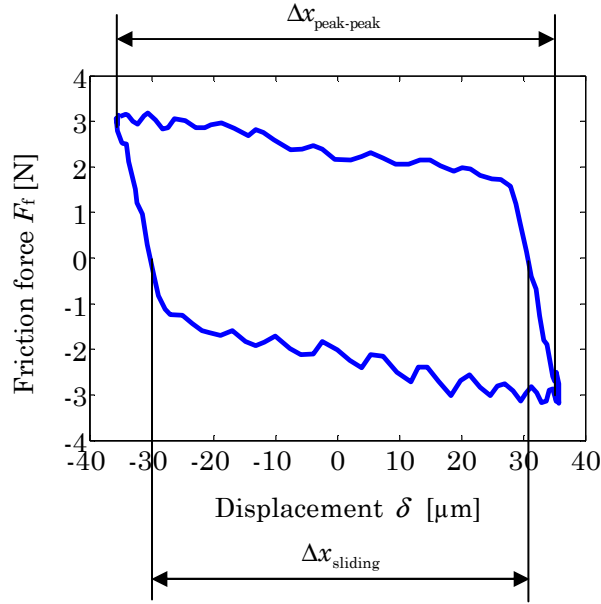


Fig. 2-8. Hysteresis loop friction force–relative displacement in a fretting wear test: definition of stroke.

#### *Frictional dissipated energy*

The frictional dissipated energy per cycle ( $E_d$ ) is defined as the area enclosed by the hysteresis loop friction force ( $F_f$ ) – relative displacement ( $\delta$ ) as shown in Fig. 2-8. This loop represents a trapezoidal shape with an inclination in its flanks due to the rigidity of the system and the fixation of the samples. This parameter can be used for both, the calculation of the coefficient of friction ( $f$ ) and for comparing the different conditions used in the tests.

The value of the dissipated energy per cycle can be obtained by numerical integration and is given in Joules (J). The energy dissipated in an entire fretting wear test ( $E_{d,\text{tot}}$ ) can be obtained also for numerical integration and represents the volume enclosed by all the hysteresis loops recorded during the entire test. The total dissipated energy in a test ( $E_{d,\text{tot}}$ ) can be calculated according to the equation (Eq. 2-15) [4]:

$$E_{d,\text{tot}} = \sum_{i=1}^{i=m-1} (n(i+1) - n(i)) \cdot E_d(i) \quad (\text{Eq. 2-15})$$

where:

$m$  : number of hysteresis loops registered in a fretting test.

$n(i)$  : number of cycles carried out in the registered number of hysteresis loop  $i$ .

$n(i+1)$ : number of cycles carried out in the registered number of hysteresis loop  $i+1$ .

$E_d(i)$ : dissipated frictional energy in the registered number of hysteresis loop  $i$ .

On the other hand, if the hysteresis loops corresponding to the entire fretting test are not recorded. The total dissipated energy can be approximated in a simple way by the product of the mean friction force ( $F_{f,mean}$ ) and the total sliding distance ( $s$ ) of the entire test. Where the mean friction force ( $F_{f,mean}$ ) is calculated by the product of the mean coefficient of friction ( $f_{mean}$ ) of the test and the normal force ( $F_n$ ), and the total sliding distance is calculated by multiplying twice the sliding stroke ( $\Delta x_{sliding}$ ) by the number cycles ( $n$ ) as shown in equation (Eq. 2-16).

$$E_{d,tot} \approx F_{f,mean} \cdot s = f_{mean} \cdot F_n \cdot 2 \cdot \Delta x_{sliding} \cdot n \quad (\text{Eq. 2-16})$$

### Friction coefficient

The friction coefficient ( $f$ ) is the main parameter used to describe the friction behaviour in any tribological test. This parameter is defined as the ratio of friction force ( $F_f$ ) and the normal force ( $F_n$ ). In fretting tests, this value is obtained from the hysteresis loop friction force-displacement. As shown in Fig. 2-9, depending on the value of the selected friction force ( $F_f$ ), different values of the coefficient of friction can be defined [4], [37].

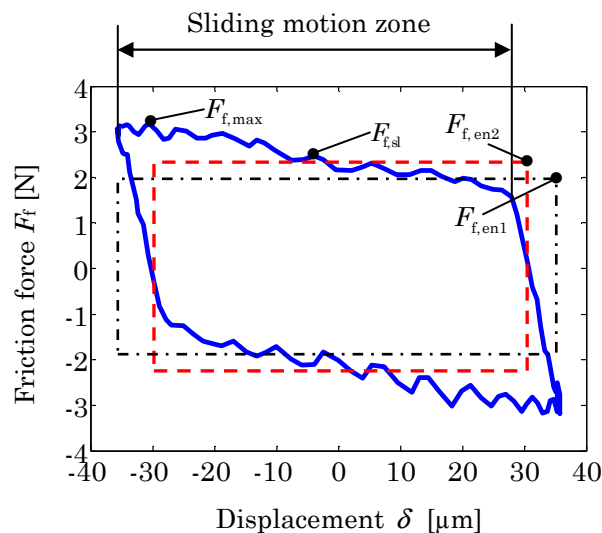


Fig. 2-9. Hysteresis loop friction force-displacement in a fretting wear test: definition of coefficient of friction.

A description of the different coefficients of friction obtained from the friction force-displacement hysteresis loop is presented here:

'Peak-to-peak' coefficient of friction value ( $f_{pp}$ ), corresponding to the maximum value of the friction force ( $F_{f,max}$ ). (Eq. 2-17).

$$f_{pp} = \frac{F_{f,max}}{F_n} \quad (\text{Eq. 2-17})$$

Coefficient of friction corresponding to the mean value of the friction force ( $F_{f,sl}$ ) in the sliding motion zone ( $f_{sl}$ ). (Eq. 2-18).

$$f_{sl} = \frac{F_{f,sl}}{F_n} \quad (\text{Eq. 2-18})$$

Coefficient of friction corresponding to the frictional dissipated energy ( $f_{en,1}$ ), and defined by the height of the rectangle ( $F_{f,en,1}$ ) with the identical area of the hysteresis loop and the width obtained by the peak to peak value of the stroke ( $\Delta x_{peak-peak}$ ) as shown in Fig. 2-9. (Eq. 2-19).

$$f_{en,1} = \frac{F_{f,en,1}}{F_n} \quad (\text{Eq. 2-19})$$

Coefficient of friction corresponding to the frictional dissipated energy ( $f_{en,2}$ ), and defined by the height of the rectangle ( $F_{f,en,2}$ ) with the identical area of the hysteresis loop and the width obtained by the value of the stroke related to the sliding part of the motion ( $\Delta x_{sliding}$ ) as shown in Fig. 2-9. (Eq. 2-20).

$$f_{en,2} = \frac{F_{f,en,2}}{F_n} \quad (\text{Eq. 2-20})$$

Klafke [37] proposed to use the  $f_{sl}$  in order to use the  $f_{en,1}$ , because the last one is affected by the rigidity of the system, so he proposed to use the coefficient of friction corresponding to the sliding part of the motion. Taking into account this consideration Urchegui [4] introduce the concept of the coefficient of friction corresponding to the dissipated frictional

energy related with the sliding part of the motion ( $f_{en_2}$ ). He reported in his study that this coefficient of friction is the more stable value for fretting wear tests with thin steel wires. Nevertheless this value is obtained for each hysteresis loop cycle, so that to obtain the friction coefficient corresponding to the entire test it can be used the mean of all the coefficients obtained during the test ( $f_{mean}$ ). Urchegui [4] proposed to use the values corresponding to the half of the test, because those represent the stable period of the coefficient of friction.

#### *Linear wear*

This parameter represents the depth of the wear scar and can be determined as the total linear wear ( $W_{l,tot}$ ) that represents the sum of the linear wear of both specimens or as the linear wear of each specimen ( $W_{l,spec}$ ). The total linear wear ( $W_{l,tot}$ ) can be obtained on-line through the tribometer measuring the displacement of the loaded specimen. Nevertheless the on-line value is affected by the layer of debris that is produced during the fretting tests. To obtain a realistic value of the total linear wear ( $W_{l,tot}$ ) the profilometer is used once the test is finished, measuring the wear depth of each specimen ( $W_{l,spec}$ ). This value is given in ( $\mu\text{m}$ ).

#### *Volumetric wear*

The volumetric wear is the most important parameter used to describe the wear behaviour. This value represents a rough estimation of the volume of the total wear of the system ( $W_{v,tot}$ ) and is the result of the wear produced by the sum of the wear of the each specimen ( $W_{v,spec}$ ). The volumetric wear can be obtained measuring the volume of the wear scar by profilometer and is given in ( $\text{mm}^3$ ). On the other hand there are different methods proposed by many authors that allows the calculation of the volumetric wear from simple geometrical considerations: the mathematical formulas proposed by Klafke [38] for tests specimens with curved shapes, the method proposed by Warburton and Bradford's [39] for the calculation the volumes of the intersections of cylinders with each other and with flats, and the interference method of two bodies proposed by Urchegui [4]. Although these methods present less precision than the measurements of the entire wear scar by profilometry [4] the reduction in time is considerable (10 times reduction in comparison with a volumetric wear obtained by confocal microscopy).

#### *Planimetric wear*

Although this parameter is not a representative value for the study of the wear behaviour, it is necessary to calculate the volumetric wear ( $W_{v,spec}$ ) according to the methods proposed

previously for the calculation of wear volume from simple geometrical considerations. The planimetric wear ( $W_q$ ) represents the area enclosed by the profile located in the middle of the wear scar perpendicular to the sliding direction. This value is obtained once the test is finished using a profilometer and is given in ( $\text{mm}^2$ ).

#### *Coefficient of wear*

The coefficient of wear ( $k$ ) is one of the most important parameters to compare the wear behaviour of different samples at different conditions. This parameter can be obtained by dividing the volumetric wear  $W_{v,\text{tot}}$  by the normal force ( $F_n$ ) and the total sliding distance ( $s$ ) and is given in ( $\text{mm}^3/\text{Nm}$ ). The total sliding distance ( $s$ ) can be obtained by multiplying twice the sliding stroke ( $\Delta x_{\text{sliding}}$ ) by the number cycles ( $n$ ) as shown in equation (Eq. 2-21).

$$k = \frac{W_{v,\text{tot}}}{s \cdot F_n} = \frac{W_{v,\text{tot}}}{2 \cdot \Delta x_{\text{sliding}} \cdot n \cdot F_n} \quad (\text{Eq. 2-21})$$

#### *Energy specific wear resistance*

The energy specific wear resistance ( $r_e$ ) is now widely used for many authors [40]-[43] to characterize the wear behaviour in fretting conditions. This parameter is obtained by the ratio of frictional dissipated energy ( $E_{d,\text{tot}}$ ) and the volumetric wear ( $W_{v,\text{tot}}$ ) as shown in equation (Eq. 2-22). As reported by Ramalho and Miranda [42], the advantage of this wear coefficient, is that the dissipated energy represents the work done by the friction force which is the representative energy in the tribosystems. This parameter is given in ( $\text{J}/\text{mm}^3$ ).

$$r_e = \frac{E_{d,\text{tot}}}{W_{v,\text{tot}}} = \frac{2 \cdot \Delta x_{\text{sliding}} \cdot n \cdot f_{\text{mean}} \cdot F_n}{W_{v,\text{tot}}} = \frac{f_{\text{mean}}}{k} \quad (\text{Eq. 2-22})$$

### **2.3.4 Multiaxial fretting parameters**

The previously mentioned experimental fretting parameters are related with the frictional and wear description of the fretting phenomenon. Nevertheless due to the multiaxial cyclic stress states produced close to the contact zone fatigue cracks are initiated, mainly in partial slip and mixed slip regimes.

In the recent years many researchers have introduced the multiaxial fatigue models to establish correlations with fretting fatigue experimental data under partial slip conditions, where the effects of wear and material removal are commonly neglected. While, some of

these models, such as the Smith-Watson-Topper [44] are focused on materials that fail predominantly by microcrack growth on planes of maximum tensile strain or stress, other models such as Fatemi-Socie [45], McDiarmid [46], and Shear stress range [47] are focused on materials that fail by the shear stress/strain. On the other hand the Dang Van's criterion [48] assumed that the cracks usually nucleate in intergranular slip bands, so that it was considered that microscopic shear stress and the microscopic hydrostatic stress will influence the opening of these cracks or slip bands. Other criterion such as Morrow's model [49] is based on the basic strain-life relation but introducing the mean stress effects. The previously mentioned multiaxial fatigue models are based on the critical plane criterion, in which it is necessary to project the stresses and strains in all directions in order to obtain the maximum value. Nevertheless there are other fatigue models, such us Crossland's criterion [50], in which it is not necessary to calculate the critical plane but requires the calculation of an invariant.

Although different multiaxial fatigue parameters have been used in the study of fretting fatigue, the two most extended multiaxial parameters are the critical plane based Smith-Watson-Topper parameter (SWT) and the Fatemi and Socie (FS) parameter.

The SWT critical plane parameter was developed by Socie [51] for cracks that grow in planes of high tensile strain. The proposed model is an extension of the SWT [44] parameter and is shown in (Eq. 2-23), where  $\sigma_{\max}$  is the maximum normal stress perpendicular to the critical plane and  $\Delta\varepsilon_a$  is the normal strain amplitude perpendicular to the same plane,  $E$  is the Young modulus,  $\sigma'_f$  is the fatigue strength coefficient,  $b$  is the fatigue strength component,  $\varepsilon'_f$  is the fatigue ductile coefficient,  $c$  is the fatigue ductile exponent, and  $N_i$  represents the number of cycles needed for the crack initiation.

$$\text{SWT} = \sigma_{\max} \cdot \Delta\varepsilon_a = \frac{\sigma_f'^2}{E} (2N_i)^{2b} + \sigma_f' \varepsilon_f' (2N_i)^{b+c} \quad (\text{Eq. 2-23})$$

As has been mentioned previously, for situations where the cracks grow on planes of high shear strain, Fatemi and Socie [45] proposed the FS parameter shown in (Eq. 2-24). Where  $\Delta\gamma$  is the shear strain increment in the plane where it is maximum,  $\sigma_{\max}$  is the maximum normal stress perpendicular to the previous mentioned plane,  $\sigma_y$  is the yield strength,  $\alpha$  is a constant fitted for the uniaxial and torsion fatigue tests,  $G$  is the shear modulus and  $\tau_f'$ ,  $\gamma_f'$ ,  $b$  and  $c$  are constants.

$$FS = \frac{\Delta\gamma}{2} \left( 1 + \alpha \frac{\sigma_{\max}}{\sigma_y} \right) = \frac{\tau_f'}{G} (2N_i)^b + \gamma_f' (2N_i)^c \quad (\text{Eq. 2-24})$$

On the other hand, Ruiz et al. [52] proposed two parameters that are applicable only to the fretting fatigue condition.  $RU_1 = \tau_{\max} \cdot \delta$  and  $RU_2 = \sigma \cdot \tau_{\max} \cdot \delta$ , where  $\tau_{\max}$  and  $\delta$  are the maximum surface shear stress and resultant relative slip and  $\sigma$  is the subsurface tangential stress parallel to the surface. While  $RU_1$  represents the fretting work expended during a fretting cycle,  $RU_2$  corresponds to the combined effect of stress and frictional work.

In the next paragraphs it is explained, the chronological use of the different multiaxial fatigue parameters by different researchers, summarizing the positive and negative aspects of the different criteria for the different studied cases. This chronological review is focused firstly in the use of these parameters in fretting fatigue loading conditions and secondly in fretting wear loading conditions.

In 1996 Szolwinski and Farris [53] were the first researchers that introduced the critical plane method with the SWT parameter to predict fretting fatigue life from fretting-induced stresses, with the aim to capture the fretting fatigue crack formation process reported consistently in the literature in a quantitative model. They showed that the so-called model predicted both the crack origin and crack orientation. Moreover for the life estimations, they coupled the SWT model with a simple Paris type propagation life, resulting in a good agreement with the published experimental lives. They concluded that the formation of a fretting fatigue crack consumed most of the total life in the tests considered and that the value of the friction coefficient had a dramatic effect on the nucleation of a fretting fatigue crack.

In 2000 Lykins et al. [54] evaluated some fatigue parameters such as SWT parameter, FS parameter, Ruiz parameter... for the prediction of fretting fatigue crack initiation in titanium alloy, Ti-6Al-4V. They concluded that the maximum strain amplitude at the contact interface was an important factor in the development of parameters to predict fretting fatigue crack initiation. Following this work in 2001 [55] they developed a combined experimental-numerical approach. A finite element analysis of the SWT critical plane parameter and the maximum shear stress range (SSR) critical plane parameter was conducted based on the experimental information. While the SWT parameter was only effective in predicting the cycles to fretting fatigue crack initiation and crack location, the SSR range critical plane parameter was also effective in predicting the crack orientation angles with respect to the surface. So, they concluded that the mechanism for fretting



fatigue crack initiation in Ti-6Al-4V was governed by the maximum shear stress range on the critical plane.

In 2002 Araújo and Nowell [56] demonstrated that the use of the SWT and the FS with analytical approach based on Muskhelishvili potential theory to determine the two-dimensional contact stress field, were not adequate for evaluating the fretting fatigue initiation life of Al-4%Cu and Ti-6Al-4V with different geometries. The reason was that these two approaches resulted in overly conservative predictions at smaller contacts due to the presence of high stress gradient. To take into account the stress gradient produced by the contact size effect, they proposed two averaging methods, which combined with a multiaxial fatigue criterion, will give less conservative prediction: the method of averaging the SWT and FS fatigue parameters over a characteristic depth on the critical plane and the method of averaging stresses over a characteristic elementary volume. They conclude that both averaging methods gave satisfactory results and that the estimated lives were more sensitive to the characteristic dimension than to the averaging method itself.

In 2004 Jin and Mall [57] developed a combined FE model with a critical plane Modified shear stress range (MSSR) parameter to predict fretting fatigue crack initiation life under partial slip and gross slip condition for the titanium alloy, Ti-6Al-4V. They showed that with increasing the applied relative slip, the MSSR parameter initially increased and the fatigue life decreased; thereafter the MSSR remained constant but the fatigue life increased. They concluded that this increase in the fatigue life appeared to be due to an increased in the wear rate, so that the analysis of gross slip regime requires the consideration of crack initiation and propagation as well as material removal.

In 2005 Sum et al. [58] developed a finite element based implementation of the critical plane SWT fatigue lifting method. They showed that this method capture the well known contact size effect of the cylinder plane configuration presented previously by Araújo and Nowell [56], correlating very closely in terms of cracking location, orientation and life with the test data and volume-averaged theoretical results. Moreover it was shown that the mesh refinement in the contact zone gives an effectively convergence life prediction with the test data. In 2007 Ding et al. [59] evaluate the effectiveness of finite element based predictions in the fretting fatigue life prediction of complex 3D aero-engine coupling. In this case they compared two parameters: the critical plane SWT and the fretting fatigue-specific Ruiz criterion. The Ruiz parameters were considered in this study because of their emphasis on the slip amplitude as a key variable on fretting fatigue. They concluded that the SWT parameter had shortcomings with respect to prediction of failure location, overestimating the life prediction. On the other hand they showed that the Ruiz parameters predicted successfully the crack location. So, they proposed a modified SWT parameter:

$D_{\text{fret}} \cdot \sigma_{\text{max}} \cdot \Delta \varepsilon_a$ , where  $D_{\text{fret}}$  is a function of the frictional work  $\tau \cdot \delta$ , resulting in a more accurate predictions of both life and fretting fatigue locations. Following these works in 2007 Madge et al. [60] proposed a finite element based method to predict and characterise the role of fretting wear on fretting fatigue for a rounded punch-on-flat Ti-6Al-4V fretting fatigue tests configuration under partial slip and gross sliding conditions. This model combines a finite element wear simulation model with the critical plane SWT fatigue model. They concluded that the prediction of fretting wear was a critical aspect for prediction of fretting fatigue, which cannot be predicted by models that do not include the effects of material removal. Moreover they corroborated [61] the hypothesis that the gross sliding in fretting could remove nucleating fatigue damage before propagation into cracks. In 2008 Madge et al. [62] included to the combined wear and critical plane multiaxial prediction of crack nucleation model, a linear elastic fracture mechanics prediction of short and crack propagation submodel. This model showed improved accuracy in the partial slip regime over the SWT only method, but under-predicted life at higher slip amplitudes. The model predicted that wear under gross sliding conditions retards propagation rate and that under partial slip conditions the crack propagation rates increase across the slip zone. Recently, in 2011 Ding et al. [63] have proposed two new parameters for the prediction of fretting: the first one  $D_{\text{fret1}}$ , was proposed to quantitatively predict fretting fatigue life as a function of normal load and applied tangential displacement and the second one  $D_{\text{fret2}}$  is a modification of the previously introduced  $D_{\text{fret}}$  [59], which emphasise the importance of frictional work  $\tau \cdot \delta$ . These two parameters were used with the cylinder plane configuration presented previously by Araújo and Nowell [56] for Ti-6Al-4V and Al-4%Cu materials. On the one hand  $D_{\text{fret1}}$  factor presented a linear tendency with respect to the fatigue life, which provided a reasonable accuracy to estimate the fretting fatigue life in from running conditions. On the other hand  $D_{\text{fret2}}$  in combination with the multiaxial fatigue parameter SWT capture successfully the effect of slip, including the prediction of slip zone cracking and contact size. Furthermore, when using this parameter with volume-averaging of the SWT parameter, as the average of grain size, effectively incorporates the wear effects along with the fatigue crack nucleation prediction.

In 2008 Navarro et al. [64] presented a review of the application of different multiaxial criteria (McDiarmid, FS, SWT and Crossland) to five different materials (four aluminium alloys (being one of these aluminium alloys Al4%Cu) and Ti-6Al-4) and two geometries (cylindrical and spherical contact) on the life assessment in fretting fatigue conditions. They proposed a life prediction model which combined the initiation with the propagation. They showed that the different multiaxial criteria predicted different initiation lives, mainly in cylindrical contacts where the initiation phase is shorter than in spherical contacts due to a smaller stress gradient. As a consequence of this, they proposed to use a

variable initiation length model. On the other hand they reported [65] that the initiation life could be very different from one test to another, so neither two phases (initiation and propagation) could be neglected.

In 2009 Buciumeanu et al. [66] reported the experimental results and analytical approaches for the prediction the fretting fatigue life of an aluminium alloy Al7175. They combined the effect of the damaged area (fretting scar) in the form of a stress concentration factor  $K_t$ , with the Morrow's parameter and with the SWT parameter. While the modified Morrow parameter was shown to provide good fretting fatigue predictions for short lives, more accurate predictions were obtained with the SWT parameter in both short and long lives.

As has been shown all the previously mentioned researches have implemented and improved the multiaxial fatigue parameters for the prediction the crack nucleation in fretting fatigue loading conditions. Nevertheless in a purely fretting or in fretting wear loading conditions, where there is not a bulk fatigue stress applied in one of the bodies, the crack nucleation has to be considered too. In this aspect few researches have implemented the multiaxial parameter damage models to analyze the crack nucleation in these conditions. In the next paragraphs are outlined the main findings.

In 1996 Fouvry et al. [67] presented a theoretical analysis of the fatigue crack nucleation in partial slip conditions using Dang Van's criterion for a ball-flat contact. In 2004 [68] they proposed the Crossland's multiaxial fatigue criterion for predicting the crack nucleation under stabilized partial slip conditions of a Ti-6Al-4V in a cylinder plane contact configuration. They showed that the crack nucleation condition was related to a threshold tangential force value. The comparison with the experimental results concluded the necessity of considering the size effect due to the very sharp stress gradient imposed below the surface. So, introducing an average stress approach based on the identification of the representative damage volume, the crack nucleation condition was predicted successfully.

In 2005 Fridici et al. [69] used the SWT multiaxial fatigue criterion for predicting the crack nucleation in Ti-6AL-4V cylinder on flat configuration under partial slip conditions. He introduced an averaging elementary cubic volume which corresponds approximately to the size of an alpha grain of the titanium alloy, resulting in a good correlation with the experimental data. They saw that some of the values predicted by the SWT parameter exceed the critical crack nucleation value, reflecting the beneficial effect of the compressive residual stresses induced by shot penning. So he proposed an extension of the SWT criterion by introducing a new residual stress parameter  $(\sigma_{\max} - \sigma^*) \cdot \Delta \varepsilon_a$ .

In 2005 Proudhon et al. [70] presented an analytical prediction of the crack nucleation under partial slip conditions with aluminium alloys contact and a cylinder plane configuration. In this case the SWT parameter was computed using the process volume approach, in which a radial shape volume was considered. From the experimental tests it was found a correlation between the process volume diameter and the mean grain radius, confirming the correlation between the mechanical crack nucleation process volume and the microstructure. Nevertheless the pressure effect on the crack nucleation boundary was not in agreement with the experimental results, so a safe crack nucleation process volume identification approach was introduced based on the smallest volume through the investigated pressure and contact size range. In 2007 [71], they proposed a variable process volume size approach based on the slip zone size, resulting in a good agreement with the crack nucleation boundaries in the partial slip regime. They concluded that the determination of the volume approach radius requires a mix of the microstructural-mechanical behaviour.

In 2006 Muñoz et al. [72] proposed a combined crack nucleation and propagation model for a cylinder on flat contact under partial slip fretting conditions and two aluminium alloys. In this case for the crack nucleation, the SWT parameter based on process volume approach was used. The good correlation between the crack extension through the specimen and the load conditions for crack nucleation was concluded.

In 2009 Mohd Tobi et al. [73] reported the evolution of plastic strain and the effects of incremental plasticity during the fretting wear of Ti-6Al-4V under partial slip and gross sliding conditions. He used a FE wear model and the SWT fatigue parameter. While in gross sliding the SWT leads an attenuation of its peak value no predicting cracking, as corroborated the tests results, in the partial slip regime the peak SWT value increase significantly predicting rapid crack nucleation. In 2011 Zhang et al. [81] concluded that if the modelling and predicting wear, especially for Hertzian contacts in partial and gross slip; was not taking into account the effects of wear on stresses and fatigue damage could be non conservative in the PSR and over-conservative in the GSR.

### **2.3.5 Fretting in steel wires**

In the last decades, with the aim to understand better the effect of fretting wear in thin steel wires and reduce this damage mechanism in wire rope systems, several authors have studied the frictional and the wear behaviour of high strength eutectoid steel wires under different operational and environmental condition.

In 1992 Batchelor and Stachowiak [76] reported the influence of different surface coatings in 3.4 mm diameter wires, under 90° crossed cylinders fretting tests. The wires where

tested in a range of maximum contact pressure from 965 MPa to 1560 MPa and with a constant amplitude of movement 50  $\mu\text{m}$ . The coating materials chosen were chromium, zirconium and molybdenum disulphide solid lubricant, all applied by vacuum coating. Most of the coatings, provided some frictional reduction in the initial stage of the test, but subsequently failed. Mainly the molybdenum disulphide coating was extremely effective at lowering the friction coefficient in the beginning of the test. All these experiments were carried out at the lower level of contact pressure, taking into account that at the higher contact pressures all lubricating effect disappeared. So the coating was described as ineffective. With the aim to improve the effectiveness of the coatings they applied the laser surface alloying after chromium and zirconium precoatings. They concluded that the zirconium precoating with the laser surface alloying treatment was the only in reducing the wear and the friction in the thin steel wires.

In 1994 Waterhouse et al. [77] studied the wear and the friction behaviour in 2.8 mm diameter wire with an iron-zinc phosphate coating and sodium stearate powder under 90° crossed cylinder fretting tests. The wires were tested in a range of normal loads from 10 to 200 N, with a constant amplitude of movement 40  $\mu\text{m}$ . They reported the linear dependency existed between the load and the wear. Moreover they saw that the wear and friction behaviour of the wire is different when the coating is removed by abrasion. There is an initial stage with a low coefficient of friction and little debris formation followed by an increase in the wear rate and friction of the abraded wire. Following this work in 1995 McColl et al. [78] studied the influence of low viscosity oils with and without graphite additions in the same steel wires and in the same testing conditions, resulting in an effective wear and friction reduction. On the other hand it was shown that at higher normal forces, when significant breakdown of the oil film occurred micro-welding and tearing of the clean metal surfaces appeared, because the presence of oil inhibits the ingress of oxygen.

In 2003 Zhang et al. [79] carried out fretting wear tests in 90° crossed cylinder arrangements with 1 mm diameter wires used in coal mines wire ropes. The wires were tested in a range of normal loads from 14 to 44 N with a constant amplitude of 75  $\mu\text{m}$ . On the one hand they showed that the friction coefficients decreased with increasing contact loads, but stabilized when the contact loads attained a certain value. On the other hand the research results demonstrated that the fretting wear depth of the steel wires increased with the increasing fretting cycles and contact loads. Moreover it was found the dependency of the wear mechanism with the contact loads. While for low contact loads, light scratch modes dominated, for higher contact loads the third body abrasion appeared on the worn surfaces. Following these tests in 2010 Shen et al. [80] proposed new tests under different fretting amplitudes ranging from 5 to 180  $\mu\text{m}$  and two normal loads 9 and 29 N. This study revealed a variation from partial slip regimes to mixed fretting regimes, and then to gross

slip regime with an increase in displacement amplitude for the same contact load as shown in Fig. 2-10, being the gross slip regime the most severe degradation regime. Continuing this work in 2011 Zhang et al. [81] developed new tests under corrosive mediums in a range of normal loads from 10 to 30 N and displacement amplitudes from 5 to 200  $\mu\text{m}$ . From these tests they contrasted fretting maps, showing that under corrosive mediums the boundaries of the three fretting regimes changed to smaller amplitudes. Furthermore a reduction of the friction coefficient and increase of the material loss was produced under corrosive mediums leading in a severe degradation mechanism in the gross slip regime.

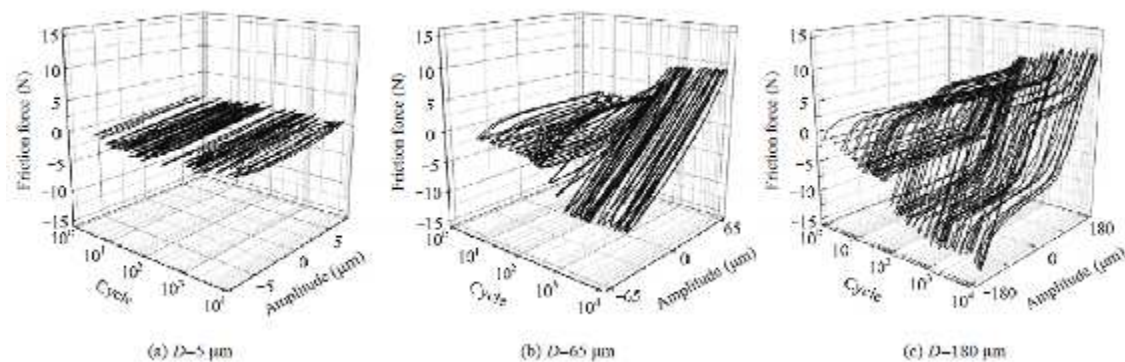


**Fig. 2-10. Evolution of friction force-displacement curves under different displacement amplitudes ( $F_n=9$  N): (a) Partial slip regime, (b) mixed slip regime, (c) gross slip regime.[80]**

In 2007 Urchegui et al. [82] described the preliminary fretting tests carried out in  $90^\circ$  crossed cylinder arrangements with 0.45 mm diameter wires used in residential lifts wire ropes. The wires were tested with two loads 1-2 N and two sliding amplitudes 32.5-65  $\mu\text{m}$ . All tests were performed under fretting wear conditions (gross-slip regime) and none significant influence of selected parameters was detected on friction and wear behaviour. In 2008 new fretting tests were carried out with a normal load of 2 N and amplitude of 130  $\mu\text{m}$  for the study the influence of different crossing angles that goes from  $15^\circ$  to  $90^\circ$ , humidity and different lubricants [83]. The strong effect of humidity and lubrication on the wear rate reduction, whereas a slight effect of contact pressure was derived.

In 2011 Périer et al. [84] reported  $90^\circ$  crossing cylinder fretting tests with 5.3 mm diameter wire used in civil engineering under dry and immerse water conditions. Two types of tests were performed, the first one with incremental displacement and the second one with fixed displacement, in both cases with 200 N normal load in a range of sliding amplitudes from 5 to 20  $\mu\text{m}$ . In both environmental conditions the three fretting regimes were identified (partial-slip regime, mixed regime and gross slip regime). On the one hand the tests carried out in immerse water showed a reduction of the friction coefficient in gross slip condition, acting as a lubricant which induced an extension of the contact area and reduced the cracking damage for higher sliding amplitudes. On the other hand for small amplitudes the

water didn't change the contact conditions and cracks were observed for both cases as shown in Fig. 2-11 (contacts in air and in water).

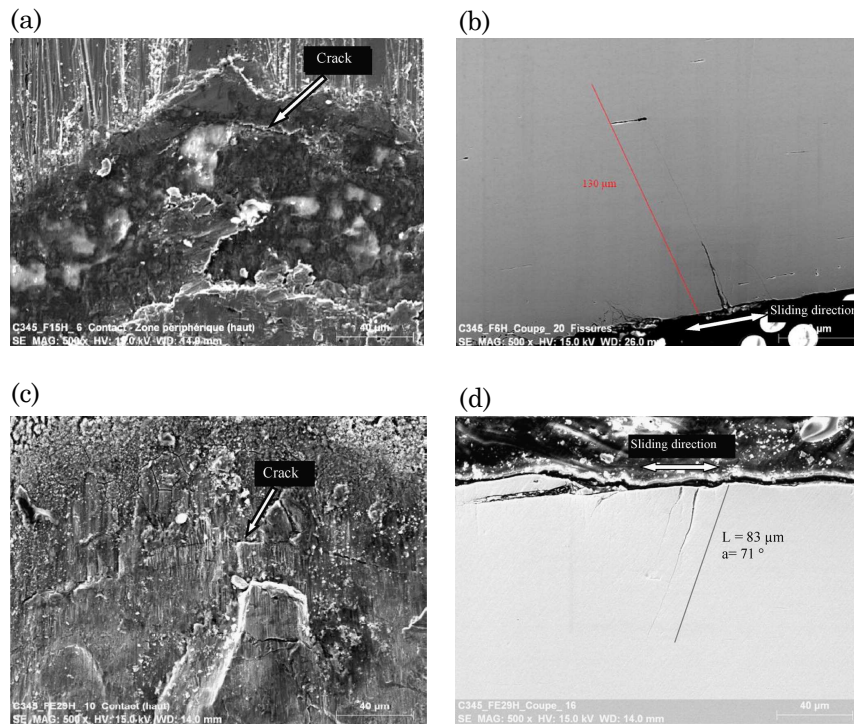


**Fig. 2-11. Fretting cracks observed in dry sliding and water conditions: (a) wear scar in dry condition, (b) transversal perspective of the crack in dry conditions, (c) wear scar in immersed condition, (d) transversal perspective of the crack in immersed condition.[84]**

## 2.4 Fretting wear modelling

### 2.4.1 Wear models

Firstly it should be pointed that the wear is not a material property, but it is a complex phenomenon produced as a consequence of the chemical and mechanical interaction between contacting bodies. Result of this phenomenon is the change in geometry and in the material properties at the surface producing a change of the material service life. Thus the estimation of the wear is presented as a great tool in engineering for the prediction the components life.

The main mechanisms involved in the wear mechanism are outlined in the following lines:

- Material removal in the interface resulting in surface changes.
- Wear particles behaviour at the interface. These particles are also called third body.

- Material flow outside and inside the contact.
- Transference of material from one body to another.
- Environmental conditions effect in the interface.

Throughout the history many wear models have been developed. These models propose theories to explain the observed phenomenon based on the experimental results, from which mathematical expressions are obtained for predicting the wear process. The main models developed throughout the history are reflected in the work carried out by Meng [85]. There are three visions of these different wear models:

- Empirical Period (1957-1970): The wear laws described in this period are completely empirical, obtained from the modification of the test conditions with the aim to determine the impact on the wear behaviour. So these laws are only valid for the type and test conditions in which have been carried out. Barwell [86] proposed a wear law where the wear rate can be explained from the worn volume  $W_v$ , which it is expressed as a function of time  $t$  with one of these three curves:  $W_v = \beta/\alpha(1 - e^{-\alpha t})$ ,  $W_v = \alpha \cdot t$ ,  $W_v = \beta \cdot e^{\alpha t}$ , where  $\alpha$  and  $\beta$  are determined empirically. On the other hand Rhee [87] proposed a wear law in which the missing mass must be a function of the normal load, time, sliding speed and the empirical coefficients.
- Wear mechanism description period (1970-1980): The wear laws proposed in this period are associated with the identification of the main material loss mechanism at the surface. On the one hand models based on contact mechanics were proposed. The Archard [88] wear law was the most important wear model developed in this period. This model was defined for conditions in which the wear behaviour of the tribosystem was stable and no fluctuations appeared. On the other hand there were models associated with the growth of an oxide layer on the surface [89] and models associated with the delamination theory [90].
- Interdisciplinary period (1980-1994): in this period, the wear resistance was not considered as an intrinsic property of materials and the only calculation of the mechanical properties of the contact (such as the real contact area) were not enough. So the wear phenomena have been studied in more detail, and have been described by theories validated in other engineering fields such as plastic deformation, fatigue, heat generation, oxidation, crack nucleation and propagation, etc.



Nevertheless, the Archard wear model was the most used in tribology. This model is expressed by (Eq. 2-25) where  $\kappa$  corresponds to the Archard wear coefficient,  $H$  the hardness of the softer material,  $F_n$  the normal force and  $W_t$  the worn volume per unit of sliding. Thus with this model it can be seen that the wear is directly proportional to the applied normal force and inversely proportional to the hardness of the material.

$$W_t = \kappa \frac{F_n}{H} \quad (\text{Eq. 2-25})$$

If it is considered that  $k = \kappa / H$ , (Eq. 2-25) can be rewritten in form of (Eq. 2-26). Where  $W_v$  represents the worn volume,  $s$  the sliding distance and  $k$  the wear coefficient obtained experimentally.

$$W_v = k \cdot F_n \cdot s \quad (\text{Eq. 2-26})$$

The units used for the wear coefficient  $k$  are  $\text{m}^2 \text{N}^{-1}$ . Nevertheless it is generally expressed as  $\text{mm}^3 \text{N}^{-1} \text{m}^{-1}$ , since these units represent the worn volume per unit force and displacement, more appropriate both experimental and physically for the comparison the wear behaviour between different tribological pairs.

Since 1994 with the arrival of computer technologies a new tendency regarding with the numerical modelling of wear was introduced. The wear modelling will be discussed exhaustively in section 2.4.2 .

In 1995 Morhbacher et al. [91] introduced the concept of frictional dissipated energy ( $E_d$ ) for the study the wear behaviour in fretting problems. In 1997 Fouvry et al. [92] showed the linear relationship existed between the dissipated energy and the worn volume in fretting wear tests with different coatings. He proposed the (Eq. 2-27), where the worn volume  $W_v$  is proportional to the frictional dissipated energy ( $E_d$ ), and  $\alpha$  is the energy wear coefficient [43].

$$W_v = \alpha \cdot E_d \quad (\text{Eq. 2-27})$$

This approach allows to quantify the wear behaviour of different tribosystems, based on the different obtained energy wear coefficients. Ramalho and Miranda [42] concluded that the main advantage of this wear coefficient is that the dissipated energy represents the work done by the friction force which is the representative energy in the tribosystems.

### 2.4.2 Wear modelling

The wear modelling consists mainly of the combination of contact mechanics and wear models, where the contact problem is solved by analytical formulas or by numerical methods, such as the FEM (finite element method) and BEM (boundary element method).

Analytical models for wear contact problems with fixed contact area were developed by Galin [93] in 1976 and lately by Galin and Goryacheva [94] in 1977. New models based on contact problems with variable contact area were introduced by Podra and Anderson [95] in 1997, Goryacheva [96] in 1998, Jiang and Arnell [97] in 1998 and Dikrell and Sawyer [98] in 2004. These analytical wear models have been provided on the basis of the use elastic foundation methods such as Winkler foundation model for the computation of contact pressure and all were based on the Archard's wear model. In 1998 [97] Jiang and Arnell and in 2006 Hegadekatte [99] proposed analytical models based on the hertzian contact model and the Archard's wear model. One of the disadvantages of both Winkler Model and Hertz contact model is that in the computation of contact pressures the shear deformation is neglected. So in the case where high coefficient of friction or in problems where stick-slip conditions are presented these models are not longer valid. Recently Argatov and Tato [100] proposed an asymptotic modelling approach for solving the two-dimensional wear contact problem with increasing contact zone under reciprocating sliding wear regime governed by Archard's law. It was reported the good correlation existed between the analytically predicted and numerically simulated worn profiles in the case of fretting when there is no stick zone between the contacting surfaces.

The previously mentioned analytical models were developed for simple contact configuration wear problems. However, to solve complex contact configuration wear problems the numerical methods approaches becomes in a better alternative.

With the aim to solve the wear modelling in more complex configurations and contact conditions the FEM wear modelling has been appeared as a good alternative in the last decade. In 1994 Johansson [101] proposed a contact algorithm that incorporated the contact resolution by FEM and the Archard's wear model, with the aim to analyze the changes in the contact pressure produced by the changes in the geometry due to the worm surface material. In 1999 Podra and Anderson [102] used the FEM wear approach for modelling sliding contacts in mild wear conditions with different 2D conforming and non conforming geometries. These models only include the wear in the softer body, taking into account that the other body is harder and the wear is negligible. In 2000 Öqvist [103] improve the previous models including the relative sliding, the wear of both bodies and the wear geometry update with different step size approach. In this analysis was shown that large time step for the geometry update caused some waviness of the surface but when the

smaller time steps were used at the end of the computation this error disappeared. McColl et al. [104] in 2004 presented an approach based on a modified version of Archard's equation and implemented within a commercial FE code. The method was implemented in 2D cylinder on flat configuration and was validated with fretting wear tests under gross sliding and partial sliding conditions. In this approach they include wear in both bodies and they maintained essentially the same surface element and sub-surface element depths, ensuring that the implementation of the wear didn't adversely affect the element sizes or shapes and that the worn meshes give equivalent quality results. In 2005 Kim et al. [105] and Hegadekotte et al. [106] implemented a re-meshing scheme for simulating wear on a block on reciprocating rotating ring 3D model and ring-on-ring sliding wear configuration 2D and 3D model respectively. The advantages of re-meshing were the maintenance of a fairly uniform mesh throughout the wearing process and speeds up the wear simulation such as less contact simulations for the same pre-determined maximum sliding distance were needed. In 2007 Ding et al. [107] applied this methodology for modelling fretting wear in a 3D spline coupling model and proposed a new finite element based approach to simulate the effects of debris on fretting wear [108]. Recently in 2008 Hegadekotte et al. [109] and in 2010 Mohd Tobi et al. [110] used the user subroutine UMESHMOTION of the commercial FE code Abaqus, for modelling sliding wear in tribosystems and fretting wear in thin W-DLC coating systems. This subroutine works in an adaptive meshing constrain framework which leads to reduce considerably the time in comparison with other remeshing FE wear models [109]. Nevertheless, although great advances have been done around the wear modelling by FEM, the great disadvantage of these models is the computational cost needed for the calculation of the contact stresses, mainly in 3D models, which requires the solution of a non linear problem that has to be repeated as many times as wear increments needed for the resolution of the complete wear problem.

With the aim to reduce the computational time needed in the wear simulation by FEM, the wear simulation by BEM has been introduced in 2006 by Sfantos et al. [111] and Gonzalez et al. [112] and in 2008 by Rodriguez-Tembleque et al. [113]. The methodology consists in the resolution of the contact problem by BEM and the wear problem using the Archard's local model. Sfantos et al. [111] proposed a 2D wear simulation model using this methodology for the study the wear behaviour in sliding contacts. This model didn't take into account the coefficient of friction on the assumption that this one didn't affect on the normal pressure. So they neglected the tangential force simplifying greatly the problem. Gonzalez et al. [112] presented a formulation for 2D stationary rolling contact problem between viscoelastic cylinders using BEM. In this case the tangential tractions were considered, so different friction coefficients were studied showing a velocity dependent slip zones. Rodriguez-Tembleque et al. [47] applied the BEM in the resolution of 3D wear contact in both sliding wear and fretting wear. In 2010 [114] they applied this methodology to consider wear under

different kinds of fretting contact conditions: gross-slip and partial slip, and on different kinds of 3D solids and surfaces. They obtained very good approximation on contact tractions with a reduced number of elements. The main advantage of BEM with respect to the FEM lies in the considerable reduction of computational time required, the facility in the meshing process and the greater precision in the calculation of the stresses [111], nevertheless greater advances have been done in the study of the wear behaviour using FEM and mainly in the resolution fretting wear problems that will be explained in more detail in section 2.4.3.

All the numerical models presented previously are based on the modified Archard's equation. This equation is based on the local implementation of the Archard's wear model as shown in (Eq. 2-28). Where  $dh$  is the incremental wear depth,  $ds$  is the slip distance increment,  $k_i$  is the local Archard coefficient and  $p(x)$  the contact pressure.

$$\frac{dh}{ds} = k_i \cdot p(x) \quad (\text{Eq. 2-28})$$

On the other hand, there are other models based on the modelization of wear particle formation due to the rupture of surface asperities. Iyer and Ko [115] in 1996 and Ko et al. [116] in 2001 were the main researches that introduce this concept for the study the wear particle formation and detachment in sliding wear. These models consist on the simulation with FE the formation of the wear particle based on the fracture mechanics as shown in Fig. 2-12. Two models were developed: the first one corresponding to the formation of wear particles from one asperity model and the second one corresponding to the study the particle detachment in a multiasperity model. The study of the wear behaviour in a multiasperity contacts leads to a much more local analysis in which the roughness of the material surface has to be taken into account. For this reason, Iyer and Ko used the theory of Greenwood and Williamson to describe the contact roughness. In 2006 Li et al. [117] presented a hybrid method which combine the FE and discrete element to simulate the cumulative micro-damage driven crack development in a double asperity wear surface.

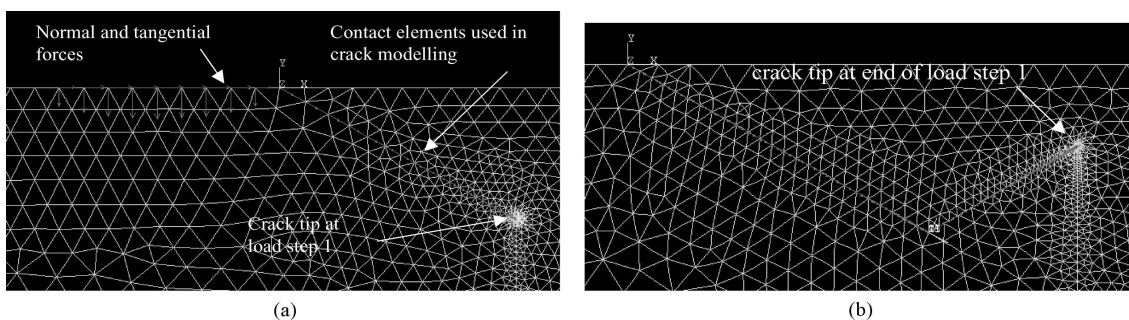


Fig. 2-12. Wear particles formation FE model based on fracture mechanics [116].

Recently, a new wear simulation model based on particles molecular dynamics has been developed. Popov et al. [118] in 2007 and Kloss et al. [119] in 2009 presented this model for understanding the wear particles formation mechanism and their movement in the contact area. This method is called movable cellular automata (MCA) and allows to simulate the formation and accumulation of damage in a tribo-interface, caused by grinding and penetration effects, as well as by fracture and fragmentation processes during friction and wear. This method was therefore used to study tribological contacts at nano-scale level, where elastic and plastic deformations, fracture, detachment of nanoparticles and their reintegration in one of the contacting surfaces as well as intensive mechanical alloying was produced. These phenomena are difficult to characterize by numerical methods based on discretization of continuum models. Moreover this model takes into account the material surface roughness.

As described by Kloss et al. [119], the medium is represented by an ensemble of discrete elements, characterized by continuous variables such as centres of mass position, values of plastic deformation, the rotation pseudo-vector as well as the discrete variables characterizing strength of cohesion between the neighbouring automata. An example of the MCA wear model is shown in Fig. 2-13.

These wear models are used mainly to understand the wear mechanism at roughness level, and not to describe the wear behaviour as presented with FEM or BEM . Moreover these methods allow to simulate the flow modelling of lubricating greases under shear deformation [120] and to understand the properties of the nanostructure surface films that occur frequently in dry sliding applications and with solid lubricants, as reported by Österle et al. [121] in 2012.

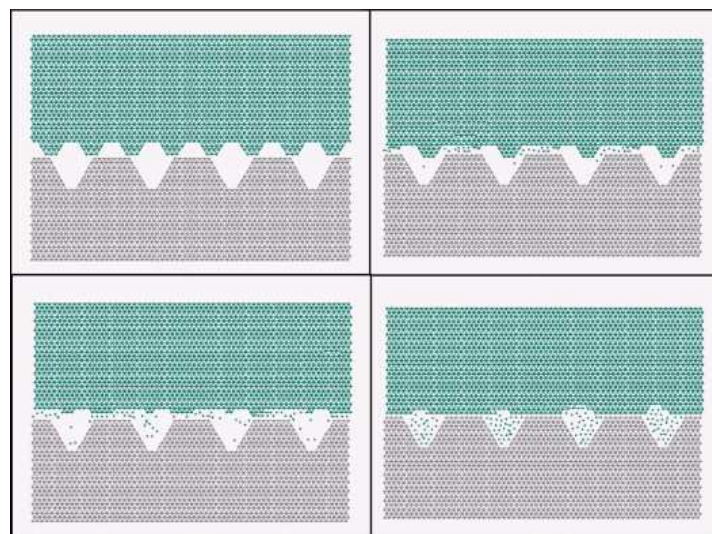


Fig. 2-13. Wear simulation example using the movable cellular automata (MCA) method [119].

### 2.4.3 FE fretting wear modelling

In the previous section the different wear modelling techniques used for different researches have been reported. Nevertheless the main advances shown in the literature are related to the modelling fretting wear with finite element method. Most of these models are developed in the commercial code Abaqus [104], [107]-[110], [124]-[126]; however there are some models presented in the commercial code Ansys [122], [123] or with the researcher own code [101].

The wear modelling by FEM consists on an iterative process, formed by different steps, in which small wear increments are introduced for each iteration. This iterative process is named wear algorithm and consists of the following steps:

1. The FE model, which includes the material properties, the contact surface definition and the finite element meshes, is created.
2. A fretting contact simulation increment is carried out, to obtain the necessary parameters (contact pressure or shear traction and slip distribution) for the application the local wear model.
3. The wear depth for each contact node is calculated using a local wear model in an external code.
4. Based on remising techniques, a new mesh is created using the worm surface from the previous step.
5. With the new worm geometry and mesh a new fretting contact increment is solved and then is go back to step 3. This loop has to be repeated, as many times as fretting contact increment needed for one fretting cycles and as many times as fretting cycles needed to reach the proposed fretting cycles.

Having explained the FE wear simulation approach methodology, in the next paragraphs are outlined the historical advances carried out around modelling fretting wear with FEM.

In 1994 Johanson [101] was the first author that incorporates in a FE model a local implementation of Archard's wear law to evaluate the contact pressure evolution due to change of contact geometry. He reported the noticeable difference in the contact pressure presented after the wear with respect the initial Hertzian contact pressure. Moreover he showed that the increase of the wear rate produced instabilities in the system.

In 2004 McColl et al. [104] developed an incremental wear approach for the simulation of fretting wear in cylinder on flat configuration with the commercial FE code Abaqus. He

proposed the Archard's modified wear local model for fretting wear problems shown in (Eq. 2-29).

$$\Delta h(x,t) = k_l \cdot p(x,t) \cdot s(x,t) \quad (\text{Eq. 2-29})$$

Where  $\Delta h(x,t)$ ,  $p(x,t)$  and  $s(x,t)$  are the incremental wear depth, the contact pressure and the relative slip for a specific point  $x$  (node) at specific time  $t$ . On the other hand  $k_l$  represents the local wear coefficient. As there is not an existing method for estimating  $k_l$  he assumed that the volumetric coefficient of wear  $k$  is the same as the local coefficient of wear. In this approach they maintained the same surface element and sub-surface element depths to ensure that the implementation of the wear didn't adversely affect the element sizes or shapes and that the worn meshes give equivalent quality results. Moreover different techniques for minimisation of the total simulation time were presented: mesh optimisation; the use of 'representative' contact pressure and slip values, to circumvent simulation of the full fretting cycle; and a cycle jump technique  $\Delta n$  were proposed. In this last technique a critical incremental wear depth technique to avoid the instability problems associated with incorrect choice of  $\Delta n$  was proposed. Finally this methodology was validated under gross sliding conditions tests. In 2004 Ding et al. [124] used this method to compare the wear behaviour under partial slip and gross sliding conditions. While in the gross slip regime, the high wear rate leads to decrease the contact pressure and increase the width of the contact wear scar, in the partial slip regime the maximum tensile normal stress increases and shifts its location from the contact edges to the boundaries between the stick and slip zones. He suggested that the dramatic increase in the shear stress at the stick-slip boundaries increases the risk of nucleation of shear type cracks. In 2007 they [107] applied this methodology for modelling fretting wear in a 3D spline coupling model. On the other hand Ding et al. [108] proposed a new simulation tool that included a thin layer of debris, whose effect permitted the redistribution of contact pressure and slip over the contact region to be estimated the debris effects on wear damage. The simulation results showed that the introduction of the debris layer causes a smaller scar width and a slightly greater wear depth, moreover it was predicted that the contact pressure distributes over a smaller width and that the maximum pressure shifts from the centre of the contact to the contact edges.

In 2004 Lee et al. [122] developed a FE wear model for simulating fretting wear in steam generators using the Archard's local wear model. They developed firstly a two dimensional finite element model that was extended to a three dimensional tube-to-tube model and in 2005 by Chai et al [123] to tube to plate contact. Moreover a control parameter which scaled up the wear constant and scaled down the cycle numbers was introduced reducing the time

required for the analysis. The wear profiles along the entire contact area were plotted using a three-dimensional graphic technique. Due to the difficulty of experimentally measuring the wear depth, parameters such as the fretting wear area and wear patterns were qualitatively validated.

On the other hand Fouvry et al. [43] introduced a new FE wear model approach based on the dissipated friction energy. The model was developed for a cylinder on flat configuration under different hard coatings. The local wear model is based on a local energy density description. So the variation of wear depth ( $\Delta h_i(x)$ ) at  $x$  position during the  $i$ th cycle is expressed by (Eq. 2-30). Where  $\alpha_i$  is the local energetic wear coefficient and  $E_{d,i}(x)$  is the local accumulated friction work dissipated at the  $x$  position during the  $i$ th cycle. The dissipated energy is obtained according to (Eq. 2-31) where  $q_i(x)$  represents the local shear traction and  $s_i(x)$  the relative sliding.

$$\Delta h_i(x) = \alpha_i \sum E_{d,i}(x) \rightarrow \sum E_{d,i}(x) = \sum_{i=1}^N E_{d,i}(x) \quad (\text{Eq. 2-30})$$

$$E_{d,i}(x) = \int_{t=0}^T q_i(x) \cdot ds_i(x) \quad (\text{Eq. 2-31})$$

It was concluded that the interface evolution was controlled by the transition from an elliptical to a homogeneous distribution of the wear depth kinetics. In 2007 Mary et al. [125] proposed an optimization methodology based on the criterion of the maximum wear depth per computation step. It was reported the apparition of instabilities at contact borders when using excessive acceleration factors, inducing abrupt surface transition and therefore generating significant pressure peaks at contact borders. It was concluded with the existence of a threshold value of the initial wear depth below which pressure distribution stays stable. On the other hand three FE models were proposed: unilateral wear on plane, on cylinder and bilateral wear both on plane and on cylinder surfaces. The results presented very close correlation of the three models, nevertheless the first model showed systematic error regarding the contact pressure width. In 2008 Paulin et al. [126] used this energetic wear modelling approach for the study of Ti-6Al-4V contact under fretting conditions. They reported that as the third body has less impact more accurate is the local wear damage prediction.

In 2007 Madge et al. [60] developed a novelty model that include the wear simulation model and the critical plane SWT multiaxial fatigue model to study the role of fretting wear in the analysis of fretting fatigue. The wear FE model was implemented into the



UMESHMOTION subroutine within Abaqus. This subroutine works in an adaptive meshing constrain framework. To take into account the stress and strain cycles with increasing number of cycles due to the material removal, the Miner-Palmgren accumulative damage rule was used. Moreover due to use of adaptive meshing to update the geometry for material removal, a material point mesh (MPM) was created for damage accumulation. So nodes on the MPM corresponding to removal material didn't accumulate any further fatigue damage. He used the methodology for modelling both gross sliding and partial slip regime. They concluded that the effect of fretting fatigue cannot be predicted by models which do not include the effect of material removal. More recently, based also on the Archard equation, Mohd Tobi et al. [73] in 2009 proposed an elastic-plastic FE wear model to analyze the evolution of plastic strain and the effects of incremental plasticity during the fretting wear of Ti-6Al-4V under partial slip and gross sliding conditions. While in partial slip the cyclic plasticity effect leads to ratchetting phenomena at the evolving stick-slip interface with associated plastic damage accumulation, in gross sliding the plastic strains were smaller but occurred from the earlier number of cycles and covered a significantly larger region of the wear scar. In 2010 Zhang et al. [81] proposed a finite element based energy wear simulation method for Ti-6Al-4V material, which includes a critical-plane multiaxial fatigue prediction method for crack nucleation using the SWT fatigue parameter and a non-linear kinematic hardening model for cyclic plasticity. They concluded that when the effects of wear on stresses and fatigue damage were not taken into account, over-conservative results could be predicted in GSR and non-conservative results in PSR.

## 2.5 Critical study of literature review

---

Many researches have reported that fretting is one of the main damage mechanisms that appeared in the thin steel wires that form the wire ropes [8]-[10]. Most of the studies carried out for the characterization of this phenomenon, have been focused on the tribological study of thin steel wires in 90° crossed cylinders arrangements [75]-[84] and few studies include configurations with other crossing angles, close to those presented in wire ropes [83]. In this chapter a review about the fretting phenomena and the different ways that could lead to modelling this phenomenon in complex configuration has been presented. This review mainly provides the framework of the present thesis.

Fretting is a well known damage mechanism due to its impact in many engineering sectors: mechanical engineering, aeronautical, biomedical, nuclear, civil engineering.... The normal force, the coefficient of friction and the stroke have been identified as the primary variables that control this phenomenon under different materials and environmental conditions. The variation of these primary variables leads to produce different fretting regimes [25]

characterized mainly for three damage mechanism: wear, cracking and the combination of both wear and cracking. So when studying fretting phenomenon it should be take into account the contact mechanics, tribology, and fatigue.

It has been identified two kinds of parameters that allow the description of the fretting phenomenon. The first one corresponds to the tribological fretting tests parameters [37] in which the coefficient of friction is the main parameter used to characterize the frictional behaviour and the wear coefficient is the main parameter that describes the wear behaviour. The second one corresponds to the multiaxial fretting parameters which are used to describe the fretting induced multiaxial stress fatigue cracking. Regarding to the last type of parameters, the critical plane approaches are the most used because variables such us stress or strain are correlated with the fatigue life prediction under multiaxial stress conditions. Mainly, these parameters have been used to characterize the fatigue life in fretting fatigue loading conditions [53]-[66] but also have been used in fretting wear loading conditions [67]-[74].

Regarding to the study of fretting wear in thin steel wires, all are based on the tribological characterization of this phenomenon. In some of this studies the frictional and wear behaviour on dry conditions is reported [77], [79], [80], [82], other studies reported the beneficial effect of different lubricants and coatings [76], [83], and other studies presented the effect of different environmental conditions in the fretting behaviour [81], [83], [84]. In most of the cases the analyses have been carried out in 90° crossed cylinders arrangements and only in one study is reported the influence of different crossing angles [83]. Nevertheless a lack of in the study of fretting wear induced multiaxial stress field that leads in the rupture of thin steel wires has been shown. Moreover the study of the severity of wear scars with configurations close to those presented in wire ropes also has not been reported. In this point the fretting wear modelling of thin steel wires could be a key challenge to take into account the previously mentioned aspects.

In the literature different wear modelling techniques have been presented. The most common techniques are based on analytical [93]-[100] and numerical methods that combine the modified Archard's equation [101]-[114]. Recently numerical models based on the energetic approach [43], [74] have been presented. The main disadvantage of the analytical models is that are limited to a simplifications, such as material behaviour, geometries... On the other hand the numerical methods can be applied in complex geometries and under complex material behaviours.

There are other numerical methods based on the analysis of the wear at the surface roughness level. One of these approaches is the analysis of the wear debris formation by the numerical modelling of fracture mechanics [115]-[117]. Other approaches are based on the

wear modelling approaches based on discrete methods [118]-[121] (movable cellular automata) used to study the wear debris dynamic in the contact interface, the flow modelling of lubricating greases under shear deformation and to understand the properties of the nanostructure surface films that occur frequently in dry sliding applications and with solid lubricants. Nevertheless these models are not practical when it is needed to analyse the wear behaviour or the stresses generated during the fretting wear as can be carried out with finite element method (FEM) or boundary element methods (BEM).

With respect to the numerical methods, the boundary element method results computationally more efficient than the finite element method, nevertheless greater improvements have been carried out in the wear modelling of fretting wear by FEM. The main advances reported in the literature are: exhaustive modelling of the different regimes produced in fretting under different contact conditions [43], [81], [124], modelling the effect of debris [108], combined wear and multiaxial fatigue modelling [60], fretting wear induced cyclic plasticity [73] and the introduction of different optimization methodologies [104], [125]. Nevertheless most of this models have been implemented and validated in 2D fretting contact problems and in few cases the researches reported a less exhaustive analysis of the FE wear modelling in 3D contact problems [107], [122]. Thus there is a need to develop an exhaustive experimental-numerical validation methodology for wear modelling in 3D systems. On the other hand most of the models reported in the literature have limitations with respect to the simulation severe wear conditions, because the computational time increases drastically and instability problems appeared in the resolution of the contact-wear problem. So the necessity of developing a robust model for modelling severe wear conditions, such as, the wear scars produced in the thin steel wires as a consequence of the aggressive contact loadings conditions appeared in wire rope systems, is presented.

Summarizing in this thesis it will be developed a new numerical-experimental approach for modelling fretting wear in thin steel wires. This new methodology will be used to provide a greater understanding about the severity of the wear scars produced by different loading and geometrical conditions and to analyze the wear-induced evolution of sub-surface stresses, which directly controls fatigue cracking. The methodology will take into account different subjects, that have not yet been analyzed together, as:

- Fretting wear behaviour of thin steel wires in configurations close to those ones presented in wire rope systems.
- Exhaustive experimental-numerical validation methodology for fretting wear modelling in 3D problems, which is the crossing cylinder fretting wear contact problem appeared in wire rope systems.

- Robust wear simulation approach for modelling severe wear conditions in high computational 3D problems.
- Numerical analysis of the severity of the wear scars with configurations close to those ones presented in wire ropes.
- Numerical analysis of the fretting wear frictionally induced multiaxial stress field, which leads the fatigue life reduction of thin steel wires.

# FRETTING WEAR CHARACTERIZATION OF THIN STEEL WIRES

---

## 3.1 Introduction

---

The development of a numerical tool for predicting fretting wear in the thin steel wires that form the wire ropes, requires the knowledge of the tribological behaviour of these type of components. In the last decades, as described in Chapter 2, different researches have performed fretting wear tests in steel wires. Summarizing the fretting behaviour has been analysed: in 5.3 mm diameter wire under dry and immerse water conditions [84], in 3.4 mm diameter wire with different surface coatings [76]; in 2.8 mm diameter wire with different coatings and low viscosity oils [77],[78] and in 1 mm diameter wire with dry [79], [80] and corrosive medium conditions [81]. All these tests have been performed in a 90° crossed cylinder arrangements and the wear behaviour have been analysed according to the application in which the wire rope have been used.

This research work is focused in the development of a FE wear methodology for predicting fretting wear scars in smaller diameter wires than those ones mentioned previously. Such as this study aims to analyse the fretting wear produced in small diameter wire ropes composed by thin steel wires as a consequence of the reduction of the sheave. The high contact pressures and sliding amplitudes appeared in these conditions, lead to produce a dry fretting wear contact problem between the steel wires, which reduce considerably the life of the wire rope [10]. Recently with the aim to understand this phenomenon, Urchegui et al. [82], [83] proposed fretting wear tests in 0.45 mm diameter thin steel wire under different loading conditions and crossing angles. Nevertheless the development of a robust wear simulation model requires to perform new fretting wear tests with a widener parameter field, performing and exhaustive analysis of the fictional and wear behaviour

that will be used as the input in the wear simulation methodology and obtaining the entire topography of the wear scar for the following validation.

This chapter describes the experimental results of the fretting wear tests carried out in 0.45 mm diameter thin steel wires. Firstly fretting wear tests in a more common 90° crossed cylinder arrangement under different contact pressures, strokes and number of cycles were carried out. The frictional behaviour was analysed in terms of the coefficient of friction and the wear behaviour in terms of the coefficient of wear and the energetic-specific wear resistance. Furthermore wear scar debris were examined using a Scanning Electron Microscope (SEM).

Secondly, with the aim of representing a more realistic wire contact configuration, fretting wear tests with different crossing angles were carried out. Two kinds of tests were performed: the first one corresponds to maintaining a constant normal load for the different crossing angles, so that the initial mean contact pressure varies for the different crossing angles and the second type of test is aimed at maintaining the same initial mean contact pressure for the different crossing angles. In both cases an evolution of the mean contact pressure is produced as a consequence of the wear effect, nevertheless this phenomenon is complex to characterize experimentally. The frictional and the wear behaviour was analysed in both cases.

Finally the main conclusions obtained in this study are summarized, reporting the influence of fretting wear in the frictional and wear behaviour of thin steel wires.

## **3.2 Fretting test rig**

---

### **3.2.1 Experimental details**

For tribological testing the contact geometry of crossing cylinders was used to simulate the fretting wear behaviour of the wires in ropes. This method allows for an exact determination of wear under the required conditions [82], [127]. The wires used for the experiments are wires which are usually fabricated into a 7x19 rope (7 strands with 19 individual wires in each one). The diameters of the wires are different and range from 0.22 mm to 0.45 mm (Fig. 1-2).

For the tests, wires with a diameter of 0.45 mm, were used. They are cold-drawn from an eutectoid carbon steel (0.8% C) with a tensile strength greater than 2800 MPa and a hardness of 659±81 (HV0.05). The surface average roughness ( $R_a$ ) of these wires along its axis was 0.35 and 0.70  $\mu\text{m}$  in perpendicular direction. These values were obtained from the

measurements carried out at an unworn wire using a confocal imaging profiler (Plμ, Sensofar). The wires were covered with a thin film of brass with a film thickness of less than  $1\ \mu\text{m}$  (Fig. 3-1), of which the exact composition is unknown.

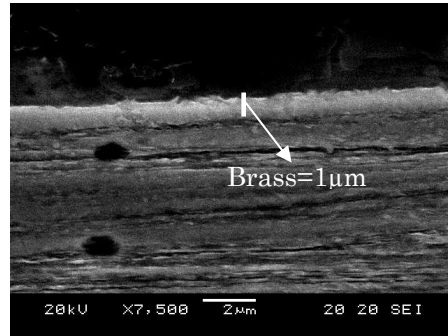


Fig. 3-1. SEM micrograph of Brass film cover in a longitudinal cut of the wire.

Fretting wear tests were carried out on a tribometer (Fig. 3-2) designed to operate under oscillating motion with small amplitudes ( $10\text{-}200\ \mu\text{m}$ ) and small loads ( $0.1\text{-}10\ \text{N}$ ). The tribometer consists of a top arm carrying sample 1 containing an integrated load cell for the measurement of the friction force and a bottom vibrating horizontal table carrying the sample 2. The movement of this table is provided by a frequency-controlled DC motor with an eccentric adjustment. After applying alternative linear movement in this table (composed for linear springs), the vibrating movement is produced [128].

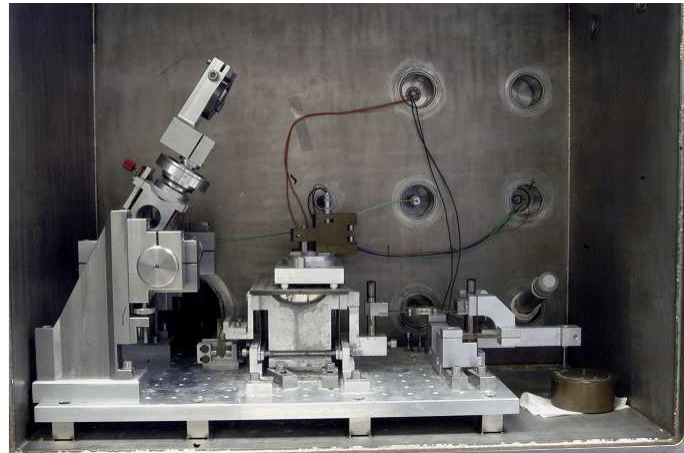
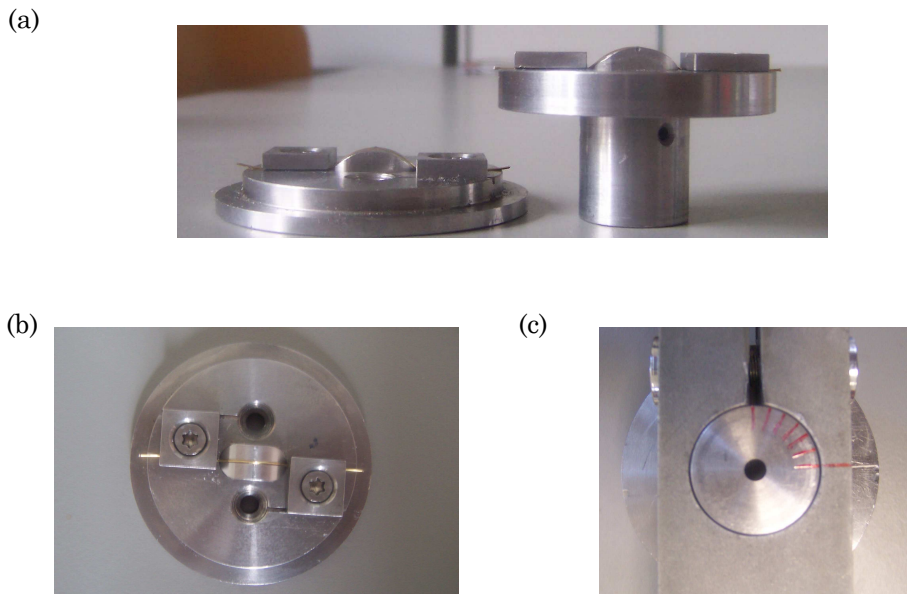


Fig. 3-2. Photograph of the fretting wear test rig.

Special holders were designed for the correct fixing of the wires as shown in Fig. 3-3. Before fixing, the wires were cleaned with acetone and alcohol. In these holders the wires represent a toroid with a curvature radius of  $10\ \text{mm}$ . The upper holder with wire 1 (stationary sample) (Fig. 3-3(a) right) was fixed at the end of a horizontal arm. This holder includes a rule, in the fixing mechanism (Fig. 3-3(c)), which allows to vary the crossing angle between the wires from  $15^\circ$  to  $90^\circ$ . The bottom holder with wire 2 (Fig. 3-3(a) left), was fixed

to the vibrating horizontal table in the tribometer, with the wire axis parallel to the direction of motion. The normal force ( $F_n$ ) was applied to the top of the arm with a dead weight and the total on-line linear wear ( $W_{l,oni}$ ) was measured as vertical displacement of the arm during the test due to occurring wear. The tribometer is placed in a steel chamber so that the relative humidity (RH) could be adjusted at a determined value between 2% RH and 99% RH by means of dried silica gel and kept constant during each test.



**Fig. 3-3. Wire supporting holders: (a) bottom holder (left) and upper holder (right), (b) top view of the bottom wire supporting holder, (c) upper holder in the fixing arm (detailed image of the marks introduced in the holder for different crossing angles configurations.).**

During each test the sliding stroke ( $\Delta x_{\text{sliding}}$ ), friction force ( $F_f$ ), total on-line linear wear ( $W_{l,oni}$ ), relative humidity (RH) and temperature ( $T$ ) near the sliding contact were measured. All measured quantities were recorded on-line multiple times. After each test friction and wear quantities are derived from the stored values. The linear wear ( $W_l$ ) and the volumetric wear ( $W_v$ ) was subsequently determined from wear scar profilometry (Hommeltester, Fa. Hommel, Homburg, Germany) as described in detail by Wäsche and Hartelt [127], after cleaning the wear debris of both specimens with alcohol.

### 3.2.2 Test program

Three types of tests have been performed with that aim to analyse the frictional and wear behaviour of thin steel wires. The first one corresponds to fretting wear tests in a common  $90^\circ$  crossed cylinder configuration under different contact pressures, sliding amplitudes and number of cycles. The second one corresponds to fretting wear tests with different crossing



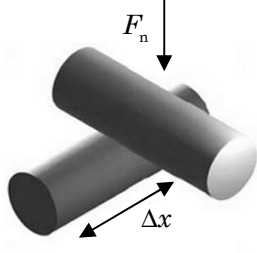
angles and the same normal load and the third one corresponds to fretting wear tests with different crossing angles but the same initial contact pressure. The aim of these last tests is to analyse the influence of the contact pressure in configurations close to those ones presented in wire ropes. A detailed description of the test parameters and values is described in the following paragraphs.

The first type of test was carried out with a 90° crossing angle cylinder-cylinder configuration. In a previous work carried out by Urchegui [4] was found that plastic deformations appeared in some of the contacts between the wires in a new unused rope. Therefore in this study values of load, whose mean pressure is around the yield strength (2800 MPa) of the wire, were used. To estimate a contact pressure and simplify the pressure problem during the tests, the mean pressure in the contact point before testing, calculated by the analytical solution for 90° crossed cylinder proposed by the Hertz theory, was taken. The values obtained for the different loads with the Young modulus of 210 GPa and the Poisson coefficient of  $\nu = 0.3$  were: 0.5 N ( $p_m = 1960$  MPa), 1 N ( $p_m = 2470$  MPa), 2 N ( $p_m = 3100$  MPa) and 3 N ( $p_m = 3560$  MPa).

On the other hand the sliding amplitude was selected according to the results of a previous study [10], in which a real situation was simulated with a rope running over a sheave of 200 mm in diameter, longitudinal abrasive scars between 60  $\mu\text{m}$  and 100  $\mu\text{m}$  were identified. These values correspond to the stroke ( $\Delta x_{\text{peak-peak}}$ ) of the contact wires, peak to peak value, equal to twice the oscillatory amplitude. These values depend on the running conditions and more importantly the sheaves used, because the smaller the diameter of the sheave the longer is the wear scar.

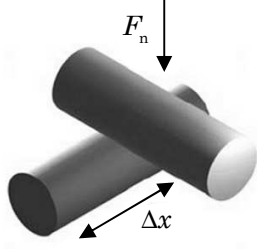
All tests were carried out with a constant frequency ( $f_r$ ) of 10 Hz. Therefore the sliding speed changes linearly with the stroke: for tests where the stroke is 65  $\mu\text{m}$ , the mean sliding speed is  $1.3 \times 10^{-3}$  m/s; while for tests where the stroke is 130  $\mu\text{m}$ , the mean sliding speed is  $2.6 \times 10^{-3}$  m/s. The running-in time of the test depends on the number of cycles used. A cycle is defined as the motion of going and returning of the wire to its initial position. The values used are:  $20 \times 10^3$ ,  $50 \times 10^3$ ,  $100 \times 10^3$  and  $200 \times 10^3$  cycles. The test conditions are shown in Table 3-1.

**Table 3-1. Fretting test conditions for different mean contact pressure and 90° crossing angle.**

Parameter	Symbol	Value	Trybosystem
Normal load (N)	$F_n$	0.5; 1; 2;3	
Mean contact pressure (MPa)	$p_m$	1960; 2470; 3100; 3560	
Maximum contact pressure (MPa)	$p_{max}$	2920; 3690; 4650; 5400	
Stroke ( $\mu\text{m}$ )	$\Delta x$	$65 \pm 5$ ; $130 \pm 5$	
Frequency (Hz)	$f_r$	10	
Number of cycles ( $10^3$ )	$n$	20; 50; 100; 200	
Lubricant		None	
Temperature ( $^{\circ}\text{C}$ )	$T$	$25 \pm 1$	
Relative humidity (%)	RH	$50 \pm 1$	

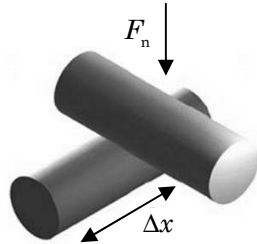
The second type of test was carried with five different crossing angles  $30^{\circ}$ ,  $45^{\circ}$ ,  $60^{\circ}$ ,  $75^{\circ}$  and  $90^{\circ}$  configuration at a constant normal load, so that the initial contact pressure is different in each stage. The normal load was maintained constant during the test, so that the contact pressure changes during the test. The different mean contact pressures calculated for the different crossing angles according to the Hertz theory with the Young modulus of 210 GPa and the Poisson coefficient of 0.3 were: 1 N ( $30^{\circ}$ ) ( $p_m = 1827$  MPa), 1 N ( $45^{\circ}$ ) ( $p_m = 2114$  MPa), 1 N ( $60^{\circ}$ ) ( $p_m = 2300$  MPa), 1 N ( $65^{\circ}$ ) ( $p_m = 2422$  MPa) and 1 N ( $90^{\circ}$ ) ( $p_m = 2500$  MPa). As can be seen the selected pressures are smaller than the yield strength. All the tests were performed with a  $130 \mu\text{m}$  stroke, 50000 cycles at a constant frequency ( $f_r$ ) of 10 Hz. The test conditions are summarized in Table 3-2.

**Table 3-2. Fretting test conditions for different crossing angles and the same normal load.**

Parameter	Symbol	Value	Trybosystem
Normal load (N)	$F_n$	1	
Crossing angle ( $^{\circ}$ )	$\beta$	$30^{\circ}$ ; $45^{\circ}$ ; $60^{\circ}$ ; $75^{\circ}$ ; $90^{\circ}$	
Mean contact pressure (MPa)	$p_m$	1827; 2114; 2300; 2422; 2500	
Maximum contact pressure (MPa)	$p_{max}$	2246; 3171; 3450; 3633; 3750	
Stroke ( $\mu\text{m}$ )	$\Delta x$	$130 \pm 5$	
Frequency (Hz)	$f_r$	10	
Number of cycles ( $10^3$ )	$n$	50	
Lubricant		None	
Temperature ( $^{\circ}\text{C}$ )	$T$	$25 \pm 1$	
Relative humidity (%)	RH	$50 \pm 1$	

The third type of test was carried out with the same initial mean contact pressure and different crossing angles. In this case two initial contact pressures were tested: while the first one with  $p_m = 3200$  MPa is higher than the yield strength and it is tested with a stroke of  $65 \mu\text{m}$ , the second one with  $p_m = 2500$  MPa is lower than the yield strength and it is tested with a stroke of  $130 \mu\text{m}$ . Therefore the normal load needed to obtain these initial contact pressures are calculated accordingly for the different angles. These values are in the case of a contact pressure of  $p_m = 3200$  MPa : 2 N ( $90^\circ$ ), 2.5 N ( $75^\circ$ ), 3 N ( $60^\circ$ ), 3.5 N ( $45^\circ$ ), and in the case of  $p_m = 2500$  MPa : 1 N ( $90^\circ$ ), 1.1 N ( $75^\circ$ ), 1.3 N ( $60^\circ$ ), 1.6 N ( $45^\circ$ ). The normal load was maintained constant, so that the contact pressure changes during the test. All the tests were performed with 50000 number of cycles at a constant frequency ( $f_r$ ) of 10 Hz. The test conditions are shown in Table 3-3.

**Table 3-3. Fretting test conditions for different crossing angles and the same mean contact pressure.**

Parameter	Symbol	Value	Trybosystem
Normal load (N)	$F_n$	2 ( $90^\circ$ ); 2.5 ( $75^\circ$ ); 3 ( $60^\circ$ ); 3.5 ( $45^\circ$ ) 1 ( $90^\circ$ ); 1.1 ( $75^\circ$ ); 1.3 ( $60^\circ$ ); 1.6 ( $45^\circ$ )	
Mean contact pressure (MPa)	$p_m$	3200; 2500	
Maximum contact pressure (MPa)	$p_{max}$	4800; 3750	
Stroke ( $\mu\text{m}$ )	$\Delta x$	$65 \pm 5$ ; $130 \pm 5$	
Frequency (Hz)	$f_r$	10	
Number of cycles ( $10^3$ )	$n$	50	
Lubricant		None	
Temperature ( $^\circ\text{C}$ )	$T$	$25 \pm 1$	
Relative humidity (%)	RH	$50 \pm 1$	

It should be pointed that the wires used for the experiments are wires which are usually used into a 7 x 19 rope. In this specific wire rope the crossing angle range of the steel wires goes from  $5^\circ$  to  $45^\circ$  [10]. Nevertheless in this study, with the aim to represent a reliable tendency of the influence of crossing angle in a general case, angles less than  $30^\circ$  were not applied because of measurement limits and the corresponding lacking measurements accuracy for the wear scar evaluation.

Now it is important to know what the predominant wear regime is: fretting wear or reciprocating sliding wear. Fretting is defined as the phenomenon occurring when two contacting surfaces are subjected to reciprocating motion of small amplitude, whereas the reciprocating wear occurs at much larger amplitude.

In section 2.3.2 of the literature review has been shown that different authors consider that the transition from fretting to reciprocating sliding appears at: 50  $\mu\text{m}$ , 70  $\mu\text{m}$ , 300  $\mu\text{m}$  (peak to peak value). Nevertheless, other studies relate this transition to the contact area [35]. In this case the transition is based on the relation between the sliding amplitude ( $\delta_d$ ) and the contacting radius ( $a$ ),  $e = \delta_d / a$ : while for  $e < 1$  fretting wear is thought to occur for  $e \geq 1$  reciprocating sliding wear is thought to occur. In the case of crossing angle less than  $90^\circ$ , where the contact area is an ellipse, the contact radius represents the length of semi-axis.

With this formula taking into account Hertzian contact radius, in the tests carried out with  $90^\circ$  crossing angles reciprocating sliding appears in the beginning on the tests, because the  $e$  relation obtained is in the range  $3.6 < e < 1$  (Table 3-4). However as the tests runs the wear scar radius increases rapidly being fretting wear the principal regime in these type of tests. In Table 3-4 the contact radius of the wear scars measured after the tests are shown. Taking into account the sliding amplitude, i.e. the half of the stroke (32.5  $\mu\text{m}$  and 65  $\mu\text{m}$ ), it can be considered that the tests were carried out mainly in the fretting wear regime, because the  $e$  relation obtained is in the range  $0.23 < e < 0.82$ .

**Table 3-4. Hertzian contact radius and wear scars contact radius limit for both 32.5  $\mu\text{m}$  and 65  $\mu\text{m}$  for the tests carried out with  $90^\circ$  crossing angle.**

$F_n$ (N)	$\delta_d$ ( $\mu\text{m}$ )	Number of cycles ( $10^3$ )	Contact radius ( $\mu\text{m}$ )	$e$
0.5	32.5	0	18	1.8
3	32.5	0	32.7	1
0.5	32.5	20	65	0.5
3	32.5	200	140	0.23
0.5	65	0	18	3.6
1	65	0	22.7	2.9
0.5	65	20	79	0.82
1	65	200	125	0.52

In the tests carried out with different crossing angles and the same normal force, reciprocating sliding appears in the beginning of the tests, as it is shown in Table 3-5, because the  $e$  relation obtained is in the range  $2.9 < e < 1.1$ . However as has been shown previously the wear scar length increases rapidly as the tests runs for a range of loads from 0.5 N to 3 N, a range of strokes from 65  $\mu\text{m}$  to 130  $\mu\text{m}$  and a range of cycles from 20000 to 200000 cycles showing that the fretting wear is the principal regime in these type of tests. Taking into account this fact, the main wear regime during these tests is fretting, being the  $e$  relation obtained for 50000 cycles in the range  $0.27 < e < 0.59$  as it is shown in Table 3-5.

**Table 3-5. Wear scars contact radius limit for the test carried out with different crossing angles the same load and 65  $\mu\text{m}$  sliding amplitude.**

$F_n$ (N)	$\beta$ ( $^\circ$ )	$\delta_d$ ( $\mu\text{m}$ )	Number of cycles ( $10^3$ )	Contact radius ( $\mu\text{m}$ )	$e$
1	90	65	0	22.7	2.9
1	30	65	0	61.9	1.1
1	90	65	50	109	0.59
1	30	65	50	238	0.27

In the last type of tests, where the same initial contact pressure for different crossing angles was analysed, fretting and reciprocating sliding occurs in the beginning of the tests as it is shown in Table 3-6, because the  $e$  relation obtained is in the range  $0.5 < e < 2.9$ . Nevertheless as it has been explained previously fretting is the main wear regime as the test runs. For these tests the  $e$  relation obtained for 50000 cycles is  $0.15 < e < 0.59$ .

Moreover it has to be pointed out that all the tests presented in this study have been carried out in gross sliding conditions.

**Table 3-6. Wear scars contact radius limit for both 32.5  $\mu\text{m}$  and 65  $\mu\text{m}$  in the tests carried out with different crossing angles and the same initial mean contact pressure.**

$F_n$ (N)	$\beta$ ( $^\circ$ )	$\delta_d$ ( $\mu\text{m}$ )	Number of cycles ( $10^3$ )	Contact radius ( $\mu\text{m}$ )	$e$
2	90	32.5	0	28.6	1.1
3.5	45	32.5	0	66.4	0.5
2	90	32.5	50	100	0.33
3.5	45	32.5	50	210	0.15
1	90	65	0	22.7	2.9
1.6	45	65	0	16.03	1.3
1	90	65	50	109.5	0.59
1.6	45	65	50	169.5	0.38

### 3.2.3 Tribological quantities

The tribological quantities have been divided in two groups, the first one corresponds to the frictional behaviour quantities and the second one corresponds to the wear behaviour quantities. An extended description of these parameters can be found in the literature review carried out in section 2.3.3. It is briefly outlined in this section for better understanding.

### 3.2.3.1 Friction behaviour

The main parameter used for the analysis of the frictional behaviour is the coefficient of friction ( $f$ ). In this study the coefficient of friction corresponding to the dissipated frictional energy related with the sliding part of the motion ( $f_{en,2}$ ), as described in detail in section 2.3.3, has been used. The coefficient of friction  $f_{en,2}$  in each cycle is obtained by dividing the friction force  $F_{f,en,2}$  by the normal force  $F_n$  and thus stored 500 times per test. However the coefficient of friction ( $f$ ) used in this study represents the average value calculated from the data of the last half of the experiment, as shown in Fig. 3-4(a). This value represents the stable period of the coefficient of friction.

Another parameter used in this study is the dissipated frictional energy ( $E_d$ ) defined as the area enclosed by the hysteresis loop friction force ( $F_f$ ) – relative displacement ( $\delta$ ). The hysteresis loop is obtained by measuring 120 times the friction force as a function of displacement during one fretting cycle. Thus, the total dissipated frictional energy ( $E_{d,tot}$ ) represents the volume enclosed by all the hysteresis loops recorded during the entire test as shown in Fig. 3-4(b). Moreover, from the hysteresis loops is possible to see that the predominant fretting regime of these types of tests is the gross sliding regime, such as Fig. 3-4(b) represents the severest test condition and no partial-slip hysteresis loops appear.

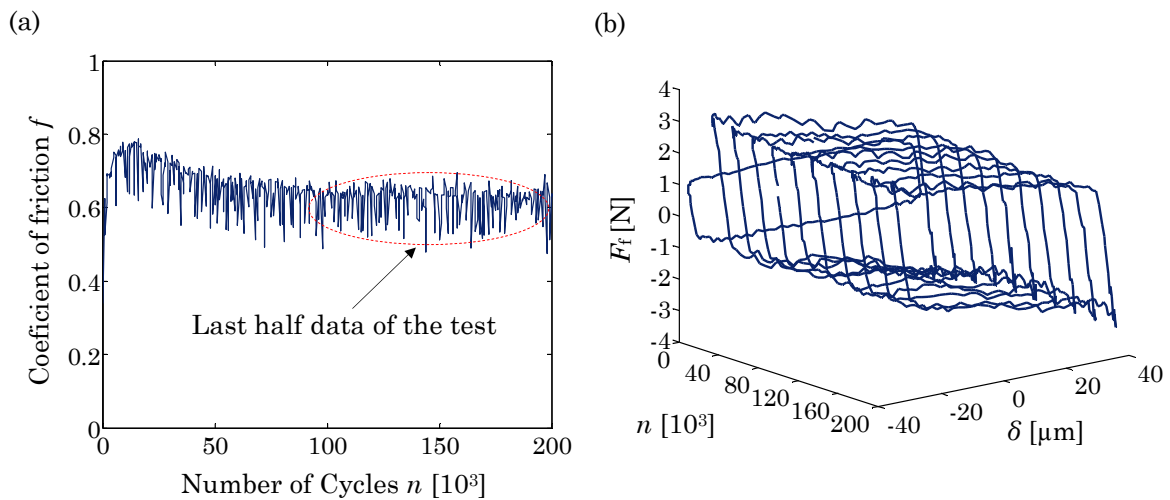


**Fig. 3-4. Friction behaviour plots for 3 N-65  $\mu\text{m}$  and 2000000 numbers of cycles: (a) coefficient of friction evolution along the cycles and (b)  $F_f$ - $\delta$  hysteresis loops during a fretting test and.**

### 3.2.3.2 Wear behaviour

The analysis of the wear behaviour requires the calculation of the wear volume. In this study the total volumetric wear  $W_{v,tot}$ , which represent the sum of the volumetric wear of both wires, has been used. As mentioned previously, the volumetric wear of each specimen

has been obtained after cleaning the surface, by diamond stylus profilometry, constructing the topography of the entire wear scar.

Other parameters used in this study are the total on-line linear wear ( $W_{l,onl}$ ) which represents the vertical displacement of the arm during the test due to occurring wear, and the total linear wear ( $W_{l,tot}$ ) obtained by profilometry, which represents the sum of the depth of the wear scars of both specimens.

Nevertheless with the aim to compare the wear behaviour at different conditions two specific coefficients have been used. The first one corresponds to the coefficient of wear described in equation (Eq. 3-1). This parameter is obtained by dividing the total volumetric wear  $W_{v,tot}$  by the normal force  $F_n$  and the total sliding distance  $s$  in terms of the sliding stroke  $\Delta x_{sliding}$ . The second one corresponds to the energy specific wear resistance as described in equation (Eq. 3-2). This equation considers the total dissipated frictional energy by summation over the number of cycles and relates it to the occurred wear volume and hence tells how much energy is needed to remove a certain volume due to the wear process. It therefore combines the occurring friction with the coefficient of wear.

$$k = \frac{W_{v,tot}}{s \cdot F_n} = \frac{W_{v,tot}}{2 \cdot \Delta x_{sliding} \cdot n \cdot F_n} \quad (Eq. 3-1)$$

$$r_e = \frac{E_{d,tot}}{W_{v,tot}} \quad (Eq. 3-2)$$

### 3.3 Results and discussion

---

#### 3.3.1 Fretting wear in 90° crossing angles thin steel wires

##### 3.3.1.1 Friction behaviour

In Fig. 3-5 the coefficients of friction ( $f$ ) of 24 different tests are shown. The obtained values (0.6-0.8) are typical for dry sliding tests of steels. There is an increase in the coefficient of friction in the first 20000 cycles followed by a decrease between 20000-50000 cycles which finalized in a stable steady state period. A similar tendency was reported by other authors [104], [129]. Fouvry et al. [129] associate this evolution with the elimination of the surface oxides promoting severe metal-metal interaction which then leads to the formation of a third body layer and the stable period of the wear coefficient. This initial

increment in the coefficient of friction coincides with the so called running-in period that will be explained in section 3.3.1.2.

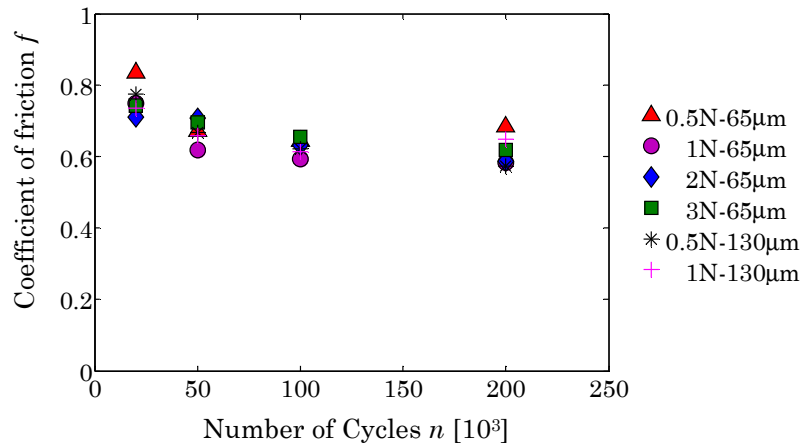


**Fig. 3-5. Coefficient of friction for 90° crossed cylinder fretting tests with different normal loads, strokes and number of cycles.**

In Fig. 3-6 the total dissipated friction energy ( $E_{d,tot}$ ), obtained from the integration of the entire hysteresis loop in each test, is shown. A linear tendency with the number of cycles and between the stroke and the dissipated energy appears: if the stroke is duplicated the dissipated energy is duplicated with the same load, as can be seen in the cases of 0.5 N-65  $\mu\text{m}$  and 0.5 N-130  $\mu\text{m}$  and in the cases of 1 N-65  $\mu\text{m}$  and 1 N-130  $\mu\text{m}$ . Another tendency concerning to the load appears: while for 1N-65  $\mu\text{m}$  and 200000 cycles the dissipated energy is about 15.8 J, for 2 N-65  $\mu\text{m}$  is about 32 J and for 3 N-65  $\mu\text{m}$  is about 49.3 J. Although it represents a nearly linear tendency between load and dissipated energy, sometimes it has a dispersion of 10%-15%; this is because the stroke and the sliding stroke are not identical, due to the stiffness of the system. Normally the sliding stroke is between 5% or 9% smaller than the nominal stroke, especially when high loads like 2 N or 3 N are used and the friction force increases. The last tendency is concerned to the relation existing between the normal force and stroke  $F_n \times \Delta x$ . As shown in Fig. 3-6 the same magnitude of  $F_n \times \Delta x$  produce the same dissipated energy as can be seen in the cases of 1 N-65  $\mu\text{m}$  and 0.5 N-130  $\mu\text{m}$  and in the cases of 2 N-65  $\mu\text{m}$  and 1 N-130  $\mu\text{m}$ .



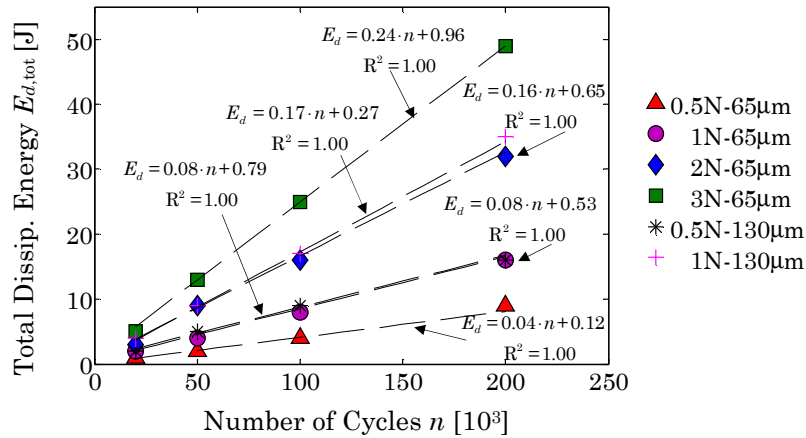


Fig. 3-6. Total dissipated energy for 90° crossed cylinder fretting tests with different normal loads, strokes and number of cycles.

3.3.1.2 Wear behaviour

In order to analyze the wear behaviour two studies were carried out: the first one corresponds to a qualitative study of the wear, in which the wear scars were analyzed in the scanning electron microscope (SEM), and the second one corresponds to a quantitative study of the wear volume after cleaning the wear debris produced during the tests.

The main wear mechanism presented in this type of tests is the tribo-oxidation as is shown in Fig. 3-7. While the wear particles are piled up outside wear scars (Fig. 3-7(a)), in Fig. 3-7(b) it is possible to see surface oxide which is prone to produce abrasive wear and it tends to create wear tracks in the scar during the plowing process.

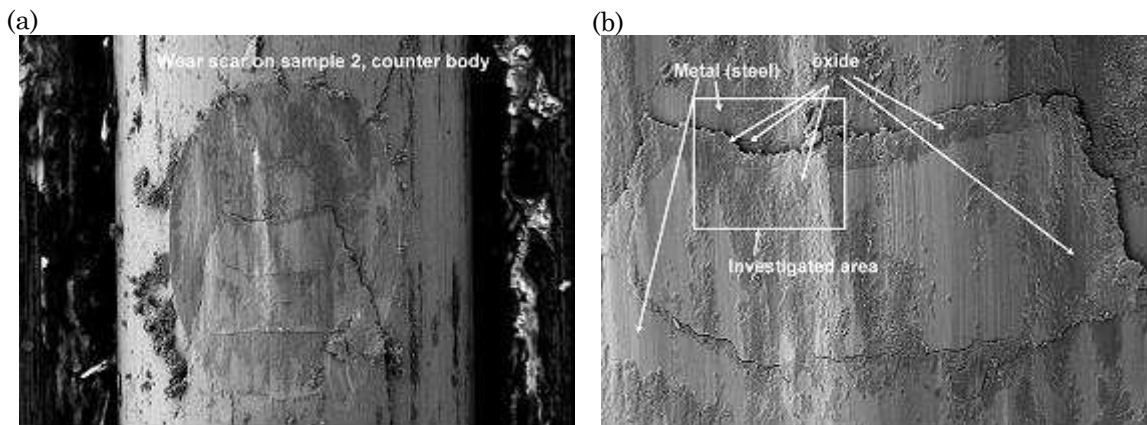
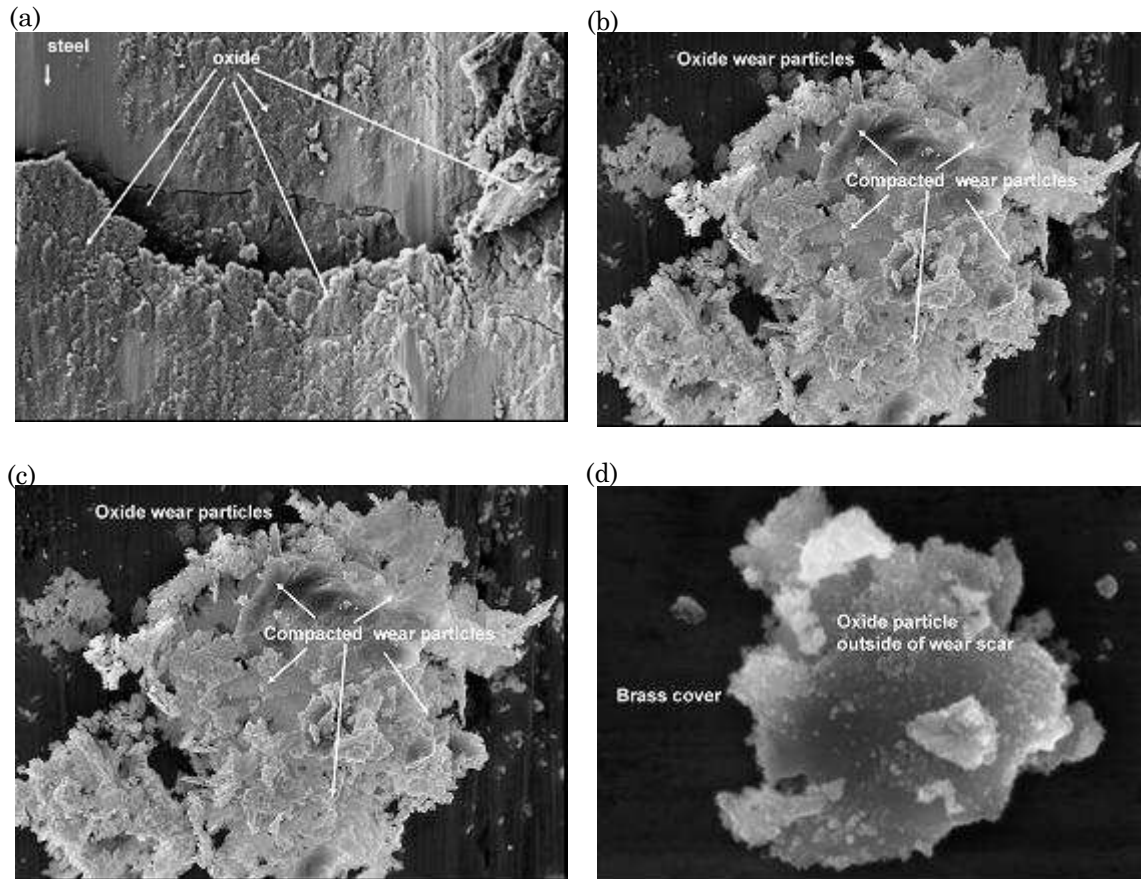


Fig. 3-7. Wear scar surface after the test: (a) wire specimen with wear scar and debris; (b) surface inside wear scar.

Analyzing the oxide wear debris (Fig. 3-8) two distinctive behaviours could be presented during the wear process: on one hand they may get locked between the sliding surfaces promoting third body wear, which should enhance wear volume loss, and on the other hand they may get compacted between the surfaces forming protective layers as it is seen in (Fig.

3-8(a) and Fig. 3-8(b)) and inducing mild wear. The last case is reported by Kato and Komai as tribo-sintering of nanometer-sized oxide [130]. Fig. 3-8(c) shows the oxide wear debris ejected outside the wear scars during the wear process. The predominant shape of these particles is rounded as it is possible to see in Fig. 3-8(d).



**Fig. 3-8. Oxide wear particles: (a) inside wear scar; (b) compacted wear particles; (c) outside wear scar and (d) shape of oxide wear particle.**

The previously mentioned protective layers appear in the bottom wear scar, being one of the great consequences the reduction of the wear volume loss of this specimen. In Fig. 3-9 it is possible to see this phenomenon, where the volumetric wear of both specimens (top wear scar Fig. 3-9(a) and bottom wear scar Fig. 3-9(b)) for different load cases, sliding distances (number of cycles) and a stroke of 65  $\mu\text{m}$  are shown. As can be seen, in the first period of the wear process the volumetric wear is slightly greater in the bottom specimen. Then during the formation process of these protective layers the volumetric wear of both specimens become the same. Finally, the formation of these protective layers, reduce considerably the wear loss in the bottom specimen, being the volumetric wear of this specimen in the same level or increasing slightly, while in the top specimen continues increasing.

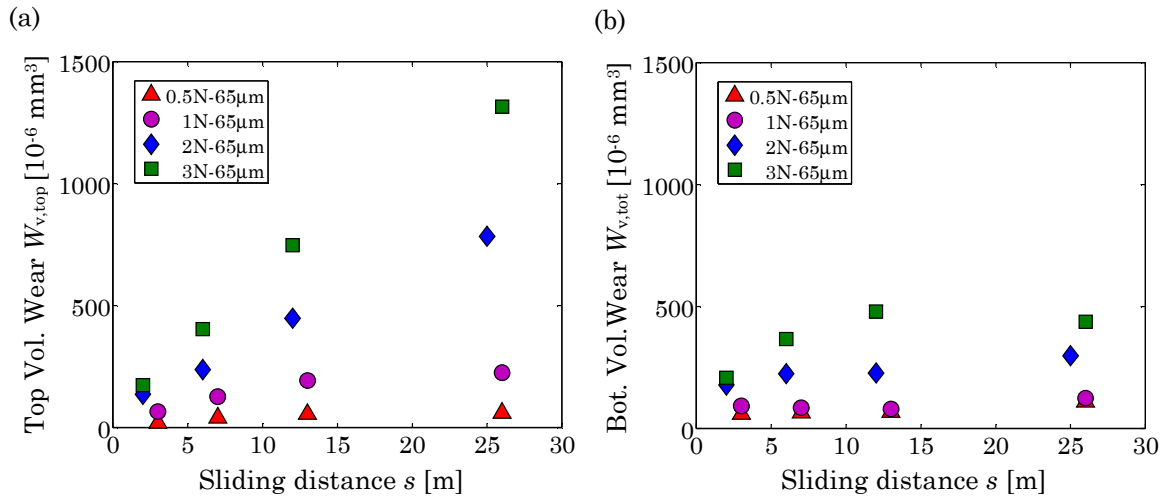


Fig. 3-9. Volumetric wear of both wear scars for 90° crossed cylinder fretting tests with different normal loads, number of cycles and a stroke of 65  $\mu$ m: (a) top specimen (b) bottom specimen.

In order to simplify the analysis of the wear behaviour, the sum of the volumetric wear of both wear scars, measured after the tests, was used. The calculation method of the volumetric wear is explained in section 3.2.3.2. Fig. 3-10 and Fig. 3-11 represent the evolution of both wear scars from 20000 to 100000 cycles for 1 N-130  $\mu$ m.

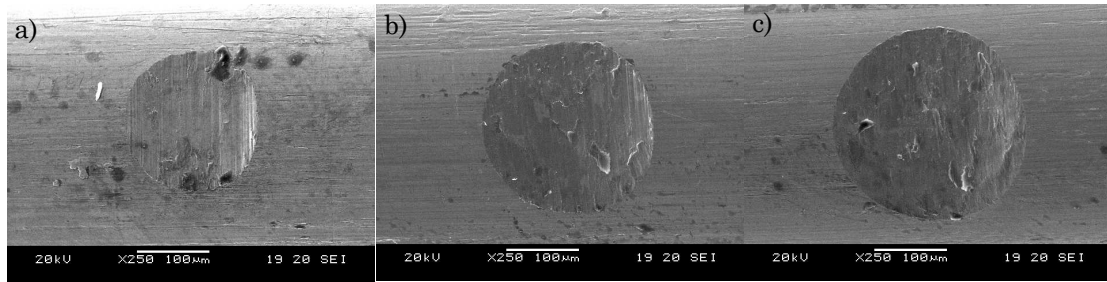


Fig. 3-10. Wear scars in upper wire (cylinder 1: perpendicular to sliding cylinder: static): (a)  $F_n = 1$  N,  $\Delta x = 130$   $\mu$ m,  $n = 20 \times 10^3$  cycles; (b)  $F_n = 1$  N,  $\Delta x = 130$   $\mu$ m,  $n = 50 \times 10^3$  cycles; (c)  $F_n = 1$  N,  $\Delta x = 130$   $\mu$ m,  $n = 100 \times 10^3$  cycles.

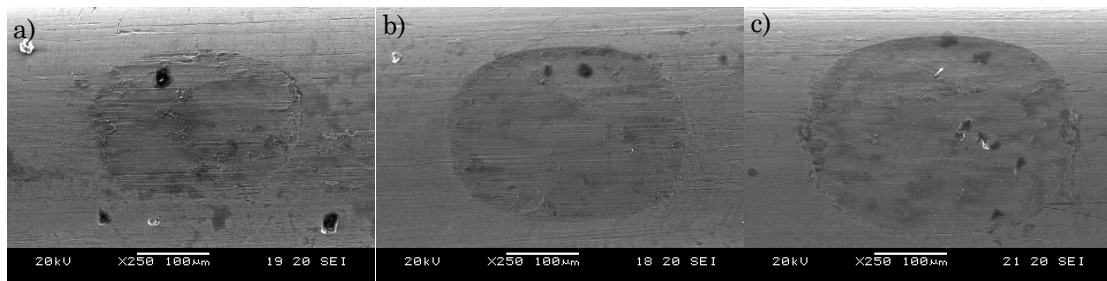


Fig. 3-11. Wear scars in bottom wire (cylinder 2: parallel to the sliding displacement: moving): (a)  $F_n = 1$  N,  $\Delta x = 130$   $\mu$ m,  $n = 20 \times 10^3$  cycles; (b)  $F_n = 1$  N,  $\Delta x = 130$   $\mu$ m,  $n = 50 \times 10^3$  cycles; (c)  $F_n = 1$  N,  $\Delta x = 130$   $\mu$ m,  $n = 100 \times 10^3$  cycles

In Fig. 3-12 the total volumetric wear ( $W_v$ ) from the 24 different tests as measured by the profilometer is presented. An increase of the wear rate (slope), by increasing the normal force for the same stroke (Fig. 3-12(a)) and increasing the stroke with the same normal force (Fig. 3-12(b)), is seen. Moreover a linear tendency with respect to the sliding distance is found.

In order to compare the results of the tests with different loads and sliding distances better, a classical study of the coefficient of wear ( $k$ ) with respect to the sliding distance was carried out. Two types of studies were done: the first one represents the influence of the normal load in the wear behaviour (Fig. 3-13(a)) and the second one represents the influence of the stroke in the wear behaviour (Fig. 3-13(b)). In both cases a variable coefficient of wear with respect to the sliding distance is obtained. The tendency represents a decrease of the coefficient of wear with respect to the sliding distance being the tendency in good correlation with logarithmic function ( $\ln(x) + y$ ). This tendency could be due to the highest pressure existing in the beginning of the tests, which decreases as the wear scar grows. For this reason, in the beginning of the tests a more aggressive wear period is produced, following by a more stable period.

When the coefficient of wear is analyzed for different loads and the same stroke (Fig. 3-13(a)) this one increases by increasing the load. As indicated previously the pressure could be the reason of this behaviour, being higher the pressure in the case of high loads than in the low loads, producing more aggressive wear and the highest coefficient of wear. On the other hand if the same load is used with different strokes, the coefficient of wear increases by increasing the stroke (Fig. 3-13(b)).

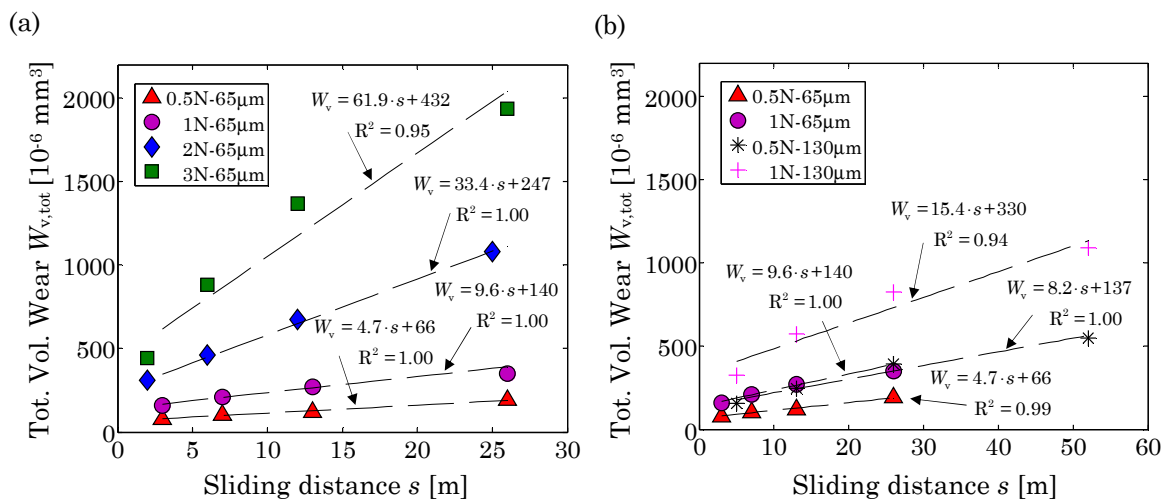


Fig. 3-12. Total volumetric wear for 90° crossed cylinder fretting tests with different normal loads, strokes and number of cycles: (a) influence of normal load and (b) influence of stroke.

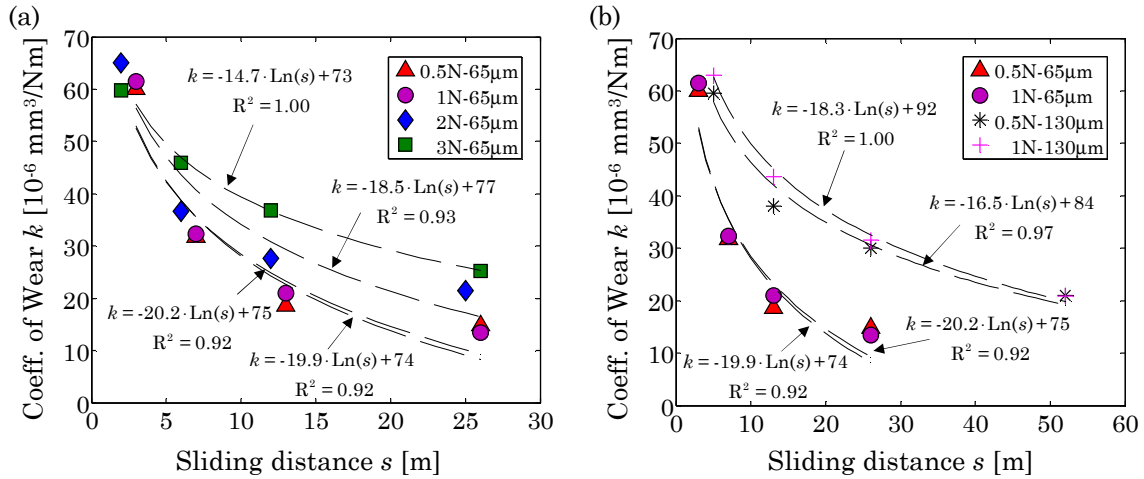


Fig. 3-13. Coefficient of wear for 90° crossed cylinder fretting tests with different normal loads, strokes and number of cycles: (a) influence of normal load and (b) influence of stroke.

Other authors, like Ramalho et al. [42], present the energy description as an alternative to describe the wear behaviour, because, as it was mentioned previously it represents the work done by the friction force which is the representative energy in the tribosystems. Using this energy-specific wear description in Fig. 3-14(a) and in Fig. 3-14(b), similar logarithmic tendency is observed, but in this case the values increase with the sliding distance, decrease by increasing the load and increasing the sliding distance. It means that it needs higher energy to obtain the same wear with low loads and small strokes. These tendencies are different to the results obtained by different authors [42], [43], [131], who observed a constant energy-specific wear resistance coefficient, with different strokes and loads, in fretting conditions.

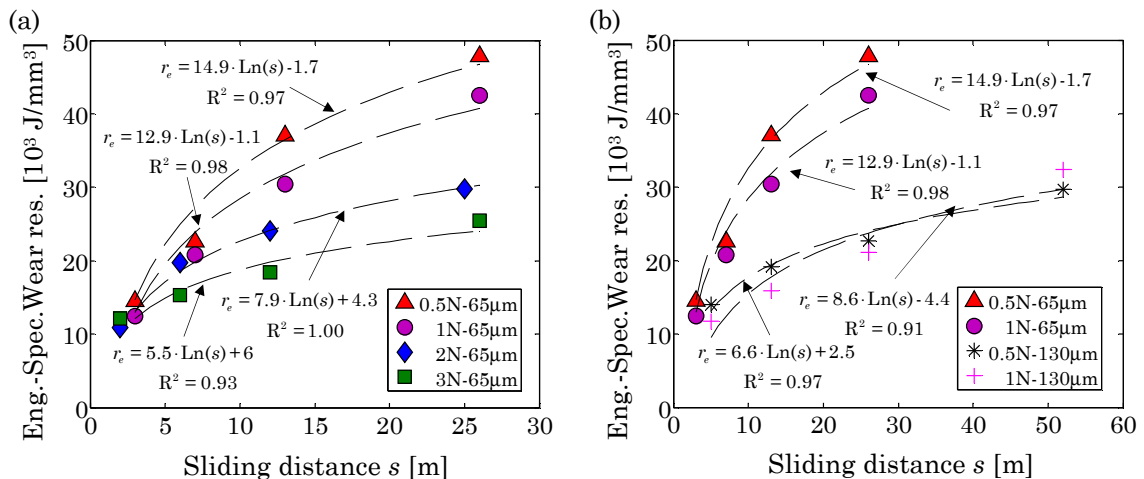


Fig. 3-14. Energy-specific wear resistance for 90° crossed cylinder fretting tests with different normal loads, strokes and number of cycles: (a) influence of normal load and (b) influence of stroke.

In order to explain better the wear behaviour, another strategy is proposed: the use of on-line volumetric wear parameter  $W_{v,oni}(t)$ , represented by the equation (Eq. 3-3), where  $R_1$  is

the radius of the cylinder 1 (upper),  $R_2$  is the radius of the cylinder 2 (lower) and  $W_{l,onl}$  is the instantaneous linear wear measured during the test. This parameter represents a driving curve of the volumetric wear and is based on the equations for the calculation of wear quantities using test specimens with curved shape [38]. In this case, as the radius of both cylinders is constant, the representative parameter to know the tendency of the  $W_{v,onl}(t)$  is the  $W_{l,onl}^2$ . In this way it is possible to know changes in the wear mechanism during the tests and it is possible to see changes in the wear rate along the tests.

$$W_{v,onl}(t) = \pi(R_1 R_2)^{1/2} W_{l,onl}^2 \quad (\text{Eq. 3-3})$$

In Fig. 3-15 the values of the  $W_{l,onl}^2$  for different tests with the same load and stroke but for different number of cycles are shown. The superposition of different tests is presented, showing the reproducibility of this type of tests. Moreover two clear wear periods appear, one corresponding to the running in period (higher slope) and the other one to the wear stable period (lower slope). In the first period that goes from 0 to 30000 cycles, approximately, a more aggressive wear mechanism is observed, being the wear rate lower in the second period.

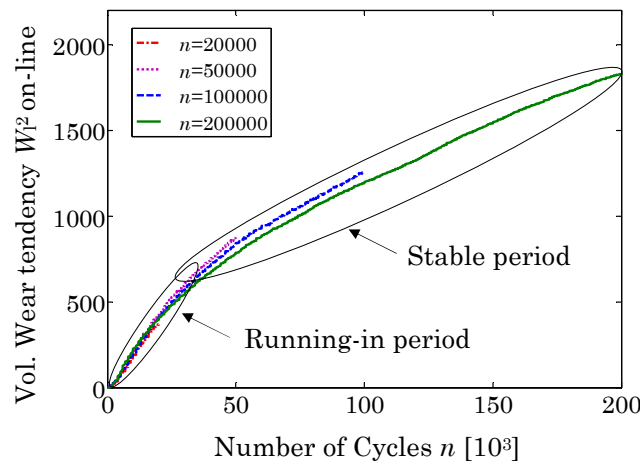


Fig. 3-15. Square of on-line linear wear  $W_{l,onl}^2$  for  $20 \times 10^3$ ,  $50 \times 10^3$ ,  $100 \times 10^3$ ,  $200 \times 10^3$ , 1 N and  $130 \mu\text{m}$ .

With these two periods, it is possible to understand better the results obtained previously with the coefficient of wear and the energy-specific wear resistance coefficient. In order to obtain coefficients that explain these two periods, in Fig. 3-16 the on-line volumetric wear  $W_{v,onl}(t)$  (Eq. 3-3) is related to Archard's loading factor  $F_n \times s$  [132], so that the slope of these curves is the coefficient of wear.

In Fig. 3-16(a) is shown that the slope of the curves in the running-in period for all normal loads is very similar, about  $50 \times 10^{-6} \text{ mm}^3/\text{Nm}$ . This result represents a linear influence of the load in the wear. However, in the stable period, this linear influence is not seen, because the slope increases with the load: for 0.5 N, the slope is  $10.4 \times 10^{-6} \text{ mm}^3/\text{Nm}$  and for 3 N, the slope is  $22.7 \times 10^{-6} \text{ mm}^3/\text{Nm}$ . The transition from the running-in period to the stable period is produced for higher loads at longer values of Archard's loading factor.

On the other hand in Fig. 3-16(b) is shown the influence of the stroke in the wear behaviour. In this case also, in the running-in period, the slope of the curves is similar with both strokes. In the stable period, the slope is higher with higher strokes: for  $65 \mu\text{m}$ , the slope is  $13.5 \times 10^{-6} \text{ mm}^3/\text{Nm}$  and for  $130 \mu\text{m}$ , the slope is  $20.1 \times 10^{-6} \text{ mm}^3/\text{Nm}$ , being the transition from the running-in period to the stable period later.

In order to validate the values obtained by the equation (Eq. 3-3), the experimental measurements of the volumetric wear  $W_{v,\text{tot}}$  are used. In Fig. 3-17 is shown this volumetric wear with respect to the Archard's loading factor represented by the product of normal load times sliding distance,  $F_n \times s$ . As it can be seen in the Fig. 3-17, the experimental results have a similar tendency than the driving curve obtained with the on-line wear. For all the cases, the running-in period is the same and is around  $60 \times 10^{-6} \text{ mm}^3/\text{Nm}$ . However, in the stable period different coefficients of wear are observed: for 0.5 N the coefficient of wear is  $9.5 \times 10^{-6} \text{ mm}^3/\text{Nm}$  and for 3 N the coefficient of wear is  $20.6 \times 10^{-6} \text{ mm}^3/\text{Nm}$  and for  $65 \mu\text{m}$  the coefficient of wear is  $9.6 \times 10^{-6} \text{ mm}^3/\text{Nm}$  and for  $130 \mu\text{m}$  the coefficient of wear is  $15.4 \times 10^{-6} \text{ mm}^3/\text{Nm}$ .

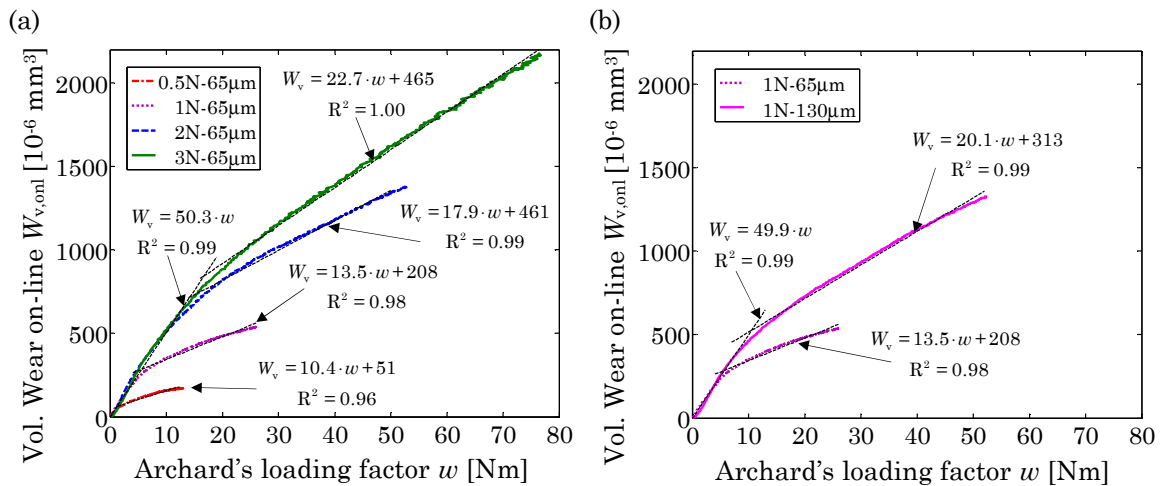


Fig. 3-16. The on-line Volumetric wear  $W_{v,\text{onl}}$  with respect to the Archard's loading factor for different tests: (a) the influence of load for  $65 \mu\text{m}$  stroke and (b) the influence of stroke for 1 N load.

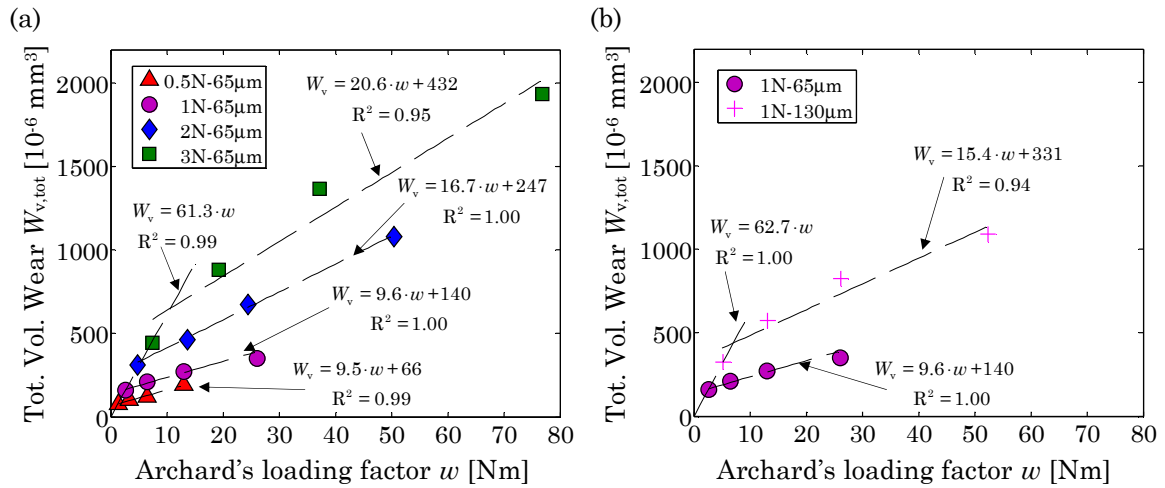


Fig. 3-17. The total volumetric wear  $W_{v,tot}$  with respect to the Archard's loading factor for different tests: (a) the influence of load for 65  $\mu$ m stroke and (b) the influence of stroke for 1N load.

If these values are compared with respect to the values obtained with the volumetric wear on line a close relation was found as is shown in Table 3-7. For this reason the on-line results are proposed to be realistic values to identify the transition period from the running-in period to the stable period.

Table 3-7. Coefficients of wear for different tests for the running-in period and the stable period.

Load-stroke	Running-in (on-line)	Running-in (off-line)	Stable period (on-line)	Stable period (off-line)
0.5 N-65 $\mu$ m	$51 \times 10^{-6}$ mm $^3$ /Nm	$61 \times 10^{-6}$ mm $^3$ /Nm	$10 \times 10^{-6}$ mm $^3$ /Nm	$9 \times 10^{-6}$ mm $^3$ /Nm
1 N-65 $\mu$ m	$50 \times 10^{-6}$ mm $^3$ /Nm	$61 \times 10^{-6}$ mm $^3$ /Nm	$14 \times 10^{-6}$ mm $^3$ /Nm	$10 \times 10^{-6}$ mm $^3$ /Nm
2 N-65 $\mu$ m	$50 \times 10^{-6}$ mm $^3$ /Nm	$61 \times 10^{-6}$ mm $^3$ /Nm	$18 \times 10^{-6}$ mm $^3$ /Nm	$17 \times 10^{-6}$ mm $^3$ /Nm
3 N-65 $\mu$ m	$50 \times 10^{-6}$ mm $^3$ /Nm	$61 \times 10^{-6}$ mm $^3$ /Nm	$23 \times 10^{-6}$ mm $^3$ /Nm	$21 \times 10^{-6}$ mm $^3$ /Nm
1 N-130 $\mu$ m	$50 \times 10^{-6}$ mm $^3$ /Nm	$62 \times 10^{-6}$ mm $^3$ /Nm	$20 \times 10^{-6}$ mm $^3$ /Nm	$16 \times 10^{-6}$ mm $^3$ /Nm

The final remark comes from the relation existing between the normal force and the stroke used  $F_n \times \Delta x$ . As it was seen before, when the different loads and strokes were compared, all present the same slope in the running in period. But as Archard's loading factor  $F_n \times s$  increases the length of the running-in period increases with the stroke. For this, in theory the same magnitude of  $F_n \times s$  could produce the same wear mechanism. Taking into account the dispersion of this type of tests, in Fig. 3-18 can be seen that for the same value of  $F_n \times \Delta x$  both curves are nearly identical, demonstrating that the wear behaviour is the same and the volumetric wear too.



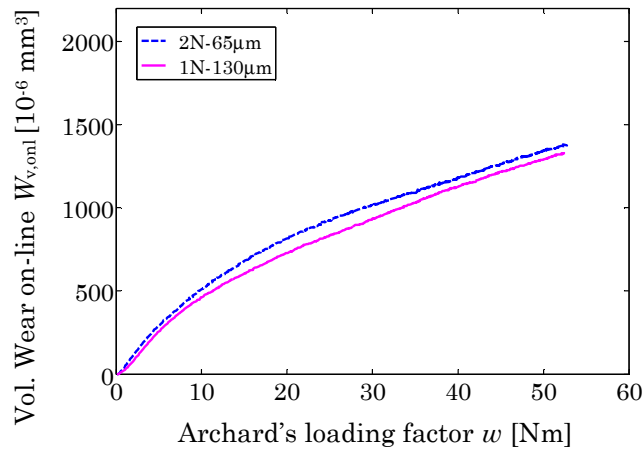


Fig. 3-18. The on-line volumetric wear as function of Archard's loading factor  $F_n \times s$ .

### 3.3.2 Fretting wear in thin steel wires with different crossing angles and the same normal force

#### 3.3.2.1 Friction behaviour

Fig. 3-19 shows the friction coefficient ( $f$ ) corresponding to the tests that have been carried out for the analysis of the influence of the crossing angle. All these tests were done with a constant normal force of 1 N. It can be seen that the friction coefficient is almost constant but nevertheless slightly decreasing from about 0.76 to about 0.67 with increasing crossing angle, thus at higher crossing angles less frictional energy is dissipated. It is in accordance with the general tendency shown by Fouvry [129] for metallic contacts in which an increase of the contact pressure tends to decrease the friction coefficient.

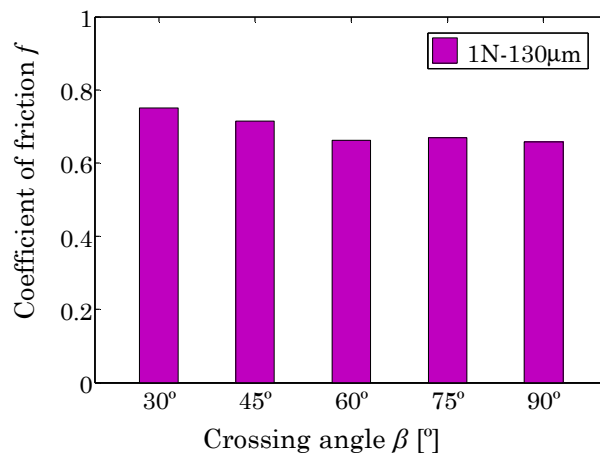


Fig. 3-19. Coefficient of friction for different crossing angles 1 N-130  $\mu\text{m}$  and 50000 cycles.

He related this tendency with the description proposed by Bowden and Tabor [133]. According to this description the interfacial shear stress  $\tau$  is expressed as a function of a

constant value  $\tau_0$  and a pressure dependence variable ( $p_m \cdot \gamma$ ), where  $p_m$  is the mean contact pressure and  $\gamma$  is the interfacial shear stress coefficient. Therefore the friction coefficient  $f$  is expressed by (Eq. 3-4).

$$f = \left| \frac{\tau}{P_m} \right| = \frac{\tau_0}{P_m} + \gamma \quad (\text{Eq. 3-4})$$

Taking into account this equation it is presumable that increasing the contact pressure decreases the friction coefficient, explaining the phenomenon appeared in thin steel wires.

### 3.3.2.2 Wear behaviour

The evolution of both wear scars from  $30^\circ$  to  $90^\circ$  for 1 N-130  $\mu\text{m}$  and 50000 cycles are shown in Fig. 3-20 and Fig. 3-21. The tendency is clear, as the crossing angle is increased; the wear scars become more elliptical. Moreover in each wear scar is possible to see the wear tracks produced due to de plowing process mentioned in the analysis that has been carried out in section 3.3.1.2 to identify the wear mechanism.

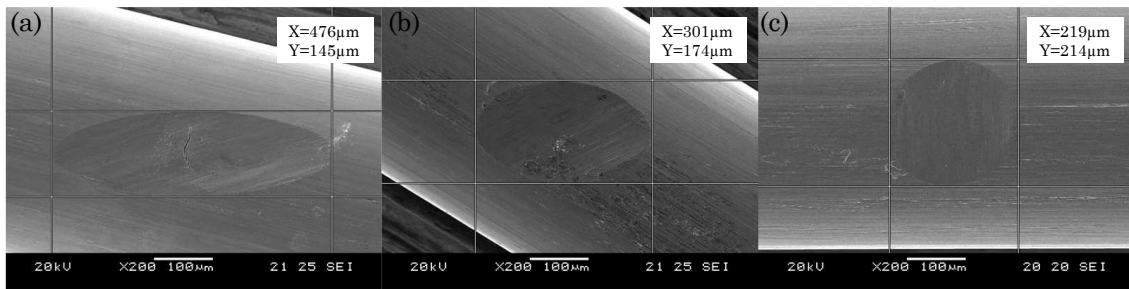


Fig. 3-20. Wear scars in upper wire (cylinder 1: perpendicular to sliding cylinder: static): (a)  $F_n = 1 \text{ N}$ ,  $\Delta x = 130 \mu\text{m}$ ,  $n = 50 \times 10^3$  cycles,  $\beta = 30^\circ$ ; (b)  $F_n = 1 \text{ N}$ ,  $\Delta x = 130 \mu\text{m}$ ,  $n = 50 \times 10^3$  cycles,  $\beta = 60^\circ$ ; (c)  $F_n = 1 \text{ N}$ ,  $\Delta x = 130 \mu\text{m}$ ,  $n = 50 \times 10^3$  cycles,  $\beta = 90^\circ$ .

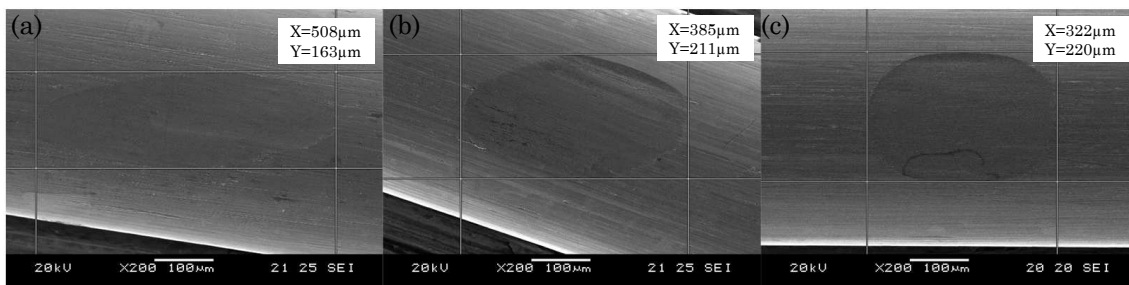


Fig. 3-21. Wear scars in bottom wire (cylinder 2: parallel to sliding cylinder: moving): (a)  $F_n = 1 \text{ N}$ ,  $\Delta x = 130 \mu\text{m}$ ,  $n = 50 \times 10^3$  cycles,  $\beta = 30^\circ$ ; (b)  $F_n = 1 \text{ N}$ ,  $\Delta x = 130 \mu\text{m}$ ,  $n = 50 \times 10^3$  cycles,  $\beta = 60^\circ$ ; (c)  $F_n = 1 \text{ N}$ ,  $\Delta x = 130 \mu\text{m}$ ,  $n = 50 \times 10^3$  cycles,  $\beta = 90^\circ$ .

Fig. 3-22(a) shows the total volumetric wear ( $W_{v,tot}$ ) for different contact angles and 1 N load. The produced wear volume is increasing with increasing contact angle. Moreover in Fig. 3-22(b) it is shown that the total linear wear  $W_{l,tot}$  increases increasing the contact angle. As a consequence of this, less cross section is obtained in the wire, being detrimental for the fatigue life of the wire rope.

Fig. 3-22(c) shows the energy specific wear resistance  $r_e$  obtained for the different crossing angles. It may be seen that under these conditions the energy necessary to remove 1 mm<sup>3</sup> is slightly decreasing from 22 x 10<sup>3</sup> Joule to 16 x 10<sup>3</sup> Joule with increasing crossing angle from 30° to 90° which means that at higher crossing angles less energy is needed to achieve the same amount of wear, or in other words, the wear process is more intense.

With a constant or decreasing friction coefficient, as it was observed, at the same time this means that the coefficient of wear ( $k$ ) is increasing. This can be seen in Fig. 3-22(d). Since the load is constant (for the same number of cycles) in this test series, an increasing coefficient of wear could be explained by 2 different reasons. First, the wear mechanism is different for all crossing angles. Or second, there is a different ratio of running-in to steady state process for different crossing angles (different contact pressures). In the tests carried out with 90° crossing angle and different normal loads (different contact pressures), it was observed that for each normal load there is a distinctive difference between an initial running in period with higher slope and a steady state period with a significantly lower slope. The running in period is represented by the first slope, which points at a higher wear intensity and is longer for higher contact pressures. The steady state period is represented by the second slope and it seems to increase with increasing contact pressures Fig. 3-17.

Taking into account the wear mechanism described in section 3.3.1.2, it looks that: on one hand the formation of protective layers could be the reason of the transition from a severe wear process to a mild wear process and on the other hand the formation of these layers is earlier with smaller contact pressures. For this reason, the smaller crossing angle, in which less contact pressure is obtained, tends to produce smaller coefficients of wear and also higher energy specific wear resistance.

Based on the previous assumptions the second reason is much more probable and therefore the test results point at a crucial dependence of the running in process from the contact situation. However, this was not further deepened in this study.

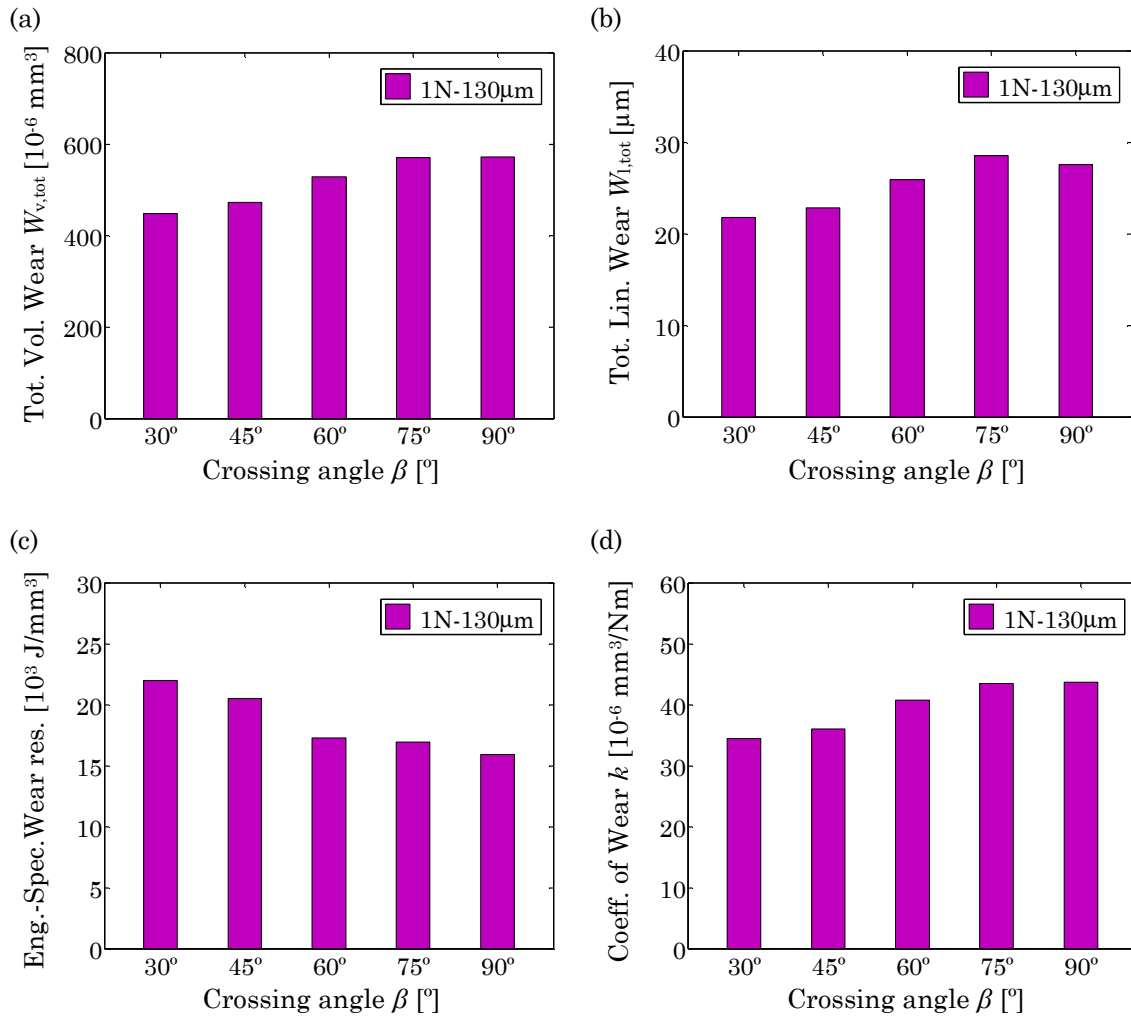


Fig. 3-22. Wear behaviour analysis results for different crossing angles 1 N-130  $\mu$ m and 50000 cycles: (a) total volumetric wear; (b) total linear wear; (c) energy-specific wear resistance and (d) coefficient of wear.

### 3.3.3 Fretting wear in thin steel wires with different crossing angles and the same initial contact pressure

#### 3.3.3.1 Friction behaviour

With the aim to understand better the influence of the contact pressure in the frictional behaviour, Fig. 3-23 shows the coefficient of friction for tests where the average contact pressure is kept constant, for two different strokes and 50000 number of cycles. In this case the friction coefficient ( $f$ ) does not change significantly, corroborating that the friction coefficient is related to the contact pressure.

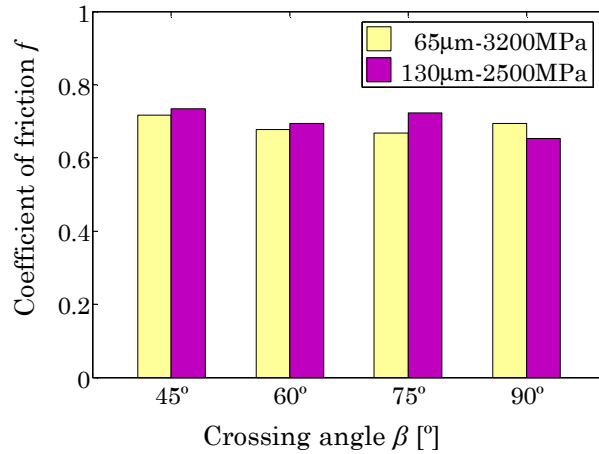


Fig. 3-23. Coefficient of friction for different crossing angles and the same initial mean contact pressure.

### 3.3.3.2 Wear behaviour

The wear scars after the test with the same initial mean contact pressure from 45° to 90° for 3200 MPa-130  $\mu$ m and 50000 cycles are shown in Fig. 3-24 and Fig. 3-25. Considering the wear mechanism described in section 3.3.1.2, in both wear scars is possible to see the wear tracks.

Fig. 3-26(a) shows the total volumetric wear ( $W_{v,tot}$ ) for different crossing angles and 2 different strokes and contact pressures. In contrast to the results of the test carried out for different crossing angles and the same normal force in section 3.3.2.2, the wear volume tends to decrease with increasing the crossing angle: less wear at higher angle. Furthermore the total linear wear ( $W_{l,tot}$ ) tends to decrease slightly with increasing crossing angle as it shows Fig. 3-26(b).

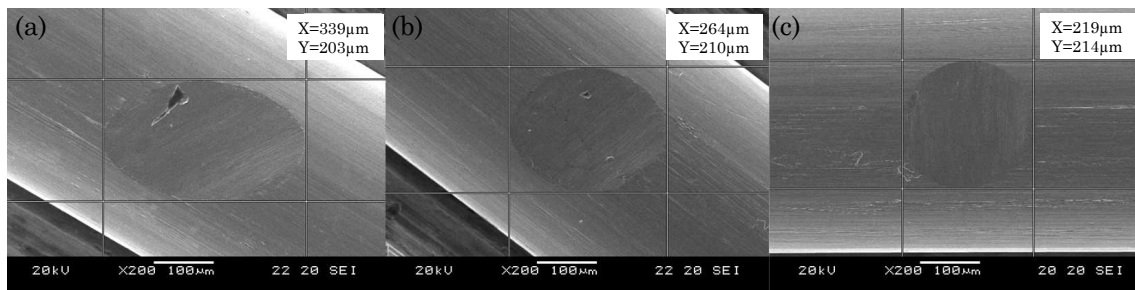
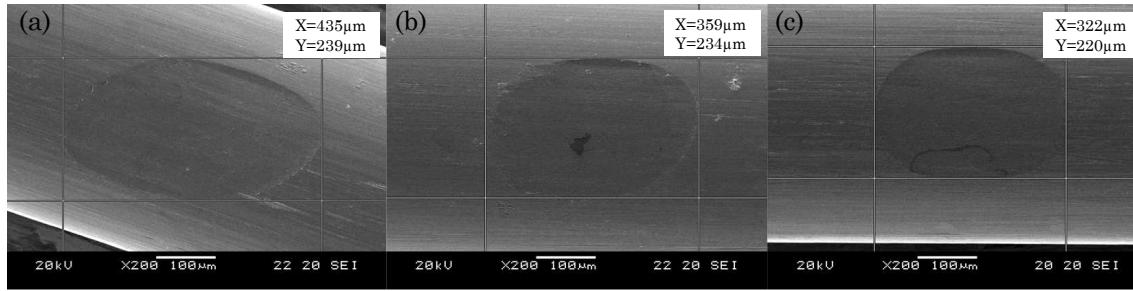


Fig. 3-24. Wear scars in upper wire (cylinder 1: perpendicular to sliding cylinder: static): (a)  $F_n = 1.6$  N,  $\Delta x = 130$   $\mu$ m,  $n = 50 \times 10^3$  cycles,  $\beta = 45^\circ$ ; (b)  $F_n = 1.1$  N,  $\Delta x = 130$   $\mu$ m,  $n = 50 \times 10^3$  cycles,  $\beta = 75^\circ$ ; (c)  $F_n = 1$  N,  $\Delta x = 130$   $\mu$ m,  $n = 50 \times 10^3$  cycles,  $\beta = 90^\circ$ .



**Fig. 3-25. Wear scars in bottom wire (cylinder 2: parallel to sliding cylinder: moving): (a)  $F_n = 1.6$  N,  $\Delta x = 130$   $\mu\text{m}$ ,  $n = 50 \times 10^3$  cycles,  $\beta = 45^\circ$ ; (b)  $F_n = 1.1$  N,  $\Delta x = 130$   $\mu\text{m}$ ,  $n = 50 \times 10^3$  cycles,  $\beta = 75^\circ$ ; (c)  $F_n = 1$  N,  $\Delta x = 130$   $\mu\text{m}$ ,  $n = 50 \times 10^3$  cycles,  $\beta = 90^\circ$ .**

Fig. 3-26(c) shows the energy specific wear resistance for this type of tests. It can be noticed that the wear resistance is more or less constant and does not change significantly taking into account the experimental error. The energy needed to remove 1 mm<sup>3</sup> is about  $18 \times 10^3$  Joule. Under these test conditions the wear intensity is roughly not dependent on the crossing angle besides the very slight tendency towards a slight minimum at an angle of  $60^\circ$  which is not interpreted further. With this result the coefficient of wear ( $k$ ) must be also more or less constant since the coefficient of friction is constant. This can be seen in Fig. 3-26(d).

The energetic consideration leads then to the conclusion that under these conditions, with the same average contact pressure, the wear intensity is roughly constant and, therefore, independent from the crossing angle. In accordance with the conditions that the contact pressure is largely kept constant by adjusting the normal load for the different crossing angles the wear intensity should also be largely constant. In contrast with the results from test carried out for different crossing angles and the same normal force in section 3.3.2.2, in this case the coefficient of wear could be constant, as seen in Fig. 3-26(d), because the ratio between the running in process and the following steady state process is kept constant which most probably is a consequence of the constant contact pressure. The observed decrease of the wear volume as shown in Fig. 3-26(a) is explained as a consequence of the decreasing normal load in this test series.

The final remark comes from the similar values obtained in the total volumetric wear ( $W_{v,tot}$ ), in Fig. 3-26(a), and also in the coefficient of wear ( $k$ ), in Fig. 3-26(d), between the two contact pressure tests: 3200 MPa with a stroke of 65  $\mu\text{m}$  and 2500 MPa with a stroke of 130  $\mu\text{m}$ . In section 3.3.1.2 for  $90^\circ$  crossing angle tests, was reported that the same magnitude of  $F_n \times \Delta x$  produces the same running in period and the same steady state period, in other words, the same wear mechanism, in two specific cases: 0.5 N x 130  $\mu\text{m}$ /1 N x 65  $\mu\text{m}$  and in 1 N x 130  $\mu\text{m}$ /2 N x 65  $\mu\text{m}$ .

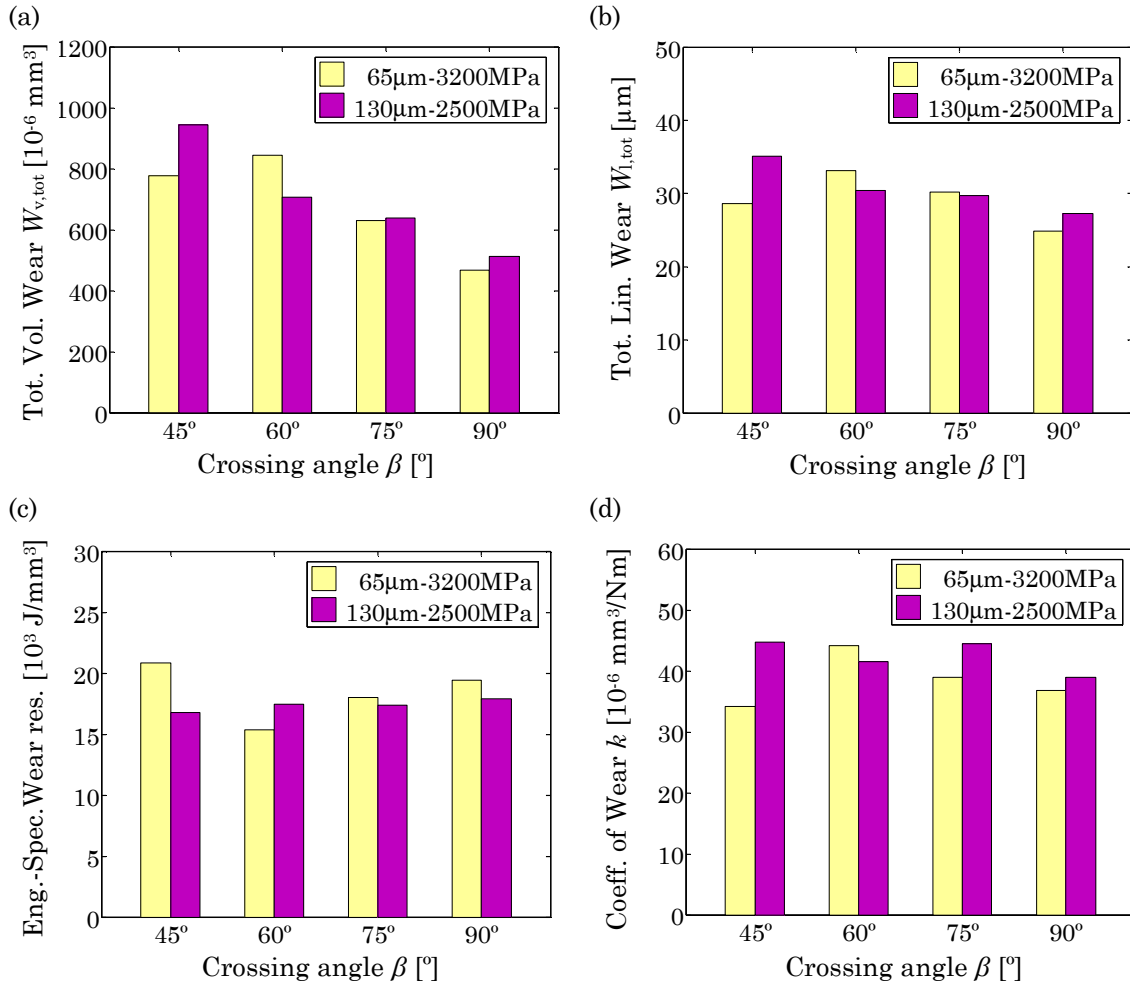


Fig. 3-26. Wear behaviour analysis results for different crossing angles the same initial mean contact pressure and two strokes: (a) total volumetric wear, (b) total linear wear, (c) energy-specific wear resistance and (d) coefficient of wear.

Taking into account that the contact pressure is directly related with the normal force  $F_n$  and the contact angle  $\beta$ , it could be related the stroke and the contact pressure with the wear behaviour. Considering the contact pressures used in these tests, it could be defined a relation  $p_m \times \Delta x$  which could explain the same wear mechanism for these specific tests. This relation is presented in equation (Eq. 3-5). Where  $p_{m,gt}$  = greater contact pressure (3200 MPa);  $\Delta x_{sm}$  = smaller stroke (65 µm);  $p_{m,sm}$  = smaller contact pressure (2500 MPa) and  $\Delta x_{gt}$  = greater stroke (130 µm).

$$\frac{p_{m,sm} \times \Delta x_{gt}}{p_{m,gt} \times \Delta x_{sm}} \approx 1.59 \quad (Eq. 3-5)$$

After this it is important to know that the wear behaviour of both periods (running in period and steady state period) not only depends on the contact pressure but it depends on the relation of contact pressure-stroke.

### 3.4 Conclusions

---

Oscillating sliding tests were carried out on thin steel wires under fretting conditions using the crossed cylinders contact geometry. A more common 90° crossed cylinder configuration and a more realistic to the wire rope system crossing angle configuration were used. It has been seen that the gross sliding regime is the predominant regime in the range of studied contact pressures and strokes values. The main conclusions related to the frictional behaviour and wear behaviour are summarized in the following lines.

Frictional behaviour:

In the tests carried out with 90° crossed cylinder, it has been shown an increase in the coefficient of friction in the first 20000 cycles followed by a decrease between 20000-50000 cycles which finalized in a stable steady state period. This tendency could be associated with the elimination of the surface oxides promoting severe metal-metal interaction in the beginning which then leads to the formation of a protective compacted debris layer as shown in the SEM micrographs obtained after the test.

Another tendency appeared in the test carried out with different crossing angles. When the same load is maintained for different crossing angles, the coefficient of friction is smaller with higher crossing angles (high contact pressures). Nevertheless when the same initial contact pressure is used for the different crossing angles, the same coefficient of friction is obtained. So there is a relation between the coefficient of friction and the contact pressure, which is in accordance with the description proposed by Bowden and Tabor [133] on metallic contacts.

Wear behaviour:

In the tests carried out with 90° crossed cylinders two different studies were presented: the classical study, where the coefficient of wear and the Energy-Specific wear resistance is represented against sliding distance and the proposed study where the volumetric wear is represented against Archard's loading factor. While the first study didn't represent clearly the wear behaviour along the test, in the second one two wear periods were detected: a running-in period, with a more aggressive wear mechanism, and a stable steady state period. The transition of the two periods could be attributed to the formation of protective layers which leads to reduce the wear formation between both surfaces. These protective



layers have a great influence in the bottom specimen, promoting variable wear behaviour between both specimens. In the beginning there is a greater wear loss in the bottom specimens. Nevertheless the formation of these protective layers, promote to reduce considerably the loss of wear in the bottom specimen while the top specimen remains increasing. Moreover it has been presented an equation for the calculation the online volumetric wear, which could help in the estimation of the transition between the running-in period and the stable period.

As a result of the tests, taking into account Archard's loading factor, all contact pressures produce the same coefficient of wear during the running-in period, but the transition to the stable period for higher loads is observed later. In the stable period, higher values of the coefficient of wear are observed with higher loads (higher contact pressures). Furthermore longer strokes produce more aggressive behaviour in the stable steady state period for the same load. It means that more aggressive wear behaviour is produced with higher contact pressures and strokes.

In all the tests, it has been observed that the coefficient of wear is not a constant parameter, as it has been reported in the works carried out by other authors. Different values of the coefficient of wear are observed in the stable period, depending on the used load and stroke. So it is important to know the transition from the running in period to the stable period that can be estimated with the equation presented for on-line volumetric wear as has been mentioned previously.

Furthermore a relation was found between the normal force, stroke and the wear behaviour. When a constant value of  $F_n \times \Delta x$  was used the wear behaviour obtained in both periods is almost the same. Thus the running in period and the stable period is the same for these loading conditions.

With the aim to understand better the influence of contact pressure tests with different crossing angles were carried out. The crossing angle was varied between 30° and 90°. Two different types of test were proposed. In the first test series (tests series 1) the normal load was kept constant at 1 N which leads to different initial contact pressures according to the applied crossing angle. In the second test series (tests series 2) the normal load was adjusted in that way that the initial contact pressure is largely kept constant at all crossing angles.

The results show that the generated wear volume and linear wear is smaller with small crossing angles due to the decrease of the contact pressure, producing a less severe wear scar in test series 1. Nevertheless when the initial contact pressure is constant for the different crossing angles (test series 2), the wear volume is higher with smaller crossing

angles. This phenomenon can be understood assuming the two different wear periods mentioned previously in the 90° crossing angle cases, namely a running-in period and a steady state period with two different wear coefficients. It has to be pointed out that the coefficient of wear and the energy specific wear resistance gives the same tendencies.

A varying length of the running-in period due to a changing contact pressure as a consequence of the crossing angle in test series 1 would then result in a different wear coefficient. According to the mentioned previously for 90° crossing angles, small contact pressures, in this case, small crossing angles, produce less severe wear coefficient. Thus the generated wear volume is smaller with small crossing angles than with high crossing angles.

On the other hand in tests series 2 a constant ratio between the running-in process and the following steady state process due to the initial same constant pressure for the different crossing angles would then explain the constant wear coefficients. Thus the generated wear volume is higher with small crossing angles than with high crossing angles, because for the same wear coefficient in the case of small crossing angles the load is higher and also the frictional dissipated energy.

Finally it is important to remark that the wear behaviour of both periods depends on the relation contact pressure-stroke which is in accordance with the relation  $F_n \times \Delta x$  explained previously for 90° crossed cylinders.

# FEM MODELLING OF FRETTING WEAR IN THIN STEEL WIRES

---

## 4.1 Introduction

---

The experimental testing of thin steel wires with configurations and operational variables close to the ones presented in wire ropes systems requires high number of tests, with high time consuming and the cost associated to these tests. Furthermore the detection of fretting wear damage in wire rope systems is not perceptible by simple visual inspection, so that the wire rope has to be disassembled with the corresponding complexity. The necessity to improve the knowledge about the wear behaviour in complex configurations mechanical components and predict fretting damage severity caused under different operational and constructive variables implies the necessity of developing numerical models.

As has been shown previously in the literature review, the FE wear modelling solution has been adopted by many authors for predicting wear in, sliding wear [99], [102], [103], reciprocating sliding wear [105] and in fretting wear conditions [43], [104], [108]. Mainly this approaches are based in the Archard's local wear model but some authors [43],[81] have developed a finite element based energy wear simulation methods. In the case of 3D complex problems, such as in the study of fretting in spline couplings, Ding et al. [107] used the FE wear methodology developed and validated previously in a tribological cylinder on plane 2D laboratory test configuration.

In this chapter a finite element based wear simulation methodology for modelling fretting wear scars in thin steel wires will be presented. This methodology will be developed with the aim to be valid for predicting fretting wear in all contact configurations presented in wire ropes systems. Nevertheless the complexity that requires to develop a FE wear methodology for a 3D crossing angles thin steel wires, has induced to develop previously a

wear simulation strategy in a more simple configurations, before implementing in crossing angles cylinders.

Firstly it has been defined a structured methodology for modelling wear in any tribosystems in a 2D cylinder on plane sliding wear case. Moreover different optimization strategies have been introduced in this methodology. This methodology was developed with the aim to acquire greater knowledge about the different strategies proposed by many authors and to facilitate the modelling of wear in 3D problems.

Secondly based on the experience acquired with the 2D FE wear simulation strategy, a FE optimized wear methodology for modelling fretting wear scars in 90° crossed cylinder arrangements have been developed. Finally this methodology has been implemented in the thin steel wires crossing angles configuration. Both models were validated with the experimental data obtained from the fretting wear tests described in Chapter 3.

The FE wear modelling was implemented using the Abaqus user subroutine UMESHMOTION, which has been validated by many authors, i.e., Madge et al. [61] has validated this subroutine for fretting problems in both partial slip regime and gross sliding regime, and Hegadekatte et al. [109] for sliding and slipping wear in pin-on-disc and twin-disc tribosystems.

## **4.2 FEM wear methodology of 2D block on ring model**

---

### **4.2.1 Introduction**

This section is focused on the development of a FE optimized wear simulation strategy for modelling wear in any tribosystem, using a simplified model. The selected model for the development this strategy was the block on ring sliding wear tribological testing configuration. One advantage of this model is that it can be modelled as a 2D problem, where the wear on the cylinder can be considered depreciable, and the effect of relative sliding in the slip distribution and the contact pressure in the contact zone can be simplified to the resolution of the contact problem without considering the tangential problem. Further around this last aspect will be discussed in point 4.2.3.1 So that, this section includes sliding wear test in a block on ring test configuration, needed for obtaining the input wear and friction coefficients used in the wear simulation methodology, the cylinder on plane FE model and the description and application of the FE structured wear methodology, which has been developed for modelling the severe wear metal-metal contact configuration, with high wear rates. The aim of this methodology is to be efficient the

modelling of this type of problem, presented also in the thin steel wires under fretting wear conditions.

## 4.2.2 Block on ring experimental testing

### 4.2.2.1 Sliding wear test rig

For tribological testing the contact geometry of cylinder on plane was used. These tests will be used to define the coefficient of friction and the coefficient of wear needed as input values in the wear simulation and for the following validation of the numerical simulation methodology.

The test specimens were initially machined from C45E steel bars. The specimens were subsequently submitted to heat treatment. Firstly, they were heated at 850°C and then water quenched at room temperature. The hardness obtained after this process was 55-60 HRC. Finally the specimens were machined and ground to obtain the required dimensions shown in Table 4-1. The contact surface average roughness ( $R_a$ ) obtained was 0.20-0.30  $\mu\text{m}$ . These values were obtained from the measured carried out using a contact stylus profilometer.

Table 4-1. Test specimens dimensions and roughness.

Specimen	Dimensions	Roughness
Cylinder	$\text{\O} 40 \times 11 \text{ mm}$	0.22 $\mu\text{m}$
Block	16 x 12 x 6 mm	0.28 $\mu\text{m}$

The sliding wear tests were carried out on a tribometer *PRIZMA TPD 95C* (Fig. 4-1(a)). The tribometer consists on a top arm carrying the block and on a shaft carrying the cylindrical specimen. While the block is pressed against the cylinder at a constant normal force ( $F_n$ ), the cylinder is rotated at a constant linear speed in the contact zone. During the tests the normal force ( $F_n$ ) and the friction force ( $F_f$ ) were continuously measured by the strain gauges located in the top arm, which can capture the deflection of this component due to the two loads. After the tests both specimens (Fig. 4-1(b)) were cleaned in ultrasonic acetone bath, which then were rinsed with alcohol and the volumetric wear ( $W_v$ ) of the block was measured by confocal microscopy. The wear of the cylinder was not considered in the simulation in order to simplify the problem. This is because the wear depth ( $W_1$ ) obtained in the severest case (0.002 mm) in comparison with the diameter of the cylinder (40 mm) is very small. So this small change in the surface could be considered depreciable in the wear simulation methodology.

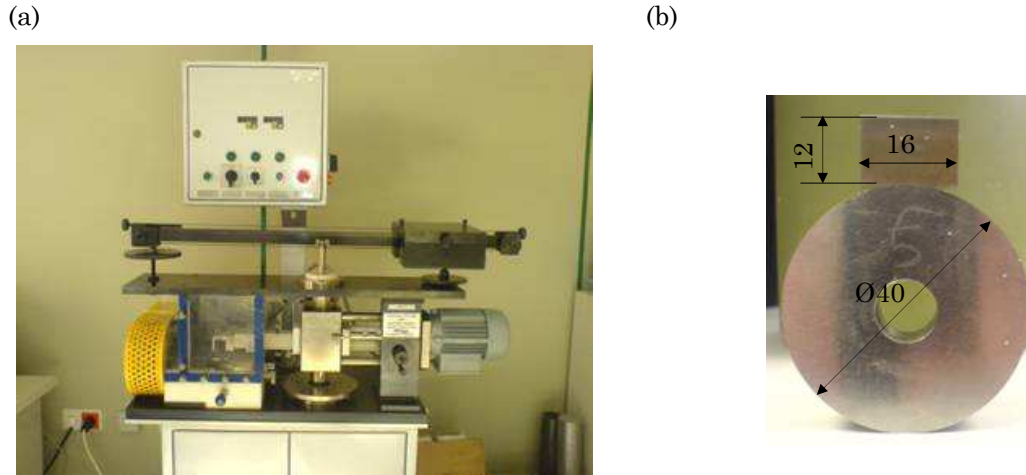


Fig. 4-1. Photograph of the block on ring test rig: (a) tribometer and (b) testing specimens.

In Table 4-2 are summarized the values used for performing sliding wear test in the block on ring tribometer. While the block was pressed against the cylinder with a constant load of 65 N, which generates a mean contact pressure of 110 MPa, the cylinder was rotated at a constant linear speed of 0.25 m/s and 0.5 m/s. Three running times were considered (2 h, 4 h, 5 h) with the aim to have enough wear and define the wear coefficient corresponding to the block specimen. The tests were carried out at a room temperature and with a relative humidity of 50%.

Table 4-2. Block on ring tests conditions values .

Parameter	Symbol	Value
Normal load (N)	$F_n$	65
Mean contact pressure (MPa)	$p_m$	110
Maximum contact pressure (MPa)	$p_{max}$	141
Linear speed (m/s)	$v$	0.25, 0.5
Time (h)	$t$	2,4,5
Temperature (°C)	$T$	25±1
Relative humidity (%)	RH	50±1

#### 4.2.2.2 Tribological quantities

For the wear simulation by FEM, there are two representative tribological quantities. The first one corresponds to the friction behaviour which is described by the coefficient of friction. The coefficient of friction  $f$  is obtained by dividing the friction force  $F_f$  by the normal force  $F_n$  according to (Eq. 4-1) and thus stored each second per sliding wear test.

However the mean coefficient of friction used in this research represents the average value calculated from the data of the last half of the experiment.

$$f = \frac{F_f}{F_n} \tag{Eq. 4-1}$$

The second one corresponds to the wear behaviour which is described by the coefficient of wear  $k$  presented in equation (Eq. 4-2). Where  $W_v$  is the volumetric wear of the block,  $F_n$  is the normal force and  $s$  is the total sliding distance.

$$k = \frac{W_v}{s \cdot F_n} \tag{Eq. 4-2}$$

The volumetric wear  $W_v$  is obtained according to equation (Eq. 4-3). Where  $W_p$  is the area of the profile of the wear scar and  $l$  is the width of the block as shown in Fig. 4-2. The planimetric wear  $W_p$  represents the mean of various profiles obtained along the wear scar. The profiles have been obtained by confocal microscopy.

$$W_v = W_p \cdot l \tag{Eq. 4-3}$$

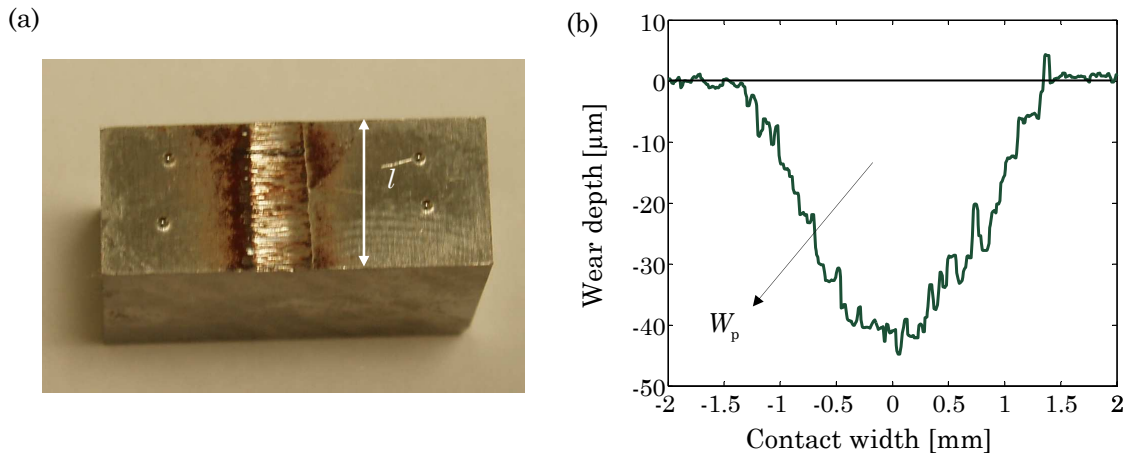


Fig. 4-2. Volumetric wear calculation: (a) testing specimen with the wear scar and (b) wear scar profile.

#### 4.2.2.3 Experimental tests results

The coefficient of friction  $f$  as a function of the time for one sliding wear test is shown in Fig. 4-3(a). An increase of the coefficient of friction in the beginning of the test following by a slightly decrease and stabilization is presented. After carrying out the tests under the

different conditions, it was obtained that the mean coefficient of friction for this configuration was 0.65.

On the other hand the volumetric wear as a function of the Archard's loading factor for the different tests is shown in Fig. 4-3(b). The slope of the line used for fitting the experimental data represents the mean coefficient of wear for all the tests. So the coefficient of wear corresponding to the block can be quantify as  $k = 2\text{E-}09 \text{ mm}^3/\text{Nmm}$ .

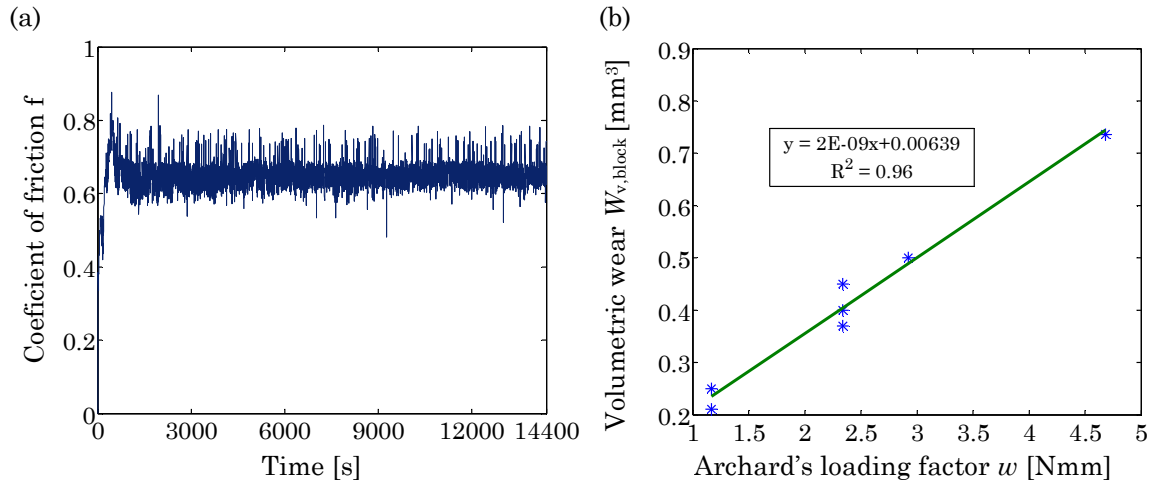


Fig. 4-3. Friction and wear behaviour results: (a) coefficient of friction and (b) Volumetric wear of the block vs. Archard's loading factor (coefficient of wear).

### 4.2.3 FEM wear methodology

#### 4.2.3.1 Cylinder on plane FE model

The FE model used for the development of the optimised wear simulation methodology for the block on ring test configuration is shown in Fig. 4-4. Two dimensional, four node, plane strain linear elements were used in the analysis (Fig. 4-4(a)). The meshes were carried out according to a partition methodology (Fig. 4-4(b)), in which a more refined mesh is used in the contact zone (Fig. 4-4(b)). The contact surface resolution taking into account the friction is implemented via the penalty method and the finite sliding contact pair algorithm which uses the master-slave algorithm to enforce the contact constraints. Taking into account this algorithm the master surface could penetrate in the slave surface. So in this study the block is considered as slave surface and the cylinder as master, such as the wear is generated mainly in the block surface. The coulomb friction model was employed and a COF of 0.65 was chosen according to the experimental results presented in section 4.2.2.3.



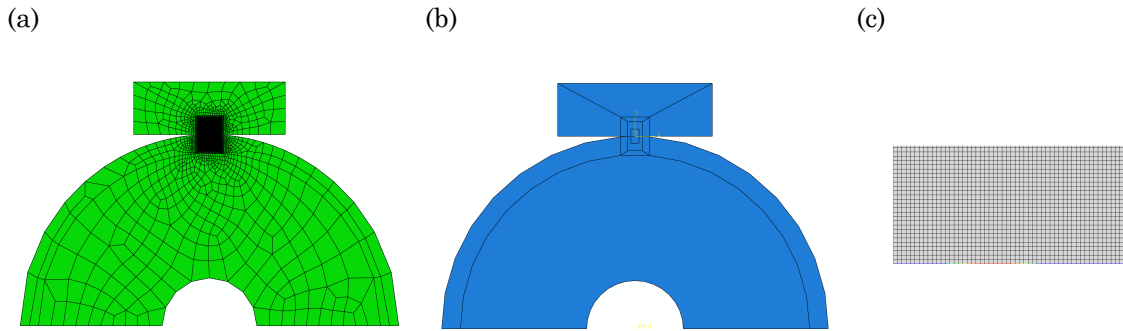


Fig. 4-4. Cylinder on plane FE model: (a) FE mesh, (b) partitions near the contact zone and (c) mesh in the contact zone.

The load and the boundary conditions were applied in the free surfaces. Two steps were considered for the analysis. While in the first step the block was pressed against the cylinder at a specific pressure in the second step the cylinder was rotate a small increment in order to study the effect of friction in the slip and in the contact pressure distribution. The elastic modulus and Poisson’s ratio of both specimens are taken as 210 GPa and 0.33 respectively.

The boundary conditions corresponding to the first step are shown in Fig. 4-5(a). While the cylinder was encastre in the central hole, a linear pressure was applied in the top surface of the block restricting the horizontal movement of this component. On the other hand the boundary conditions of the second step are shown in Fig. 4-5(b). In this case the linear pressure in the block was maintained and a small rotation was imposed in the central hole of the cylinder, producing a small sliding increment  $\Delta s$  in the contact zone.

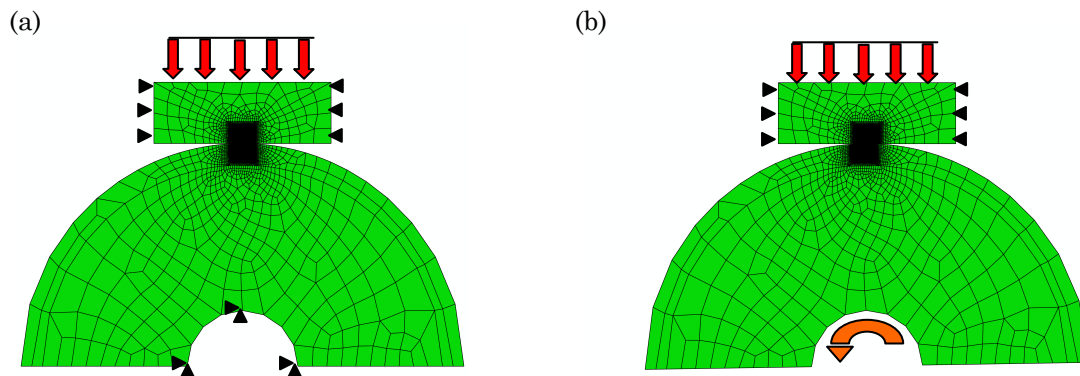
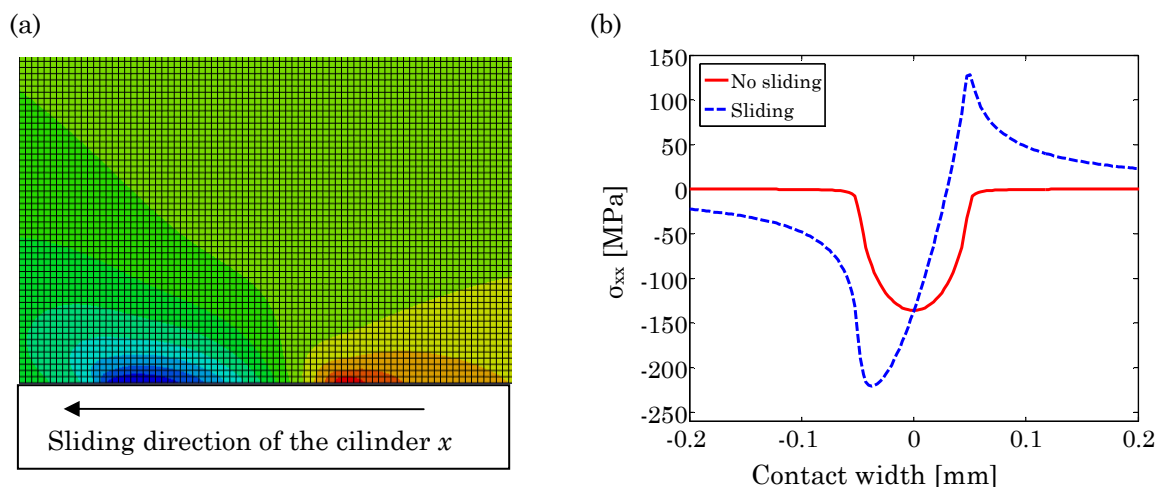


Fig. 4-5. Boundary conditions in the block on ring FE model: (a) step 1 and (b) step2.

In order to simplify the wear optimized methodology study the imposed rotation corresponding to the second step was neglected. Performing this simplification, it is assumed that in each wear increment all the nodes corresponding to the contact zone slide the same magnitude, which corresponds to the sliding increment  $\Delta s$ . In cases like this one,

in which there is continuous sliding this simplification is efficient. However, in cases where reciprocating sliding appears or cases in which the stick-slip phenomenon has a great importance, this simplification should not be considered.

To validate this assumption, the effect of a small sliding increment in the contact pressure and in the slip distribution is presented in the following lines. In Fig. 4-6 the surface stresses of the block, in the tangential direction to the sliding are shown. It can be seen that while in the not sliding case, the stress field is symmetrical, in the sliding case the leading edge of the contact is subjected to a compressive tractions and the trailing of the contact edge is subjected to a tensile tractions.



**Fig. 4-6. Surface stress distribution  $\sigma_{xx}$  in the block: (a) FEM model and (b) surface stresses with and without sliding.**

Nevertheless the effect of these stresses in the contact pressure Fig. 4-7(a) and in the slip distribution Fig. 4-7(c) is depreciable. As shown in Fig. 4-7(a) the contact pressure in both cases is near the same, nevertheless the contact pressure distribution shifts slightly in the direction of sliding in the case of the sliding conditions with respect to the not sliding condition. As shown in the deviation curve (Fig. 4-7(b)), the contact pressure is slightly higher in the leading edge and slightly lower in the trailing edge. Nevertheless these values are small for this test configuration and contact conditions, so the previously presented assumption can be confirmed. This effect was reported by Hegadekatte [99] for pin on disk sliding configuration, and was named as leading edge effect.

On the other hand the second parameter needed in the wear modelling is the slip distribution of each node. As can be seen in Fig. 4-7(c) the slip distribution along the contact zone remains constant and is nearly equal to the sliding increment  $\Delta s$  value used in this study, which corresponds to a  $\Delta s = 0.0157\text{mm}$ , so the second assumption has been corroborated.

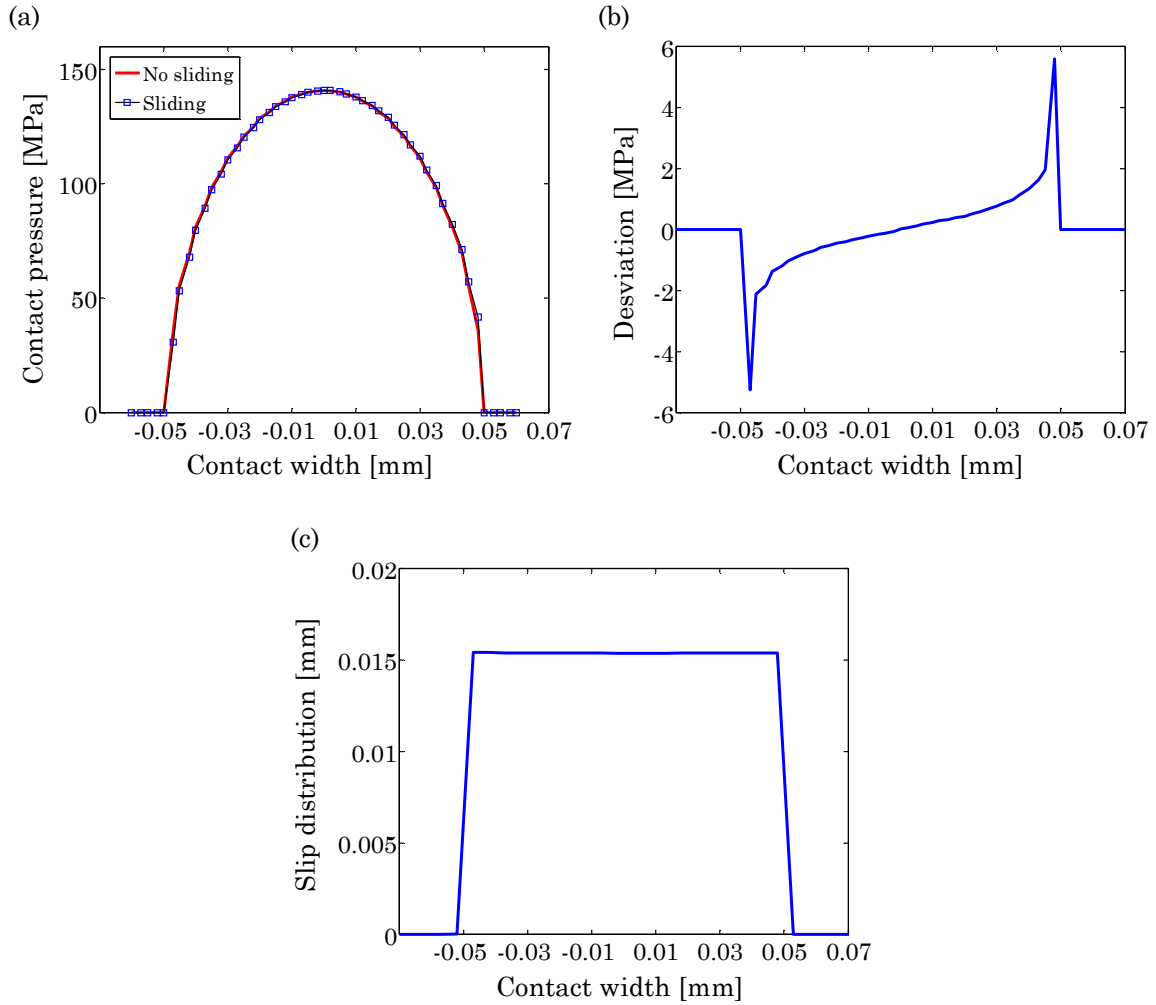


**Fig. 4-7. Contact pressure and slip distribution study: (a) comparison of the contact pressure distribution with and without sliding (b) Deviation of the contact pressure with sliding and (c) slip distribution in the contact width.**

In order to validate the FE model, the contact pressure obtained by FEM will be compared in section 4.2.4 with the contact pressure distribution obtained according to the analytical solution for the linear contact reported by Hertz and described by Johnson [13]. Therefore the contact pressure distribution is given by (Eq. 4-4):

$$p(x) = p_{\max} \sqrt{1 - \frac{x^2}{a^2}} \tag{Eq. 4-4}$$

where  $a$  is the semi-contact width and the  $p_{\max}$  is the maximum contact pressure given by (Eq. 4-5):

$$p_{\max} = 2 \cdot F_{n,l} / (\pi \cdot a) \tag{Eq. 4-5}$$

$F_{n,l}$  is the applied normal load per unit length  $l$ . The semi contact width  $a$  is obtained according to (Eq. 4-6), where  $R_e$  and  $E_e$  are the reduced radius of curvature and the equivalent Young modulus respectively given by (Eq. 2-3) and (Eq. 2-4):

$$a = \left( \frac{4 \cdot F_{n,l} \cdot R_e}{\pi \cdot E_e} \right) \quad (\text{Eq. 4-6})$$

#### 4.2.3.2 Wear local model

For the wear simulation in any tribological system it is necessary to develop a local wear model. In this study the Archard modified equation as presented by Hegadekatte et al. [106] for sliding contacts was used. The local wear model begins with the Archard model presented in equation (Eq. 4-7), where the volumetric wear  $W_v$  is proportional to the normal force  $F_n$  and the sliding distance  $s$  and inversely proportional to the hardness of the material  $H$ .  $K$  is the dimensionless wear coefficient of the material.

$$W_v = K \cdot \frac{F_n \cdot s}{H} \quad (\text{Eq. 4-7})$$

If equation (Eq. 4-7), is considered in each nodal contact point  $dA$  of the FE model contact surface over an incremental local slip  $ds$ , the incremental nodal wear  $dh$  can be expressed according to (Eq. 4-8), where  $\Delta h$ ,  $p(t)$ ,  $\Delta s$  are the incremental wear depth, the contact pressure and the sliding increment respectively. On the other hand  $k_1$  represents the local wear coefficient, nevertheless as a simplification it is assumed that this coefficient is similar to the volumetric coefficient of wear. So, the volumetric coefficient of wear  $k$  obtained in section 4.2.2.3 was used.

$$\Delta h(t) = k_1 \cdot p(t) \cdot \Delta s \quad (\text{Eq. 4-8})$$

#### 4.2.3.3 Wear simulation method

Wear simulation consists of an iterative process called wear simulation algorithm which is presented in Fig. 4-8 and it is implemented via the commercial FE code Abaqus (Version 6.9) and the user-defined subroutine UMESHMOTION. This subroutine allows defining the

motion of nodes inside an adaptative mesh constraint node set an amount equal to the local wear obtained by the Archard's modified wear equation shown in (Eq. 4-8). The nodes are moved in the local normal direction [134].

The wear algorithm begins with the construction of the FE model described previously. Once the equilibrium equations for one sliding increment  $\Delta s$  converge, the adaptative meshing algorithm of Abaqus applies the local wear in two steps in an Eulerian analysis. First, the surface nodes are moved an amount equal to the local wear creating a new mesh through a process called sweeping. The main objective of the mesh sweeping is the reduction of the element distortion. Second, the material quantities from the old mesh to the new mesh are remapping with a process called advection by solving the advection equations using a second order numerical method called the Lax-Wendroff method. Nevertheless the advection of the material quantities will generally result in loss of equilibrium, which is corrected by solving the last time increment of the contact problem. This procedure is repeated many sliding increments  $\Delta s$  as needed to complete the entire sliding distance  $s$ .

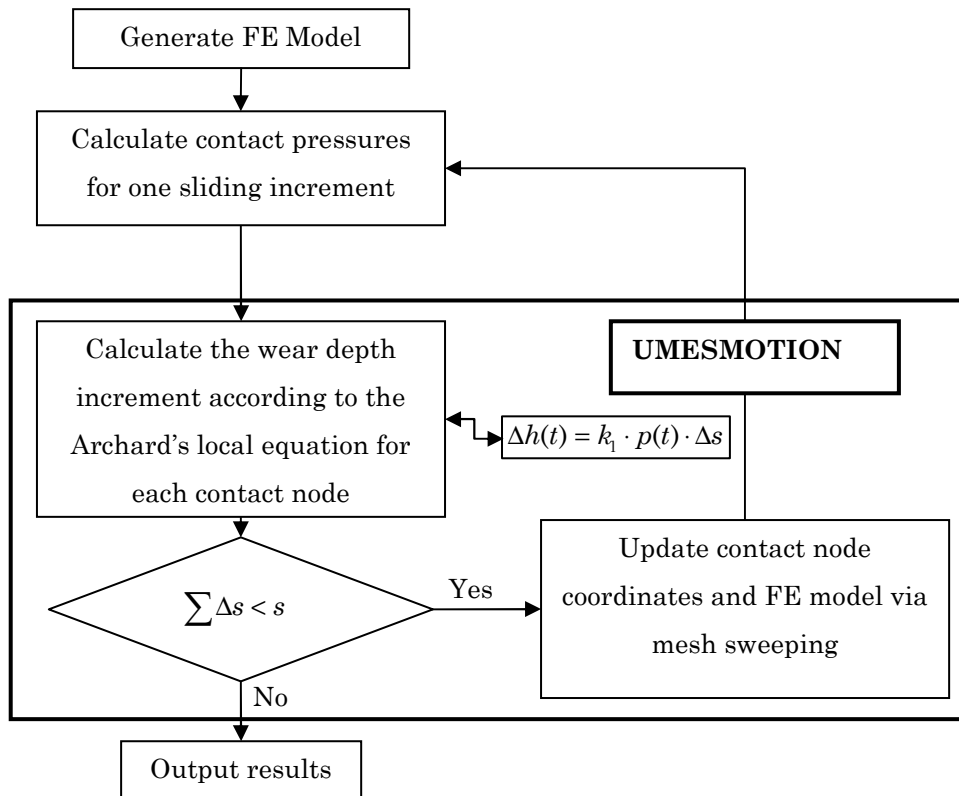


Fig. 4-8. Wear simulation algorithm including UMESHMOTION subroutine for the sliding wear case.

#### 4.2.3.4 Optimized wear simulation methodology

Making the assumption that the wear simulation is a process that requires a high computational cost, it will be defined a structured FE wear simulation methodology that allows the simulation of wear in the most optimal way possible. This methodology consists of the following steps:

1. FE model validation against the Hertzian analytical contact solution.
2. Definitions of the optimum mesh size in the contact zone.
3. Definition of the maximum sliding increment without any instability in the system.
4. Introduction of variable speed factor (variable sliding increment).
5. Comparison of the error with and without variable speed factor.
6. Validation of the FE optimized wear methodology with respect to the experimental profiles.

#### 4.2.4 Results and discussion

The proposed structured methodology for the optimization the FE wear simulation is discussed in this section. For this purpose each step of the methodology was applied in the cylinder plane FE model described previously.

In the first step the validation of the FE contact model has been carried out. The contact pressures obtained for different mesh sizes have been compared with respect to the analytical formulation proposed by Hertz. In Fig. 4-9(a) is shown the contact pressures obtained by different discretization and the Hertzian contact pressure. While small mesh sizes such as 5  $\mu\text{m}$  or 10  $\mu\text{m}$  fit closely to the analytical curve, greater mesh sizes, such as 30  $\mu\text{m}$ , overestimate both the width and the maximum contact pressure.

Nevertheless, as the wear is produced the Hertzian contact pressure decrease drastically, due to the increase of the contact area, tending to produce an uniform contact pressure as shown in Fig. 4-9 (b). Although small mesh sizes capture correctly the Hertzian contact pressure distribution, the rapidly varying contact pressure to and uniform contact pressure suggests that greater mesh sizes could represent correctly this uniform contact pressure, reducing considerably the computational time.

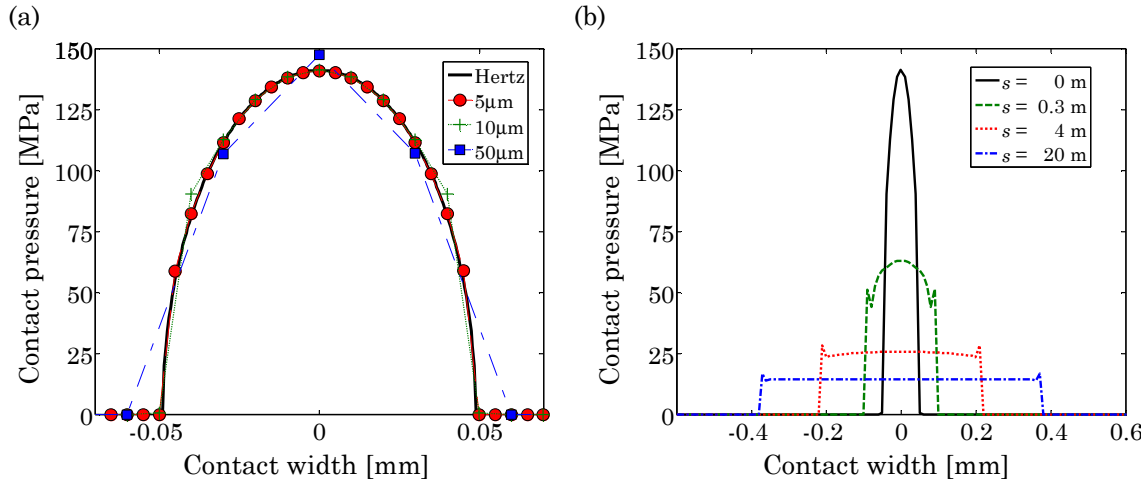


**Fig. 4-9. Contact pressure: (a) for different mesh sizes, (b) evolution of the contact pressure with the sliding distance.**

In the second step the optimum mesh size in the contact zone is discussed. This study is carried out because the small mesh sizes, which capture correctly the initial Hertzian contact pressure, may result in a very high computational cost. For that purpose the correlation between the mesh size and the final contact width after the wear process is defined, in order to obtain the possible coarser mesh size, without altering the final result. To perform this study two cases are considered. The first one for a shorter sliding distance of 240 m and the second one for a longer sliding distance of 1800 m, which corresponds to the tribometer test of 0.25 m/s-2 h.

Fig. 4-10 shows that the error in the maximum contact pressure as the mesh size increase is less than 3% in both cases, however the uniform part of the contact pressure is reduced considerably, e. g. in the 240 m sliding case (Fig. 4-10 (a)) this part is reduced from 1 mm to 0.72 mm. Taking into account the previously mentioned effect, it is considered as optimal mesh size the one that corresponds to the 10% of the uniform part of the contact pressure with respect to the smallest mesh size, which has been 10 μm in this study. Thus, while for the case of 240 m (Fig. 4-10 (a)) the optimal mesh size is about 30 μm in the case of 1800 m (Fig. 4-10 (b)) is about 50 μm.

If the optimal mesh size is associated with the final contact width after wear, in the case of 240 m it is obtained a ratio of 0.026 and in the case of 1800 m a ratio of 0.024. Thus it can be seen that the optimal mesh size to reduce computational time should be between 2-3% of the final contact width approximately. It means that for longer sliding distance or greater final contact width greater mesh sizes can be used. So that, depending on the desired goal greater or smaller element size will be required. When the analysis of the evolution of the contact pressure in the early stages it is carried out, a greater refinement of the mesh size is required. However, when it is needed to analysed the wear and the contact pressure after

a high number of cycles, a coarser element size can be used, although in the beginning of the test the initial contact pressure doesn't fit well with the analytical Hertzian contact pressure.

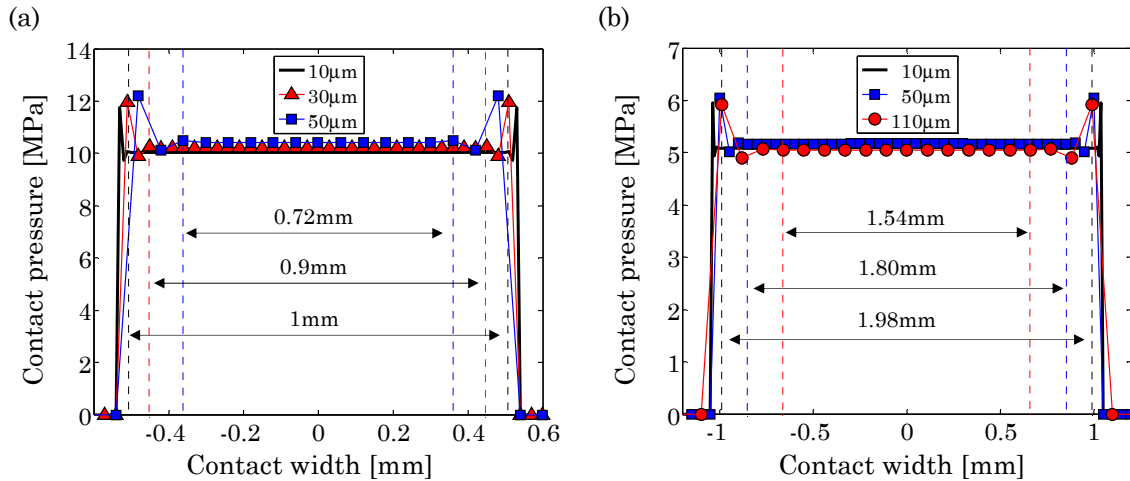


**Fig. 4-10. Mesh size analysis with respect to the contact pressure for two sliding distance: (a) 240m, (b) 1800 m (0.25m/s-2h) tribometer test.**

In Fig. 4-11(a) is shown the evolution of the maximum contact pressure as a function of the different mesh sizes. Two periods are observed, the first one corresponds to the initial period in which it is observed a rapidly decreases of the maximum contact pressure and the second one corresponds to the stable period, where the contact pressure remains approximately constant over the entire contact width.

As can be seen the different meshes only fluctuate in the initial period, since in the beginning of the stable period all converge to the same curve. So the previously mentioned optimal mesh size of 50 µm for the testing case of 0.25 m/s-2 h represents adequately the stable period. Moreover, it can be seen in Fig. 4-11 (b) that the wear profile obtained with the optimal mesh size and with the refiner mesh sizes are identical, with errors in depth less than 0.5% and in width of 0%. Thus in this step a great reduction of the computational time is obtained for the simulation the testing case of 0.25 m/s-2 h-65 N: while with a mesh size of 10 µm which adjust properly with the initial Hertzian contact pressure, 18.3 h are needed for predicting the final wear scar, with the optimum mesh size of 50 µm only 1.2 h are needed.



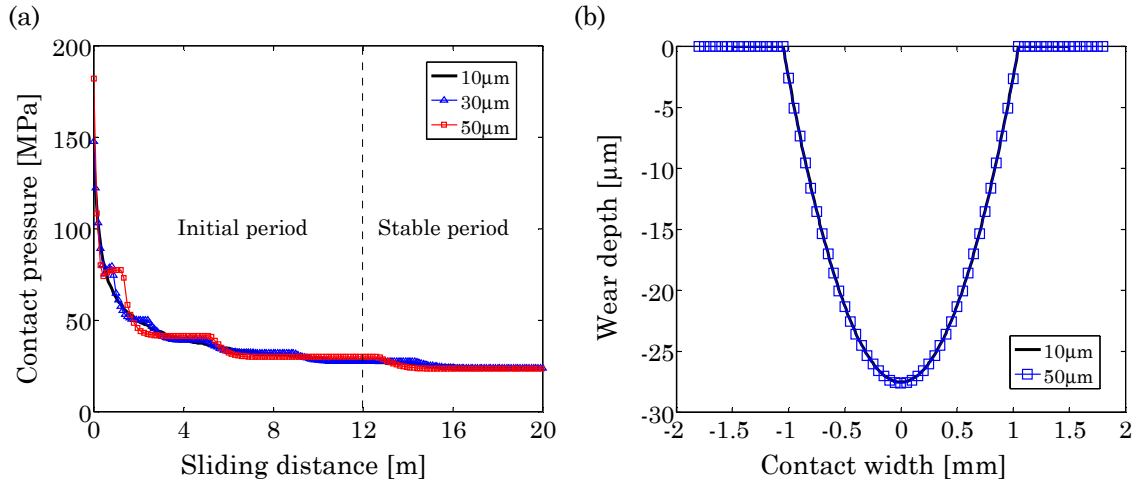


Fig. 4-11. Effect of the mesh size for a 0.25 m/s-2 h-65 N test: (a) evolution of the maximum contact in the first 20 m and (b) final wear scars for different meshes .

In the third step the analysis of the maximum sliding increment  $\Delta s$  without producing instabilities in the system is carried out. The advantage of this study is that the instabilities appear in the first wear increments, so that the time required to find the optimum sliding increment  $\Delta s$  should not be too high. Fig. 4-12(a) shows the contact pressure distribution obtained for a total sliding distance of 480 mm and different sliding increments  $\Delta s$ , considering that during a sliding increment  $\Delta s$ , the contact pressure distribution remains constant. This implies that smaller sliding increments  $\Delta s$  could increase drastically the computational time. It can be seen that while for a  $\Delta s = 60$  mm (8 increments) many instabilities appear; as the sliding increment  $\Delta s$  is reduced these instabilities start decreasing ( $\Delta s = 43$  mm , 11 increments). On the other hand it can be seen that from  $\Delta s = 40$  mm (12 increments) all the contact pressures converge to the same value, no presenting improvements with smaller sliding increments ( $\Delta s = 0.48$  mm , 1000 increments).

This maximum sliding increment is directly related with the maximum wear depth increment  $\Delta h_{max}$  that can be given in each model. Fig. 4-12(b) shows the influence in the maximum wear depth  $h_{max}$  with respect to the maximum wear depth increment  $\Delta h_{max}$  after a sliding distant of 480 mm. On the one hand it can be found the critical increment of wear depth  $\Delta h_{critic}$ . This increment represents the limit value beyond this point the system becomes unstable. If this critical increment is reduced, the error committed in the maximum wear depth is reduced, reaching a value in which there is not improvements in the maximum wear depth  $h_{max}$ . This last value is named as convergence increment of wear  $\Delta h_{convergence}$ . However, while the error committed in the maximum wear depth between the  $\Delta h_{critic}$  and the  $\Delta h_{convergence}$  is 0.5% the reduction in the computational time is about 95%.

Thus it is considered that the  $\Delta h_{\text{critic}}$  is the optimal value for any simulation. Similar study has been presented previously by McColl et al. [104] for fretting wear problems. Therefore, the critical increment of wear depth  $\Delta h_{\text{critic}}$  is characteristic of each model and depends on the initial contact pressure, the wear coefficient and the mesh size. Around this last aspect, it should be pointed out that the greater mesh sizes defined as optimum in step 2 allow greater  $\Delta h_{\text{critic}}$  values. This implies a double reduction in the computational time: on the one hand it is reduced the number of elements for each contact resolution and on the second hand it is reduced the number of times that has to be solved the contact problem for each wear simulation.

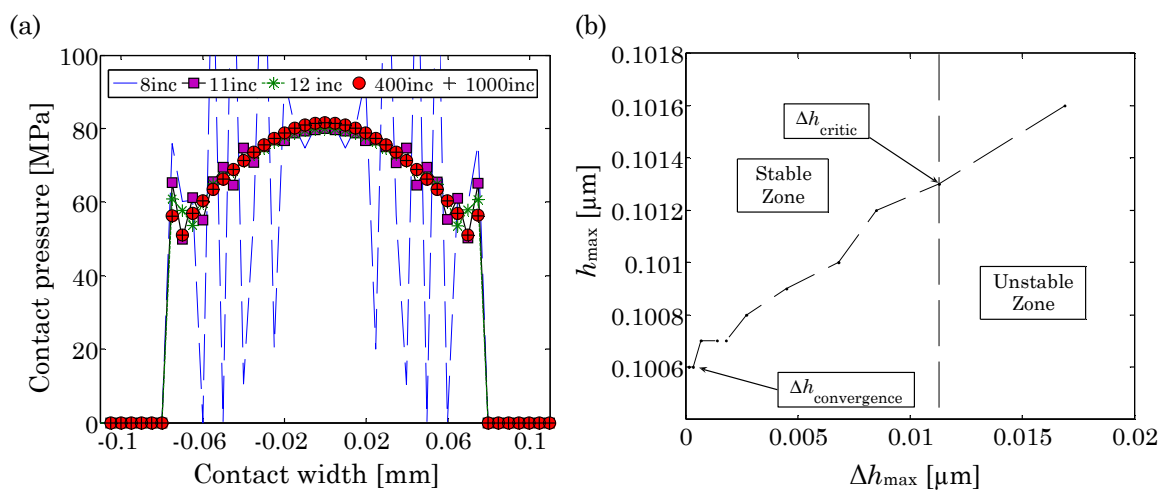
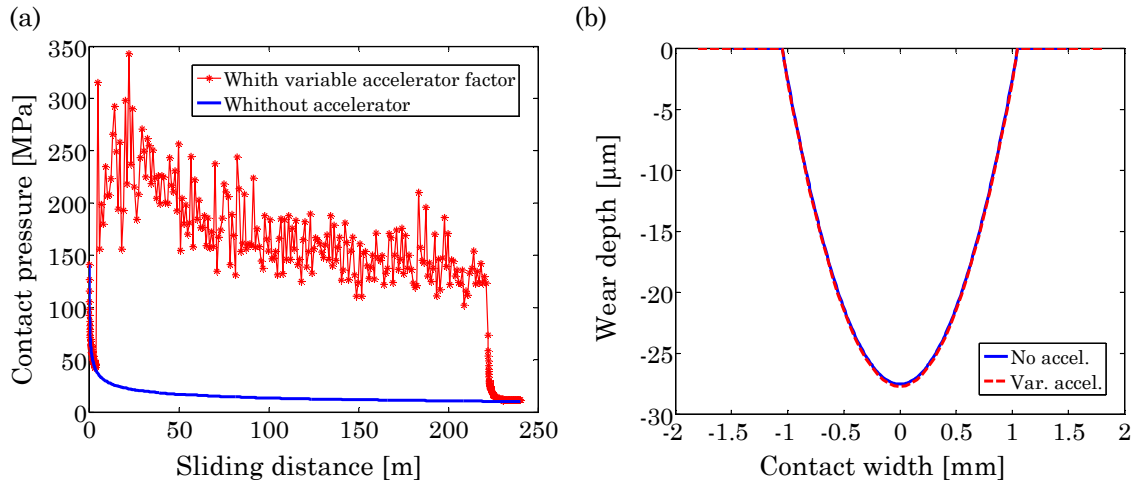


Fig. 4-12. Analysis of the maximum wear increment for a sliding distance of 480 mm: (a) influence of the sliding discretization in the contact pressure and (b) maximum wear increment vs maximum wear depth.

The fourth step consists of the introduction of a variable sliding increment  $\Delta s$  in order to speed up the wear simulation. Several authors have already introduced this concept using variable speed factors, e. g, Ding [135] introduced a variable incremental number of wear cycles in fretting wear problems. Nevertheless the proposed variable sliding increment  $\Delta s$  has two advantages with respect to that one reported in the literature. On the one hand is a self-adjustable speed factor, which is defined automatically with respect to the critical increment of wear depth  $\Delta h_{\text{critic}}$  ( $\Delta s(\Delta h_{\text{critic}})$ ). On the other hand the introduction of this speed factor it is carried out according to the considered difference between the maximum contact pressure evolution of the present wear increment with respect to the previous wear increment. This last approach aims to activate this speed factor (the introduction of a greater sliding increment  $\Delta s$ ) in the stable period, in order to model adequately the rapidly variation of the maximum contact pressure in the initial period. This speed factor stops working the last 300 cycle in order to eliminate all the produced instabilities. Fig. 4-13(a) shows this effect. When the speed factor is removed the instabilities in the maximum

contact pressure disappear and converge to the same contact pressure without introducing any speed factor.

In the fifth step the error committed in the final wear scar width and depth with and without introducing the variable speed factor it is analysed. As shown in Fig. 4-13(b) the error committed by the introduction of the variable speed factor is depreciable, obtaining errors in the wear scar width and depth less than 1%. Nevertheless it is achieved a reduction in the computational time of 87%.



**Fig. 4-13. Effect of the variable accelerator factor: (a) influence in the maximum contact pressure and (b) influence in the final wear scar.**

The last step consists of correlating the experimental results with the results obtained by optimized wear simulation methodology. Fig. 4-14 shows the correlation between the profile of the wear scar obtained experimentally for three different tests carried out with 0.5 m/s-2 h-65 N and that one obtained by the FEM wear simulation. Considering that in tribological testing could be dispersions greater than 15% [136], it can be said that the results obtained with the optimized wear simulation methodology correlate properly with those ones obtained experimentally.

In this section has been demonstrated the great reduction of computational time that can be obtained using this methodology. Because, while a mesh size of 10  $\mu\text{m}$  which adjust properly with the initial Hertzian contact pressure distribution needs a computational time of 18 h for simulating the entire wear test, a mesh size of 50  $\mu\text{m}$  with the variable speed factor needs 12 minutes for the entire calculation.

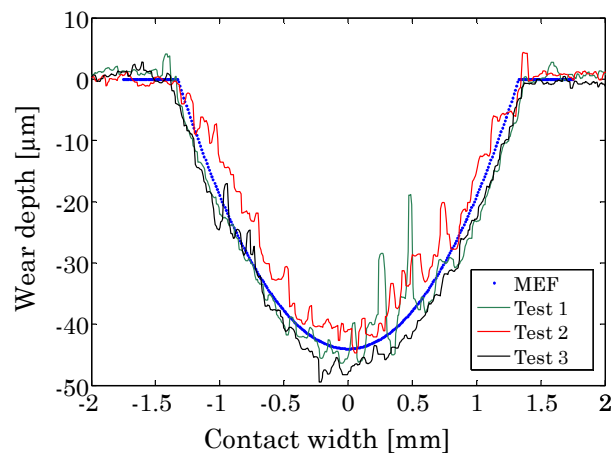


Fig. 4-14. Experimental wear scar vs FEM wear scar for the test conditions: 0.25 m/s-2 h-65 N.

### 4.3 FEM methodology of fretting wear in thin steel wires

#### 4.3.1 Introduction

Based on the knowledge acquire in the 2D problem, and the great advantage that presents the developed structured simulation methodology, it is proposed to develop an optimized methodology for modelling the high computational time consuming thin steel wires 3D problem.

The great differences that present the modelling fretting wear of thin steel wires, with respect to the previously carried out modelling of block on ring tribosystem, are: the high computational cost 3D FE model, the introduction of the tangential problem in the resolution of the contact problem and the consideration of the wear in both bodies. So that, the optimized methodology proposed in the 2D problem has to be adapted in these type of problems.

According to the experimental testing carried out with thin steel in Chapter 3, firstly the optimized wear methodology has been implemented in the 90° crossed cylinder arrangements and secondly in the different crossing angles model.

#### 4.3.2 FEM wear modelling

##### 4.3.2.1 FEM model

The FE model used for the simulation of fretting wear in 90° crossing angle thin steel wires is shown in (Fig. 4-15). A 90° crossed cylinders configuration, the same as the specimens in

the tests, with a diameter of 0.45 mm has been chosen. Moreover the curvature radius that acquires the wire in the fixation support (10 mm) is included. The meshes are carried out according to a partition methodology, in which a more refine mesh is used in the contact zone, to capture precisely the variation of contact pressures and geometry. Moreover the meshes in the contact zone have a square shape. A study of the optimum mesh size for minimal computational time will be presented in section 4.3.4.

Moreover the parametrization of the different parameters of the model (geometry, partitions and meshes) are included with the aim to reduce the cost that implies new models with different geometrical parameters. In this case the great advantage is that the contact partitions shown in Fig. 4-15 (b) and (c) can be modelled easily for different wear scars dimension, with the aim to reduce de computational time depending on the intensity of the wear.

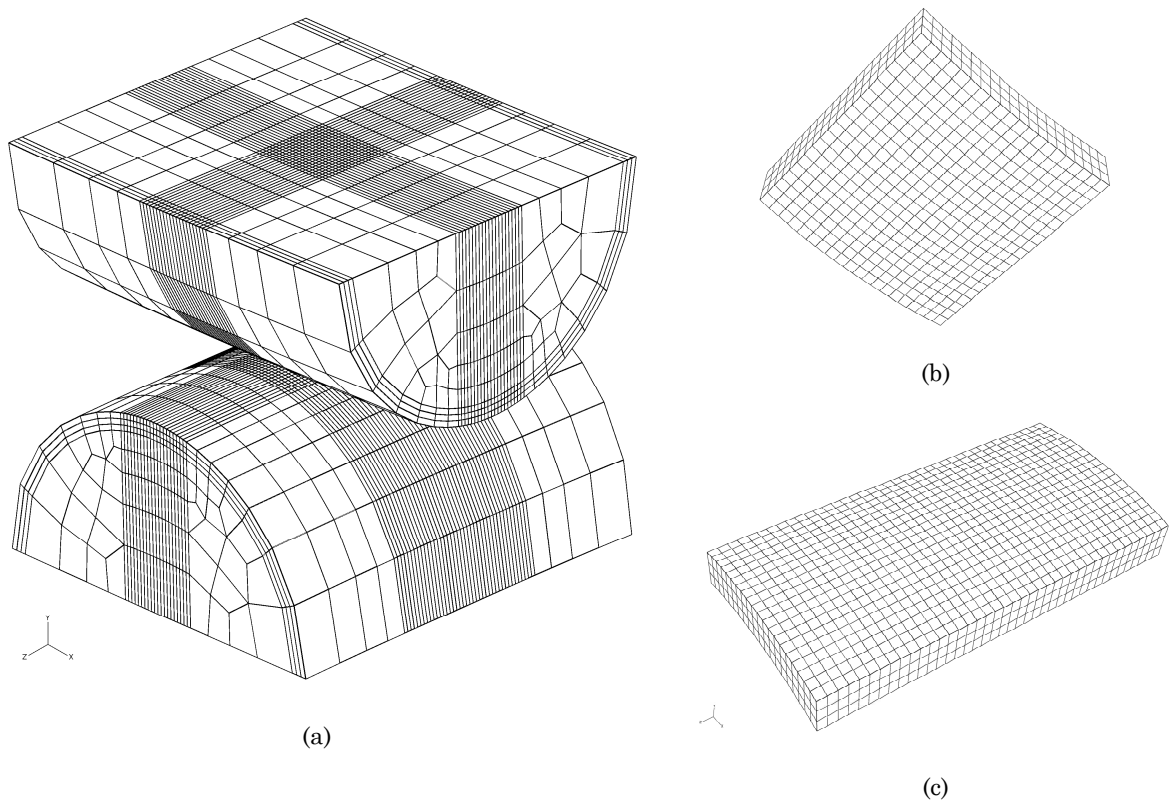


**Fig. 4-15. FE model end mesh details of 90° crossed cylinders: (a) full model, (b) contact region detail for top cylinder, (c) contact region detail for bottom cylinder.**

The FE model used for the simulation of fretting wear in crossed cylinder configurations is shown in Fig. 4-16. The models used are developed for crossing angles that goes from 15° to 60° with a diameter of 0.45 mm. Moreover the curvature radius that acquires the wire in the fixation support (10 mm) is included. The meshes are carried out according to a partition methodology, in which a more refine mesh is used in the contact zone, to capture precisely the variation of contact pressures and geometry. The partition of the contact zone

is created in the direction formed by the half of the crossing angle used. Moreover the meshes in the contact zone have a rectangular shape. A study of the optimum mesh size and the direction of the partition will be presented in section 4.3.5. The mesh is composed of eight nodes lineal brick elements and four nodes linear tetrahedral elements as it is shown in Fig. 4-16. While brick elements are used to define the contact zone Fig. 4-16(b) and (c), tetrahedral elements are used outside the contact zone in order to reduce the time costs Fig. 4-16(a).

As in the case of  $90^\circ$  the parametrization of the different parameters of the model (geometry, partitions, meshes, crossing angles) is included in this model. In this case, the great advantage is that different models for different crossing angles can be created easily.

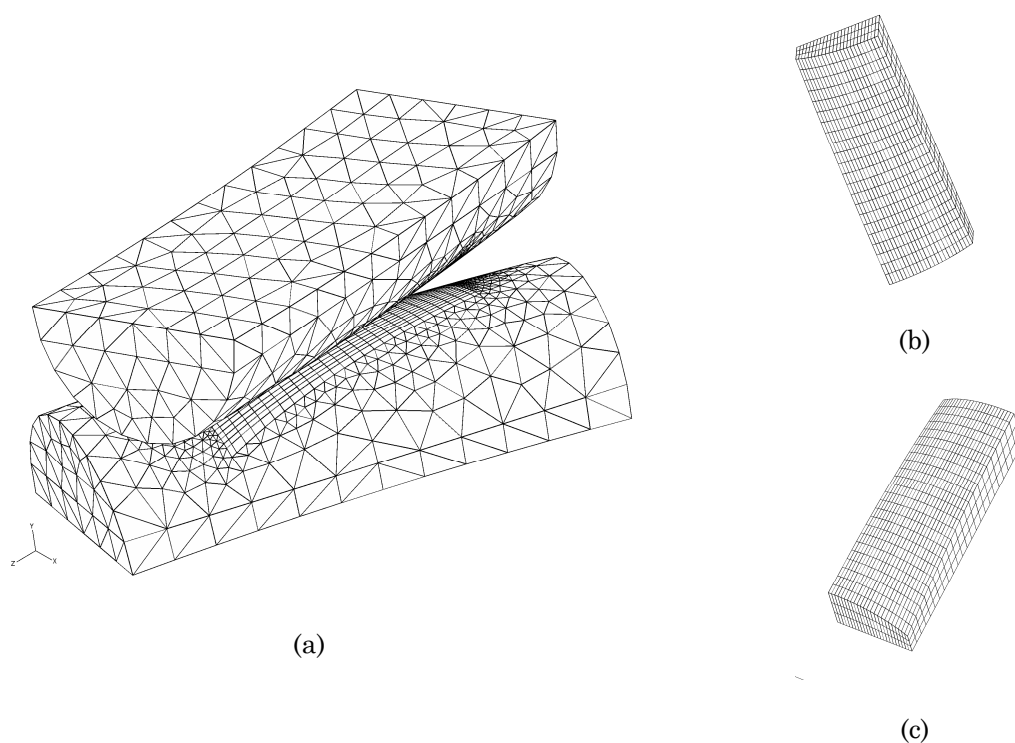


**Fig. 4-16. FE model and mesh details of  $30^\circ$  crossed cylinders: (a) full model, (b) contact region detail for top cylinder, (c) contact region detail for bottom cylinder.**

The contact surface interaction between both cylinders is defined via the finite sliding contact pair algorithm, which uses the master–slave algorithm to enforce the contact constraints. In this study the top surface is chosen as slave surface and the bottom one as master. The Lagrange multiplier contact algorithm was used to ensure the exact stick constrain when the shear stress is less than the critical value according to the Coulomb friction law. A COF of 0.7 is chosen according to the experimental tests showed in Chapter 3.

The load and the boundary conditions are applied in the free surfaces of the model through a surface-based coupling, which couples the motion of all free surfaces to the motion of a reference node. Moreover a kinematic coupling is used, so as the rigid body motion is defined by the reference node. It allows in the upper wire, where a normal force is applied in the reference point, only the vertical movement and in the bottom wire, where an alternative displacement condition is imposed, only the horizontal movement. This is because the wire maintains the rigid body movement of the holder in the testing machine. The analysis consists of two steps. While in the first step the normal load has been applied in the top cylinder, in the second step the sliding amplitude has been introduced in the bottom cylinder according to the triangle wave function in terms of Fourier series as shown in Fig. 4-17. This function has been introduced, in order to discretize the entire fretting cycle with the same sliding increments  $\Delta s$ . The elastic modulus and Poisson's ratio of both cylinders are taken as 210 GPa and 0.33, respectively.

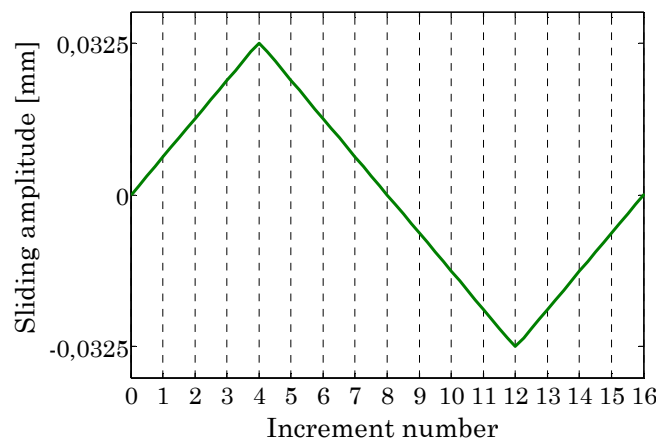


Fig. 4-17. Ramp amplitude graph for the application the reciprocating movement in step 2.

In order to validate the model, the contact pressure obtained by FEM has been compared with the well know contact pressure distribution obtained according to the analytical solution for the general cases given by Hertz and described by Johnson [13]. Therefore the contact pressure distribution is given by (Eq. 4-9)

$$p(x) = p_{\max} \sqrt{1 - \frac{x^2}{a^2}} \leftrightarrow p_{\max} \sqrt{1 - \frac{x^2}{b^2}} \tag{Eq. 4-9}$$

where the maximum contact pressure is given by (Eq. 4-10):

$$p_{\max} = 3 \cdot F_n / (2 \cdot \pi \cdot ab) \tag{Eq. 4-10}$$

where  $F_n$  is the applied normal load and  $a$  and  $b$  are the semi-axes of the elliptical contact. In the  $90^\circ$  crossing angle case  $b$  is equal to  $a$  and represents the contact radius. To obtain both semi-axes the (Eq. 4-11) and (Eq. 4-12) are solved using the bisection method:

$$R_{\text{rel}} = \frac{(a/b)^2 E(e) - K(e)}{K(e) - E(e)} \quad (\text{Eq. 4-11})$$

$$(ab)^{3/2} = \left( \frac{3F_n R_e}{4E_e} \right) \frac{4}{\pi e^2} (b/a)^{3/2} \times \left[ \left\{ (a/b)^2 E(e) - K(e) \right\} \{ K(e) - E(e) \} \right]^{1/2} \quad (\text{Eq. 4-12})$$

$E(e)$  and  $K(e)$  are complete elliptic integrals of argument  $e = (1 - b^2/a^2)^{1/2}$ ,  $b < a$ .  $R_e$  is the equivalent radius of curvature and  $R_{\text{rel}}$  is the ratio of the relative curvatures  $R'$  and  $R''$ . Both parameters are obtained according to (Eq. 4-13) and (Eq. 4-14) respectively:

$$R_e = \frac{1}{2} (AB)^{-1/2} \quad (\text{Eq. 4-13})$$

$$R_{\text{rel}} = \frac{B}{A} = \left( \frac{R'}{R''} \right) \quad (\text{Eq. 4-14})$$

where  $A$  and  $B$  are positive constants and are obtained solving (Eq. 4-15) and (Eq. 4-16):

$$(A + B) = \frac{1}{2} \left( \frac{1}{R_1'} + \frac{1}{R_1''} + \frac{1}{R_2'} + \frac{1}{R_2''} \right) \quad (\text{Eq. 4-15})$$

$$|B - A| = \frac{1}{2} \left\{ \left( \frac{1}{R_1'} - \frac{1}{R_1''} \right)^2 + \left( \frac{1}{R_2'} - \frac{1}{R_2''} \right)^2 + 2 \left( \frac{1}{R_1'} - \frac{1}{R_1''} \right) \left( \frac{1}{R_2'} - \frac{1}{R_2''} \right) \cos 2\beta \right\}^{1/2} \quad (\text{Eq. 4-16})$$

$R_1'$ ,  $R_1''$ ,  $R_2'$ ,  $R_2''$  are the principal radius of curvature of upper and bottom wire and  $\beta$  is the crossing angle between the cylinders.  $E_e$  is the composite modulus of the two contacting bodies and is obtained according to (Eq. 4-17)

$$E_e = \frac{1 - \nu_1^2}{E_1} + \frac{1 - \nu_2^2}{E_2} \quad (\text{Eq. 4-17})$$



where  $E_1$ ,  $E_2$  are the elastic modulus and  $\nu_1$ ,  $\nu_2$  are the Poisson's ratios of upper and bottom wires, respectively. The resolution of these equations is done with a specific program developed in MATLAB®. For this specific study,  $\beta$  represents the desired crossing angle between the wires,  $R'$  represents the radius of the wire (0,225 mm) and  $R''$  represents the curvature radius of specimen in the holder (10 mm).

#### 4.3.2.2 Wear local model

The local wear model used in this study is the one proposed by McColl et al. [104] for fretting wear problems. This model is based on the Archard's modified equation that can be expressed in terms of (Eq. 4-18).

$$\Delta h(x,t) = k_1 \cdot p(x,t) \cdot \Delta s(x,t) \quad (\text{Eq. 4-18})$$

where  $\Delta h(x,t)$ ,  $p(x,t)$  and  $\Delta s(x,t)$  are the incremental wear depth, the contact pressure and the relative slip for a specific point  $x$  (node) at specific time  $t$ . On the other hand  $k_1$  represents the local wear coefficient. This coefficient in principle could not be the same as the volumetric coefficient of wear, because the last one represents an average value across the complete wear scar. As there is not any method for estimating the local wear coefficient  $k_1$ , in this study and with the aim to simplify the problem it is assumed that the volumetric coefficient of wear  $k$  is the same as the local coefficient of wear  $k_1$ . Moreover some authors like McColl et al. [104] or Fouvry et al. [132] has justified the close relation existed between the local wear coefficient and the volumetric wear coefficient. So the specific wear coefficient obtained in Chapter 3 for each test and specimen was used.

Taking into account (Eq. 4-18), one fretting cycle is divided in small slip increments; it implies that the FE wear simulation is the product between these increments and the total number of cycles. As a consequence, high computational time is needed for the simulation of one fretting test. In this point the cycle jump technique proposed by different authors like McColl et al. [104] and Mary et al. [125] is used, where it is made the assumption that the contact pressure and the slip distribution remain constant in each finite element analysis over the next  $\Delta n$  cycles. In this way (Eq. 4-18) is multiply by  $\Delta n$  to obtain (Eq. 4-19), such that the wear corresponding to  $\Delta n$  cycles can be simulated in one fretting cycle.

$$\Delta h(x,t) = \Delta n \cdot k_1 \cdot p(x,t) \cdot \Delta s(x,t) \quad (\text{Eq. 4-19})$$

#### 4.3.2.3 Wear simulation method

As has been shown previously, the wear simulation consists of an iterative process called wear simulation algorithm. For the fretting wear problem studied in this section this algorithm is shown in Fig. 4-18 and it is implemented via the commercial FE code Abaqus (Version 6.9) and the user-defined subroutine UMESHMOTION. The detailed explanation about how it works this subroutine has been reported previously in section 4.2.3.3. In this case the iterative process has to be repeated as many times as increments has one fretting cycle  $inc_{cycle}$  and as many times as cycles jumps needed  $\sum \Delta n$  to reached the desired number of cycles.

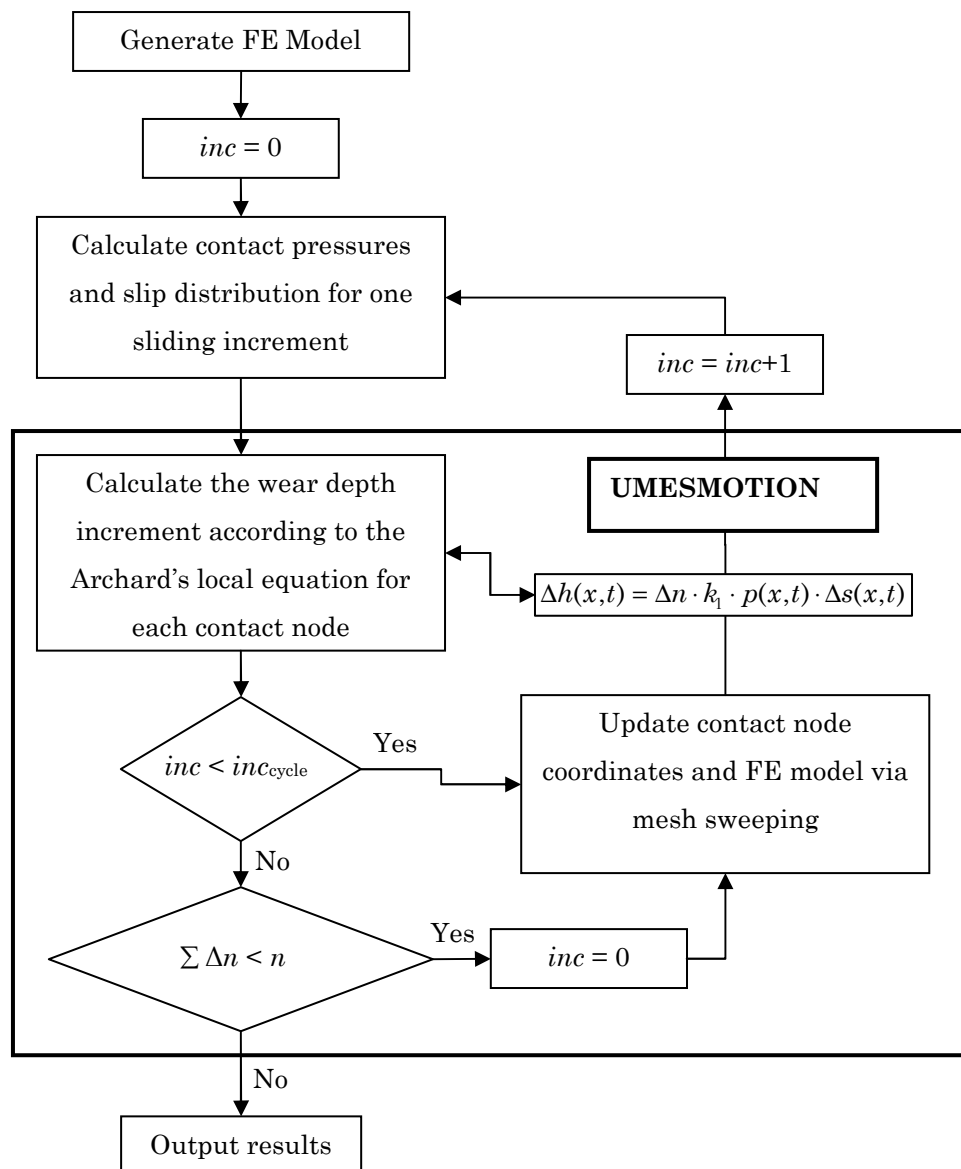


Fig. 4-18. Wear simulation algorithm including UMESHMOTION subroutine for fretting wear problems.

On the other hand UMESHMOTION subroutine only gives the contact results for one of the contacting surfaces (slave surface), i.e., in situations that can be modelled as deformable rigid contact problems, where it is enough to simulate the wear in one of the contacting surfaces because the wear in the other surface is negligibly [137] as in the case presented in section 4.2. As in this work, according to the experimental results, the wear in both contacting bodies is significant, the study of different interpolation methods were carried out. It lies in interpolating the contact pressures and the slip distribution from slave nodes to the master nodes, taking into account the nodal coordinates of each contact surface.

The studied interpolation methods were: bivariate interpolation, triangle-based linear interpolation (baricentric interpolation) and nearest interpolation. And extended description of the bivariate method is found in the work developed by Akima [138]. In this method the plane is divided into triangles which maximize the minimum interior angle of the triangles cells according to the nodal coordinates and then the desired  $z$  value is obtained by interpolating in the closest  $x$  and  $y$  position triangle with a bivariate fifth-degree polynomial as presented in (Eq. 4-20). Where  $q$  are the 21 coefficients of each local polygon,  $x$  and  $y$  are coordinate distances relative to some local origin, and  $j$  and  $k$  are dummy variables. Moreover Akima's method can also be used for extrapolation, though the accuracy decreases for such an application. The coefficients of the local polynomials are obtained once the triangles are formed, such that the partial derivatives of the surface are continuous across the sides of the triangles and at the vertices.

$$z(x, y) = \sum_{j=0}^5 \sum_{k=0}^{5-j} q_{jk} x^j y^k \quad (\text{Eq. 4-20})$$

The second interpolation method consists of triangle-based linear interpolation, described in detail by Watson [139]. In this case the desired  $z$  value is obtained by (Eq. 4-21), where  $z(i)$  represents the  $z$  value of one node of the closest triangle in the position  $(x, y)$  and  $bc$  represents the baricentric coordinates of the triangle, which can be obtained following (Eq. 4-22)-(Eq. 4-25).

$$z(x, y) = \sum_{i=1}^3 z(i) \times bc(i) \quad (\text{Eq. 4-21})$$

$$del = [(x(2) - x(1)) \times (y(3) - y(1))] - [(x(3) - x(1)) \times (y(2) - y(1))] \quad (\text{Eq. 4-22})$$

$$bc(3) = \frac{[(x(1) - xi) \times (y(2) - yi) - (x(2) - xi) \times (y(1) - yi)]}{del} \quad (\text{Eq. 4-23})$$

$$bc(2) = \frac{[(x(3) - xi) \times (y(1) - yi) - (x(1) - xi) \times (y(3) - yi)]}{del} \quad (\text{Eq. 4-24})$$

$$bc(1) = \frac{[(x(2) - xi) \times (y(3) - yi) - (x(3) - xi) \times (y(2) - yi)]}{del} \quad (\text{Eq. 4-25})$$

In the case of the nearest interpolation it is not needed any triangulation of the surface, because it consists of obtaining the desired  $z$  value according to the  $z$  value of the nearest point  $npi$  to the desired  $x$  and  $y$  position as described in (Eq. 4-26), where  $npi$  is obtained according to the node point position that meets with the condition of the minimum distance described in (Eq. 4-27). The distance between the desired  $x$  and  $y$  position (master node) and each slave node  $xi$  and  $yi$  is obtained according to the (Eq. 4-28), where  $ndp$  represents the number of data points in the slave surface, which cover the interval of numbers between the first slave node and the last number of slave points  $nsp$ . These three methods are compared in section 4.3.4.2.

$$z(x, y) = z(npi) \quad (\text{Eq. 4-26})$$

$$npi \rightarrow ndp(\min(dist)) \quad (\text{Eq. 4-27})$$

$$dist = (x(ndp) - xi)^2 + (y(ndp) - yi)^2 \rightarrow ndp[1, nsp] \quad (\text{Eq. 4-28})$$

### 4.3.3 Validation methodology

The validation of the FE wear simulation methodology has been carried out following three different procedures. The first one corresponds to the validation of wear scars dimension, comparing both dimensions of each wear scars obtained by FEM with the dimensions obtained by Scanning Electronic Microscopy (SEM), as presented in Fig. 4-19(a) and (c) for the 90° crossing angle. In the case of the different crossing angles model the validation it is carried out comparing the dimensions of both axes of the elliptical wear scars obtained in the specimens as shown in Fig. 4-20(a).

The second procedure corresponds to validate the wear scar depth with the profile obtained by FEM comparing the longitudinal profile of the wire in the middle of the wear scar, where the maximum wear depth is found, as is shown in Fig. 4-19 (b) and (d).

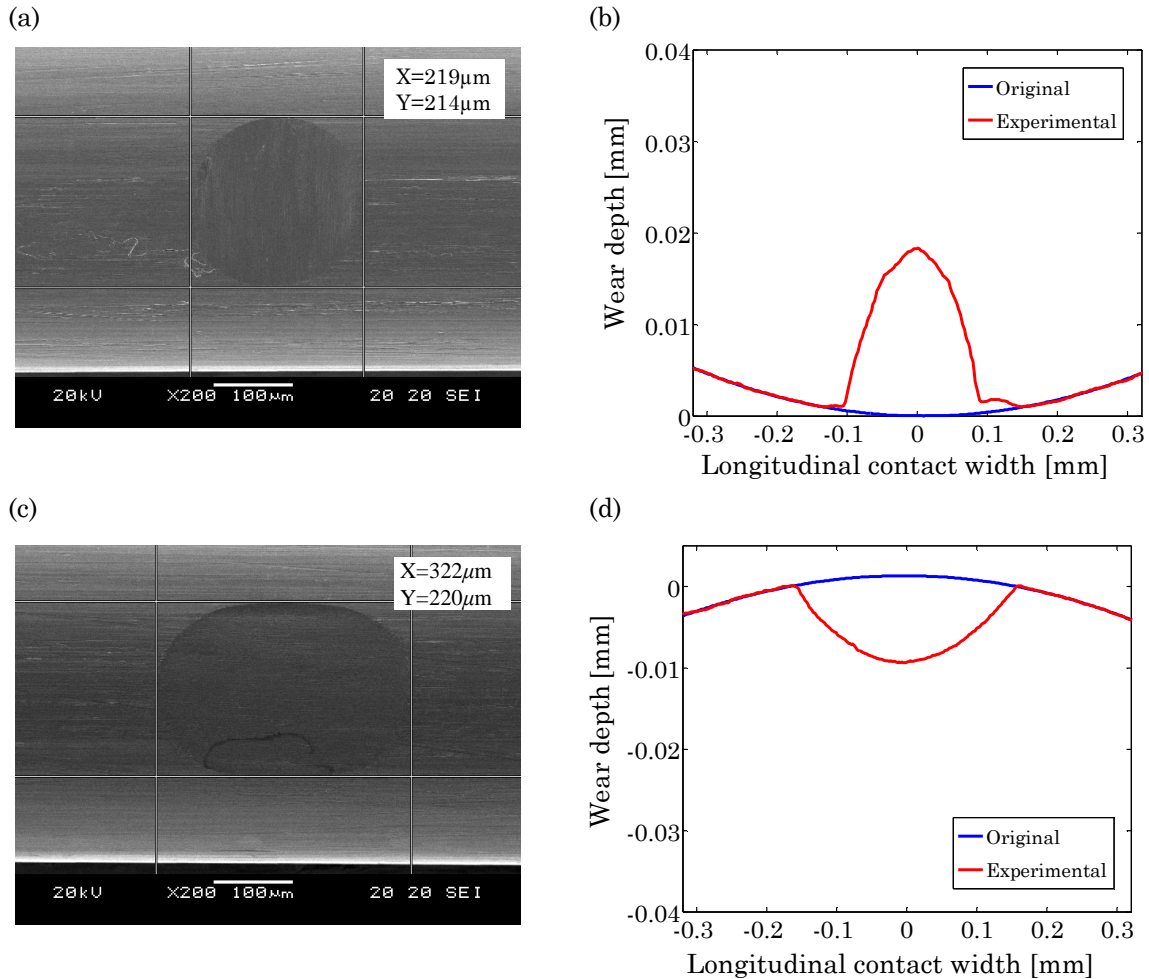


**Fig. 4-19. Wear scars of top and bottom: (a) top wear scar obtained by SEM, (b) top longitudinal profile obtained by confocal microscopy, (c) bottom wear scar obtained by SEM, (d) bottom longitudinal profile obtained by confocal microscopy.**

In the case of the different crossing angle the second validation procedure needs to be more exhaustive. For the top wear scar the validation is carried out comparing two profiles: the first one corresponds to the maximum wear depth profile obtained in the direction of the major axes which it is in the middle of the crossing angle formed by the top and bottom specimens as it is shown in Fig. 4-20(a) and (b) and the second one corresponds to the profile obtained in the longitudinal direction of the wire axis which it is more precise and easier to measure with the confocal microscopy, as it is shown in Fig. 4-20(c) and (d). In the case of the bottom wear scar, as the direction of the major axis is unknown, because of the relative motion produced in this wear scar, only the profile obtained in the longitudinal direction of the wire is used, as it is shown in Fig. 4-21(a) and (b).

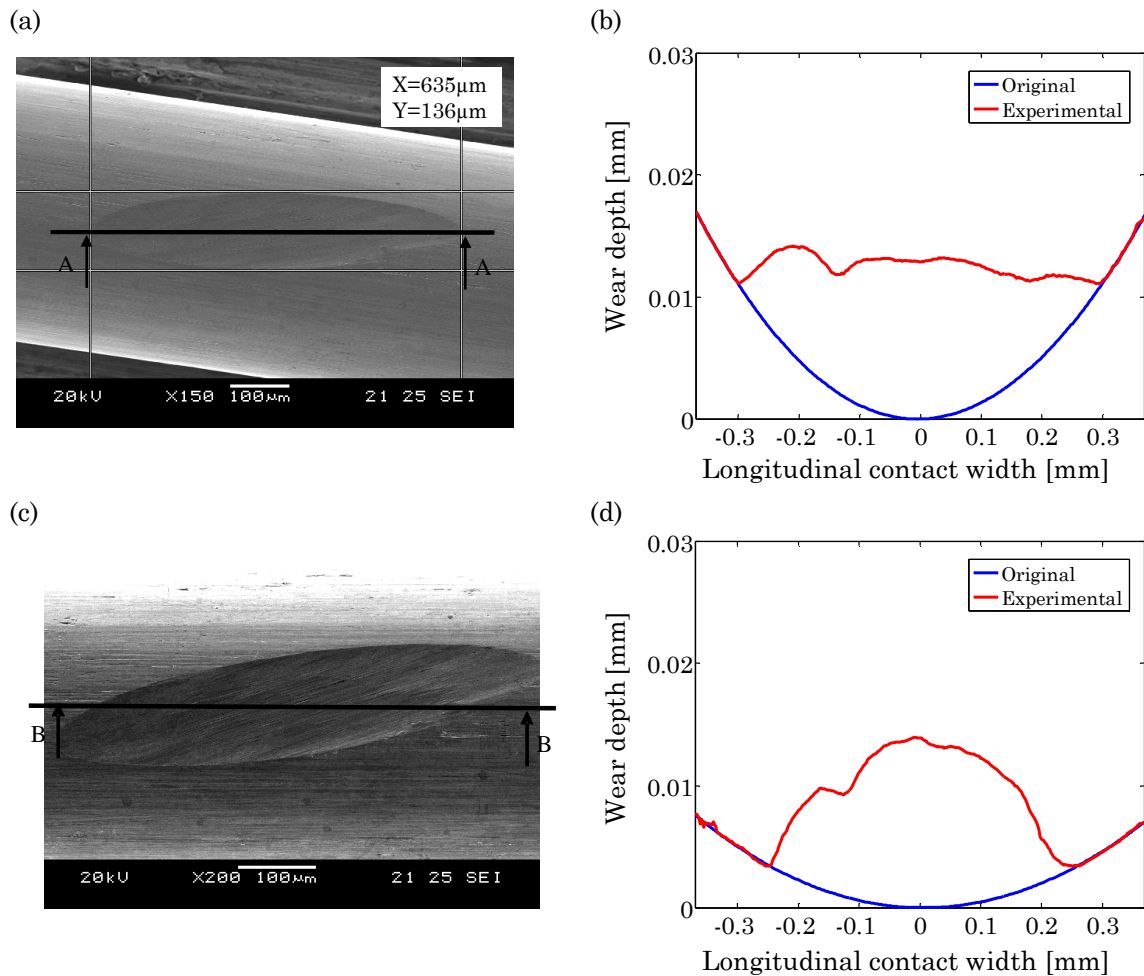


Fig. 4-20. Wear scars of top specimen: (a) top wear scar obtained by SEM in the direction of the major axis, (b) top longitudinal profile obtained in the direction of the major axis by confocal microscopy, (c) top wear scar obtained by SEM in the longitudinal direction of the wire axis, (d) top longitudinal profile obtained in the longitudinal direction of the wire by confocal microscopy.

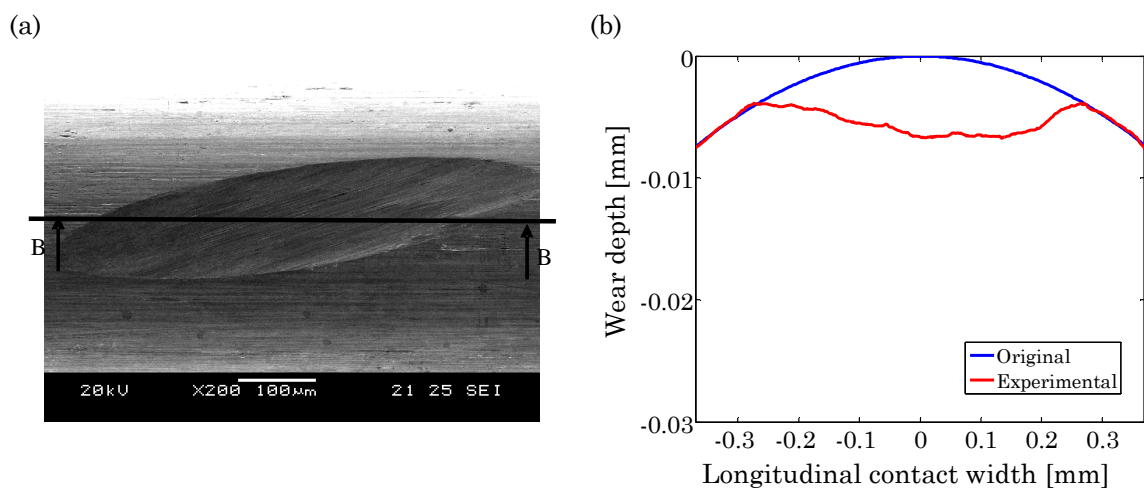
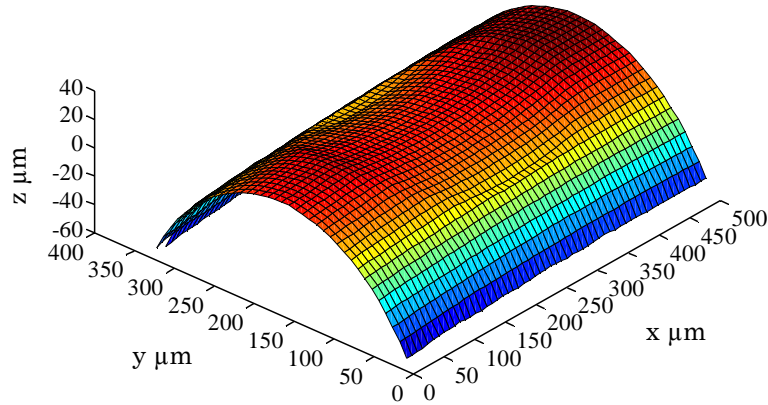


Fig. 4-21. Wear scars of bottom specimen: (a) bottom wear scar obtained by SEM in the longitudinal direction of the wire axes, (b) bottom longitudinal profile obtained in the longitudinal direction of the wire by confocal microscopy.

Moreover the second validation methodology has been carried out by confocal microscopy, obtaining the topography of the entire wear scar as shown in Fig. 4-22(a) for 90° crossing angles and in Fig. 4-22(b) for different crossing angles, and selecting the desired profiles.

(a)



(b)

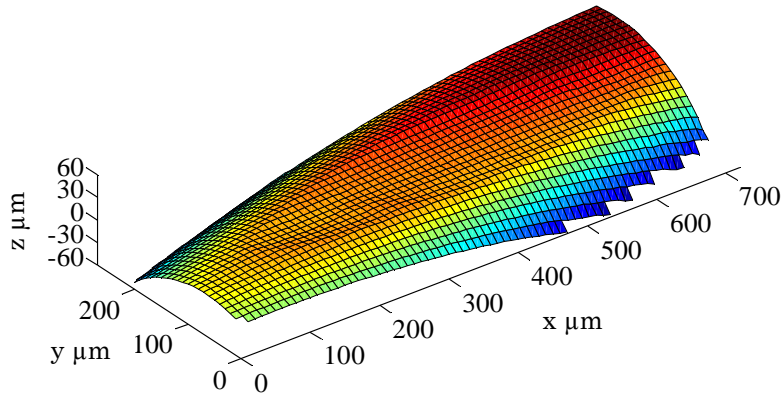


**Fig. 4-22. Confocal 3D image of the bottom wear scar: (a) 90° crossing angle and (b) 15° crossing angle.**

The last validation corresponds to the comparison of the wear scar volume obtained experimentally with the volume obtained by FEM. The volume ( $W$ ) of the wear scar was calculated by numerical integration (trapezoidal rule): the planimetric wear ( $W_p$ ) of each profile obtained in the longitudinal direction, as it is shown in Fig. 4-23, is multiplied by the mesh size along the transversal direction of the specimen. This procedure allows to validate accurately the shape of the entire wear scar in both top and bottom specimens.

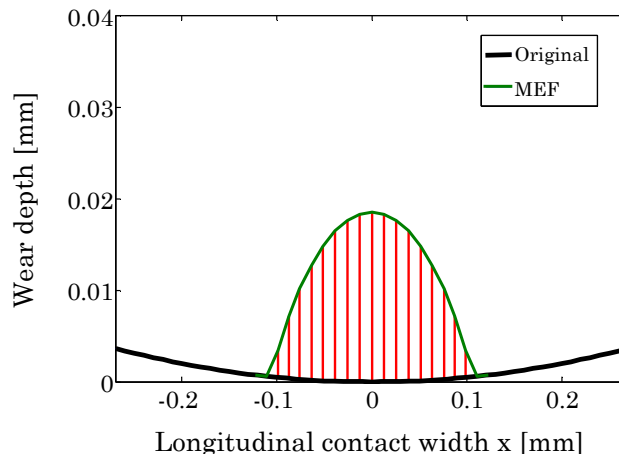


Fig. 4-23. Planimetric wear of the centre profile of top wear scar obtained by FEM.

#### 4.3.4 FEM wear simulation in 90° crossing angle arrangements

##### 4.3.4.1 Introduction

As has been mentioned previously, the FE wear simulation method consists of an iterative process which requires too much time for one wear scar simulation. In the case of 3D problems or in cases where high number of fretting cycles is analyzed, this time increase drastically because of the increase in the freedom degrees and in the number of iterations, respectively.

To reduce the computational time, in this section, two different studies are presented. In the first one the analysis of the three interpolation methods presented previously will be carried out. In the second one the study of the principal parameters involved in the FE wear method will be studied: contact zone mesh size refinement, FE wear increments per fretting cycle and the cycle jump technique  $\Delta n$ . After this study the relation between the error committed in the final wear scar and the reduction in computational time will be obtained. It should be pointed that for this study the same wear coefficient  $k = 30 \times 10^{-6} \text{ mm}^3/\text{Nm}$  in both specimens, a normal force of  $F_n = 2 \text{ N}$  and stroke of  $\Delta x = 65 \mu\text{m}$  has been used.

Finally the optimized wear simulation methodology proposed in this work will be validated using the experimental data reported in Chapter 3.

##### 4.3.4.2 Interpolation method study

This section presents the analysis of the three interpolation methods (bivariate, baricentric and nearest) described in section 4.3.2.3. The differences obtained in the longitudinal wear scar with the different interpolation methods in each specimen are compared.



Fig. 4-24 shows the longitudinal wear scars of top (Fig. 4-24(a)) and bottom (Fig. 4-24(c)) specimens. In the slave surface the difference in the wear between the three methods scar is depreciable, as it can be seen in the magnification of the profile (Fig. 4-24(b)). However, in the master surface (Fig. 4-24(d)) the different interpolation methods present different wear depth; nevertheless the wear scar width is the same in all cases. The baricentric method produce the shallowest wear scar, the nearest method produce the deepest one and the bivariate method is in the middle of both methods. Analyzing Fig. 4-24(d) it is obtained that the difference between baricentric and nearest method is around 9%. Nevertheless the nearest method is three times faster than the other two methods, because it is not needed any triangulation method.

If only the contact pressure is interpolated and the relative sliding of each node is considered the same as the imposed displacement, Fig. 4-24(d) shows that the difference due to the interpolation is depreciable. After this it can be concluded that the difference presented previously between the different methods is due to the interpolation the relative slips of each node.

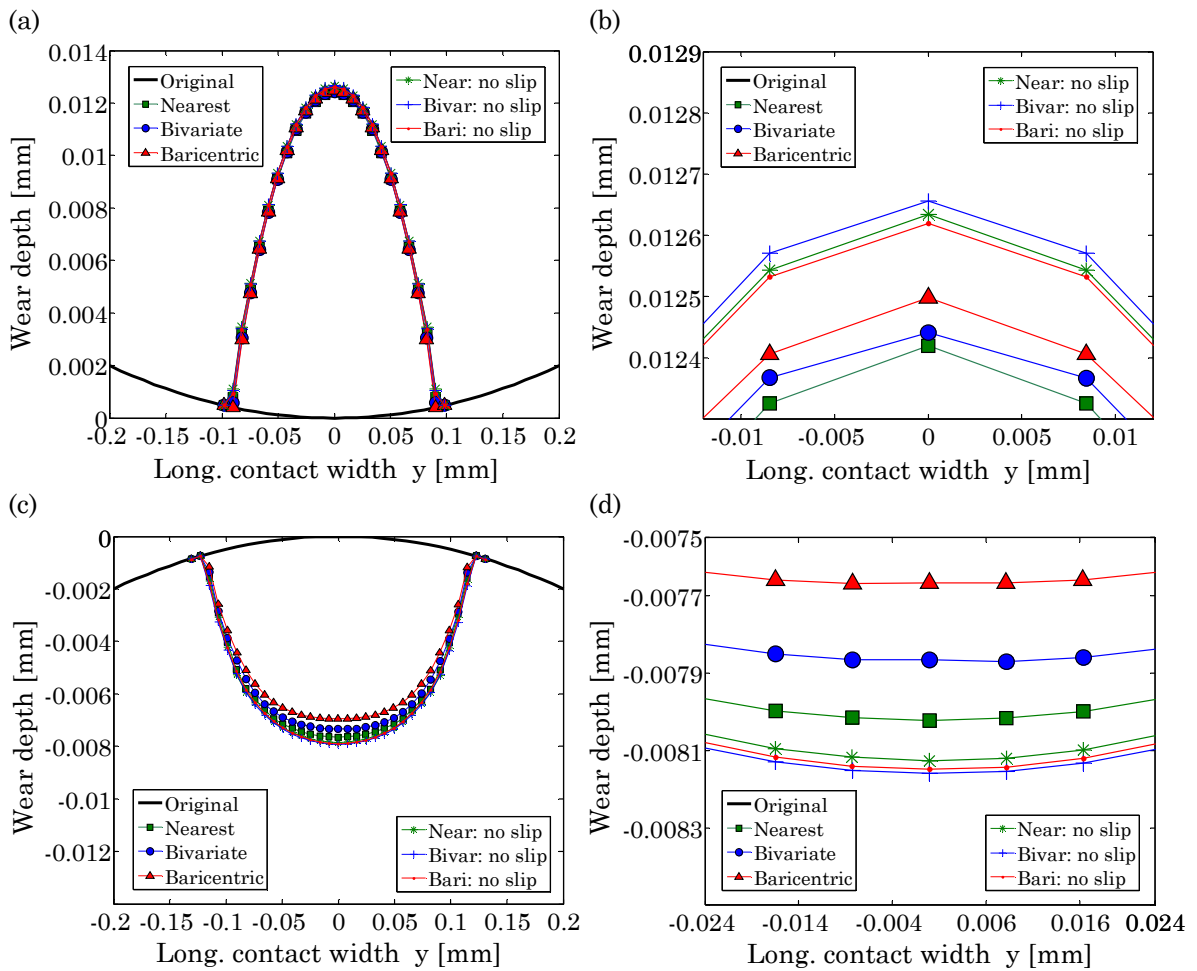


Fig. 4-24. Longitudinal wear scars comparison with different interpolation methods: (a) top wear scar, (b) magnification of (a), (c) bottom wear scar and (d) magnification of (c).

As the nearest method is presented as the fastest method, now the validation of this methodology is analyzed. For this, the bottom surface is considered as the slave surface and the interpolation is done in the top surface. After this the interpolated wear scars can be compared directly with the wear scars obtained by Abaqus without interpolating. When the interpolation is made in the top surface Fig. 4-25(a) the difference is less than 1% and when the interpolation is made in the bottom surface Fig. 4-25(b) the difference is less than 2%, being in both interpolation the wear scar width the same. Nevertheless if the interpolation is made in the top surface, problems with respect to the contact problem stability appears and a little bit more time is needed for interpolation, because more points enter in the nearest method for each node interpolated, as a consequence of the greater number of nodes that are in the bottom surface.

Taking into account that the nearest interpolation is the less time consuming method and that the differences in comparison with Abaqus results is less than 2%, the wear FE methodology for thin steel wires it is carried out with nearest interpolation.

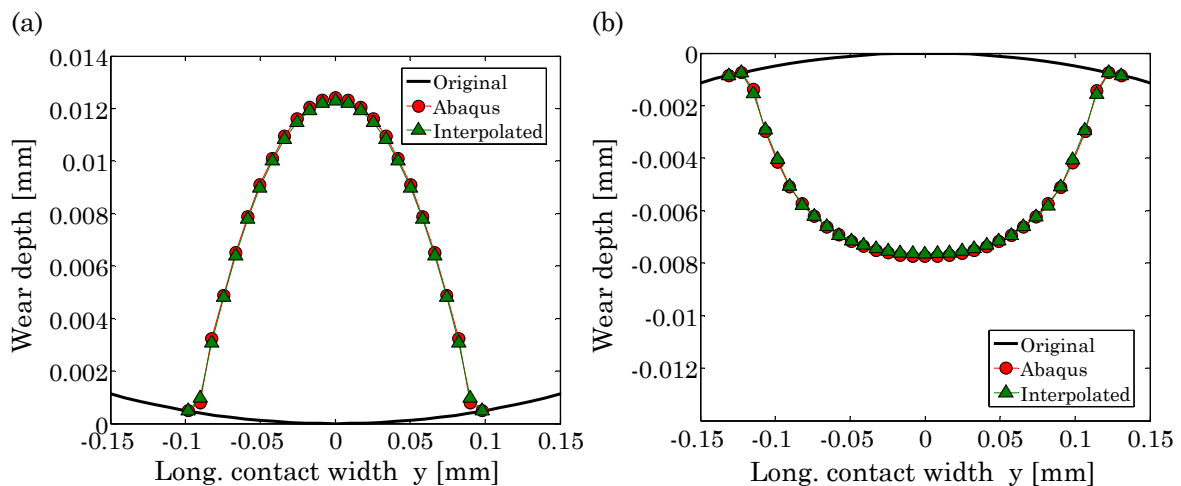


Fig. 4-25. Longitudinal wear scar with and without interpolation: (a) top and (b) bottom wear scar.

#### 4.3.4.3 FE wear parameters optimization

This section presents the analysis of the three principal parameters involved in wear simulation (mesh size, increments per fretting cycle and cycle jump). For this analysis the longitudinal profile of the bottom wear scar is studied, because it is the most critical. On the one hand it is the wear scar obtained with the contact pressures and slip distribution interpolated from the top surface (slave surface) with the nearest interpolated method mentioned in section 4.3.4.2 and on the other hand this profile presents distortions in geometry faster than the top one.

The first and the most important parameter to reduce the computational time is the mesh size in the contact zone. For this analysis the other two parameters and the number of

cycles have been fixed: a cycle jump of  $\Delta n = 200$ , 40 wear simulation increments per fretting cycle and two different numbers of cycles 1000 and 20000. The range of mesh size studied goes from  $3 \mu\text{m}$  to  $24 \mu\text{m}$ .

In figure Fig. 4-26(a) it is shown that the mesh size has a great influence in the initial contact pressure distribution in comparison with the Hertzian contact pressure. While small mesh size ( $3 \mu\text{m}$ ) adjusts properly with the Hertzian contact pressure distribution, greater mesh size ( $10 \mu\text{m}$ ) increase both contact pressure and contact size. Nevertheless as the wear happens it can be seen in Fig. 4-26(b) that despite the contact pressure in the initial cycles is greater, this difference is reduced considerably during the exponential decrease of the contact pressure and stabilized during the stable period of the contact pressure, being the error during this period around 2%. This effect has been shown previously in section 4.2.4 for the 2D block on ring FE model.

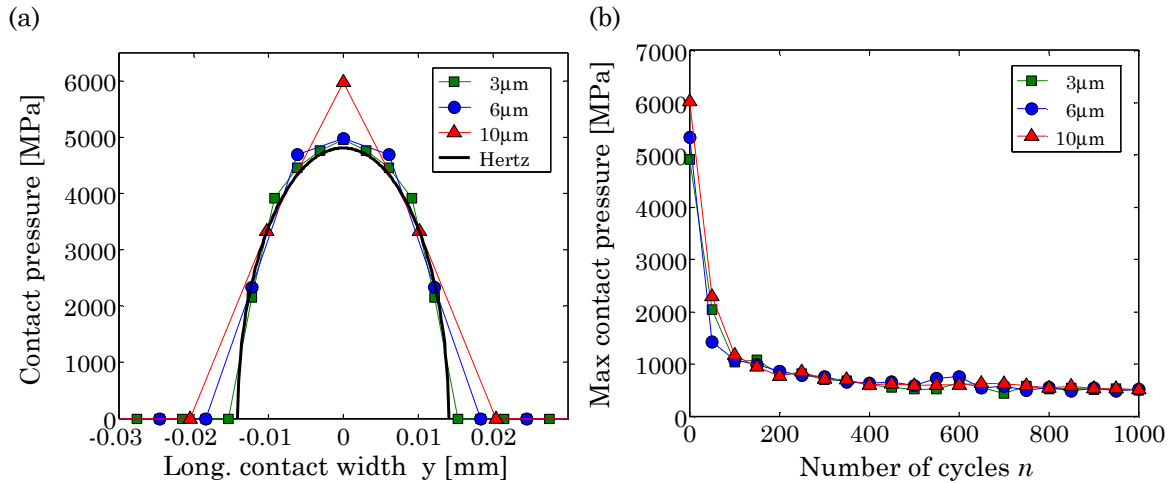


**Fig. 4-26. Hertzian contact pressure vs FEM contact pressure for different mesh: (a) contact pressure distribution without wear and (b) maximum contact pressure evolution in the first 1000 wear cycles.**

Although this study presents that the mesh size has not a great influence in the contact pressure once the wear reach the stable period, it is necessary to study the profile of the wear scar to validate an optimum mesh size to reduce the computational time. For this, in the next paragraphs the influence of the mesh size in the dimension and the shape of the wear scar profile is studied. Fig. 4-27(a) and (b) show the wear scars produced as a consequence of different mesh size for 1000 and 20000 cycles respectively. It can be seen that an increase from  $6 \mu\text{m}$  to  $24 \mu\text{m}$  (Fig. 4-27(b)) of the mesh size produce a trapezoidal wear scar profile due to the poor discretization, nevertheless the error in contact width is less than 6% and in wear depth is less than 5%.

After this it is proposed that the optimum mesh size without any distortions in geometry should be in the range from 3%-4% of the final longitudinal wear width. In the case of

20000 cycles, using an optimum mesh size of  $8\ \mu\text{m}$  a reduction of two times in the computational time is obtained with respect to a refined mesh of  $6\ \mu\text{m}$  which is close to the Hertzian contact pressure (Fig. 4-26(a)). Nevertheless the application of the proposed relation between the mesh and the longitudinal wear scar width requires to know the dimensions of the wear scar. So that, in this work with the aim to obtain the approximated dimensions of the wear scar width it is proposed to use greater mesh sizes, because the difference in the final wear scar between greater mesh sizes and small mesh sizes is small as shown in Fig. 4-27. In this case using a greater mesh of  $24\ \mu\text{m}$ , which corresponds to a mesh size that is around 10% of the final longitudinal wear width, a reduction of 4 times in the computational time with respect to the optimum mesh size of  $8\ \mu\text{m}$  is achieved.

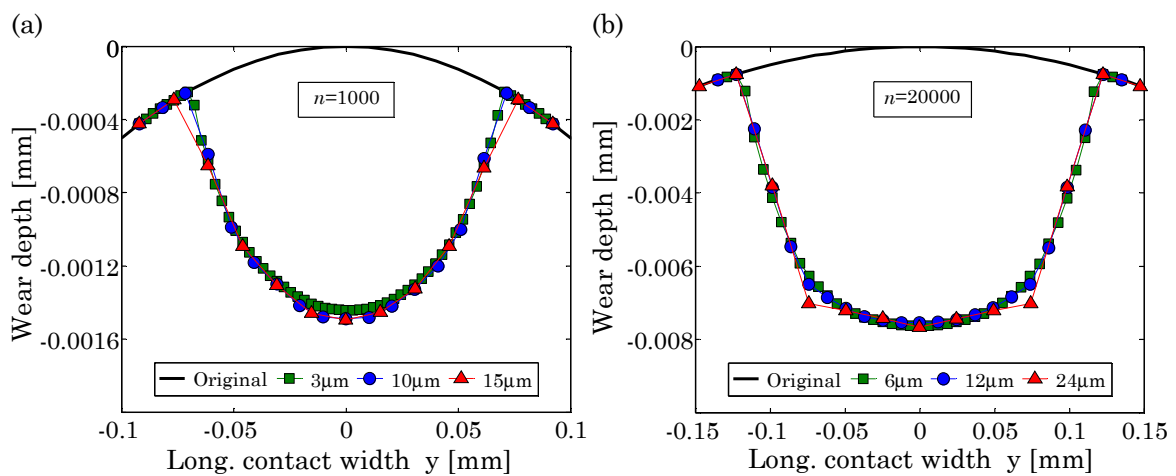


**Fig. 4-27. Longitudinal wear scar in the bottom specimen for different mesh sizes: (a) 1000 number of cycles and (b) 20000 number of cycles.**

The second and the third parameter to reduce the computational time are based on the determination of the maximum sliding increment  $\Delta s$ . For this, two different studies were carried out: the first one corresponds to the contact wear simulation increments per fretting cycle, and the second one consists of the study of the cycle jump  $\Delta n$  technique. In these studies, an optimum mesh size of  $6\ \mu\text{m}$  for the case of 1000 cycles and  $8\ \mu\text{m}$  for the case of 20000 cycles is used, following the relation proposed previously between the longitudinal wear scar width and the mesh size.

On the one hand, Fig. 4-28(a) shows that the influence of the increments discretization per cycle in the wear scar is depreciable. For this study 40 increments/cycle is selected as the optimum discretization, because smaller increments per cycle produce convergence problems during the contact problem resolution and greater values don't present significant differences in the wear scar profile.

On the other hand, in Fig. 4-28(b) a great influence of the cycle jump  $\Delta n$  in the wear scar profile is seen. The wear scar becomes deeper and slender with high cycle jumps, such that

with excessive cycle jumps the profile is distorted. While for 1000 cycles there is an increase in the wear depth of 5% between a cycle jump of  $\Delta n = 100$  to  $\Delta n = 200$ , for 20000 cycles there is the same increase between  $\Delta n = 100$  and  $\Delta n = 400$ . It means that with higher wear cycles greater cycle jumps can be used. For this study it is proposed that the optimum value for the study of different cases along different number of cycles without any distortions in profile and with an error in depth less than 3% should be 100 fretting FE cycles and the corresponding  $\Delta n$ , i.e., in the case of 20000 cycles  $\Delta n = 200$  or in the case of 50000 cycles  $\Delta n = 500$ . Taking into account that each fretting cycle is discretized in 40 increments, any wear simulation, regardless the conditions used, is modelled with 4000 FE wear increments. On the other hand greater cycle jumps could be used in order to define the approximated dimension of the wear scar, taking into account that the differences in the wear scar dimensions are small as shown in Fig. 4-28(b). After this study was observed that 2000 FE wear increments (50 fretting FE cycles) and the corresponding cycle jump can be used to obtain the approximated wear scar dimensions with the minimum computational time and without any differences in the final wear scar width dimensions

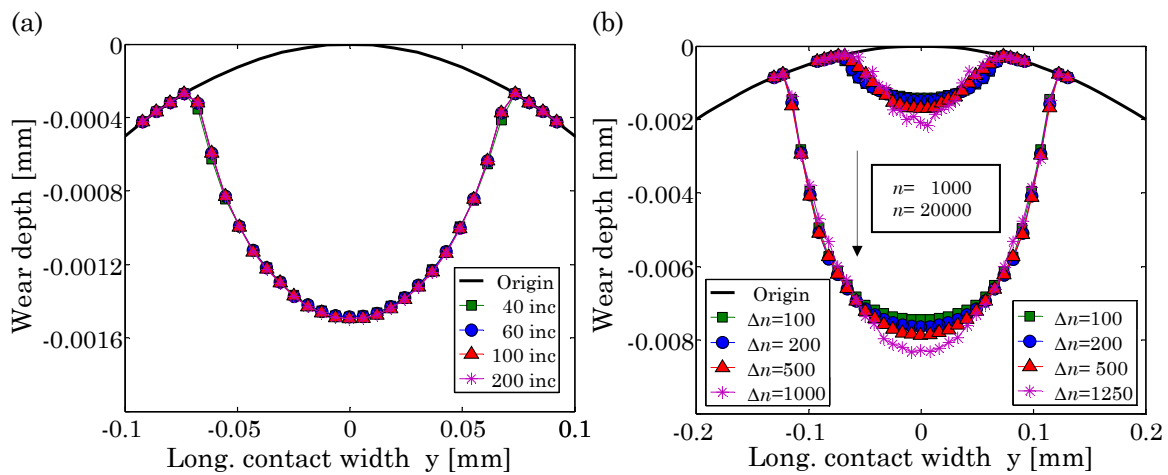


Fig. 4-28. Longitudinal wear scar in the bottom specimen: (a) for different increments per cycle and 1000 number of cycles and (b) for different cycle jumps for 1000 and 20000 number of cycles.

In this study an optimized methodology for the definition the optimum wear simulation parameters was carried out. For the application the entire methodology it is proposed to do two simulations. The first one consist of a faster wear simulation which it is used to obtain the approximated dimensions of the wear scars width and the second one consist of the simulation based on the optimized parameters. Here are summarized the steps and the parameters that should be used in order to perform an optimum wear simulation:

- A first simulation with a great mesh size to obtain the approximated dimension of the wear scar it should de carried out. This simulation is composed by 50

fretting FE cycles, with 40 increments per fretting cycle and the corresponding cycle jump to achieve the desired number of cycles.

- After this simulation it should be checked that the used mesh size is around the 10% of the final longitudinal wear width. If this condition is not satisfied a new faster simulation it is carried out taking into accounts the dimensions of the obtained wear scar.
- Knowing the wear scar dimensions, a new FE model is constructed with the optimum mesh size parameters which corresponds to a mesh size in the contact zone around 4% of the final longitudinal wear width. For the optimum wear simulation 100 fretting FE cycles, with 40 increments per fretting cycle and the corresponding cycle jump to get the desired number of cycles have to be used.

#### 4.3.4.4 Wear modelling validation

In this point, the wear scars (Fig. 4-29) obtained by the optimized wear methodology presented in section 4.3.4.3 are validated using the experimental wear scars obtained in section 3.3.1.2 under different tests conditions of: load, stroke and number of cycles with the aim to present a global methodology for simulation any experimental cases. As has been mentioned previously the validation methodology consists of three steps, which will be analyzed in detail in the next paragraphs. For the validation of all cases the specific wear coefficients obtained in each specimen and test has been chosen. The sum of the coefficient of wear of both specimens can be found in Fig. 3-13.

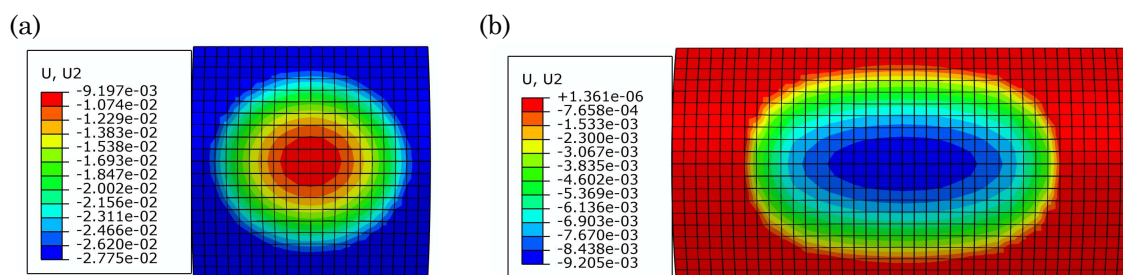


Fig. 4-29. FEM wear scars for a 1 N-130  $\mu\text{m}$ -50000 cycles: (a) top wear scar, (b) bottom wear scar.

The first validation method consists of the determination of the wear scar dimensions in top and bottom wear scars, taking into account that each wear scar is composed by two principal dimensions: the longitudinal and the transversal direction with respect to the wire. Table 4-3 shows the values obtained experimentally and by FEM for different load, stroke and number of cycle cases, where the first value represent the wear scar width in the transversal direction and the second one represents the wear scar width in the longitudinal direction to the wire. It can be seen that the error in the transversal direction is greater

than in the longitudinal direction, nevertheless the error is less than 10%, acceptable in this type of tests taking into account that the experimental results could present dispersions greater than 15% [136]. In the range of loads, strokes and number of cycles studied the dimensions of the wear scar could be predicted with an error that goes from 1% to 9%.

**Table 4-3. FEM vs experimental wear scar dimension analysis for both top and bottom specimens.**

		Top wear scar ( $\mu\text{m}$ )	Error (%)	Bottom wear scar ( $\mu\text{m}$ )	Error (%)	Coefficient of wear ( $10^{-8} \text{ mm}^3/\text{Nmm}$ )
1N-65 $\mu\text{m}$ 20000 cycles	Experimental	151-166	3-1	161-200	9-6	2.59-3.65
	FEM	146-164		146-212		
2N-65 $\mu\text{m}$ 20000 cycles	Experimental	189-190	6-1	190-230	7-4	2.65-3.46
	FEM	178-192		176-240		
3N-65 $\mu\text{m}$ 20000 cycles	Experimental	200-200	8-2	200-250	9-2	2.31-2.76
	FEM	184-204		182-245		
3N-65 $\mu\text{m}$ 50000 cycles	Experimental	230-230	3-6	239-280	6-2	2.10-1.91
	FEM	224-245		224-286		
1N-130 $\mu\text{m}$ 20000 cycles	Experimental	180-180	2-2	190-280	4-2	3.01-4.08
	FEM	183-184		183-286		
1N-130 $\mu\text{m}$ 50000 cycles	Experimental	200-210	3-5	210-310	5-3	2.32-2.34
	FEM	196-221		200-319		
1N-130 $\mu\text{m}$ 200000 cycles	Experimental	250-250	8-3	260-359	8-3	1.54-0.69
	FEM	230-257		240-372		

The second validation method consists of the comparison of the maximum wear depth profile in the longitudinal direction of the specimen in top and bottom wear scar with the profile obtained by FEM, as it is shown in Fig. 4-30 and Fig. 4-31 respectively for different number of cycles. On one hand the top wear scar profile obtained by FEM adjust precisely to the profile obtained experimentally (Fig. 4-30(d)-(f)) with an error in the maximum wear depth less than 6% as it is shown in Table 4-4. On the other hand the bottom wear scar (Fig. 4-31(d)-(f)), obtained by FEM presents more uniform shape than the profile obtained experimentally. In this case the error in the maximum wear depth goes up to 14%. The reason of this error could be the following three.

- Influence of the error assumed by the FEM wear simulation in the bottom wear scar.
- Influence of the error committed by the bending curvature that acquires the wire in the fixation holder during the experimental tests.

- Influence of the error committed by the used coefficient of friction and coefficient of wear.

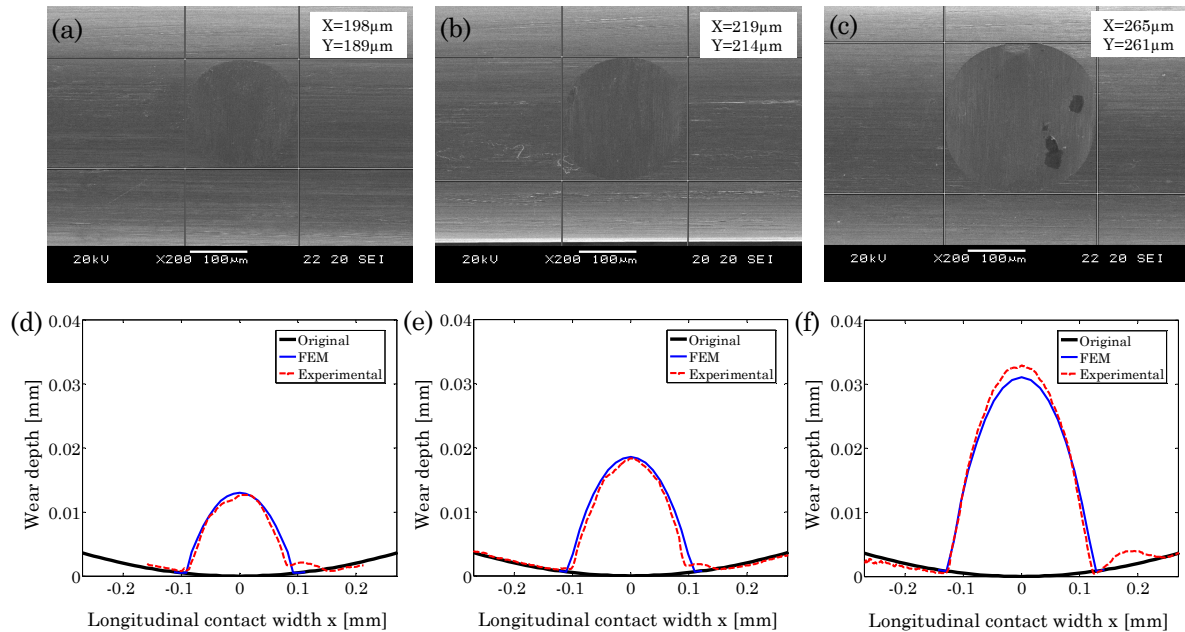


**Fig. 4-30. Wear scars of top specimen for 1 N-130  $\mu\text{m}$ : (a) 20000 cycles SEM, (b) 50000 cycles SEM, (c) 200000 cycles SEM, (d) 20000 cycles FEM vs experimental, (e) 50000 cycles FEM vs experimental and (f) 200000 cycles FEM vs experimental.**

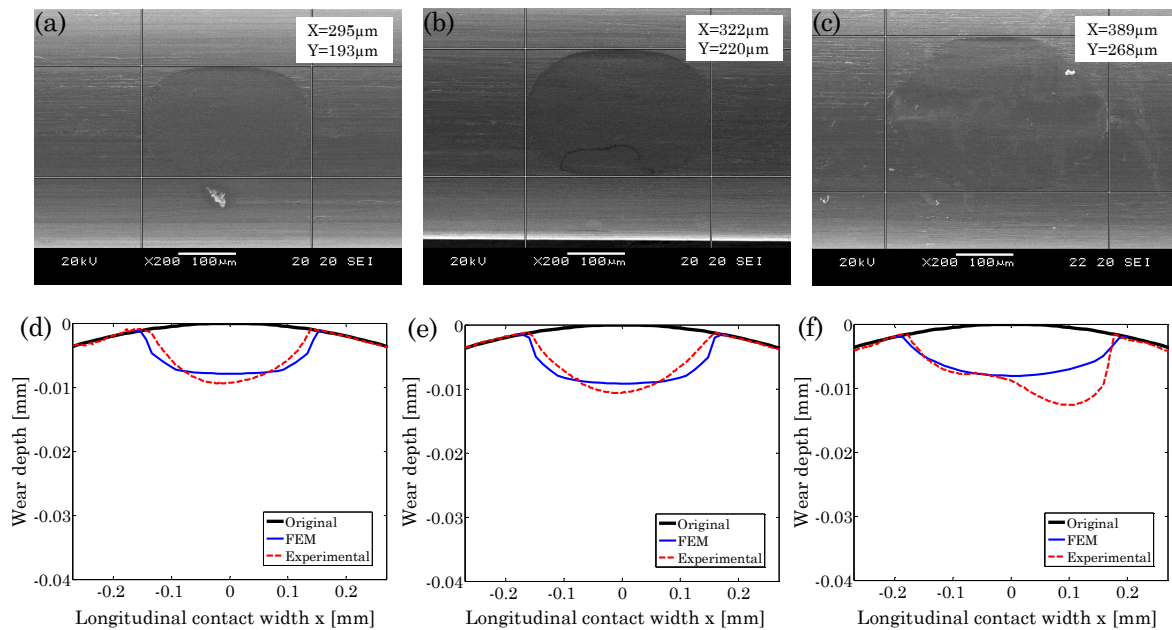


**Fig. 4-31. Wear scars of bottom specimen for 1 N-130  $\mu\text{m}$ : (a) 20000 cycles SEM, (b) 50000 cycles SEM, (c) 200000 cycles SEM, (d) 20000 cycles FEM vs experimental, (e) 50000 cycles FEM vs experimental and (f) 200000 cycles FEM; vs experimental.**

The first reason corresponds to the error assumed by the optimized FEM wear simulation methodology which is less than 3%.



The second reason corresponds to an error that is committed in this type of tests as a consequence of the bending curvature that acquired the wire in the fixation holder. In the case of longest wear scars, as it happens in the bottom wire, greater is the part of the bending that is covered by the wear scar. Taking into account that the FEM model represents the ideal configuration and in the experimental tests the radius of the curvature could not be exactly 10 mm or the wires could not be perfectly centred, the error could be come from both the experimental tests and the measurement of the wear scar profile.

**Table 4-4. FEM vs experimental wear scar depth analysis for both top and bottom specimens.**

		<b>Top wear scar (<math>\mu\text{m}</math>)</b>	<b>Error (%)</b>	<b>Bottom wear scar (<math>\mu\text{m}</math>)</b>	<b>Error (%)</b>
1N-130 $\mu\text{m}$ 20000 cycles	Experimental	12.7	2.3	9	12
	FEM	13		7.9	
1N-130 $\mu\text{m}$ 50000 cycles	Experimental	18.3	1.1	10.6	13
	FEM	18.5		9.17	
1N-130 $\mu\text{m}$ 200000 cycles	Experimental	32.8	5.2	10.07	14
	FEM	31.1		8.65	

The final reason could be due to an error committed by the used coefficient of friction and coefficient of wear. On the one hand, in Fig. 4-32 is shown the effect of the coefficient of friction in both wear scars, top Fig. 4-32 (a) and bottom Fig. 4-32 (b). As can be seen the influence of the different coefficient of friction in the final wear scar profile is depreciable for this type of tests.

On the other hand in Fig. 4-33 is shown the influence of the ratio between the coefficient of wear of the top and the bottom wear scar. One of the characteristic of this type of tests is that the coefficient of wear decrease with the number of cycles. This effect is attributed to the formation of protective layers in the bottom wear scar as shown in section 3.3.1.2, which produce the reduction of the coefficient of wear in both specimens but with greater influence in the bottom wear scar. So in the beginning of the tests the coefficient of wear of the bottom specimen is greater than the top specimen, then both coefficients converge to the same value and finally the coefficient of the bottom specimen is smaller. To analyze this influence the same coefficient of wear has been used in the bottom specimen and greater, smaller and equal in the top specimen. As shown in Fig. 4-33(a) the wear depth and width of the top wear scar increase increasing the ration of the coefficient of wear. Nevertheless in the bottom wear (Fig. 4-33(b)) scar the opposite tendency is produce, as the ratio decrease the wear scar becomes deeper and narrower. As greater ratios only appear in the beginning of the tests and in these simulations the specific wear coefficient, which represent the mean coefficient of wear along the test, have been used, the variable effect of the coefficient of

wear is not considered. Thus, this could explain the lower wear depth obtained by simulation in comparison with the experimental data. Nevertheless the error committed during the simulation is assumable for this type of tests.

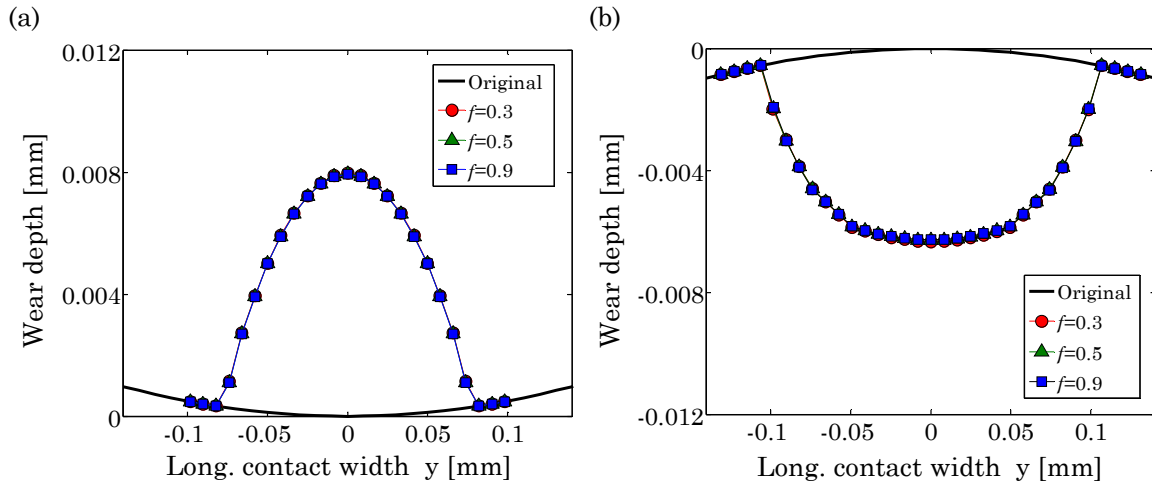


Fig. 4-32. Longitudinal wear scar for different coefficient of friction: (a) top wear scar (b) bottom wear scar.

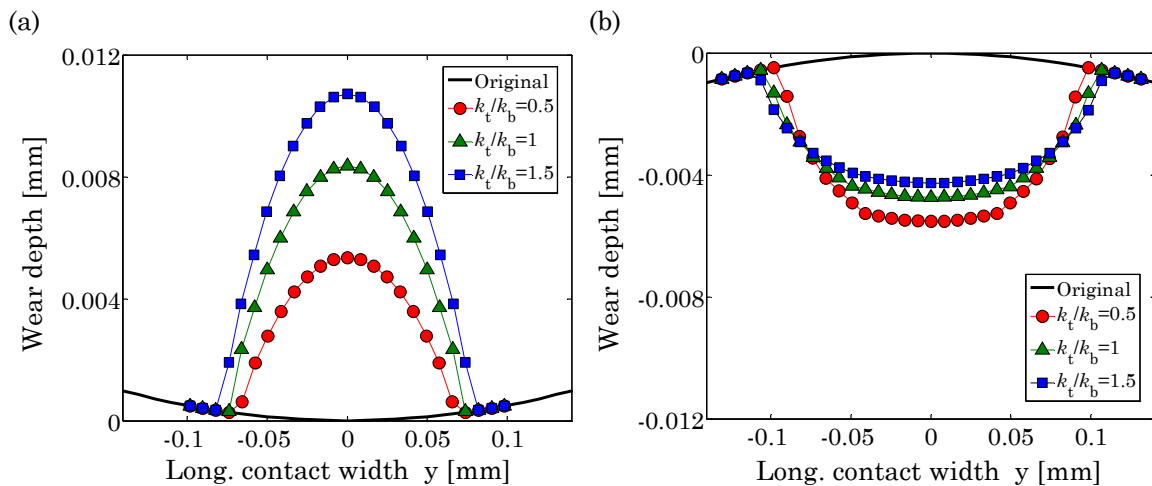


Fig. 4-33. Longitudinal wear scar for different coefficient of wear ratios: (a) top wear scar (b) bottom wear scar.

Taking into account the good correlation existed in the wear scar dimensions and in the wear scar profile in the maximum wear depth point, the final validation procedure consists of the comparison of the volume of both wear scars as can be seen in Table 4-5. In all cases the wear volume predicted by FEM is smaller than the one obtained experimentally. Nevertheless this error is smaller than 10%. This validation has demonstrated that this optimized methodology for simulation fretting wear in crossed cylinder arrangements predict within an mean error less than 10% the entire shape of wear scar in both top and bottom specimens.

**Table 4-5. FEM vs experimental wear scar volume analysis for both top and bottom specimens.**

		Top wear scar ( $\mu\text{m}^3$ )	Error (%)	Bottom wear scar ( $\mu\text{m}^3$ )	Error (%)
1N-65 $\mu\text{m}$ 20000 cycles	Experimental	66000	0.5	93000	1.2
	FEM	65644		91992	
2N-65 $\mu\text{m}$ 20000 cycles	Experimental	135000	1.2	177000	2.5
	FEM	133430		172710	
3N-65 $\mu\text{m}$ 20000 cycles	Experimental	172000	3	206000	4
	FEM	166930		197660	
3N-65 $\mu\text{m}$ 50000 cycles	Experimental	404000	3.6	367000	5
	FEM	389380		348930	
1N-130 $\mu\text{m}$ 20000 cycles	Experimental	157000	2.3	212720	1.7
	FEM	153470		209130	
1N-130 $\mu\text{m}$ 50000 cycles	Experimental	305250	3.1	307590	3.1
	FEM	295790		297920	
1N-130 $\mu\text{m}$ 200000 cycles	Experimental	820000	8	365770	10
	FEM	75345		328520	

### 4.3.5 FEM wear simulation in different crossing angle arrangements

#### 4.3.5.1 Wear modelling optimization

This point describes the optimized methodology used for the computational time reduction in the FE wear simulation for crossing angles model. This methodology is basically the same used for 90° crossed cylinder arrangements and consists of the optimization of the main three parameters involved in the FE wear simulation: mesh size, increments per fretting cycle and cycle jump technique.

Nevertheless, as the wear scars obtained have elliptical shape, greater effort was done in the study of optimum meshes used in the FE model. Fig. 4-34 shows the contact pressures obtained for two different crossing angles. In both cases the direction of the contact pressure is given at the middle of the crossing angle used. Taking into account this phenomena the partition of both specimens are done in this direction, so the brick elements used in this partition are structured in this direction with the aim to obtain better resolution of the contact pressure. As the contact pressure has an elliptical shape, two types of mesh have been used; the first one corresponds to a rectangular mesh shape and the second one to a square mesh shape.

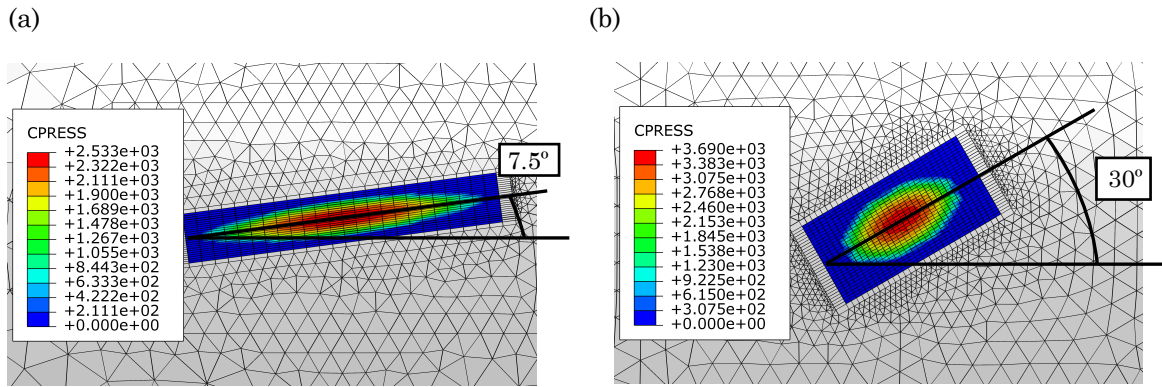


Fig. 4-34. Contact pressure distribution: (a) for 15° crossing angle and (b) for 60° crossing angle.

Fig. 4-35 shows the results of the contact pressures obtained by the square shape meshes and rectangular meshes in both semi-axis for 30° crossing angle case. Both the rectangular mesh (3 x 1.5  $\mu\text{m}$ ) and the square mesh (1.5 x 1.5  $\mu\text{m}$ ) give similar results, close to the Hertzian solution. Nevertheless the use of rectangular shape elements reduce three times the computational time in comparison with the square shape elements, and the small square shape elements (1.5 x 1.5  $\mu\text{m}$ ) produce small fluctuations in the peak contact pressure. So that, the rectangular shape elements are the optimum elements taking into account the computational time and the precision in the obtained results.

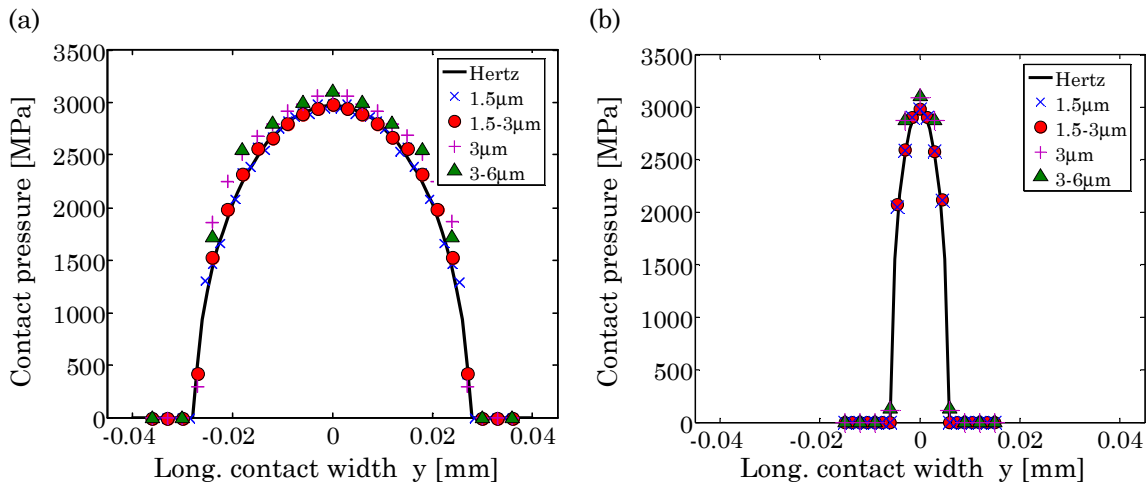


Fig. 4-35. Contact pressure distribution FEM vs HERTZ for 30° crossing angle: (a) major axis contact width, (b) minor axis contact width.

On the other hand greater mesh size 3 x 3  $\mu\text{m}$  or 3 x 6  $\mu\text{m}$  gives results a bit higher than those ones presented by the Hertzian solution. However, in 90° crossed cylinder configuration was seen that, although greater mesh size tends to give initial contact pressure greater than the Hertzian contact pressure, as the wear happens this contact pressure becomes uniform and the final wear scar is similar to those presented with refiner meshes. In this case it was proposed that the optimum mesh size (for square shape

elements) without any distortions in geometry should be in the range from 3% to 4% of the final longitudinal wear width of the bottom wear scar.

Nevertheless in this study it is not possible to use this criterion. On the one hand, previously has been discussed that due to the elliptical distribution of the contact pressure, the optimum element mesh shape should be rectangular. On the other hand it is more difficult to know the length of the major axis in the bottom wear scar than in the top wear scar because the orientation of this axis is unknown. This phenomenon is produced due to the relative motion that happens in the contact zone as a consequence of the crossing angle. So that, the new optimized parameter of the mesh size will be defined based on the rectangular mesh shape and according to the top wear scar (the stationary specimen), whose major axis is oriented at the middle of the crossing angle used.

To define the optimum rectangular mesh size, the aspect ratio between the semi-major axis and the semi-minor axis of the elliptical wear scar is analysed. Fig. 4-36 shows the two line tendencies obtained for the relation between the semi-axis ratio and the crossing angle for the Hertzian contact ellipse and the experimental top wear scar obtained for 50000 cycles, 1N and 130 μm. It is possible to see that as a consequence of the wear and mainly with small crossing angles the ratio obtained in the wear scar is smaller than the ratio obtained by the Hertzian solution. Hence in this study it is proposed to use the ratio given by the wear scar. On the other hand it was observed that for smaller angles than 15°, using the criterion proposed in this study convergence problems appeared in the resolution of the contact problem, due to the excessive rectangular mesh shape. Therefore for these crossing angles it is proposed to use the same ratio used for the 15° crossing angle.

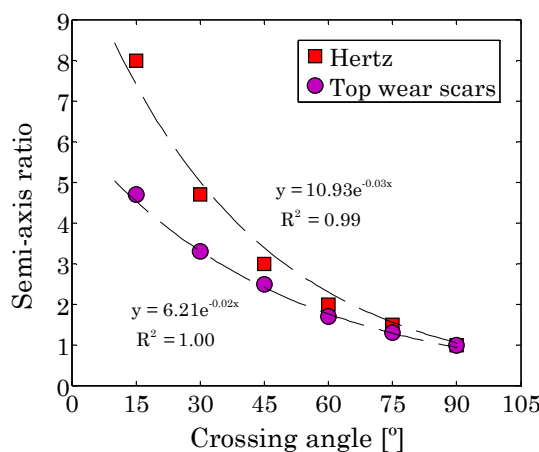
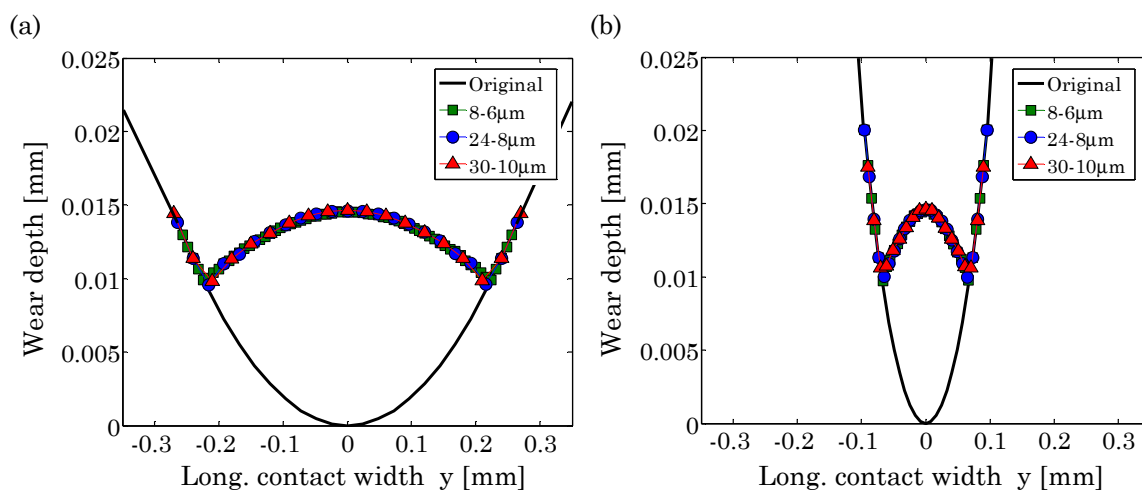


Fig. 4-36. Semi-axes ratio vs crossing angle for Hertzian contact ellipse and for 50000 cycles 1N and 130 μm experimental top wear scar.

Having defined the criterion to obtain the optimum aspect ratio of the rectangular shape meshes the next step is to define the mesh size in the major axis of the wear scar. Fig. 4-37

shows the wear scar profiles obtained in both axis for 50000 cycles 1N-130  $\mu\text{m}$ ,  $30^\circ$  crossing angle and different meshes. While the 24  $\mu\text{m}$  mesh size represents the 5% of the major axis the 30  $\mu\text{m}$  mesh size represents the 6.25% of the major axis. In both cases (24-8  $\mu\text{m}$  and 30-10  $\mu\text{m}$ ) an aspect ratio of 3 that is in accordance with the ratio shown in Fig. 4-36 has been used. As can be seen, the profiles obtained in both axes with these two meshes are similar to those obtained with a finer mesh size 8-6  $\mu\text{m}$ . Nevertheless the mesh of 30  $\mu\text{m}$  and meshes with sizes greater than the ones used in this study represent a poor discretization of the profile of the wear scar. These meshes can be used as first wear simulation step to define the wear scar dimensions and the optimum mesh parameters. As described in section 4.3.4.3 for the  $90^\circ$  crossing angles FE wear model, this methodology requires to perform a faster wear simulation, in order to define the approximated wear dimensions. Therefore it is proposed to use meshes which are around the 10% of the top wear scar major axis dimension.

After this study it is proposed that the optimum mesh size in the major axis should be in the range from 5%-6% of the top wear scar major axis dimension. Comparing the optimum mesh size of (24-8  $\mu\text{m}$ ) with the smallest mesh size (8-6  $\mu\text{m}$ ) the computational time is reduced from 94 hours to 14 hours.



**Fig. 4-37. FEM top wear scar profiles for 1 N-130  $\mu\text{m}$ -50000 cycles  $30^\circ$  crossing angles and different meshes: (a) longest axis position, (b) shortest axis position.**

On the other hand the increments per cycle and the cycle jump  $\Delta n$  are selected according to the optimum values proposed in the case of  $90^\circ$  crossed cylinders, which corresponds to 100 fretting FE cycles, 40 increments/cycle and the corresponding  $\Delta n$ . Fig. 4-38 shows the influence of the cycle jump in the top wear profile obtained in both axis for 50000 cycles 1N-130  $\mu\text{m}$  and  $30^\circ$ . The proposed optimum value is  $\Delta n = 500$ , as can be seen neither small values nor great values don't present differences. Nevertheless greater values are prone to produce convergence problems in the contact resolution. As shown in the  $90^\circ$  model, greater

values of cycle jump combined with greater mesh sizes can be used in order to define the approximated wear scar dimensions in the faster wear simulation. Therefore 2000 FE wear increments and the corresponding cycle jump are proposed to this end.

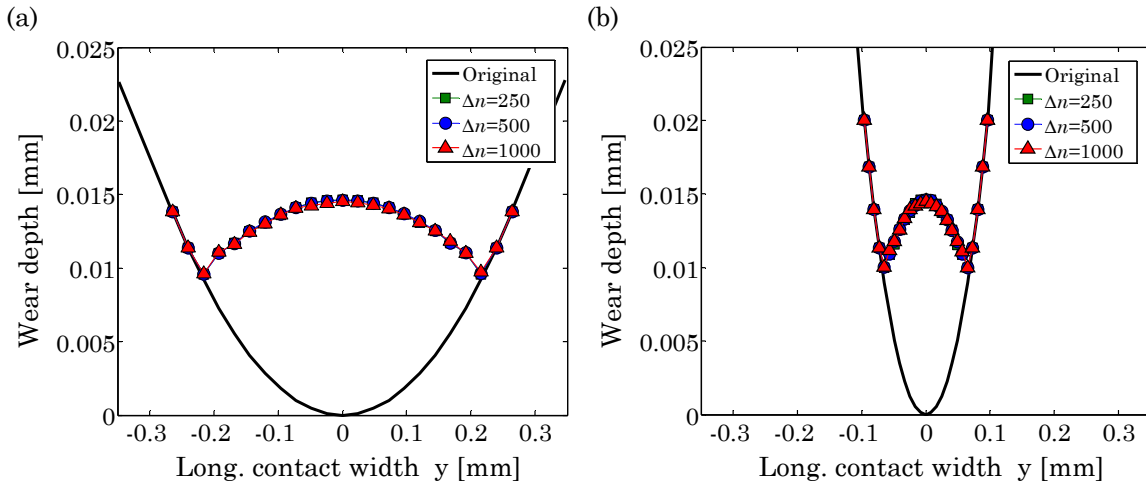


Fig. 4-38. FEM top wear scar profiles for 1 N-130  $\mu\text{m}$ -50000 cycles 30° crossing angles and different cycle jumps: (a) longest axis position, (b) shortest axis position.

As in the case of 90° crossing angles simulation explained in section 4.3.4.3 the application of the optimized parameters require to perform two simulations. The first one consist of a faster wear simulation which it is used to obtain the approximated dimensions of the wear scars width and the second one consist of the simulation based on the optimized parameters. Here are summarized the steps and the parameters that should be used in order to perform an optimum wear simulation:

- A first simulation with a greater mesh size and with the aspect ratio corresponding to the desired crossing angle shown in Fig. 4-36, to obtain the approximated dimension of the wear scar it should be carried out. This simulation is composed by 50 fretting FE cycles, with 40 increments per fretting cycle and the corresponding cycle jump to achieve the desired number of cycles.
- After this simulation it should be checked that the used mesh size is around the 10% of both semi axis. If this condition is not satisfied a new faster simulation it is carried out taking into accounts the dimensions of the obtained wear scar.
- Knowing the wear scar dimensions, a new FE model is constructed with the optimum mesh size parameters, which correspond to a rectangular mesh size that should be around 6% of the top wear scar major axis dimension of the final longitudinal wear width and with the aspect ratio between the semi-major axis and the semi-minor axis of the final elliptical wear scar. For the optimum wear

simulation 100 fretting FE cycles, with 40 increments per fretting cycle and the corresponding cycle jump to get the desired number of cycles have to be used.

#### 4.3.5.2 Wear modelling validation

In this section, the wear scars (Fig. 4-39) obtained by the optimized wear methodology are validated using the experimental wear scars obtained in tribometer under different crossing angles ( $15^\circ$  -  $60^\circ$ ) with the same test conditions: 1N normal load,  $130\ \mu\text{m}$  stroke and 50000 number of cycles. As has been mentioned previously the validation methodology consists of three steps, which will be analyzed in detail in the next paragraphs. For the validation of all cases the specific wear coefficients obtained in each specimen and test has been chosen that can be found in section 3.3.2.2.

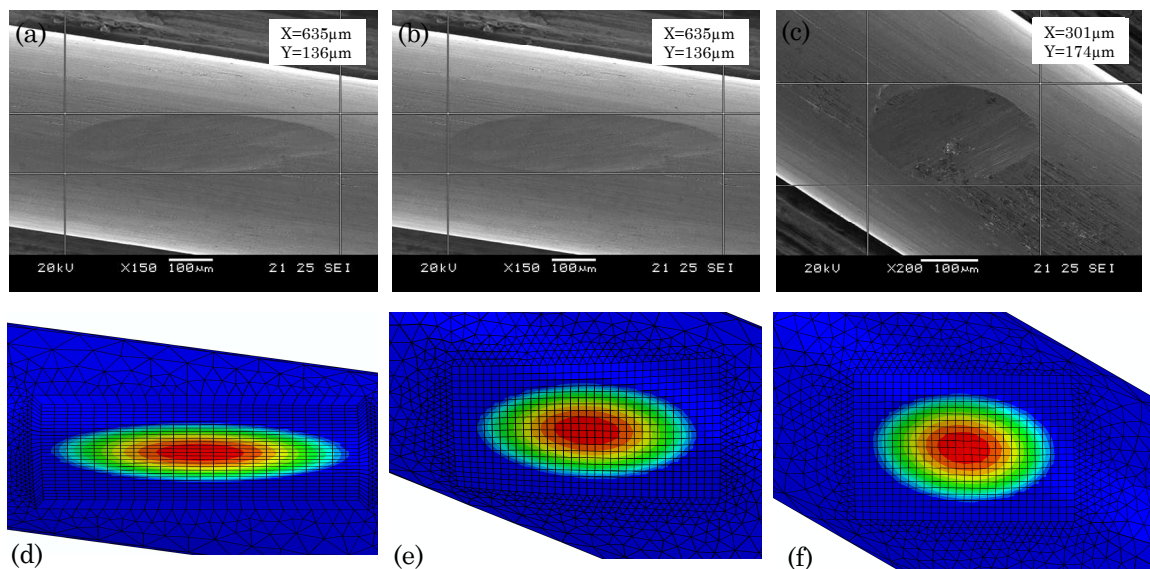


**Fig. 4-39. Wear scars of top specimen for 1 N-130  $\mu\text{m}$ -20000 cycles: (a)  $15^\circ$  experimental, (b)  $45^\circ$  experimental, (c)  $60^\circ$  experimental, (d)  $15^\circ$  FEM, (e)  $45^\circ$  FEM, (f)  $60^\circ$  FEM.**

The first validation method consists of the determination of the wear scar dimensions in top and bottom wear scars, taking into account that each wear scar is composed by two principal dimensions: the longest axis and the shortest axis of the elliptical wear scar. Table 4-6 shows the values obtained experimentally and by FEM for different angles, where the first value represent the wear scar longest axis and the second one represents the wear scar shortest axis. It can be seen that the error in both axes and specimens is less than 10%, acceptable in this type of tests taking into account that the experimental results could present dispersions greater than 15% [136].



**Table 4-6. FEM vs experimental wear scar dimension analysis for both top and bottom specimens.**

		Top wear scar ( $\mu\text{m}$ )	Error (%)	Bottom wear scar ( $\mu\text{m}$ )	Error (%)	Coefficient of wear ( $10^{-8} \text{ mm}^3/\text{Nmm}$ )
15°-1N-130 $\mu\text{m}$ 50000 cycles	Experimental	635-136	1-6	604-143	5-10	3.20-1.45
	FEM	644-128		636-128		
30°-1N-130 $\mu\text{m}$ 50000 cycles	Experimental	476-145	1-1	508-163	1-5	2.62-1.78
	FEM	480-146		507-155		
45°-1N-130 $\mu\text{m}$ 50000 cycles	Experimental	381-154	8-1	455-188	4-4	2.93-1.6
	FEM	352-155		435-181		
60°-1N-130 $\mu\text{m}$ 50000 cycles	Experimental	301-174	2-6	385-211	3-8	2.92-2.16
	FEM	308-192		373-194		

The second validation method consists of the comparison of the maximum wear depth profile in the longitudinal direction of the specimen in top and bottom wear scar with the profile obtained by FEM. Fig. 4-40 shows the profiles of the top wear scar obtained by FEM and experimentally. On one hand the top wear scar profile obtained by FEM adjust precisely with the profile obtained experimentally in both directions: in the direction of the greater semi axes (Fig. 4-40 (a)-(c)) and in the longitudinal direction of the specimen (Fig. 4-40(d)-(f)) with an errors in the maximum wear depth less than 10% as it is shown in Table 4-7. On the other hand the bottom wear presents greater errors 7%-20% as it is shown in Table 4-7. This error was presented in section 4.3.4.4 for the 90° crossed cylinders arrangements and was attributed to three different errors.

The first one corresponds to the error committed due to the error assumed in the bottom wear scar as a consequence of the optimized wear simulation methodology.

The second one corresponds to an error that is committed in this type of tests as a consequence of the bending of the wire in the holder, because longest is the wear scar greater is the part of the bending that is covered. For this reason if the radius of the curvature is not exactly 10 mm or the wires are not perfectly centred, the error is committed both in the experimental tests and in the measurement of the profile. As can be seen in Table 4-7 this error is greater with the smallest crossing angle (15°) where it is greater the part of the bending covered by the wear scar.

The last error is associated to the variable coefficient of wear ratio produced between the top and the bottom specimen along the test, which is not considered in this simulation. This error leads to produce smaller wear depths.

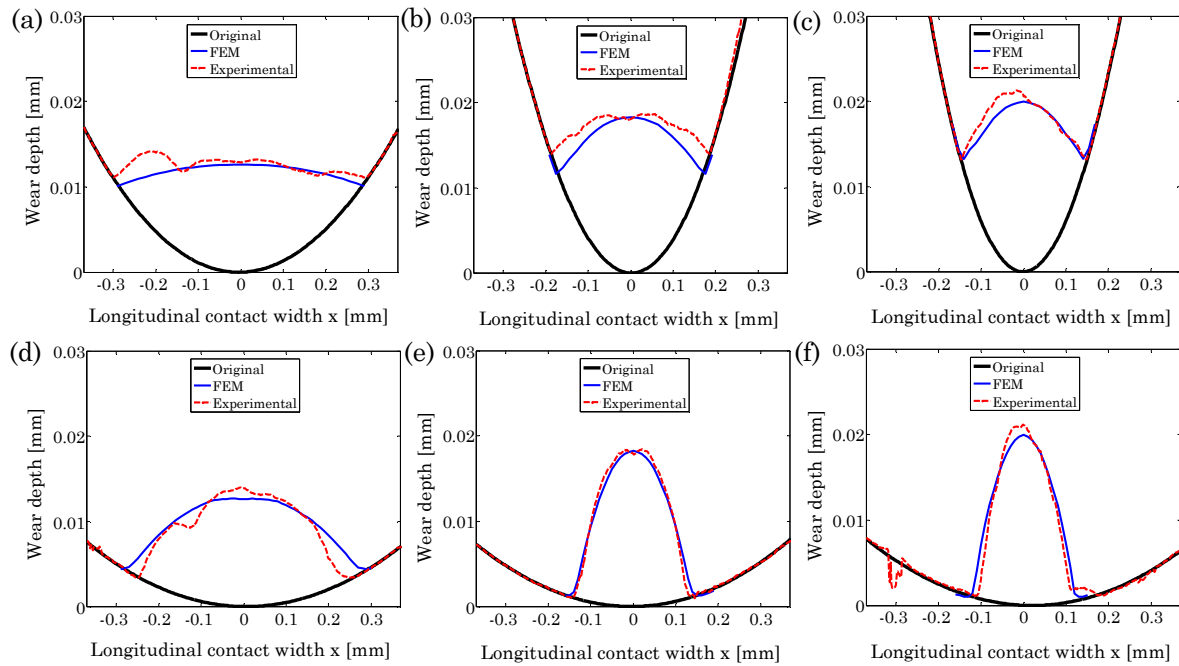


**Fig. 4-40. Wear scars of top specimen for 1 N-130  $\mu\text{m}$ -20000 cycles: (a) 15° longest axis, (b) 45° longest axis (c) 60° longest axis, (d) 15° longitudinal direction of the specimen, (e) 45° longitudinal direction of the specimen, (f) 60° longitudinal direction of the specimen.**

**Table 4-7. FEM vs experimental wear scar depth analysis for both top and bottom specimens.**

		Top wear scar ( $\mu\text{m}$ )	Error (%)	Bottom wear scar ( $\mu\text{m}$ )	Error (%)
15°-1N-130 $\mu\text{m}$ 20000 cycles	Experimental	13.1	0	6.6	21
	FEM	13.1		5.2	
30°-1N-130 $\mu\text{m}$ 20000 cycles	Experimental	16.4	10	7	7
	FEM	14.6		6.5	
45°-1N-130 $\mu\text{m}$ 20000 cycles	Experimental	18.3	0	7.1	14
	FEM	18.3		6.1	
60°-1N-130 $\mu\text{m}$ 20000 cycles	Experimental	21.2	6	9.2	15
	FEM	20		7.8	

Taking into account the good correlation existed in the wear scar dimensions and in the wear scar profile in the maximum wear depth point, the final validation procedure consists of the comparison of the volume of both wear scars as can be seen in Table 4-8. In all cases the wear volume predicted by FEM is smaller than the one obtained experimentally. Nevertheless this error is smaller than 3%.

This validation has demonstrated that this optimized methodology, for simulation fretting wear in crossed cylinder arrangements with different crossing angles, predict with errors less than 15% the entire shape of wear scar in both top and bottom specimens.

**Table 4-8. FEM vs experimental wear scar volume analysis for both top and bottom specimens.**

		Top wear scar ( $\mu\text{m}^3$ )	Error (%)	Bottom wear scar ( $\mu\text{m}^3$ )	Error (%)
15°-1N-130 $\mu\text{m}$ 20000 cycles	Experimental	418660	0.7	190110	0.5
	FEM	415770		189220	
30°-1N-130 $\mu\text{m}$ 20000 cycles	Experimental	341050	0.2	231999	1
	FEM	340590		229860	
45°-1N-130 $\mu\text{m}$ 20000 cycles	Experimental	384560	2.4	210860	2.6
	FEM	375540		205530	
60°-1N-130 $\mu\text{m}$ 20000 cycles	Experimental	378340	1	280320	2
	FEM	37800		274713	

#### 4.3.6 Conclusions

In this chapter an optimized wear simulation methodology for predicting wear scars in thin steel wires has been developed. In order to simplify the problem, the methodology has been developed previously in a 2D cylinder on plane sliding wear FE model. Then the main strategies of this methodology have been applied in the case of 90° crossed cylinder arrangements and finally the methodology has been implemented in the crossing angle configuration presented in wire rope systems.

The main conclusions obtained with the application of this optimized methodology in the 2D cylinder plane sliding wear model are:

- It has been demonstrated that the optimum mesh size for the wear simulation should be in the range of 2-3% of the final wear scar width. Following this rule a reduction in time from 18.3 h to a 1.2 h is found with respect to the use of a smaller mesh size, which fit properly with the Hertzian contact pressure.
- It is found that each model has a critical value of the sliding increment  $\Delta s$ , from which the system becomes unstable. Moreover the use of greater mesh sizes leads to use greater  $\Delta s$  reducing the wear increments needed for one simulation. This  $\Delta s$  can be related with a critical wear depth increment  $\Delta h$ .
- The used of a variable sliding increment, based on the wear depth increment  $\Delta h$  has reduced the 87% of the computational time, inducing errors in the final wear scar profile less than 1%. This variable speed factor consists of introducing a greater  $\Delta s$  in the stable period of the contact pressure, based on the critical wear depth increment  $\Delta h$ ,

and reducing this value in the final stage of the test with the aim to disappear the instabilities.

- Finally a good correlation between the experimental profiles and those ones obtained by FEM has been found. Therefore this methodology is presented as a useful tool for models that require high computational time such as in the 3D cases that will be discussed in the following lines.

The main conclusions obtained with the application of this optimized methodology in 90° crossed cylinder model are:

- One of the disadvantages of the UMESHMOTION subroutine is that the contact pressures and slips distributions, only are given in the slave surface. As the wear has to be considered in both specimens, firstly a study of different interpolations methods has been carried out. The nearest interpolation method is presented as the optimum method for the transition of the contact pressure and slip distribution from the slave surface to the master surface. In comparison with the other two methods studied in this paper (bivariate method and baricentric method), the differences obtained in the resulting final wear scar are depreciable, nevertheless the computational time needed for the resolution of the wear simulation problem is considerably inferior, three times faster than the other two methods.
- In the analyzed range, the mesh size in the contact zone has not a great influence in the final wear scar dimensions and depth. Nevertheless with high mesh sizes the profile presents a trapezoidal wear scar profile, for this, an optimum mesh size that could be around 4% of the final longitudinal wear width has been define. This proposal achieves the best compromise between the wear scar shape and the computational time spending.
- With respect to the sliding increment  $\Delta s$ , two studies have been carried out: the first one corresponds to the simulation increments per fretting cycle and the second one corresponds to the cycle jump  $\Delta n$  approach. The discretization of the FE wear simulation increments per fretting cycle doesn't present influence in the final wear scar profile. An optimum value of 40 increments/cycle is found, since below this value convergence problems appear in the contact problem resolution and above this value the differences in the wear profile are negligible. On the other hand, the cycle jump technique is very sensitive to the wear profile. After this study, it is proposed that an optimum simulation without any distortions in profile and with an error in depth less than 3% should be carried out with 100 fretting FE cycles, 40 increments/cycle and the corresponding  $\Delta n$ .

- The application of the optimized wear simulation requires to perform two simulations: the first one corresponds to a faster simulation in which the approximated wear scars dimensions are obtained and the second one corresponds to the simulation with the optimized parameters. For the faster simulation mesh sizes that are around 10% of the final wear scar size, 50 fretting FE cycles, 40 increments/cycle and the corresponding  $\Delta n$  can be used in order to obtain the final wear scar dimensions without errors in these values.
- The optimized simulation methodology presents very good correlation with respect to the experimental data, which implies that the entire wear scar can be predicted with errors less than 10%. Acceptable in this tribological system, where the experimental data may presents a dispersion greater than 15%.
- The great part of the error presented previously comes from the bottom wear scar depth and was attributed to three different aspects related to the FEM simulation and the experimental setting: the error committed by the optimized FEM simulation, the error committed in the experimental setting and the corresponding measurement of the wear scar and the error committed as a consequence of the frictional and the wear behaviour variables used in the FEM simulation.
- A FEM wear simulation for the analysis the influence of the coefficient of friction and the coefficient of wear ratio in the bottom specimen was carried out. It was seen that in the fretting conditions studied in this thesis (gross sliding conditions) the influence of the coefficient of friction was depreciable in the resulting final wear scar dimensions. However different ratios between the coefficient of wear of the top and the bottom specimen produced different wear depth in the bottom specimen. As reported in chapter 3 the formation of compacted debris protective layers produce different wear behaviours in the top and in the bottom wear scars. It means that the ratio between the coefficients of wear between both specimens vary a long the number of cycles. In order to simplify this problem the simulations carried out in this study were performed with a constant coefficient of wear ratio. Therefore the specific coefficient of wear obtained for each test condition and specimen, which represents the mean of the variable coefficient of wear reported in these tests, was used.

The main conclusions obtained with the application of this optimized methodology in the different crossing angles model is:

- The mesh of the contact zone is oriented in the direction of the contact pressure, which is the direction formed by the half of the crossing angle used. The optimum mesh size should be rectangular, with a value in the longest side around 6% of the major axis of

the final top wear scar and with a rectangular ratio close to the ratio obtained between the major axis and the minor axis of the final wear scar.

- It has been verified that the optimum values of the cycle jump  $\Delta n$  which has been selected according to the optimum values proposed in the case of  $90^\circ$  crossed cylinders are valid for the crossing angles FE wear model. These values correspond to a 100 fretting FE cycles, 40 increments/cycle and the corresponding  $\Delta n$ .
- As in the case of  $90^\circ$  crossing angles the validation methodology proposed in this work demonstrated the good correlation existed between the wear scars obtained by the optimized FEM methodology and those ones obtained experimentally predicting wear scars with errors less than 15%. These errors are considered acceptable because in tribological system, the experimental data presents dispersion greater than 15%.

It can be concluded that with this approach, it can be modelled the fretting wear scars presented in thin steel wires with the minimum computational time, making efficient and useful this methodology for that purpose. This tool will be used in the next chapter for the analysis of the severity of the wear scars under the different geometrical and operational variables presented in wire rope systems.

---

CHAPTER V

# FEM ANALYSIS OF THE SEVERITY OF THE WEAR SCARS

---

## 5.1 Introduction

---

From the fretting wear scars appeared in the wire rope systems it can be derived two damage mechanisms. The first damage mechanism could be the catastrophic rupture of the wire as a consequence of the increase of the stresses due to the excessive reduction of the cross section area produced by the wear scar. The second damage mechanism could be the so called notch effect caused by the wear scar, which leads to the reduction of the fatigue life of this component and the rupture of the wire. Around this last aspect Zhang et al. [79] studied the effect of fretting wear scars in 1mm diameter wire, obtained from 90° crossing cylinders arrangements fretting tests that subsequently were subjected to a fatigue tests. It was observed that the rupture of the wire was located in the deepest point of the wear scar, demonstrating that the fatigue life of thin steel wires was inversely proportional to the fretting wear depth. The main reason of this effect is the stress concentration at this point, and the following crack initiation, propagation and fracture of fretted wire.

The complexity that requires the previously mentioned analysis in the thin steel wires studied in this research work, with configurations and conditions close to those ones presented in the wire rope systems, has led to develop the FEM wear simulation tool described in Chapter 4. This tool aims to predict fretting wear scars with the contact conditions and geometries presented in the wire rope systems.

In this chapter it is presented a sensitive analysis of the severity of the wear scars, based on the elliptical wear scars predicted by the wear simulation methodology. For this purpose, it was analyzed the influence of both geometrical and operational parameters, firstly in the reduction of the cross section area, that is in relation with the catastrophic rupture of the wire, and secondly in the stress concentration factor produced by the wear

scars in the thin steel wire subjected to a pure traction, which is in relation with the fatigue life reduction. In this last case, a new FE model, optimized for this study has been developed. To this end the fretting wear scars obtained from the FEM wear simulation tool were transferred to this new FE model. With the aim to identify the most dangerous operational and geometrical parameters affected in thin steel wires a DOE (Design of Experiment) [140] was carried out.

From the results provided by this tool, an increase in the knowledge of the evolution of the degradation of steel wires has been presented and criteria for increasing safety and durability of these elements have been defined.

## **5.2 Methodology description**

---

### **5.2.1 Geometrical parameters of the wire rope**

In this chapter mainly, it is proposed to analyse the influence of the different geometrical parameters needed to construct a wire rope, in the severity of the produced fretting wear scars. With the aim to delimit the values of the different geometrical parameters, a 7x19 wire rope (7 strands with 19 individual wires in each one) has been analysed. In the tests carried out by Urchegui et al. [10] with this type of wire rope running over a sheave, two types of contacts were detected as the more dangerous in the fretting wear problem. The first one, named nick type B, corresponds to the point contacts appeared between the outermost wires of adjacent strands and the second one, named nick type A, corresponds to the contacts appeared between the outermost wires of strands and core, as shown in Fig. 5-1. In both cases the resulting wear scar shape is elliptical.

The wires are twisted around a central wire and subsequently around the different layers that form the strand or the core. It means that the outermost wires are twisted at a radius approximately equal to the radius of the core or the strand, and form a helix with respect to the central axis of the core or the strand. Due to the helix geometry that acquires the wire in the wire rope, three are the geometrical parameters needed to define the fretting wear contact problem: the diameter of the wire, the crossing angle between both contacting wire and the curvature of the wire.



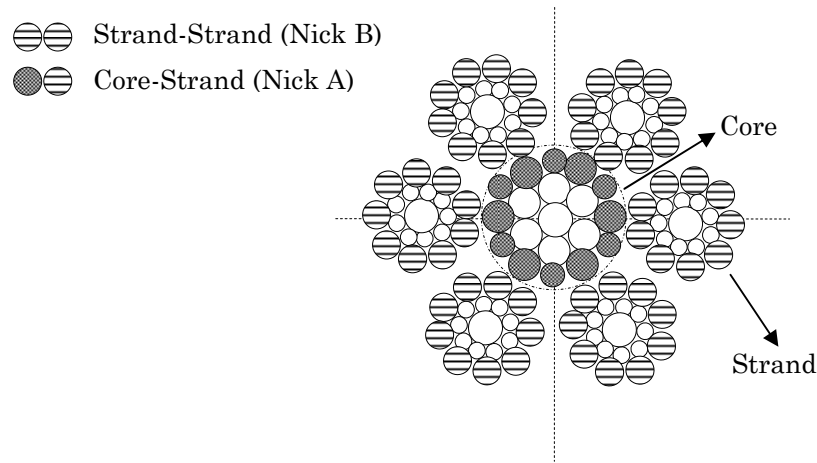


**Fig. 5-1. Description of the contacts produced between the outermost wires of strands (Nick B) and the outermost wires of strands and core (Nick A) in a 7 x 19 stranded wire rope.**

On the one hand the crossing angle between the contacting wires can be obtained calculating the twisting angle of the wire in the strand and in the core shown in (Eq. 5-1). In this equation  $\gamma, r_s, p_l$  represent the twisting angle, the theoretic radius of the strand or the core and the twist pitch length, respectively. Knowing the twisting angle of the outermost wire of the strand and the core, it can be calculated the crossing angle.

On the other hand the curvature of the wire can be calculated according to the equation proposed by Costello [141] shown in (Eq. 5-2). In this equation  $r_c, r_s, \gamma$  represent the curvature radius of the helix, the theoretic radius of the strand or the core and the twisting angle, respectively.

$$tg\gamma = \frac{2 \cdot \pi \cdot r_s}{p_l} \tag{Eq. 5-1}$$

$$r_c = \frac{2 \cdot \pi \cdot r_s}{\cos^2 \gamma} \tag{Eq. 5-2}$$

According to these equations the twisting angle and the radius of curvature of the outermost wire of the strand are 22.43° and 5.69 mm respectively and in the outermost wire of the core are 28.95° and 8.16 mm. Taking into account that in nick type B the wires crossed with opposite direction angles and in nick tick type A crossed at the same direction, in Table 5-1 are summarised the values corresponding to the geometrical parameters of the two type of contacts.

**Table 5-1. Values corresponding to the geometrical values of nick type A and nick type B contacts in 7x19 stranded wire rope.**

	Diameter [mm]	Crossing angle [°]	Curvature [mm]
Nick type A	0.32-0.42	6.52	5.69-8.16
Nick type B	0.37	44.86	5.69

### 5.2.2 Wear scar severity parameters description

As it has been mentioned previously the two parameters that describe the severity of the wear scar are: the reduction of the cross section area and the stress concentration factor. To obtain the values of these parameters, the FEM wear simulation has to be carried out according to the parameters that will be defined in section 5.2.3 and according to the optimized FE wear simulation methodology described in Chapter 4 for crossing angles arrangements. Following this methodology two FEM wear simulation has to be performed for each wear scar conditions, the first one with a bigger mesh sizes, to define approximately the wear scar dimensions, and the second one with the optimized parameters proposed in that methodology. After carrying out the optimized wear simulation, the wear scars are analysed in MATLAB® and the value of the first parameter (the reduction of the cross section area) is obtained.

The reduction of the cross section area is calculated according to the percentage of resistant area loss ( $A_{R,loss}$ ) as it is shown in (Eq. 5-3):

$$A_{R,loss} (\%) = \frac{\text{Resistant area loss}}{\pi \cdot (d/2)^2} \times 100 \quad (\text{Eq. 5-3})$$

where the Resistant area loss represents the area loss in the deepest point of the wear scar in the transversal direction to the wire axis as it is shown in Fig. 5-2, and  $d$  represents the diameter of the analyzed wire.

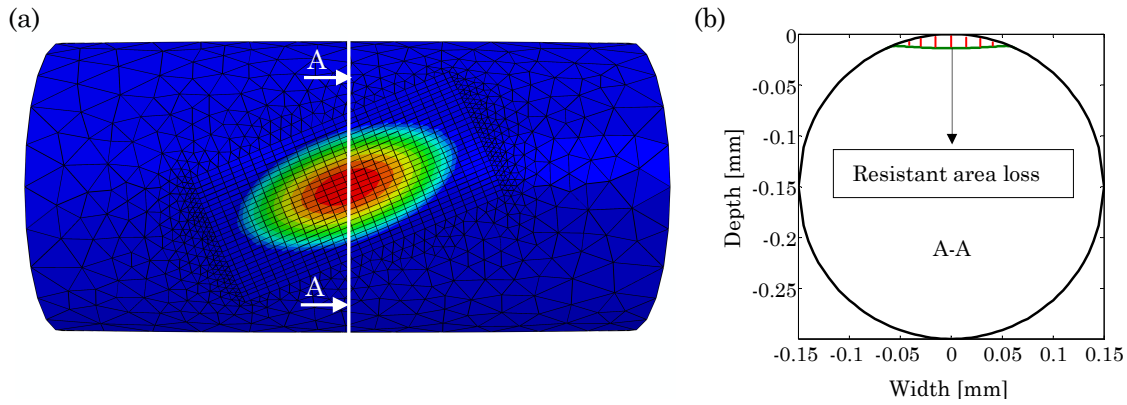


**Fig. 5-2. Wear scars of top specimen for 1 N-130  $\mu\text{m}$ -20000cycles: (a) longitudinal perspective, (b) transversal cut.**

The calculation of the second parameter analysed in this chapter (the stress concentration factor) is not a direct process that can be done from the resulting wear scar. As there is not analytical solution for an elliptical shape notch in a cylinder specimen the FE methodology was used. Walter [142] reported the good correlation obtained between the FE models and analytically solved stress concentration factors. For this a new FE model for the simulation the stress field produced by a fretting wear scar subjected to a tensile test, as shown in Fig. 5-3(a), was developed. The reason of developing another FE model for the calculation of the stress concentration factor is because in the transition zone between the brick elements and the tetrahedral elements as shown in Fig. 5-2(a), peak stresses appeared when this model is subjected to pure traction, giving erroneous results of the stress field in the wear scar. To this end it has been developed a program in MATLAB® for the transference of the wear scar, from the FE wear simulation model to the stress concentration factor FE model, based on the interpolation of the wear scar from one mesh to the other. This methodology allows the transference of all the wear scars produced by different crossing angles and wire diameters.

The meshes are carried out according to a partition methodology, in which a more refine mesh is used in the wear scar zone, to capture precisely the variation of the stress field in that critical point. The partition of the wear scar zone is created in the longitudinal direction parallel to the axis of the wire. The mesh is composed of eight nodes lineal brick elements. Moreover the meshes in the contact zone have a rectangular shape. After doing a convergence study of the mesh size it has been shown that the optimum mesh size should be in the range of  $7 \mu\text{m} \times 3 \mu\text{m} \times 3 \mu\text{m}$ . The convergence study is explained in the following paragraphs. A tensile stress of 1200 MPa was applied in the both free surfaces of the cylinder. While the longitudinal axis of the cylinder is fixed in  $x$  and  $y$  direction, the transversal axis in the middle of the cylinder is fixed in  $y$  and  $z$ , to avoid the lateral movement of the cylinder. The elastic modulus and Poisson's ratio of the cylinder were taken as 210 GPa and 0.33, respectively. The detailed FE model is shown in Fig. 5-3(a).

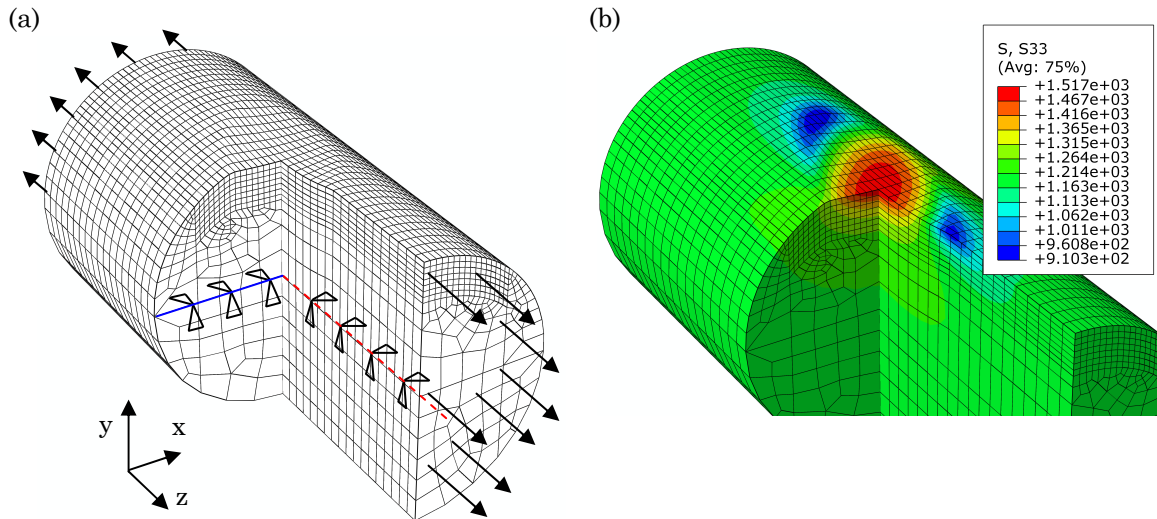


Fig. 5-3. FE model and mesh for the Stress Concentration Factor calculation: a) FEM, b) S33 stress distribution.

In order to define the optimum mesh size, the maximum stress S33, obtained in the axial direction z, was compared for different mesh sizes and two different wear scars. These wear scar represents the maximum and minimum limit of the wear depth values obtained in the DOE that will be defined in section 5.2.3. The first wear scar corresponds to a maximum wear depth of  $3.4 \mu\text{m}$  and was obtained with a crossing angle configuration of  $15^\circ$  and the second wear scar corresponds to a maximum wear depth of  $14.2 \mu\text{m}$  and was obtained with a crossing angle configuration of  $45^\circ$ . In Table 5-2 are summarized the results obtained for the different meshes. In this table the MATLAB® time represents the time needed to transfer the wear scar from the wear FE model to the stress concentration factor FE model and the Abaqus time represents the FE computational time. Two types of meshes were used; the first one corresponds to a square shape brick element and the second one to a rectangular shape brick element. The first type of mesh was used as the reference mesh size, thus very small mesh size was used. As can be seen the use of a rectangular shape meshes reduce considerable the degrees of freedom (DOF) and thus both the MATLAB® time and the FEM computational time with very small differences in the S33 value. Moreover, greater is the mesh size smaller is the computational time but greater the difference in the stress value. Nevertheless this difference is less in the case of the smallest wear depth wear scar than in the highest wear depth wear scar. Considering a difference in the stresses less than 1% in all range of the studied wear depth, it is defined as the optimum mesh size the one corresponding to  $7 \times 3 \times 3 \mu\text{m}$ . Moreover it can be seen that the time needed for all process (MATLAB® plus Abaqus) is less than 15 minutes.

Table 5-2. Values obtained in the sensibility analysis of the optimum mesh size selection .

Mesh size [ $\mu\text{m}$ ]	MATLAB® time [s]	Abaqus time [s]	DOF	S33 [MPa] (Wear Scar 1)	Diference [%]	S33 [MPa] (Wear Scar 2)	Diference [%]
3x3x3	3789	3331	952956	1241	0	1535	0
7x3x3	816	76	419004	1239	0.16	1528	0.45
14x6x6	41	13	81904	1238	0.24	1517	1.17
28x12x12	24	10	37407	1236	0.4	1502	2.14

Once the stress field in the wear scar was calculated, the stress concentration factor  $K_t$  was obtained according to the equation (Eq. 5-4):

$$K_t = \frac{\sigma_{\max}}{\sigma_{\text{nom}}} \quad (\text{Eq. 5-4})$$

where  $\sigma_{\max}$  represent the maximum stress obtained in the axial direction, and  $\sigma_{\text{nom}}$  is the stress obtained in the net section. Fig. 5-3(b) shows the stress distribution in the axial direction. The maximum stress is produced in the middle of the wear scar where it is located the deepest point. As the transversal area in this point (net section) is close to the transversal area of the wire the  $\sigma_{\text{nom}}$  is considered equal to 1200 MPa.

### 5.2.3 Experimental design

In order to predict tendencies about the severity of the wear scar in a range of geometrical and operational values, the methodology of the design of experiments (DOE) is proposed in this chapter. To this end two DOEs were carried out. While in the first DOE, both the operational and geometrical parameters were analyzed, in the second DOE only the geometrical parameters, but in a greater range of values were analyzed. Moreover in this second DOE only the main geometrical parameters identified in the first DOE were selected.

In the first DOE the main geometrical (diameter, crossing angle and radius of curvature) and operational (normal force and stroke) parameters were analyzed. For this purpose a two level factorial design has been selected. Nevertheless, as for a two full factorial design with 5 factors 32 runs are required, the fractional factorial design ( $2^{5-1}$ ) as described in [140] was selected, in order to minimize the time and cost. This type of design presents a resolution V, where no main effect or two-factor interaction is aliased with any other main effect or two factor interaction. As the three factor interactions are normally depreciable, these type of designs give good results with the lowest number of experiments.

The geometrical parameters were chosen in accordance, with those presented in wire rope systems shown previously in section 5.2.1. So that, the DOE were carried out in a range of crossing angles that goes from  $15^{\circ}$ - $45^{\circ}$ , in a range of diameter that goes from 0.3 mm to 0.5mm and in a range of curvature that goes from 2.5 mm to 10 mm. The selection of the lower limit of the crossing angle as  $15^{\circ}$  is because the wear simulation methodology has been validated in a range of crossing angles that goes from  $15^{\circ}$  to  $60^{\circ}$ . It is assumed that the tendency given by the selected range of values could be extrapolated to smaller crossing angles.

The operational parameters were selected according to a previous study carried out by Urchegui et al. [10] in which a real situation was simulated with a rope running over a sheave of 200 mm in diameter. In this work longitudinal abrasive scars between  $60\ \mu\text{m}$  and  $100\ \mu\text{m}$  were identified. These values correspond to the stroke ( $\Delta x_{\text{peak-peak}}$ ) of the contact wires. On the other hand the values of the normal load were selected according to the values of the maximum contact pressure, such as in new unused rope plastic deformations appeared in some of the contacts between the wires. Therefore in this study values of load whose maximum contact pressure is higher and smaller than the yield strength (2800 MPa) of the wire were selected. Thus a range of maximum contact pressure  $p_{\text{max}}$  that goes from 1200-3641 MPa was analysed. The specific details of the lower and upper level of the studied parameters are shown in Table 5-3.

The simulations have been carried out for 50000 number of cycles and a mean coefficient of wear in the top specimen of  $k_{\text{top}} = 2.98 \cdot 10^{-8}\ \text{mm}^3/\text{Nmm}$  and in the bottom specimen of  $k_{\text{bot}} = 1.74 \cdot 10^{-8}\ \text{mm}^3/\text{Nmm}$ . These values have been obtained by the mean of the coefficient of wear values for the different crossing angles reported in Table 4-6.

**Table 5-3. Lower limit and upper limit of the different parameters used in the fractional factorial DOE for the analysis of the percentage of resistant area and the stress concentration factor  $K_t$ .**

	Diameter [mm]	Crossing angle [°]	Curvature [mm]	Normal force [N]	Stroke [ $\mu\text{m}$ ]
<b>Lower limit</b>	0.3	15	2.5	0.125	60
<b>Upper limit</b>	0.5	45	10	0.5	100

As the easiest parameters that can be change in the design of the wire ropes are the geometrical parameters, and having identified in the first DOE, as will be discussed in section 5.3, that the diameter and the crossing angle are the two parameters that cause the most impact in the severity of the wear scars, an exhaustive analysis of the diameter and the crossing angle is carried out in this second DOE. For that a general full factorial design as described in [140] was selected. In this case each factor can have any number of levels and include all combinations of these factor levels. This DOE is carried out in order to have

a more precise tendency curve in the range of studied values. To this end four different diameters that varies from 0.3 mm to 0.6 mm in a range of crossing angles that ranges from  $15^\circ$  to  $45^\circ$  as it is shown in Table 5-4 were selected. A normal force of 1 N and a radius of curvature of 10 mm have been used. This normal force produces a range of maximum contact pressures that goes from 2145 MPa to 4266 MPa. The simulations have been carried out for 50000 number of cycles and with a mean coefficient of wear in the top specimen of  $k_{\text{top}} = 2.98 \cdot 10^{-8} \text{ mm}^3/\text{Nmm}$  and in the bottom specimen of  $k_{\text{bot}} = 1.74 \cdot 10^{-8} \text{ mm}^3/\text{Nmm}$ .

**Table 5-4. Values of the different parameters used in the general full factorial DOE for the analysis of the percentage of resistant area and the stress concentration factor  $K_t$ .**

	Lower limit			Upper limit
<b>Diameter [mm]</b>	0.3	0.4	0.5	0.6
<b>Crossing angle [°]</b>	15	30		45

### 5.3 Results and discussion

In this section the results obtained from the proposed two DOEs are presented. In both DOEs firstly it is analysed the influence of the different parameters in the percentage of resistant area loss and secondly in the stress concentration factor. Finally different guidelines for the optimization of the wire rope design are proposed.

As it has been mentioned previously, a first DOE in which the influence of both operational and geometrical parameters in the percentage of resistant area loss and in the stress concentration factor was carried out.

The main effect plots for the percentage of resistant area loss are shown in Fig. 5-4. These plots represent the means of the response variable for each level of a factor. For the analysed range of values it is seen, that the diameter, the normal force and the crossing angle respectively, are the parameters which cause more change in the reduction of the resistant area. Moreover, the factor with the greatest effect in the percentage of resistant area loss is the diameter. On the other hand the effect of the curvature in the percentage of resistant area loss could be considered depreciable.

The main effect plots indicate that on one hand the diameter and curvature have similar effects tendency, as the values moves from the low level to the high level the percentage of resistant area decrease. On the other hand the crossing angle, normal load and stroke present the opposite effect, as the values move from the low level to the high level the

percentage of resistant area increase. So in order to improve the resistant area loss, on the one hand big diameters, small crossing angles and big curvature has to be used and on the other hand small normal forces and strokes are preferable. Nevertheless according to this DOE the main parameters that should be changed in order to reduce the resistant area loss are the diameter and the normal force.

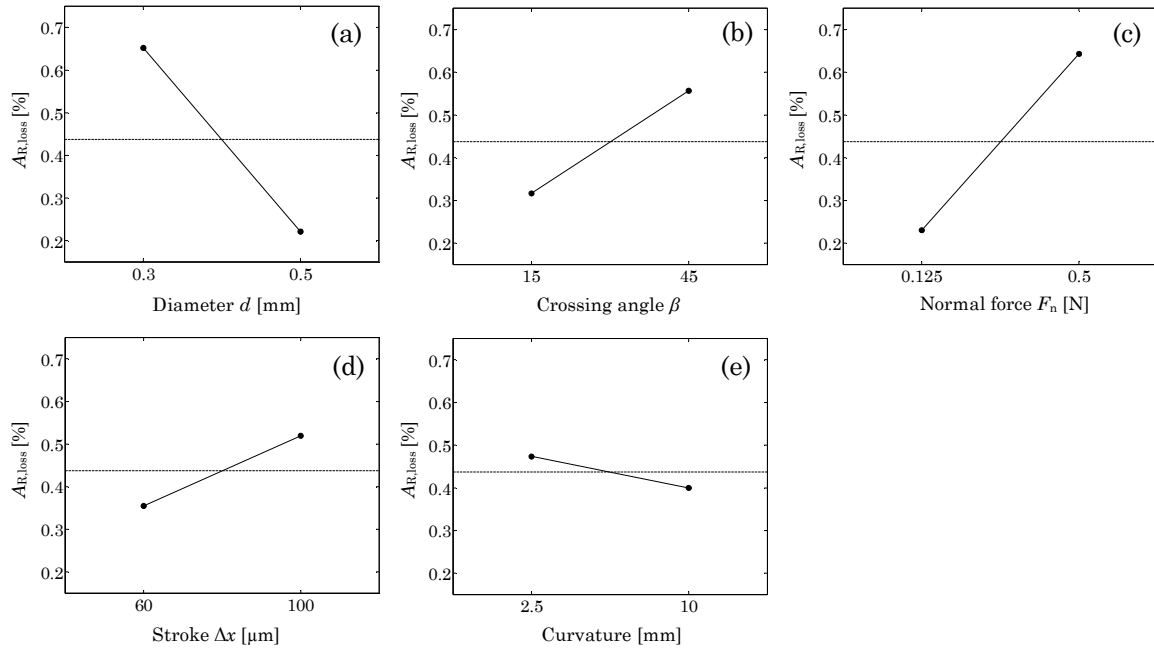


**Fig. 5-4. Main effects plot for the percentage of resistant area loss  $A_{R,loss}$  [%] under different factors: (a) diameter, (b) crossing angle, (c) normal force, (d) stroke, (e) curvature.**

The main effects plots for the stress concentration factor ( $K_t$ ) are shown in Fig. 5-5. For the analyzed range of values it is seen, that the crossing angle, the normal force and the diameter respectively, are the parameters which cause more change in the reduction of  $K_t$ . In this case the crossing angle is the factor with the greatest effect in the  $K_t$ .

The main effects plot indicates that on one hand the diameter and curvature have similar effects tendency, as the values moves from the low level to the high level the stress concentration factor decreases. On the other hand the crossing angle, normal load and stroke present the opposite effect, as the values move from the low level to the high level the stress concentration factor increases. Taking into account the geometrical parameters, small crossing angles, big diameters and big curvatures reduce the stress concentration factor, and taking into account the operational parameters small normal forces and strokes are better for the reduction of the stress concentration factor. Nevertheless according to this DOE the main parameter that should be changed in order to reduce the stress concentration factor is the crossing angle.



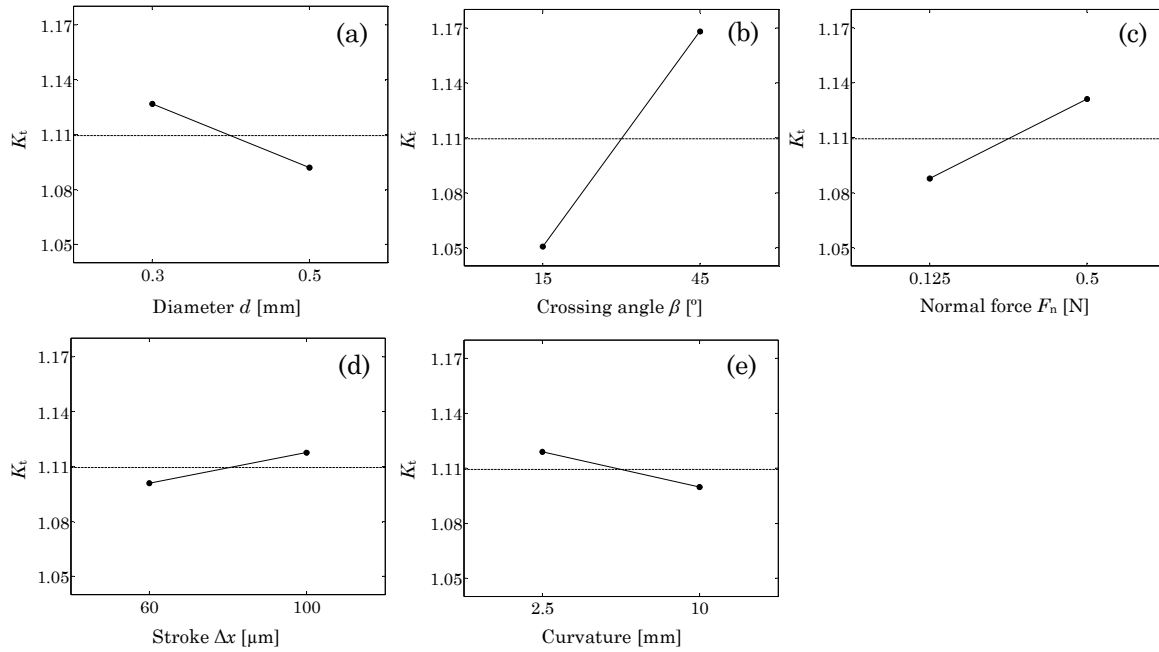


**Fig. 5-5. Main effects plot for Stress concentration factor  $K_t$  under different factors: (a) diameter, (b) crossing angle, (c) normal force, (d) stroke, (e) curvature.**

Taking into account that the geometrical parameters are the only parameters that can be changed from the design of the wire rope, and having seen in the previous DOE that the diameter of the wire and the crossing angle are the main parameters that could reduce the severity of the wear scar in the percentage of resistant area loss and in the stress concentration factor, a second DOE was carried out. This DOE is focused on analysing exhaustively the severity of the wear scar in a wider range of values, selecting more values located between the lower limit and the upper limit.

The main effects plots of the percentage of resistant area loss and the stress concentration factor for the second DOE are shown in Fig. 5-6. The same tendencies presented in the previous DOE are shown, while the diameter is the parameter that causes the greatest effect in the percentage of resistant area loss, the crossing angle is the parameter that causes the greatest effect in the stress concentration factor  $K_t$ .

Moreover it is possible to see that while the effect of the crossing angle is more or less linear in the percentage of resistant area loss and in the stress concentration factor, the diameter presents a greater influence in the range from 0.3 to 0.4 than from 0.4 to 0.6 mm, in both the percentage of resistant area loss and in the  $K_t$ . So, lower is the diameter, greater is the effect in the percentage of resistant area loss and in the  $K_t$ .

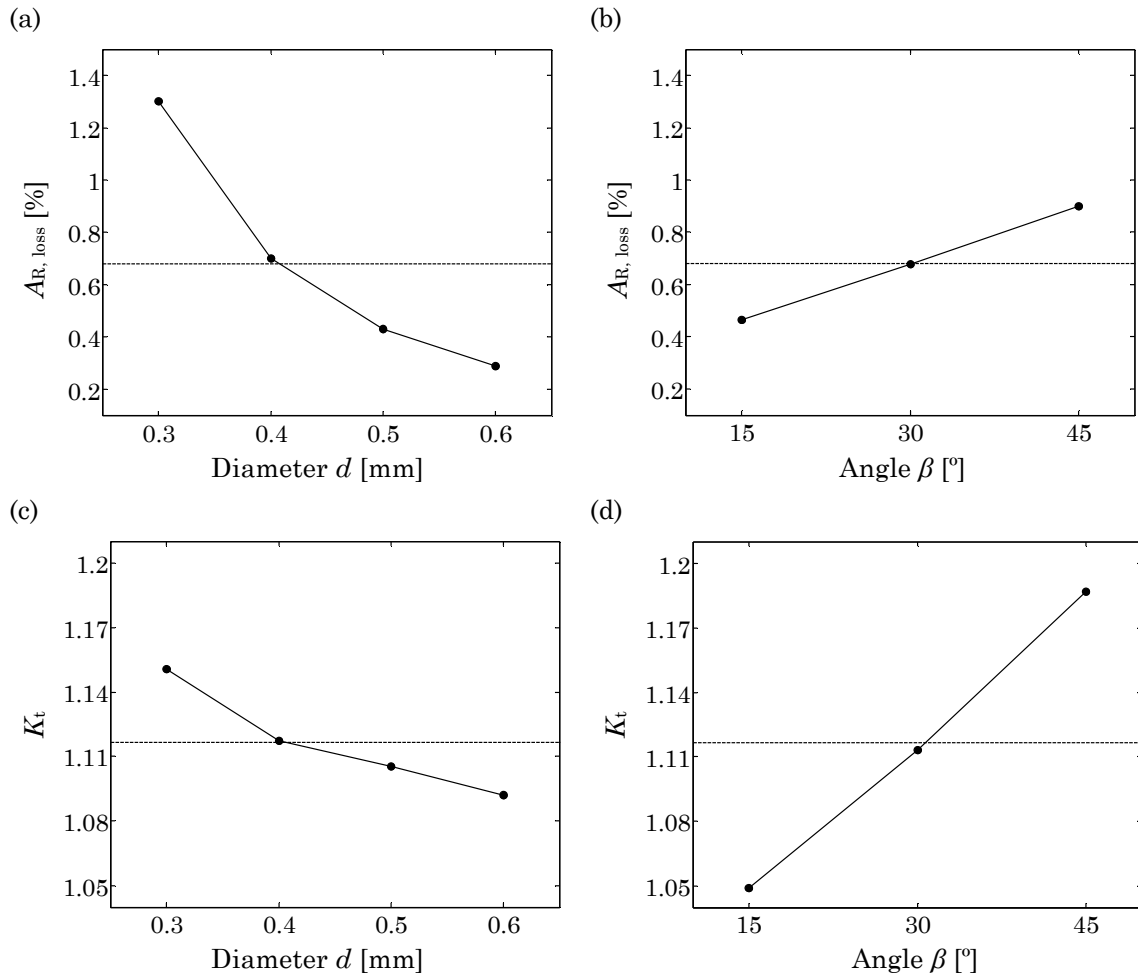


**Fig. 5-6. Main effects plot for: the percentage of resistant area loss  $A_{R, loss}$  [%] under different factors: (a) diameter, (b) crossing angle; and for the stress concentration factor  $K_t$  under different factors: (c) diameter, (d) crossing angle.**

Taking into account the tendencies presented in the mean effects graphics, the coefficients of the quadratic equations that describe the percentage of resistant area loss (Eq. 5-5) and the  $K_t$  (Eq. 5-6), according to the crossing angle and the diameter of the wire were obtained. In both equations is possible to see that while the diameter has the effect of the quadratic term, the crossing angle mainly has the influence of the linear term. This equations could be used to evaluate quantitatively the effect of the geometrical parameters in the severity of the wear scar.

$$A_{R, loss} (\%) = 2.93 + 0.047\beta - 11.45d + 2.257e^{-5}\beta^2 + 11.558d^2 - 0.075\beta d \quad (\text{Eq. 5-5})$$

$$K_t = 1.06 + 0.007\beta - 0.378d + 2.17e^{-5}\beta^2 + 0.501d^2 - 0.0086\beta d \quad (\text{Eq. 5-6})$$

The interaction plots for the percentage of resistant area loss and the  $K_t$  are shown in Fig. 5-7. The different plots show the good correlation obtained by the equations presented previously and the FEM data. While for both parameters the influence of the diameter (Fig. 5-7(a) and (c)) is described by quadratic equations, the influence of crossing angle (Fig. 5-7(b) and (d)) is described by linear equations. Although there is no interaction between the selected parameters, the increase in the percentage of resistant area and in the  $K_t$  is greater when the diameter is small than when the diameter is big.

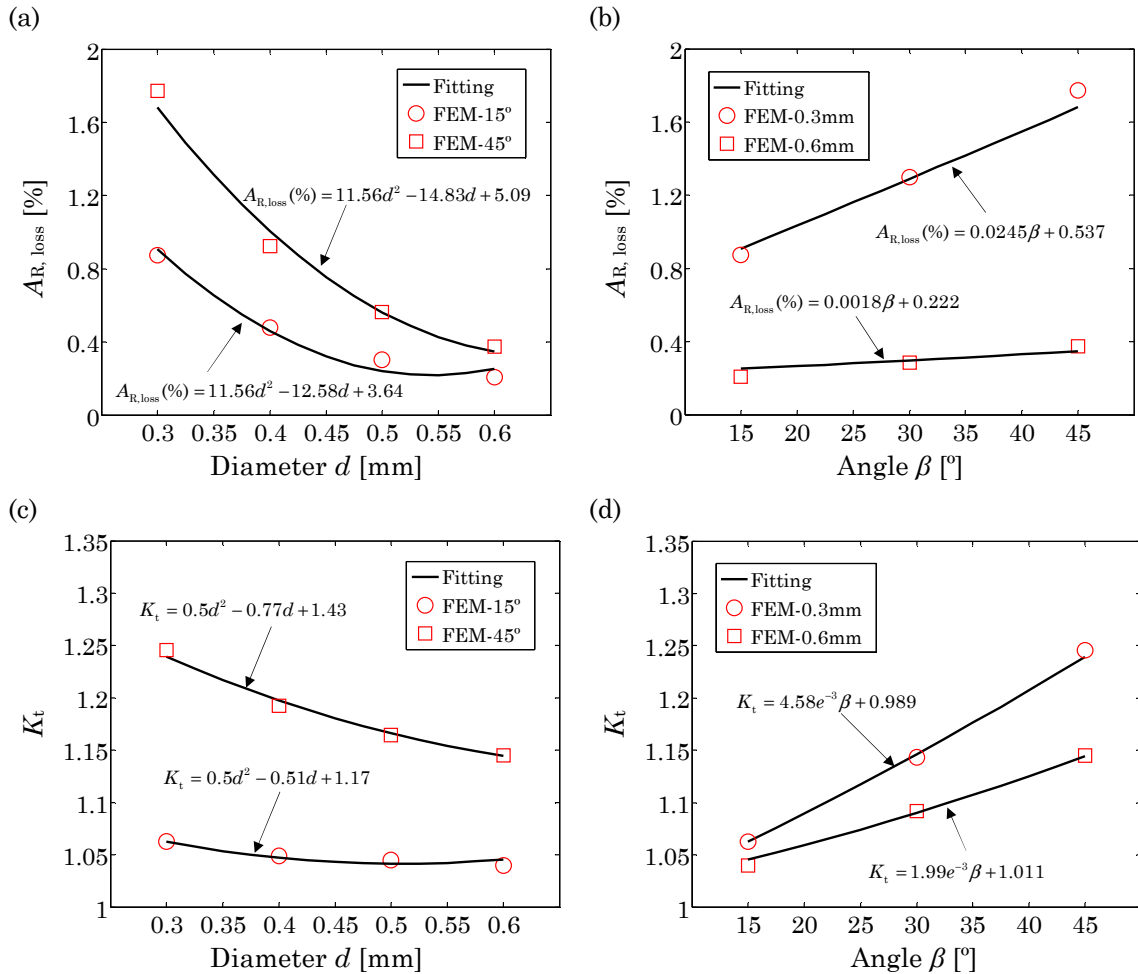


**Fig. 5-7. Interaction plots for: the percentage of resistant area loss  $A_{R,loss}$ [%] under different factors: (a) diameter, (b) crossing angle; and for the stress concentration factor  $K_t$  under different factors: (c) diameter, (d) crossing angle**

Taking into account the sensibility analysis carried out previously, the diameter, the crossing angle and the normal load are the main parameters that increase the severity of the wear scar. Nevertheless as the load is difficult to modify, because it is given by both operational and geometrical parameters of the system, this work has been focused in the two main geometrical variables, the diameter and the crossing angle.

On the one hand, if the damage mode presented in the thin steel wire is the catastrophic rupture of the wire as a consequence of the excessive reduction of the cross section area, the diameter is the main parameter that has to be modified. The tendency of the percentage of resistant area loss can be explained by a quadratic equation in which the percentage of resistant area loss decreases when the diameter of the wire increases. Due to this quadratic tendency the decrease in the percentage of resistant area loss is greater when the increase is produced in the smaller range of diameters than in the higher range of diameters. So that, when this type of damage is produced in the smallest diameter wires, small increase of the wire diameter can reduce significantly the percentage of cross section area loss increasing the life of the wire. Furthermore this tendency is greater with higher crossing angles than with smaller crossing angles.

On the other hand, if the damage mode presented in the thin steel wire is the reduction of the fatigue life of this component and the rupture of the wire due to the stress concentration produced by the wear scar, the crossing angle is the main parameter that has to be modified. In this case, the tendency of the  $K_t$  can be explained by a linear equation, in which the  $K_t$  decreases when the crossing angle decreases. Moreover the decrease in the  $K_t$  is greater when the diameter is small than when the diameter is high. So that, when this type of damage is produced in the smallest diameter wires, a small change in the crossing angle can reduce considerably the  $K_t$ .

#### 5.4 Conclusions

---

In this chapter the design of experiments (DOE) methodology has been used in order to analyse the severity of the wear scars obtained by the wear simulation tool developed in Chapter 4 under different operational and geometrical parameters of the wire rope systems.

The analysis of the severity has been focused on two aspects: the percentage of resistant area loss which is in relation with the catastrophic rupture of the wire and the stress concentration factor which is in relation with the fatigue life reduction of this component. While the percentage of resistant area loss can be obtained directly from the simulated wear scar, the stress concentration factor is obtained from a new FE model optimized for the simulation the stress field produced by a fretting wear scar subjected to a tensile test. Therefore, a program that transfer the wear scar from the wear FE model to the stress concentration model has been carried out.

The results obtained in the DOE show that the diameter, the crossing angle and the load are the main parameters that should be taking into account to reduce the severity of the

wear scar. While the diameter is presented as the main geometrical parameter that affects in the percentage of resistant area loss the crossing angle is the main geometrical parameter that affect in the stress concentration factor. Therefore, increasing the diameter of the wire or reducing the crossing angle can be improved the live of this components.

Finally two equations that describe quantitatively the percentage of resistant area loss and the stress concentration factor for the diameter and the crossing angle have been obtained. While the effect of the diameter in both severity parameters is described by a quadratic equation, the influence of the crossing angle is described by a linear equation. From these equations it was obtained that the decrease in the  $K_t$  or in the percentage of resistant area loss is greater when the diameter is small than when the diameter is big.

In order to reduce the diameter of the sheaves, one of the solutions that are using now a day consist of reducing the diameter of the wire rope, thus using smaller diameter wires. So that, when the previously mentioned damages are produced in the smallest diameter wires, a small change in the crossing angle can reduce considerably the  $K_t$  and small change in the diameter could reduce considerably the percentage of resistant area loss.



---

CHAPTER VI

# FEM-BASED FATIGUE LIFE ANALYSIS DUE TO FRETTING WEAR

---

## 6.1 Introduction

---

In Chapter 5 was presented the study of two parameters related with the severity of the wear scars. The first parameter was related with the catastrophic rupture of the wire due to the considerable reduction of the resistant area produced by the wear. The second parameter was related with the fatigue life reduction due to the stress concentration factor produced by the wear scar. Nevertheless, it was not reported the influence of the fretting frictionally induced fatigue cracks initiation in the rupture of the thin steel wires. This damage mechanism leads to reduce considerably the fatigue life of these components.

In the literature different studies about the fatigue life prediction of steel wires have been reported. LLorca and Sánchez-Gálvez [143] presented a model to determine the fatigue limit and the fatigue life to explain the results obtained experimentally in 7 mm diameter wires. This study takes into account that the fatigue fracture initiates in all cases at a surface flaw and neglect the crack initiation. Beretta and Boniardi [144] proposed a suitable method for fatigue strength prediction and quality control of wires which consist of: tensile tests for estimating fatigue threshold of long cracks ( $\Delta K_{th,lc}$ ), cyclic tensile tests for evaluating the theoretical fatigue limit, determination of the extreme value of sampling and fatigue strength prediction using El-Haddad model. In this study wires of 1 and 0.9 mm diameter were used. Petit et al. [145] presented a study of fatigue crack propagation in 0.95 mm steel wires. Lambrighs et al. [146] showed the influence of the inclusion parameters, such as the inclusion size, location, composition and geometry on the fatigue properties in a 0.175 mm and 0.3 mm diameter wires. Navaei et al. [147] used three damage models to predict the fatigue life of 1 mm diameter wires: linear damage rule (LDR), damage curve approach (DCA) and Double linear damage rule (DLDR). After comparing with experimental results the DCA approach is presented as the best method for patented steel

wires. Brighenti et al. [148] analyzed the effect of the residual stresses on fatigue behaviour of a notched wire with surface crack subjected to alternating tension, showing that the crack propagation phenomenon is accelerated by increasing residual stresses.

These studies mainly show that the fatigue crack initiates from inner or surface defects presented in the steel wires. Nevertheless in the case of wire rope systems, as has been mentioned previously, the cracks initiate in the wear scars, as a consequence of the fretting induced multiaxial stresses. Recently, in order to analyse this phenomenon, Wang et al. [149] have proposed a new fretting fatigue test rig for the analysis of this behaviour in 1 mm diameter steel wires. All the tests were performed under mixed fretting regime conditions. It was concluded that an increase of displacement amplitude at each cyclic strain level increases the tangential force and relative slip range at the stabilized stage, accelerating the fretting damage of the contact surface. Nevertheless it has not been proposed any methodology for predicting fretting cracks in steel wires being one of the key factors in this analysis the material removal.

In the recent years many researchers have introduced the multiaxial fatigue models to establish life predictions in fretting problems as shown in Chapter 2. Nevertheless the analysis with FEM of the combined fatigue and material removal due to fretting only has been studied by few authors. Sum et al. [58] developed first a finite element based implementation of the critical plane SWT fatigue life method. It was shown that this methodology capture the well known contact size effect of the cylinder plane configuration shown previously by Araujo and Nowel [56]. Following with this methodology Madge et al. [61] proposed then, a finite element based method to predict and characterise the role of fretting wear on fretting fatigue for a rounded punch-on-flat Ti-6Al-4v under partial slip and gross sliding conditions. This model combined the finite element wear simulation model with the critical plane SWT fatigue model. They concluded that the prediction of fretting wear was a critical aspect for prediction fretting fatigue, which can not be predicted by models that do not include the effects of material removal. Recently Zhang et al. [74] used a similar model in a round of flat and round punch on flat configuration for the wear evolution and crack nucleation predictions. It was concluded that if the modelling of wear was not taken into account the fatigue damage prediction could be under-conservative in the partial slip regime (PSR) and over conservative in the gross slip regime (GSR).

In this chapter it is proposed to study the fretting wear caused fatigue life reduction of the wires, using the frictionally induced multiaxial contact stresses obtained from FEM wear model developed in Chapter 4 for the 90° crossed cylinder model. To this end the multiaxial critical plane SWT approach with a new damage accumulation methodology for the adaptive mesh simulation, based on the cyclic material removal, was developed for 3D crossed cylinders problems. The results obtained from this tool have been compared with



the experimental data obtained from the fretting wear tests of thin steel wires, giving in the end guidelines for the construction a more robust tool in future works.

## 6.2 Experimental details

### 6.2.1 Introduction

The fretting wear tests proposed in this section include higher values of contact pressures than those ones reported in Chapter 3 in order to identified the crack initiation conditions. An extended description of the experimental testing has been presented in Chapter 3. In this section it is briefly outlined the test conditions that were selected for the analysis of the subsurface stresses and the crack initiation life prediction using the FE damage approach. Moreover it is included the tensile properties of the material used in section 6.3.3 to obtain the fatigue constants from the different methods reported in the literature.

### 6.2.2 Material

For the tests, wires with a diameter of 0.45 mm, were used. They are cold-drawn from eutectoid carbon steel with 0.8% C with a hardness of  $659\pm 81$  HV0.05. The tensile properties obtained from the measured stress-strain curve shown in Fig. 6-1 were an ultimate tensile strength ( $\sigma_u$ ) of 3000 MPa and an offset 0.2% yield strength ( $\sigma_y$ ) of 2688 MPa. The surface average roughness ( $R_a$ ) of these wires along its axis was 0.35 and 0.70  $\mu\text{m}$  in perpendicular direction. These values were obtained from the measurements carried out at an unworn wire using a confocal imaging profiler (Pl $\mu$ , Sensofar). The tensile properties and the Vickers hardness are summarized in Table 6-1.

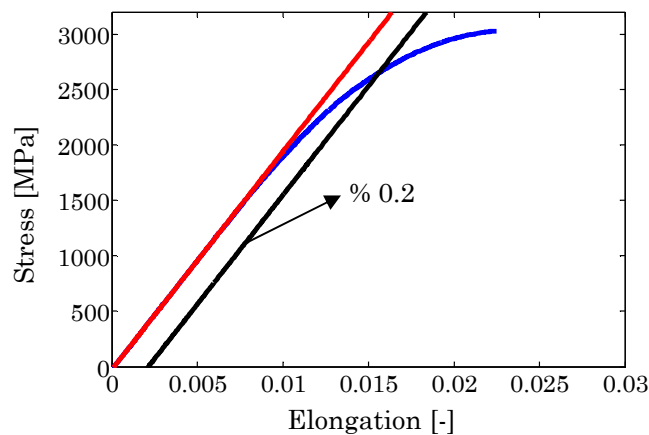


Fig. 6-1. Experimentally obtained engineering stress- strain curve for 0.45 mm diameter wire.

**Table 6-1. Mechanical properties of the 0.45 mm diameter wire.**

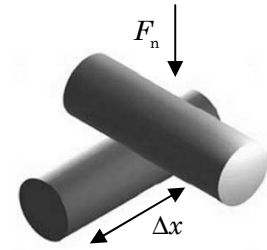
	$E$ [GPa]	$\sigma_u$ [MPa]	$\sigma_y$ [MPa]	$RA$ [%]	HV 0.05
Wire	200	3000	2688	58	470±30

### 6.2.3 Tribological testing

The tests were carried out with 90° crossing angle configuration in a range of average contact pressures that goes from 2470 MPa to 3933 MPa, two strokes 65  $\mu\text{m}$  and 130  $\mu\text{m}$  in a range of cycles that ranges from 20000 to 200000. The specific details of these tests are shown in Table 6-2. After the tests the contact surfaces were analyzed by optical microscopy in order to find crack and no crack conditions. Only fretting cracks were found in the bottom specimen, so the FE analysis will be focused on this specimen.

**Table 6-2. Fretting test conditions for the study of crack initiation process in 90° crossed cylinders steel wires.**

Parameter	Symbol	Value	Trybosystem
Normal load (N)	$F_n$	0.5; 1; 2; 3; 4	
Mean contact pressure (MPa)	$p_m$	2470; 3100; 3560; 3933	
Maximum contact pressure (MPa)	$p_{max}$	3690; 4650; 5400; 5900	
Stroke ( $\mu\text{m}$ )	$\Delta x$	65 $\pm$ 5 (2 N, 3 N, 4 N) 130 $\pm$ 5 (1 N, 2 N)	
Frequency (Hz)	$f_r$	10	
Number of cycles ( $10^3$ )	$n$	20; 50; 100; 200	
Lubricant		None	
Temperature ( $^{\circ}\text{C}$ )	$T$	25 $\pm$ 1	
Relative humidity (%)	RH	50 $\pm$ 1	



## 6.3 FEM Methodology description

### 6.3.1 FEM model

The FE model used in this study is the same that has been validated in Chapter 4, for the simulation fretting wear in thin steel wires under different loads conditions. For better understanding it is briefly described the model. The model consists of two cylinders with a diameter of 0.45mm contacting together at 90° crossing angle as shown in Fig. 6-2. Moreover the curvature radius that acquires the wire in the fixation support (10 mm) is

included. The load and the boundary conditions are applied in the free surfaces of the model through a surface-based coupling, which couples the motion of all free surfaces to the motion of a reference node. Moreover a kinematic coupling is used, so as the rigid body motion is defined by the reference node. It allows in the upper wire, where a normal force is applied in the reference point, only the vertical movement and in the bottom wire, where an alternative displacement condition is imposed, only the horizontal movement. This is because the wire maintains the rigid body movement of the holder in the testing machine. The elastic isotropic material model was specified in both cylinders, in which a standard values for steel (Young's modulus of 210 GPa and Poisson's ratio of 0.33) have been used.

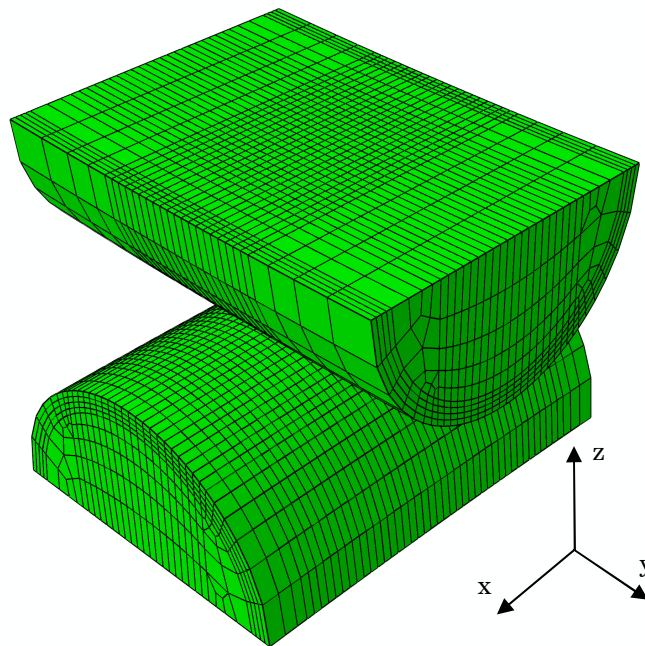


**Fig. 6-2.** FE model and mesh details of the 90° crossed cylinder fretting wear test.

The meshes are carried out according to a partition methodology, in which a more refine mesh is used in the contact zone, to capture precisely the variation of contact pressures and geometry. The mesh is composed of square shape eight nodes lineal brick elements. The size of the meshes in the contact zone is defined following the optimized mesh criterion to reduce the computational time proposed for fretting wear scars modelling in Chapter 4. Taking into account that, an optimum mesh should be in the range from 3% to 4% of the final longitudinal wear width and that the dimensions of the wear scars analysed in this study are in the range from 250  $\mu\text{m}$  to 310  $\mu\text{m}$ , a 10  $\mu\text{m}$  x 10  $\mu\text{m}$  x 7.5  $\mu\text{m}$  mesh size which corresponds to the 4% of the smallest wear scar dimension is chosen. As reported in Chapter 4 smaller size meshes only increases the computational time without any

improvement in the final result and greater mesh size only gives a poor discretization of the wear scar.

The contact surface interaction between both cylinders is defined via the finite sliding contact pair algorithm, which uses the master–slave algorithm to enforce the contact constraints. In this study the top surface is chosen as slave surface and the bottom one as master. The Lagrange multiplier contact algorithm was used to ensure the exact stick constrain when the shear stress is less than the critical value according to the Coulomb friction law. A coefficient of friction (COF) of 0.7 is chosen according to the experimental tests carried out in thin steel wires. In order to implement the wear via UMESHMOTION subroutine as described in section 4.3.2.3 the specific wear coefficients obtained for each specimen and test conditions, which are shown in table 3, have been used. It has to be pointed out that the wear simulations presented in this study will be carried out till 50000 number of cycles.

**Table 6-3. Coefficients of wear obtained from fretting wear tests under different loads-stroke conditions.**

	Coefficient of wear ( $10^{-8}\text{mm}^3/\text{Nmm}$ ) Top-Bottom		Coefficient of wear ( $10^{-8}\text{mm}^3/\text{Nmm}$ ) Top-Bottom	
2 N-65 $\mu\text{m}$ -50000 cycles	2.11-1.57	1N-130 $\mu\text{m}$ -50000 cycles	2.32-2.34	
3N-65 $\mu\text{m}$ -50000 cycles	2.10-1.91	2N-130 $\mu\text{m}$ -50000 cycles	2.32-2.34	
4N-65 $\mu\text{m}$ -50000 cycles	2.32-2.34			

### 6.3.2 Damage modelling

Fretting wear in thin steel wires leads to produce a frictionally induced multiaxial contact stress distribution, which is in constant changing due to the wear induced evolution of the subsurface stress. This condition with the combination of high loads and strokes leads to produce fatigue cracks in the contact surface. With the purpose to study the multiaxial fatigue phenomenon presented in thin steel wires, the critical plane Smith-Watson-Topper (SWT) multiaxial fatigue criterion has been used. This criterion has been applied satisfactorily by many researchers for the prediction the crack nucleation life and location in fretting problems, both in fretting fatigue loading conditions [53], [56], [58], [64] and in fretting wear loading conditions [69], [72], [74]. The SWT parameter predicts that the crack initiation and growth occurs on a certain plain, where the normal stress and strain in that plane is maximum. The parameter is shown in (Eq. 6-1), where  $\sigma_{\max}$  is the maximum normal stress in the critical plane and  $\Delta\epsilon_e$  is the normal strain amplitude in the same plane,  $E$  is the Young modulus,  $\sigma_f'$  and  $b$  are the Basquin's strength coefficients

corresponding to the high cycle fatigue (HCF),  $\epsilon'_f$  and  $c$  are the Coffin–Manson fatigue ductile coefficients corresponding to low cycle fatigue (LCF) and  $N_i$  represents the number of cycles needed for the crack initiation.

$$SWT = \sigma_{\max} \cdot \Delta\epsilon_a = \frac{\sigma_f'^2}{E} (2N_i)^{2b} + \sigma_f' \epsilon_f' (2N_i)^{b+c} \quad (\text{Eq. 6-1})$$

The implementation of this method in the FE model presented previously has been carried out according to the methodology proposed by Sum et al. [58] and Das and Sivakumar [150] for 3D problems. This methodology consists of the three-dimensional transformation (Mohr's circle) of the stress and strains of each element centroid according to (Eq. 6-2)-(Eq. 6-6) at intervals of  $5^\circ$  over  $180^\circ$ , analyzing all the planes that can be found in a semi-sphere. In these equations  $\sigma_\theta$  and  $\epsilon_\theta$  are the stress and strains normal to the plain formed by the angles  $\theta_v$  and  $\theta_h$  as described in detail in [58]. So in each centroid 1296 planes for each element and for each increment that form one fretting cycle are recorded. From this data the maximum normal stress  $\sigma_{\max}$  and the normal strain amplitude  $\Delta\epsilon_a$  are recorded in each plane of each element, where  $\Delta\epsilon_a$  represents the difference between the maximum and the minimum value of strain normal to the candidate plane over the entire fretting cycle. Finally the SWT values are obtained for each candidate plate and each element, which are then used to obtain the maximum SWT value in the critical plane of each element. With the maximum SWT value and solving (Eq. 6-1), the numbers of cycles to failure for each fretting cycle are obtained.

$$\sigma_\theta = \sigma_{11}n_x^2 + \sigma_{22}n_y^2 + \sigma_{33}n_z^2 + 2\tau_{12}n_xn_y + 2\tau_{23}n_y n_z + 2\tau_{13}n_x n_z \quad (\text{Eq. 6-2})$$

$$\epsilon_\theta = \epsilon_{11}n_x^2 + \epsilon_{22}n_y^2 + \epsilon_{33}n_z^2 + \gamma_{12}n_xn_y + \gamma_{23}n_y n_z + \gamma_{13}n_x n_z \quad (\text{Eq. 6-3})$$

$$n_x = -\sin\theta_v \sin\theta_h \quad (\text{Eq. 6-4})$$

$$n_y = \cos\theta_h \quad (\text{Eq. 6-5})$$

$$n_z = \sin\theta_h \cos\theta_v \quad (\text{Eq. 6-6})$$

Nevertheless, due to the material removal effect, the stresses and strain are changing from cycle to cycle. To capture this phenomenon a fatigue accumulation damage rule was used, the Miner-Palmgren linear accumulation damage rule. Thus the crack nucleation is

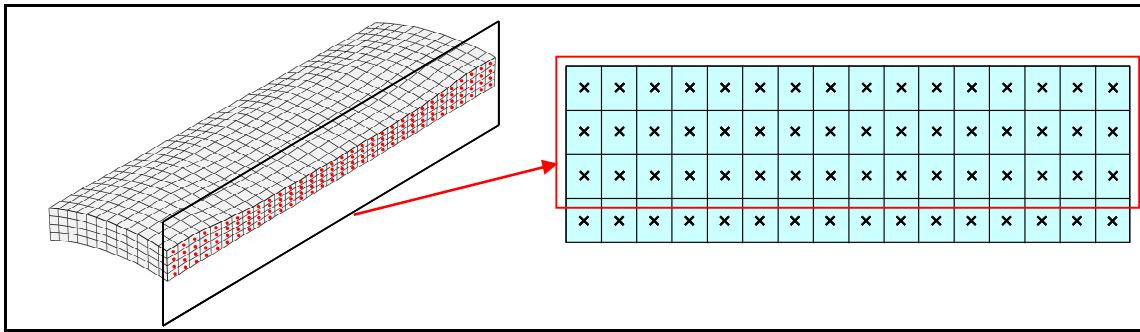
occurred when the total accumulated damage  $w$  in a material point reaches 1. In this study, as the wear simulation problem is computationally costly, a cycle jump technique was used for the wear modelling optimization. Therefore, the damage accumulation model is expressed as (Eq. 6-7), where  $N_{i,l}$  is the predicted SWT critical plane number of cycles for failure in the FE fretting wear simulation cycle  $l$ ,  $n$  is the total experimental number of fretting cycles and  $\Delta n$  is the cycle jump value.

$$w = \sum_{l=1}^{\frac{n}{\Delta n}} \frac{(l \cdot \Delta n)}{N_{i,l}} \quad (\text{Eq. 6-7})$$

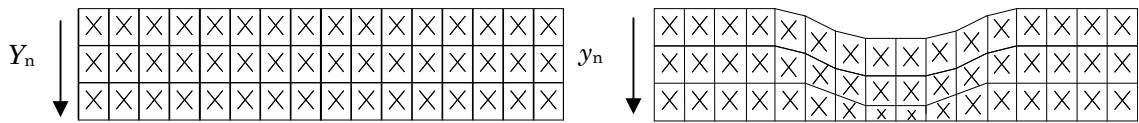
On the other hand, as a consequence of the adaptive meshing used in the FE wear simulation approach to update the mesh due to the material removal, the damage can not be accumulated in the same centroidal point from cycle to cycle. The reason is because the centroidal position of each element is changing from cycle to cycle, so the damage accumulated in the centroid position of a previous wear cycle could not be the same in the new centroidal position of the current cycle. The previously accumulated damage in this point should be less, such as the damage goes decreasing from the surface to the inner of the material. So the effect of material removal in the damage eradication has to be considered.

To solve this problem Madge et al. [61] proposed to create a material point mesh (MPM) as the global reference model for damage accumulation. In this method the nodes of the MPM have fixed coordinates through the analysis, so the cyclic damage calculated at the centroid of each element was linearly interpolated back to the MPM for accumulation, and the nodes corresponding to removed material don't accumulate any fatigue damage.

In this study, due to the high amount of wear produced by the fretted thin steel wires a new damage accumulation model based in the previous and in the current location position of the element centroid due to wear has been developed. This approach leads to update the damage in the new centroidal position after the FE wear simulation cycle. The mesh used for the wear modelling in the adaptive meshing framework is shown in Fig. 6-3. Taking into account that the crack initiation is produced close to the surface layers and due to the great amount of data that is collected in a 3D problem, only the third first layers of the centroid points will be used in this new methodology.



(a)



(b)

**Fig. 6-3. FE mesh in the adaptative meshing framework and each centroid points: (a) 3D FE mesh with a cut of one of the longitudinal plans, (b) FE mesh with the centroid points before and after the wear process.**

A flowchart which summarises the proposed process for determining the accumulation of damage due to the wear removal is shown in Fig. 6-4. So the following methodology for the application the accumulative damage rule due to wear is outlined here:

1. Cyclic damage  $D_n$  due to the first fretting cycle is calculated at the centroid point location  $Y_n$  of each element in the first three layers (Fig. 6-3(b) left).
2. As a consequence of the material removal, the damage obtained in the centroidal points  $Y_n$  of the first cycle will not be maintained in the new centroidal position location  $y_n$  reached after the second cycle due to wear (Fig. 6-3(b) right): so two linear equations as shown in (Eq. 6-8) and (Eq. 6-9), which represent the damage evolution between the first and the second layer and the second and the third layer, are constructed. The graphic representation is shown in Fig. 6-5(a).

$$D_1(Y) = \frac{D_2 - D_1}{Y_2 - Y_1}(Y - Y_1) + D_1 \tag{Eq. 6-8}$$

$$D_2(Y) = \frac{D_3 - D_2}{Y_3 - Y_2}(Y - Y_2) + D_2 \tag{Eq. 6-9}$$

3. Cyclic damage  $d_n$  due to the second fretting cycle is calculated at the new centroid point location  $y_n$  of each element in the first three layers as it is shown in Fig. 6-5(b).

4. The damage of the first fretting cycle is interpolated back to the new position at the centroidal point's location  $y_n$  of the second cycle, as presented in (Eq. 6-10)-(Eq. 6-12) and in Fig. 6-5(c).

$$d'_1 = \frac{D2 - D1}{Y2 - Y1}(y_1 - Y1) + D1 \quad (\text{Eq. 6-10})$$

$$d'_2 = \frac{D3 - D2}{Y3 - Y2}(y_2 - Y2) + D2 \quad (\text{Eq. 6-11})$$

$$d'_3 = \frac{D3 - D2}{Y3 - Y2}(y_3 - Y2) + D2 \quad (\text{Eq. 6-12})$$

5. In the new centroid position (Eq. 6-13) of each element, as it is shown in Fig. 6-5(d), the interpolated damage  $d'_n$  due to the first cycle is accumulated with the damage of the second cycle  $d_n$  (Eq. 6-14).

$$Y_n = y_n \quad (\text{Eq. 6-13})$$

$$D_n = d_n + d'_n \quad (\text{Eq. 6-14})$$

6. Two new linear equations (Eq. 6-8) and (Eq. 6-9) are constructed for the new centroid position due to wear (Eq. 6-13), and the new damage values (Eq. 6-14), as represented in Fig. 6-5(d).

7. This process is repeated as many times as number of cycles needed to reach the damage failure, when (Eq. 6-14) reaches 1.

Summarising;  $D_n$  = Damage of the first cycle & Acumulated damage in the current cycle;  
 $d'_n$  = Interpolated damage from the previous cycle to the current cycle;  $d_n$  = Damage of the current cycle;  $Y_n$  = y coordinate of the first cycle & y coordinate of the Acumulated damage;  
 $y_n$  = y coordinate of the current cycle;  $n$  = layer number.



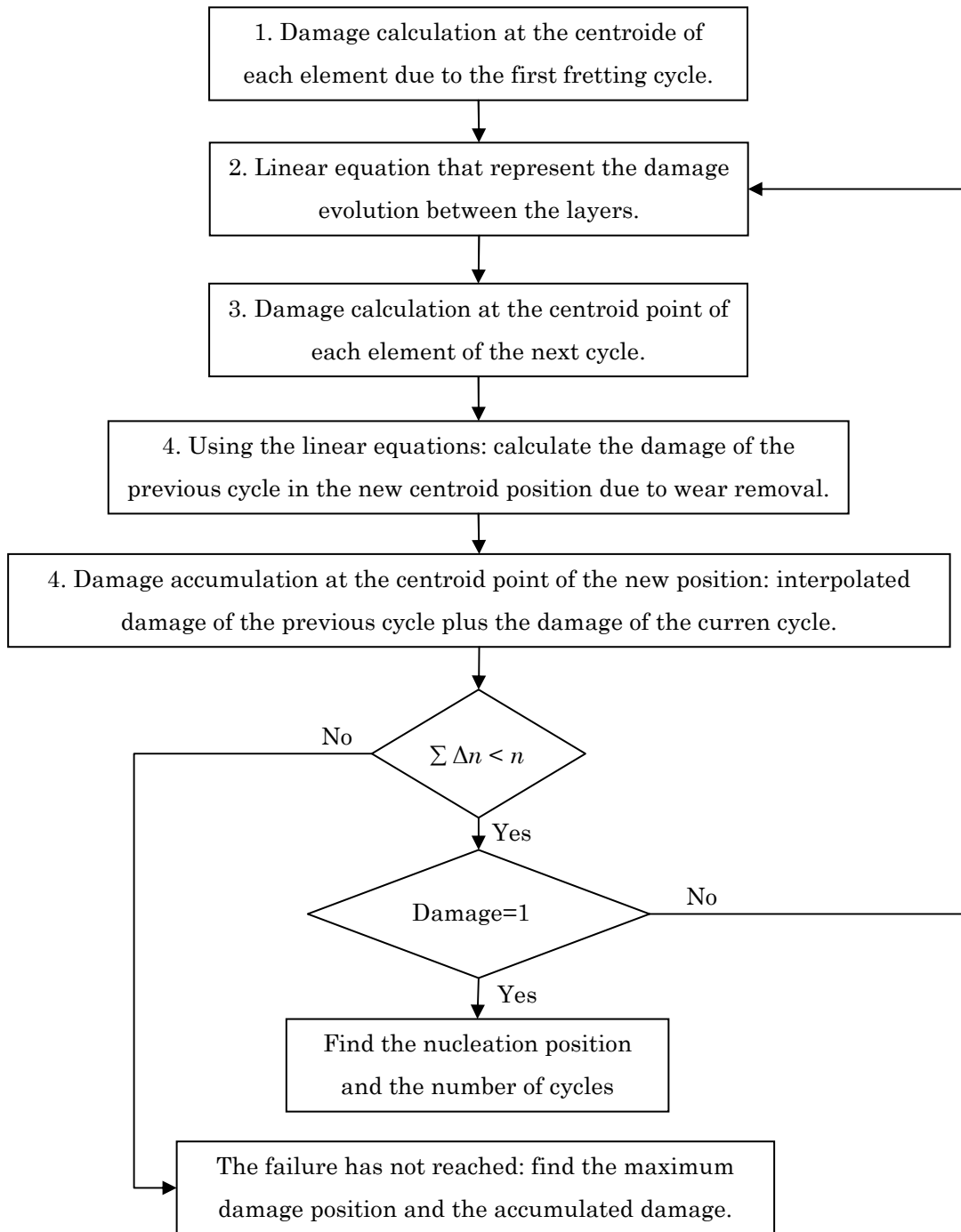
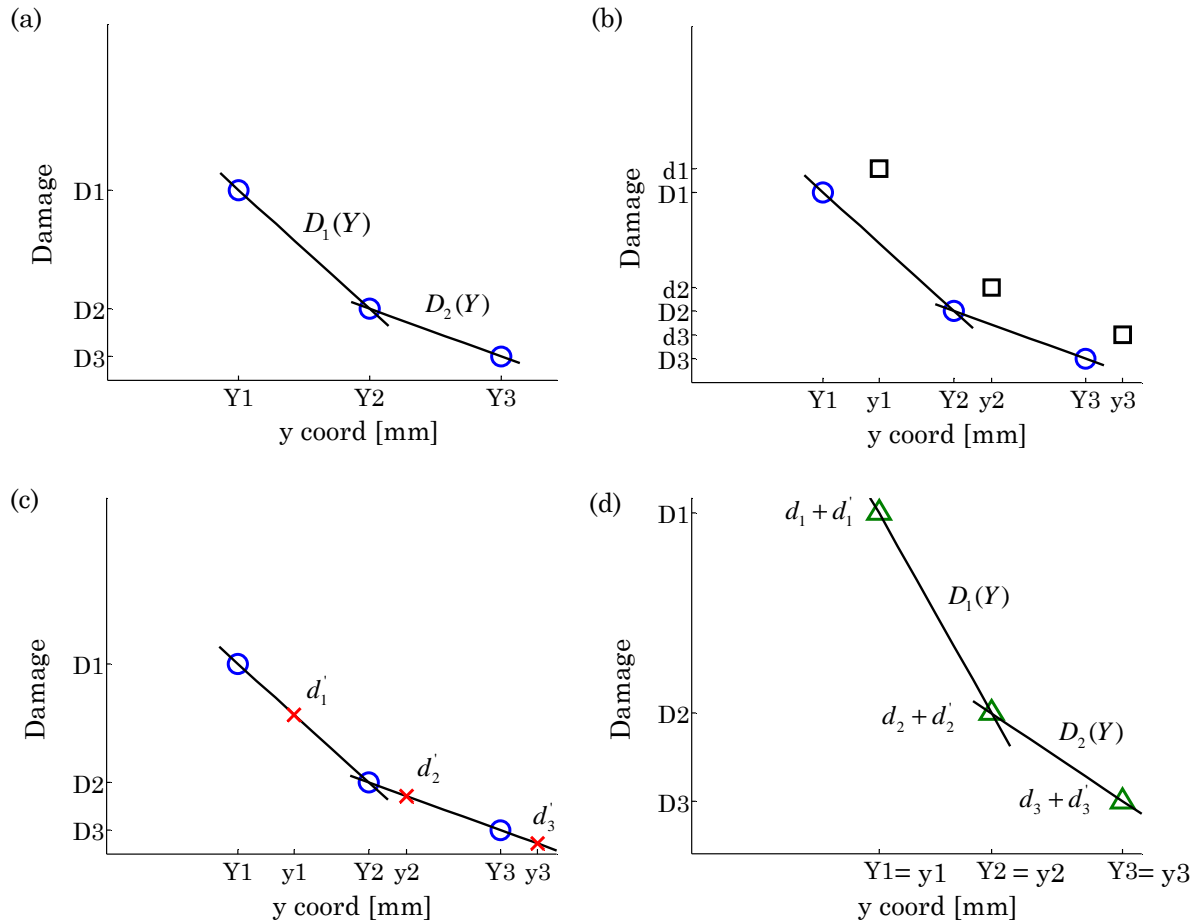


Fig. 6-4. Flow chart of the accumulative damage model due to the effect of the material removal.



**Fig. 6-5. Damage accumulation process: (a) Damage of the first cycle (circle) in the first three layers and the two linear equations which represent the evolution of the damage between the layers, (b) damage in the second FE cycle due to wear (square), (c) damage of the first cycle interpolated back to the new centroid position of the second cycle (x), (d) accumulated damage in the second cycle (triangle) and the new linear equations (graphic b plus graphic c).**

### 6.3.3 Material fatigue constants

In the absence of fatigue properties of the wire studied in this work, different approaches, for obtaining the fatigue strength coefficients and the fatigue ductility coefficients needed for the life prediction according to the SWT model (Eq. 6-1), are discussed in this section.

The first approach is based on the methods proposed by different authors for estimating the fatigue coefficients based only on the available monotonic tensile test data. This methodology has been used previously by Del Llano-Vizcaya et al. [151] for predicting the fatigue lives in helical compression springs which are made by high carbon steel wires, using different multiaxial fatigue criteria. In Table 6-4 are shown the different estimation methods proposed in this study. The first one corresponds to the Manson's universal slope method [152], which takes into account the ultimate tensile stress of the material  $\sigma_u$  and

the true fracture strain  $\epsilon_f$  which is calculated using the reduction in area  $RA$   $\epsilon_f = \ln(1/1 - (RA/100))$ . The second one is a modified universal slopes method proposed by Muralidharan and Manson [153], in which both fatigue exponents are increased and the  $\sigma_u / E$  term is introduced for the calculation of both fatigue coefficients. The last method named Medians method for steel is introduced by Meggiolaro and Castro [154], which combines good average life predictions with one of the lowest standard deviations for a higher range of different steels.

**Table 6-4. Estimation methods of fatigue coefficients from monotonic tensile tests. [28-30].**

Parameter	Universal Slopes	Modified Universal slopes	Medians (steels)
$\sigma_f'$ [MPa]	$1.9 \cdot \sigma_u$	$0.623 \cdot \sigma_u^{0.823} E^{0.168}$	$1.5 \cdot \sigma_u$
$b$	-0.12	-0.09	-0.09
$\epsilon_f'$	$0.76 \cdot \epsilon_f^{0.6}$	$0.0196 \cdot \epsilon_f^{0.6} (\sigma_u / E)^{-0.53}$	0.45
$c$	-0.6	-0.56	-0.59

The second approach is based on obtaining the fatigue properties from an eutectoid high strength steel wire reported in the literature. So, the Basquin's (HCF) coefficients were obtained from the R=0.1 uniaxial fatigue tests reported by Beretta and Mateazzi [155] in a 1.97 mm diameter wire with an interlamellar spacing of about 0.1  $\mu\text{m}$ . The mechanical properties of this wire are shown in Table 6-5 and are in accordance with those ones reported by Verpoest et al. [156] for 1.99 mm diameter wire.

**Table 6-5. Mechanical properties of Beretta's 1.97 mm diameter wire. [155]**

	$\sigma_u$ [MPa]	$\sigma_y$ [MPa]	$RA$ [%]	$e$ [%]	HV
Beretta	1855	1540	58	1.61	470±30

To obtain the  $\sigma_f'$  and  $b$  in fully alternated tension-compression fatigue tests R=-1 the standard Goodman relationship presented in (Eq. 6-15) was used to correct the mean stress effect. Where  $\sigma_a$  is the alternating stress,  $\sigma_m$  is the mean stress and  $\sigma_u$  the ultimate tensile stress. The fitting curve is shown in Fig. 6-6. In the absence of low cycle strain controlled fatigue data,  $\epsilon_f'$  and  $c$  were obtained applying the monotonic tensile stress properties in the Manson's universal slope method presented previously.

$$\sigma_{ar} = \sigma_f' (2N_f)^b = \frac{\sigma_a}{1 - \frac{\sigma_m}{\sigma_u}} \tag{Eq. 6-15}$$

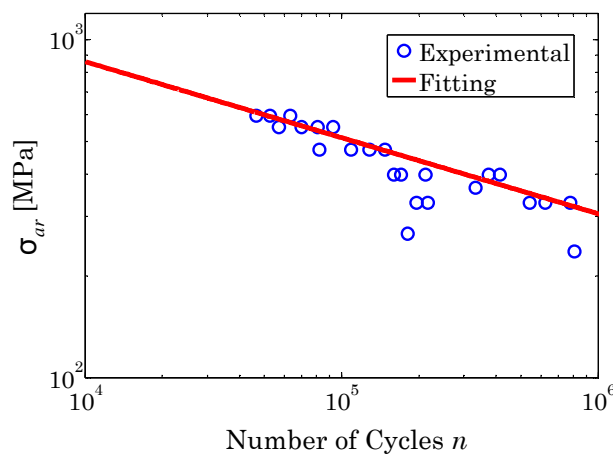


**Fig. 6-6. Fitting curve to obtain the Basquin's coefficients from the uniaxial fatigue tests data reported by Beretta and Mateazzi [155] according to the Goodman relationship.**

A summary of the fatigue coefficients obtained from the monotonic tensile test properties of the studied steel wire shown in Table 6-1 and for the different methods proposed in Table 6-4 are shown in Table 6-6. Moreover in this table are included the fatigue coefficients obtained from the S-N curves reported by Beretta and Mateazzi [155] in a 1.97 mm diameter wire.

**Table 6-6. A summary of the fatigue coefficients obtained from the different methods.**

Parameter	Universal Slopes	Modified Universal slopes	Medians (steels)	Beretta
$\sigma_f'$ [MPa]	5700	3521	4500	8000
$b$	-0.12	-0.09	-0.09	-0.225
$\varepsilon_f'$	0.441	0.105	0.45	0.697
$c$	-0.6	-0.56	-0.59	-0.6

## 6.4 Results and discussion

### 6.4.1 Introduction

The FE analysis presented in this section corresponds to the fretting wear tests carried out on a 0.45 mm diameter pre-stressed wire, as a consequence of the bending that was applied in the wire for the correct fixation in the holder. With the aim to analyze the fretting wear frictionally induced crack nucleation, firstly a study of the subsurface stress distribution in a not pre-stressed steel wire has been carried out. Secondly the effect of the bending imposed pre-stresses in the fretting induced subsurface stresses has been analysed. Thirdly

the results obtained from combined FE wear model and the critical plane SWT and damage approach proposed in this paper has been discussed and compared with the results obtained experimentally. Finally different strategies for the improvement the developed methodology for predicting fretting wear cracks in thin steel wires have been proposed.

### 6.4.2 Subsurfaces stress distribution analysis

The wear-induced material removal evolution of sub-surfaces stresses which directly controls the crack initiation in the bottom cylinder after different number of cycles and 1N-130  $\mu\text{m}$  is discussed in the following paragraphs. A three dimensional local axis coordinate system with the local 1 direction parallel to the direction of the movement (x direction in Fig. 6-2); the local 3 direction normal to the contact surface (z direction in Fig. 6-2), and the local 2 direction making a right hand set with the other two has been used. The sub-surface stresses have been plotted at a depth of 3.5  $\mu\text{m}$ , which corresponds to the first row of centroidal values.

In Fig. 6-7 the  $\sigma_{11}$  and  $\sigma_{13}$  stresses value after 20000 number of fretting wear cycles and different displacement amplitude locations are shown. It can be seen from these plots that there is an increase of the peak stress value from the centre position to the end position of the displacement amplitude, being its greater value in this last position. This is because of the shape acquired by the wear scar, composed by a uniform surface geometry that goes from the centre to the near edge of the wear scar and with inclined flanks in edge the wear scar.

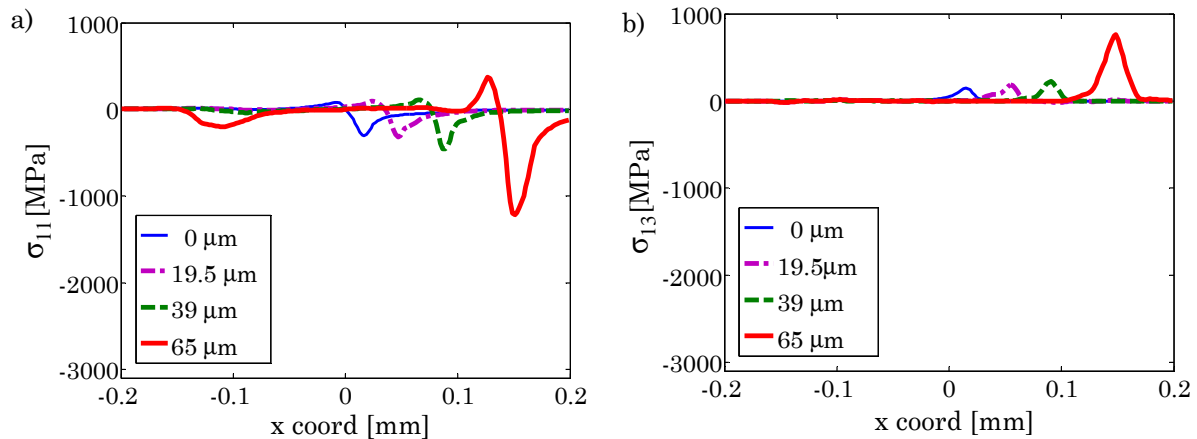
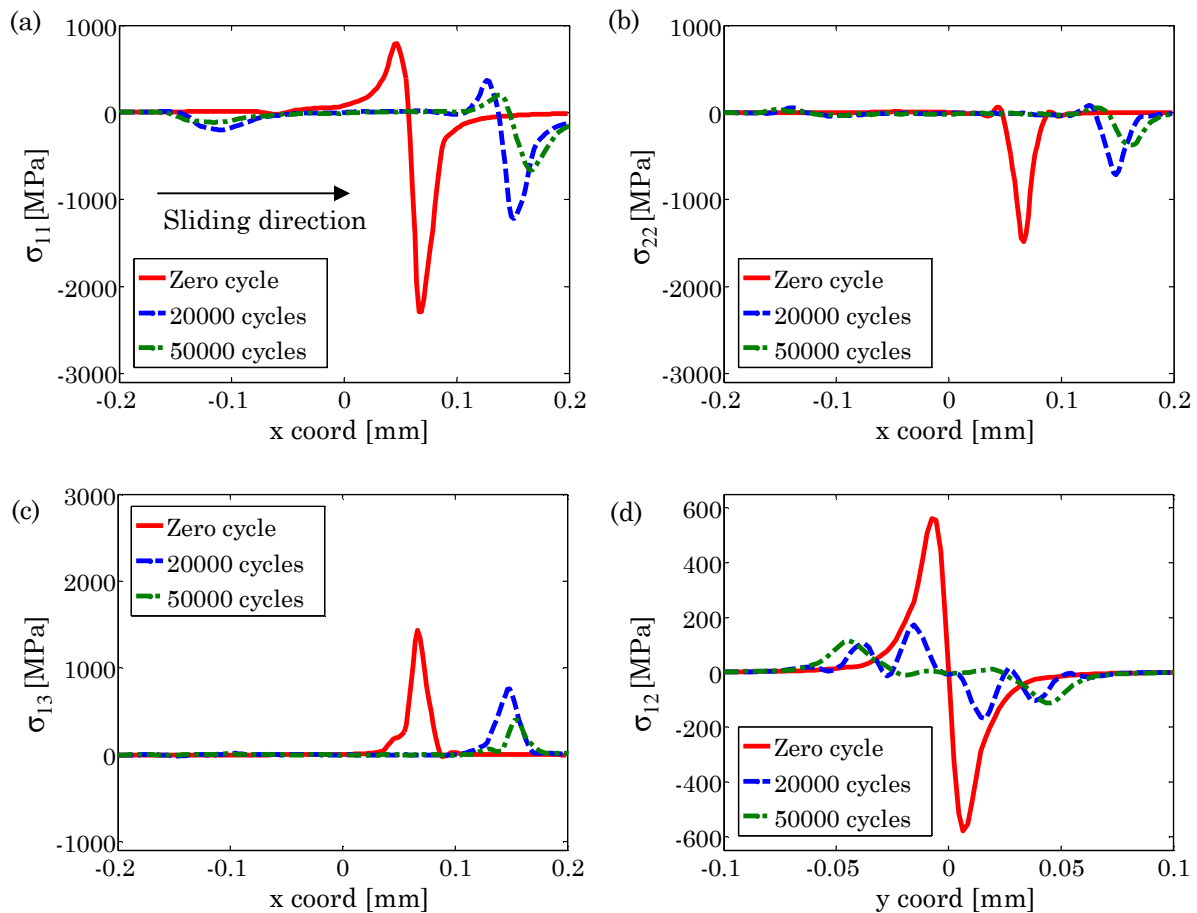


Fig. 6-7. Subsurface stress distribution for 1 N-130  $\mu\text{m}$ , 20000 number of cycles and different amplitude displacement locations: a) stress distribution  $\sigma_{11}$ , b) stress distribution  $\sigma_{13}$ .

Fig. 6-8 shows the multiaxial subsurface stress distribution for different number of cycles at a displacement amplitude position of 65  $\mu\text{m}$  which corresponds to the maximum stresses peak value presented in Fig. 6-7. It can be seen that there is a drastic reduction in the peak

stress value before and after wear, as a consequence of the decrease at the peak contact pressure in the first few hundred of cycles, as reported in section 4.3.4.3. On the other hand, while a tensile stress parallel to the surface promotes a crack nucleation a compressive traction retards it. So the  $\sigma_{11}$  axial stress in the direction of sliding and the  $\sigma_{13}$  shear stress are the key components in the crack nucleation process, as  $\sigma_{22}$  mainly presents compressive stresses. Moreover while  $\sigma_{13}$  is only governed by tensile stresses,  $\sigma_{11}$  is governed by both states. It can be seen in Fig. 6-8(a) that while the leading edge of the contact (the front side in the sliding direction) is subjected to compressive stresses, the trailing edge of the contact (the back side in the sliding direction) is subjected to a tensile stresses. Furthermore, due to the increase of the length of the wear scar, a translation of the peak stresses in the sliding direction is produced. This effect is smaller as the number of cycles increase.



**Fig. 6-8. Multiaxial subsurface stress distribution in the bottom cylinder for 1 N-130  $\mu\text{m}$  and different number of cycles in the amplitude displacement position of 65  $\mu\text{m}$ : (a) stress distribution  $\sigma_{11}$ , (b) stress distribution  $\sigma_{22}$ , (c) shear stress distribution  $\sigma_{13}$  and (d) shear stress distribution  $\sigma_{12}$ .**

The effect of the coefficient of friction in the previously shown key components in the crack nucleation, the axial stress  $\sigma_{11}$  and the shear stress  $\sigma_{13}$  for 1 N-130  $\mu\text{m}$  before wear is

illustrated in Fig. 6-9. A reduction of the coefficient of friction implies a reduction of the subsurface tensile stresses. It means that reducing the coefficient of friction could be increase the crack nucleation life. As has been mentioned in section 3.1, in this study a friction coefficient of 0.7, which is in accordance with the coefficient of friction obtained experimentally in the stable period as shown in section 3.3.1.1, has been used.

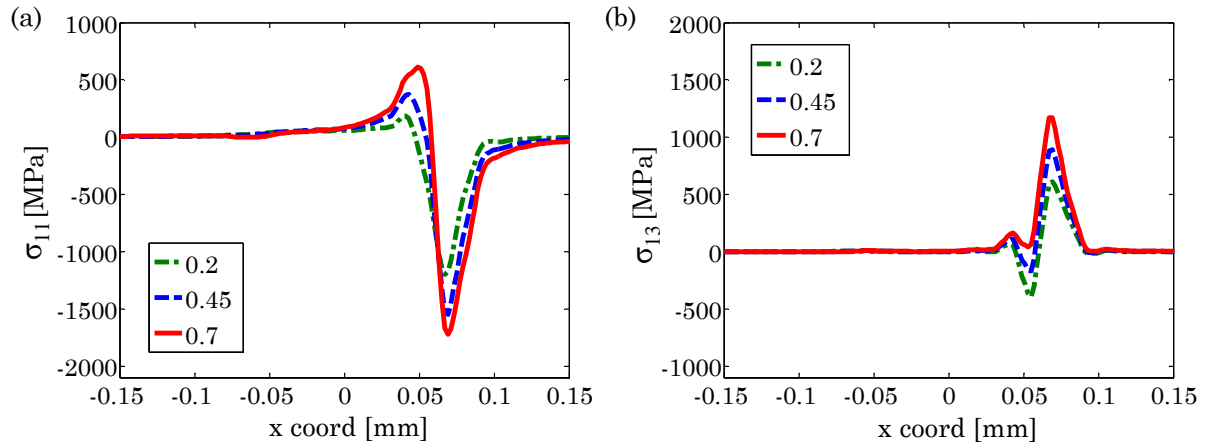


Fig. 6-9. The axial subsurface distribution for 1 N-130  $\mu\text{m}$  and different coefficient of friction: (a) stress distribution  $\sigma_{11}$ , (b) shear stress distribution  $\sigma_{13}$ .

#### 6.4.3 Subsurface stress distribution in a pre-stressed wire

In the previous paragraphs the analysis of the fretting induced subsurface multiaxial stress distribution has been described. Nevertheless, the curvature used to correctly fix the wire in the holder, produces a bending deformation in the wire which leads to introduce tensile stresses near the contact surface.

To analyse the stress field produced in the wire as a consequence of the bending, in Fig. 6-10 it is shown the FE model used for modelling the wire fixation procedure in the holder. While the wire supporting holder and the two fixation washer have been modelled as a 3D analytical rigid body, the wire has been modelled according to an elastic plastic model with isotropic hardening. The elastic plastic model has been introduced using the measured stress-strain curve shown in Fig. 6-1. The mesh is composed of eight nodes lineal brick elements. The contact surface interactions between the rigid surfaces and the wire are defined via the finite sliding contact pair algorithm. With the aim to simplify the problem no frictional contact has been considered.

Fig. 6-10 shows the stress produced in the axial direction of the wire  $\sigma_{11}$  which is in accordance with the axis coordinate system defined in the previous section. This stress, in combination with fretting induced multiaxial stresses, will affect in the crack nucleation process. It can be seen that in the region corresponding to the contact surface in fretting

tests, it is produced a compressive stress in the bottom side of the wire and a tensile stress in the top side of the wire which corresponds to the contact surface. The results show that there is a tensile stress  $\sigma_{11} \approx 2000\text{MPa}$  near the contact surface. On the other hand the stresses  $\sigma_{22}$  and  $\sigma_{33}$  in the contact region are less than 5% of the stress obtained in  $\sigma_{11}$ , so they will be neglected in the study of the combined fretting and bending produced bulk stress study.

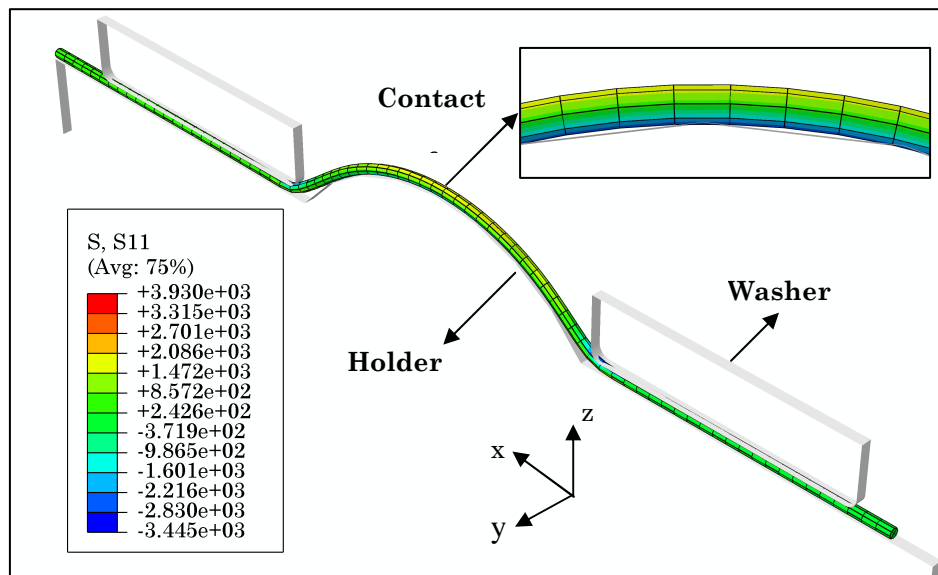


Fig. 6-10. Elastic-plastic finite element analysis of the wire fixation  $\sigma_{11}$  axial stresses.

To analyse the effect of the pre-stresses in the fretting wear analysis, an initial predefined state, obtained after applying a tensile pressure of 2000 MPa in the extremes of the wire, has been introduced in the bottom cylinder of the FE fretting wear model.

Fig. 6-11 shows the axial stress  $\sigma_{11}$  and the shear stress  $\sigma_{13}$  for 1 N-130  $\mu\text{m}$  and 50000 number of cycles, with and without pre-stresses. The effect of the pre-stress is significant in the  $\sigma_{11}$  axial stress, where an increase of the tensile stresses along the entire contact region is shown. Moreover it can be seen a decrease of the tensile stresses in the front side of the contact. This is because of the compressive stresses produced by the leading edge of the contact as has been discussed previously. On the other hand the  $\sigma_{13}$  shear stress presents a less significant increase in the tensile stresses. It suggests that a decrease of the wire pre-stresses, e.g. increasing the bending radius, can be increase the crack nucleation life.



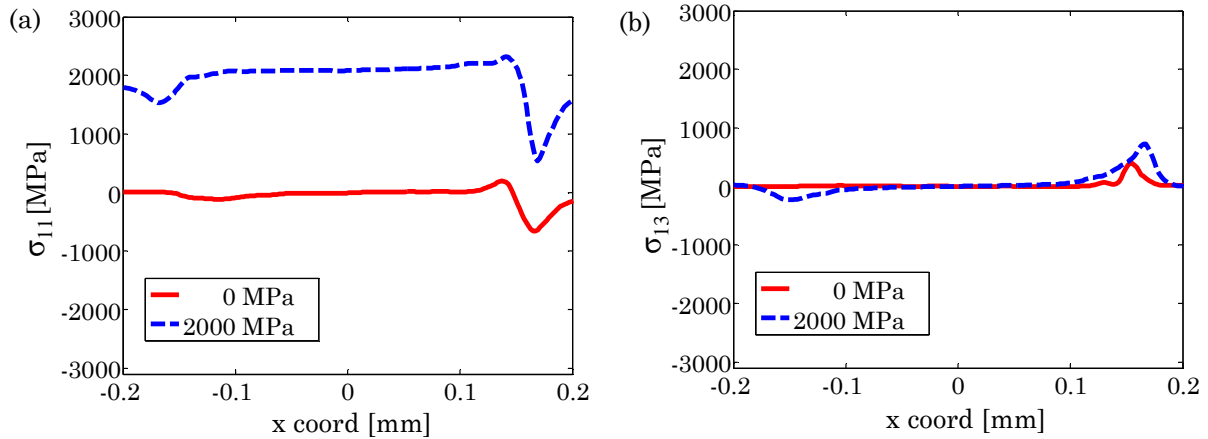


Fig. 6-11. The axial subsurface stress distribution for 1 N-130  $\mu\text{m}$ , 50000 number of cycles and different pre-stresses in the amplitude displacement position of 65  $\mu\text{m}$ : (a) stress distribution  $\sigma_{11}$ , (b) shear stress distribution  $\sigma_{13}$ .

#### 6.4.4 Fatigue crack nucleation analysis

Firstly, the analysis of the crack nucleation prediction due to fretting wear in thin steel wires has been carried out according to the proposed FE methodology. Secondly, the results have been compared with the experimental data obtained from fretting wear tests.

Fig. 6-12 illustrates the critical plane SWT crack nucleation predictions plots for the case of 1 N-130  $\mu\text{m}$  pre-stressed at 2000 MPa. Fig. 6-12(a) shows the maximum SWT critical plane value along the axial direction of the bottom wire (sliding direction). The results show that there is a drastic decrease of the SWT peak value (Fig. 6-12(b)) in the first thousand of cycles and then, this value stabilizes and decreases at a lower slope. This effect is attributed to the material removal produced by the wear, which causes stress redistribution as shown previously due to the increase of the contact area that promotes a decrease of the contact pressure. While the maximum SWT value is distributed along the entire contact surface in a fretting cycle in which there is no wear, as the wear occurs a peak value appears in the edge of the contact. Moreover as a consequence of the wear and the widening of the wear scar this peak value suffers and outward movement, the same tendency presented previously with the axial stress  $\sigma_{11}$  and the shear stress  $\sigma_{13}$ .

On the other hand the 3D SWT contour plots are shown in Fig. 6-12(c) for the no wear case and in Fig. 6-12(d) after 50000 fretting wear cycles. As the wear is produced it can be seen the two symmetrical SWT peaks in both edges of the axial direction. This peak value start in the middle of the transversal direction of the wear scar and goes decreasing outside this position.

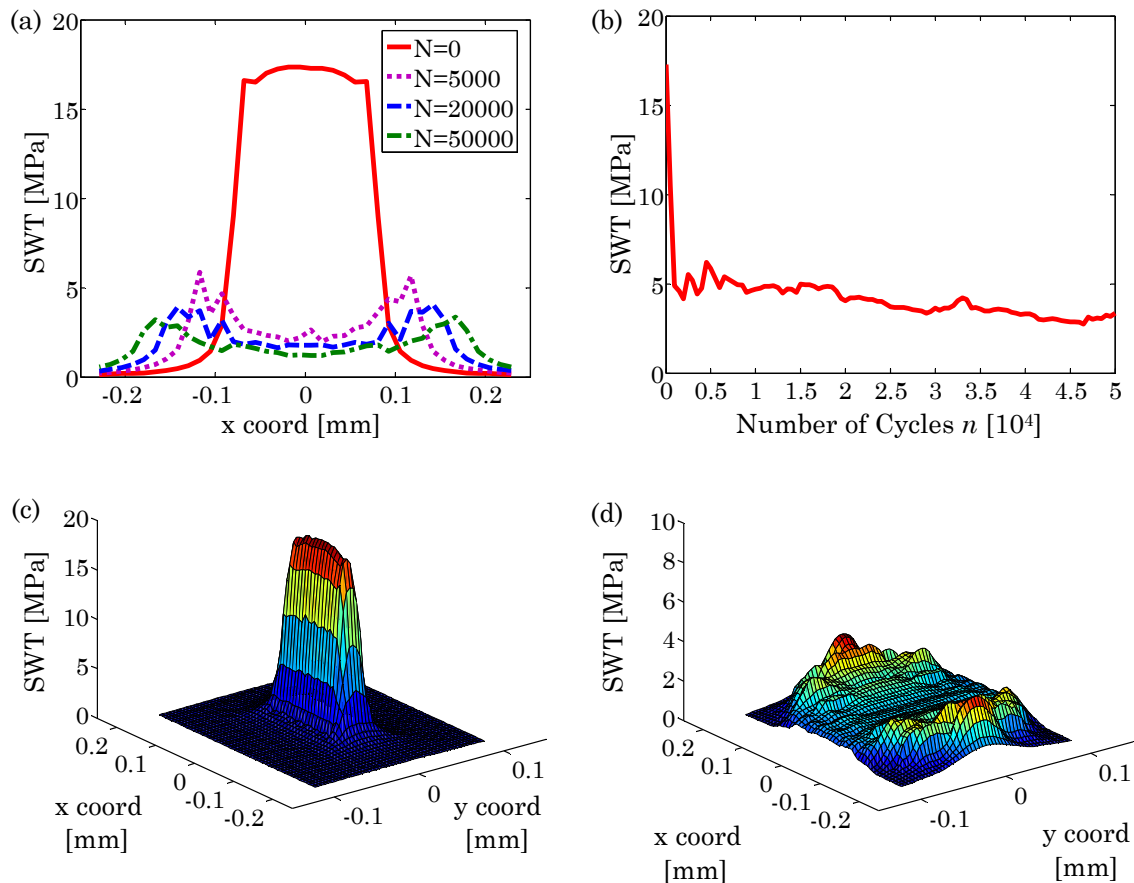


**Fig. 6-12. FE critical plane SWT plots for 1 N-130  $\mu\text{m}$  and 2000 MPa pre-stress: (a) longitudinal SWT value plot for different number of cycles, (b) evolution of SWT peak value, (c) 3D plot of the SWT value without wear, (d) 3D SWT value plot after 50000 number of cycles.**

Fig. 6-13 shows the effect of the bending induced pre-stresses in the SWT peak value. In both cases the pre-stressed and the not pre-stressed wire, the tendency is the same, there is a decrease of the maximum peak value in the first thousand of cycles and then stabilised. Nevertheless, the influence of the tensile stresses produced as a consequence of the bending leads to a drastic increase in the peak value, which could reduce considerably the fretting induced crack initiation life. Furthermore in Fig. 6-13(b) is shown that the location of the maximum SWT peak value in the axial direction after 50000 numbers of cycles, in both cases is in the edge of the contact, being this distance from the centre of the wear scar a little bit higher in the pre-stressed case than in the not pre-stressed case. So reducing the bending of the wire it can be increase drastically the life of this component.

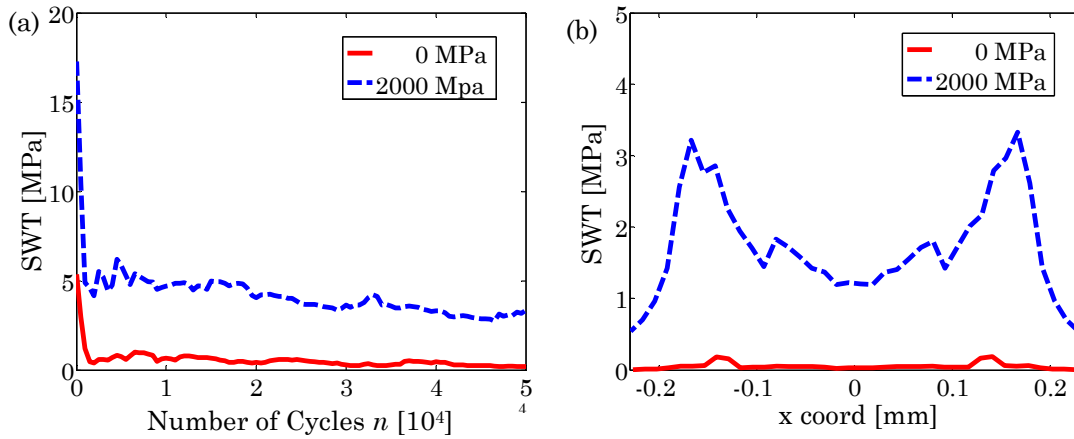


Fig. 6-13. FE critical plane SWT plots for 1 N-130  $\mu\text{m}$  with and without pre-stress: (a) SWT peak value evolution, (b) longitudinal plot of the maximum SWT value.

Fig. 6-14 shows the crack initiation locations of the bottom wear scars after carrying out fretting wear tests with 4 N-65  $\mu\text{m}$  (Fig. 6-14(a)) and 2 N-130  $\mu\text{m}$  (Fig. 6-14(b)) and 20000 cycles. Two symmetrical transversal cracks at a specific distance from the centre of the wear scar are produced. This is in accordance with the SWT critical plane plots presented previously in Fig. 6-13(b). On the other hand the crack propagation is produced in the longitudinal plane to the contact surface, as a consequence of the fiber structure presented by the wire. This is because during the cold drawn process the pearlitic structure of the eutectoid steel is formed by lamellas of cementite and ferrite oriented in the longitudinal direction of the wire. The wear scars obtained with the FE wear simulation model, for the two cracks experimental cases presented previously are shown in Fig. 6-15. The good correlation of this methodology is shown in the dimensions of the wear scars.

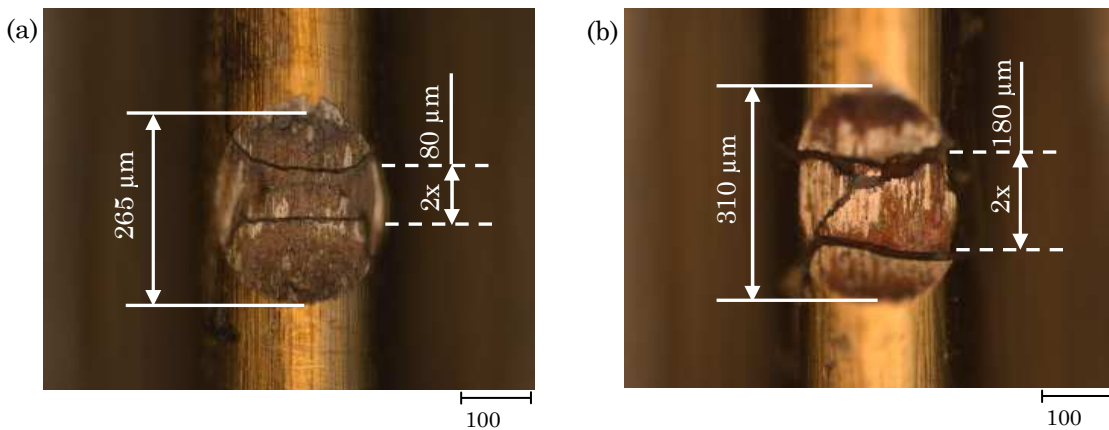


Fig. 6-14. Failure of the wire under different conditions fretting wear tests: (a) 4 N-65  $\mu\text{m}$ -2 x  $10^4$ , (b) 2 N-130  $\mu\text{m}$ -2 x  $10^4$ .

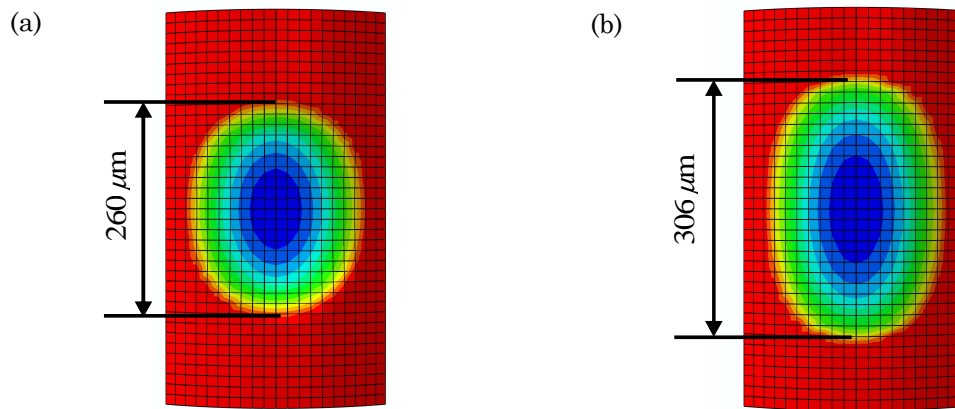


Fig. 6-15. FEM simulated wear scars for: (a) 4 N-65  $\mu\text{m}$  - $2 \times 10^4$ , (b) 2 N -130  $\mu\text{m}$ - $2 \times 10^4$ .

The life predictions made combining the SWT critical plane approach and the damage accumulation model, which takes into account the continuum evolution of the subsurface stresses due to wear removal are summarised in Table 6-7. The life predictions have been carried out according to the fatigue coefficients obtained from the three methodologies, based on the monotonic tension test properties of the wire and from the coefficients obtained from the axial fatigue tests reported by Beretta. In all cases the FE wear simulation has been carried out for 50000 cycles, so in the cases where not crack appears the maximum accumulated damage value and the location of this damage has been listed. The crack location value has been considered as the distance from the centre of the wear scar to the predicted crack position. On the other hand, the experimental tests have been carried out till 200000 number of cycles, so conditions in which cracks could nucleate at longer number of cycles has not been predicted. The case of 3 N-65  $\mu\text{m}$ -200000 number of cycle is considered as no crack case, nevertheless when repeating this test several times, cracks appears in some cases. Therefore 200000 cycles could be the no crack number of cycles crack limit for this test.

The Manson's Universal slopes method predict correctly the lives in the 130  $\mu\text{m}$  cases; nevertheless under predict cracks in the case of 2 N-65  $\mu\text{m}$  and 3 N-65  $\mu\text{m}$ . The Modified Muralidharan's universal slopes method is more conservative that the previous method, mainly with higher loads such us 4 N-65  $\mu\text{m}$ , where the life decrease drastically. Nevertheless the predicted crack location is closest to that one obtained experimentally. The Medians method, which is the last method used to obtain the fatigue coefficients of the thin steel wire analyzed in this study is the less conservative method. In the case of 2N-130  $\mu\text{m}$  no crack is predicted. Moreover the crack location position is over predicted. On the other hand the fatigue coefficients obtained from the fatigue tests reported by Beretta, looks to be the most conservative, under predicting cracks in all cases. Nevertheless the predicted crack position is the closest to the one obtained experimentally.

In all cases it is clear that the increase of the load reduce drastically the life of the wire, nevertheless, it is not clear that an increase of the stroke also reduce drastically the life of the wire as shown in the experimental results reported in this study and in the conclusions reported by Wang et al. [149], where this effect was associated with an increase of the tangential force. Taking into account this last affirmation, the values predicted with the proposed methodology for 2 N-65  $\mu\text{m}$  and 2 N-130  $\mu\text{m}$  are similar, so there are more aspects that have to be analyzed in order to improve this methodology. These aspects will be summarized in the next section.

**Table 6-7. Comparison of measured and predicted lives and failure locations under different SWT coefficients fitting methods (x represents de location from the centre of the wear scar, D represent the damage after  $50 \times 10^3$  number of cycles ).**

Test conditions	Experime ntal $N_f$	Predicted $N_f$			
		Universal slopes	Modified Universal	Medians (steels)	Beretta
90°-4N-65 $\mu\text{m}$ (Crack) (x= 20-50 $\mu\text{m}$ )	2x10 <sup>4</sup> - 1x10 <sup>5</sup>	5.5 x10 <sup>3</sup> (x=92.9 $\mu\text{m}$ )	200 (x=0 $\mu\text{m}$ )	1.35 x10 <sup>4</sup> (x=92.9 $\mu\text{m}$ )	500 (x=18.31 $\mu\text{m}$ )
90°-3N-65 $\mu\text{m}$ (No crack-Crack)	2x10 <sup>5</sup>	8.5 x10 <sup>3</sup> (x=92.9 $\mu\text{m}$ )	4.5 x10 <sup>3</sup> (x=80.5 $\mu\text{m}$ )	3.05 x10 <sup>4</sup> (x=105.3 $\mu\text{m}$ )	2.5 x10 <sup>3</sup> (x=55.781 $\mu\text{m}$ )
90°-2N-65 $\mu\text{m}$ (No crack)	>>2x10 <sup>5</sup>	2.55 x10 <sup>4</sup> (x=80.5 $\mu\text{m}$ )	7.5 x10 <sup>3</sup> (x=80.5 $\mu\text{m}$ )	D=0.2042 (x=80.5 $\mu\text{m}$ )	2.5 x10 <sup>3</sup> (x=68.13 $\mu\text{m}$ )
90°-2N-130 $\mu\text{m}$ (Crack) (x=80 $\mu\text{m}$ )	1.5x10 <sup>4</sup> - 5x10 <sup>4</sup>	2.45 x10 <sup>4</sup> (x=142 $\mu\text{m}$ )	1.05 x10 <sup>4</sup> (x=117.5 $\mu\text{m}$ )	D=0.258 (x=159.7 $\mu\text{m}$ )	3 x10 <sup>3</sup> (x=105.2 $\mu\text{m}$ )
90°-1N-130 $\mu\text{m}$ (No crack)	>>2x10 <sup>5</sup>	D=0.313 (x=142 $\mu\text{m}$ )	D=0.314 (x=142.3 $\mu\text{m}$ )	D=0.0208 (x=142.3 $\mu\text{m}$ )	4.5 x10 <sup>3</sup> (x=105.2 $\mu\text{m}$ )

Fig. 6-16 shows the damage location plots of the two crack cases presented previously, using the fatigue coefficients obtained from Manson’s universal slope method, which is the most consistent with the experimental lives. While Fig. 6-16(a) and Fig. 6-16(b) shows the top view and the axial cut in the transversal maximum damage position (0 ycoord position) for 4 N-65  $\mu\text{m}$  and 5500 number of cycles Fig. 6-16(c) and Fig. 6-16(d) show the plot for 2 N-130  $\mu\text{m}$  and 24500 cycles. In both cases it is shown the symmetrical position of the crack location as shown in the experimental tests.

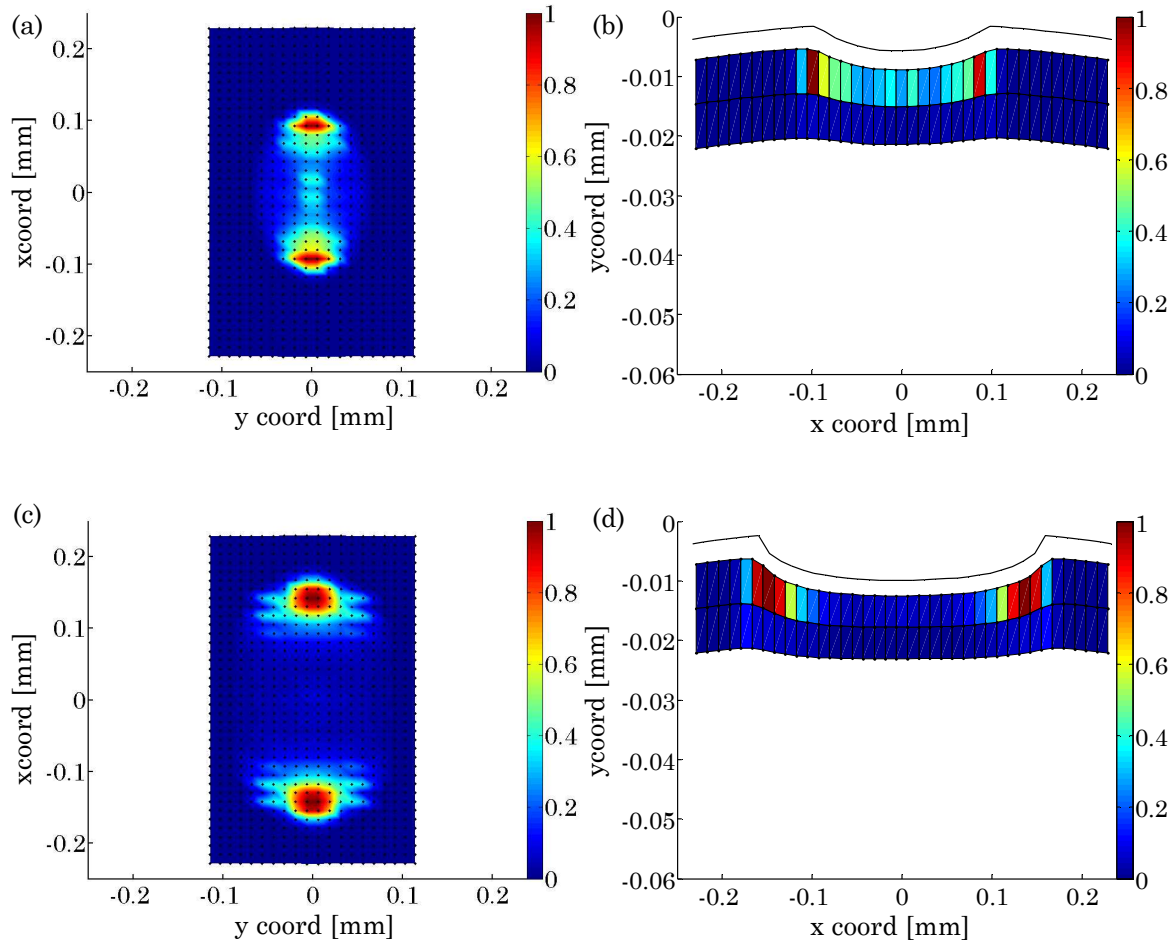


**Fig. 6-16. Predicted location of the failure according to Manson's universal slope coefficients: 4 N-65  $\mu\text{m}$ - $5.5 \times 10^3$ , (a) Top view, (b) longitudinal cut; 2 N-130  $\mu\text{m}$ - $2.45 \times 10^4$ , (c) Top view, (d) longitudinal cut.**

#### 6.4.5 Fretting wear life prediction methodology discussion

This is the first step to develop a consistent methodology for predicting fretting wear induced cracks in the thin steel wires used in wire rope systems. The presented FE fretting wear simulation model with the combined SWT critical plane and the accumulative damage methodology, has demonstrated that there are some aspects that have to be improved in order to predict this complex phenomenon in the thin steel wires.

As reported by Meggiolaro and Castro [154], the different methods proposed in this work for obtaining the fatigue coefficients of the wire from the uniaxial monotonic tests, may results in life prediction errors of an order of magnitude, which is in accordance with the values obtained in Table 6-7 in specific loading cases and methods (over predicting or under predicting cracks). So he proposed these methods as the first stages of design, requiring the experimental fatigue parameters for correct predictions.

On the other hand, when using the fatigue coefficients obtained from the experimental fatigue data reported by Beretta [155] for 1.97 mm wire, the results are over conservative. As shown in the S-N curves reported in the literature [144], [147], [155], different diameters thin steel wires could have different fatigue properties. This is because the fatigue properties of the wires are related to different parameters: such as the interlamellar spacing of the pearlite obtained by the cold-drawn process, the diameter of the wire or the size of the inner defects. The diameter of the wire studied in this work is smaller than those ones reported in the literature. Moreover this wire presents higher ultimate tensile strength and higher yield strength. So future work will be focused in characterize the fatigue behaviour of this wire with the complexity associate to the very small diameter.

The results obtained by the combined FE wear model and SWT critical plane damage methodology, mainly are over conservative. One approach used by many researches to solve this problem is the application of the volume averaging techniques [56], [68] such as these methods can capture in more realistic way the stress field corresponding to the crack nucleation. On the other hand, to improve the prediction corresponding to the crack location Ding et al. [59] proposed to combine the Ruiz parameters, which emphasise the importance of the frictional work, with the SWT critical plane approach. When using these types of parameters with volume averaging of the SWT parameter, as the average grain size, Ding et al. [63] reported the effectiveness in the incorporation the wear effects along with the crack nucleation prediction.

One of the key factor that has to be consider in this methodology, is the introduction a crack propagation model in combination with the developed crack initiation methodology. Such as the methodology proposed by Madge et al. [62] for 2D problems. This approach could explain, that e.g for the 2 N-65  $\mu\text{m}$  and 2 N-130  $\mu\text{m}$  cases the wear could initiate at the same time, but due to the effect of the wear in the case of 1 N-130  $\mu\text{m}$  the crack could propagate and in the case of 2 N-65  $\mu\text{m}$  the crack could arrested and disappear.

## 6.5 Conclusions

---

This chapter has presented a finite element prediction methodology which combines a FE wear model and a critical plane SWT damage accumulation approach for the prediction fretting wear induced cracks in thin steel wires. Four different methods for estimating the fatigue coefficients of the steel wire have been analysed. The first three methods (Manson's universal slope, Muralidharan modified universal slopes and Medians) are based only on the available monotonic tensile test data. The fourth method is based on S-N curves reported by Beretta [155] for 1.97 mm diameter wire. The fatigue life predictions carried

out with this methodology have been compared to the fretting wear experimental tests carried out on thin steel wires. The main conclusions are:

- A significant reduction of the fretting wear frictionally-induced multiaxial contact stresses within the first thousand of cycles is predicted. The maximum tensile stresses are located in the edge of the wear scar in the sliding direction.
- The friction coefficient and the bending produced tensile stresses in the wire are two of the parameters that can reduce crack nucleation. Low friction coefficients and low bending pre-stresses are indispensable for increasing the life of the wires.
- Symmetrical cracks, about the centre of the wear scar, are predicted, as shown experimentally. However the locations of the cracks obtained experimentally are closer to the centre than the predicted ones.
- The lives predicted with this methodology are conservative relative to those obtained experimentally. Manson's method and the Median's method gives lives closer to those obtained experimentally, while those predicted with the fatigue coefficients obtained from the modified universal slopes method and Bereta's fatigue data are the more conservative.
- While this approach predicts that the increasing load reduces drastically the life of the wire, it does not predict that increasing stroke also reduces drastically the life of the wire, as shown experimentally.
- Finally different solutions for the improvement of this methodology in future works are proposed. These include: the fatigue characterization of the thin steel wires; the introduction of volume-averaging techniques or the Ruiz parameters in the SWT critical plane approach to improve the life predictions and the crack locations and development of crack nucleation and propagation methodologies which can explain better the effect of crack propagation or arrest due to the wear.



---

CHAPTER VII

# GENERAL CONCLUSIONS, RECOMMENDATIONS AND FURTHER WORK

---

## 7.1 Introduction

---

An optimized FE wear simulation methodology for modelling fretting wear in 3D systems has been developed in this thesis. This methodology has been used for modelling successfully fretting wear scars in the thin steel wires that form the wire rope systems. The tool has been used for the study of the severity of the wear scars and to analyse the fretting wear frictionally induced multiaxial contact stresses on the fatigue life reduction of thin steel wires.

This chapter first summarizes the general conclusions obtained from this research work. Secondly the potential areas in which further work can be carried out, in order to develop a more robust simulation tool for increasing the knowledge about the fretting wear in the fatigue live reduction of thin steel wires are described. To this end recommendations around the main three aspects reported in this thesis are discussed: fretting tests, FEM modelling of fretting wear in thin steel wires and FEM modelling of the effect of fretting wear in the fatigue life reduction of thin steel wires.

## 7.2 Conclusions

---

A FEM wear methodology for modelling fretting wear in thin steel wires has been developed in this thesis. The main conclusions of this thesis are structured according to the fourth objectives proposed in Chapter 1: characterization of the tribological properties of thin steel wires in laboratory fretting wear tests; development of a FEM simulation

methodology for predicting fretting wear in thin steel wires; determination of the influence of the different geometrical and operational variables in the severity of the wear scars and determination of the influence of the fretting wear induced multiaxial stress distribution in the fatigue life reduction of thin steel wires.

#### Tribological properties of thin steel wires

Fretting wear tests on thin steel wires with  $90^\circ$  and different crossing angles configurations were carried out first, in order to describe the frictional behaviour and wear behaviour needed as the input values in the wear simulation methodology.

Regarding to the frictional behaviour it was reported that the coefficient of friction suffer and increase in the beginning of the test followed by a decrease and stabilization of this one. The increase of the coefficient of friction in the beginning of the tests was attributed to the elimination of the surface oxides that promote the severe metal-metal interaction. The following reduction of the coefficient of friction was attributed to the formation a compacted protective layers which reduce the metal-metal interaction. Moreover it was seen a slightly decrease of the coefficient of friction increasing de contact pressure, which is in accordance with the description proposed by Bowden and Tabor [133] on metallic contacts.

On the other hand, with respect to the wear behaviour it has been shown that the coefficient of wear varies with respect to the sliding distance (number of cycles). This is attributed to the two wear periods detected in this type of tests: a running-in period, with a more aggressive wear mechanism and a stable steady state period. The running-in period has been related with the previously mentioned initial metal-metal interaction period, in which apart from a higher coefficient of friction higher wear loss is produced too. On the other hand the stable period is associated with the formation of the compacted protective debris layers. These protective layers have a greater influence in the bottom specimen, promoting a variable wear behaviour between both specimens. In the initial period there is a greater wear loss in the bottom specimen. Nevertheless the formation of these protective layers, promote to reduce considerably the loss of wear in the bottom specimen while the top specimen remains increasing.

The transition between these two periods varies with respect to the normal force (contact pressure) and stroke. At higher contact pressures and strokes the transition is given at longer sliding distances. Moreover it was shown that while in the running-in period all the contact pressures and strokes produced the same coefficient of wear in the stable period higher is the contact pressure and stroke higher is the coefficient of wear. This tendency explained the lower coefficient of wear obtained with that smaller crossing angles, such us

decreasing the crossing angle the contact pressure is reduced too. It should be pointed out that all the tests were carried out under gross sliding conditions.

#### FEM simulation methodology for predicting fretting wear in thin steel wires

Based on the experimental data obtained in the fretting wear tests, a FEM model for predicting fretting wear scars in thin steel wires was developed then. The FEM wear model was implemented via Abaqus user subroutine Umeshmotion, using the Archard's modified equation in a local perspective. So that the wear depth of each surface node has to be computed incrementally (contact problem and the following application of the Archard's local model) as many times as sliding increments needed for modelling one fretting cycle and as many times as cycles needed to reach the desired number of cycles. Nevertheless one of the great disadvantages of the wear modelling with FEM is the required computational time, which increase drastically in the 3D problem presented in wire rope systems, where the computational time increase drastically. To solve this problem an optimized methodology to get the minimum computational time with the minimum difference in the final wear scar in any tribological systems has been proposed. The methodology is based on the optimization of the main parameters involved in the wear modelling: mesh size, sliding increment and speed factor. This methodology has been applied first in a cylinder on plane 2D FE model, secondly was adapted to the 90° crossed cylinder model and finally was implemented in the crossing angle FE wear model.

From the application of this methodology in the fretting wear modelling of thin steel wires, it was derived the following conclusions. There is a relation between the optimum mesh size and final wear scar size. Each FE fretting cycle can be modelled with the same number of increments independent of the stroke and the load used, for the studied range of parameters, which are in the gross sliding conditions. The optimum number of increments in each fretting wear simulation is the same for all cases regardless of the number of cycles that are simulated. Therefore, taking into account that each FE cycle is composed by a specific number of cycles, for the fretting wear simulation of longer number of cycles higher cycle jumps can be used without affecting in the final wear scar. The error assumed by the optimized FEM wear simulation methodology is less than 3%.

An exhaustive validation methodology based on the wear scar dimensions, wear scar depth and wear scar volume was conducted. The good correlation with respect to the experimental data was derived. It implies that the entire wear scar can be predicted with errors less than 15%, acceptable in this tribological system, where the experimental data presents dispersion greater than 15% [136].

It was seen that the great part of this error was located in the bottom wear scar depth and was attributed to different aspects: the error committed by the optimized FEM simulation, the error committed in the experimental setting and the corresponding measurement of the wear scar and the error committed as a consequence of the frictional and the wear behaviour variables used in the FEM simulation. Around this last aspect it was seen that the influence of the coefficient of friction is depreciable in the final wear scar shape for the studied range of conditions. However the ratio between the coefficient of wear of the top and the bottom specimen mainly could affect in the wear depth of the bottom specimen. As has been mentioned previously, the formation of compacted debris protective layers produces different wear behaviours in the top and in the bottom wear scars. It means that the ratio between the coefficients of wear between both specimens is variable with respect to the number of cycles. The simulations carried out in this study were performed with a constant ratio in order to simplify the problem. For this the specific coefficient of wear obtained for each test condition and specimen was used. This coefficient represents the mean of the variable coefficient of wear reported in these tests.

#### FEM analysis of the severity of the wear scars under different operational and geometrical variables.

The FEM optimized wear simulation model for different crossing angles was then used to study the severity of the wear scars, using the design of experiments (DOE) methodology, under the different operational (normal load, stroke) and geometrical (diameter, crossing angle, curvature) parameters presented in the wire rope systems. The study of the wear scar severity was focused on two aspects that can be presented in wire rope systems: the percentage of resistant area loss which is in relation with the catastrophic rupture of the wire and the stress concentration factor of the wear scar which is in relation with the fatigue life reduction of this component.

The results showed that the diameter, the crossing angle and the normal load (contact pressure) were the main parameters that have to be reduced in order to increase the live of these components. While the diameter is the main geometrical parameter that has to be modified for the reduction of the percentage of resistant area loss, the crossing angle is the main parameter that has to be modified for the reduction of the stress concentration factor. Therefore, in cases where the catastrophic rupture of the wire is presented, an increase of the diameter increase the life of the wire and in cases where the fatigue life reduction is presented, a decrease of the crossing angle increase the life of the wire. When both damages are presented in small diameter wires, a small change of the diameter or a small change in the crossing angle can increase considerably the life of the component.

### FEM analysis of the fretting wear induced multiaxial stress distribution in the fatigue life reduction of thin steel wires

Finally the fretting wear induced crack initiation in the fatigue life reduction of the thin steel wires was studied. To this end the SWT critical-plane approach was applied in the optimized 90° crossed FE model. A new damage accumulation methodology for the adaptive mesh simulation, based on the cyclic removal was developed. Four methods for the estimation the fatigue coefficients of the wire were used. Three of these methods (Manson's universal slope, Muralidharan's universal slopes and Medians) are based on the monotonic tensile test date. The fourth method is based on fatigue S-N curves reported in the literature. The results obtained with this methodology were compared with the fretting wear tests carried out in the same conditions.

It was shown that Manson's method and medians method gave lives closer to those obtained experimentally. The other methods gave results more conservative. The method predicts that that an increase in load reduces the life of the wire, as observed experimentally, but does not predict a reduction in life with increasing stroke, as also observed experimentally.

It has to be pointed out that the coefficient of friction and the bending tractions produced by the curvature of the wire are two parameters that have to be considered also for the crack nucleation. Previously it was seen that the friction coefficient is depreciable in the final wear scar shape, being depreciable in the study of the severity of the wear scar. On the other hand it was seen that in the severity study carried out with different geometrical (diameter, curvature and crossing angle) and operational (load and stroke) the curvature was the parameter with less influence in the wear scar severity. Nevertheless taking into account this last study both parameters have to be considered in the frictionally-induced multiaxial contact stress produced by the fretting wear in thin steel wires. This study has demonstrated, that for the study the real fretting behaviour presented in wire rope systems the effect of the fretting induced multiaxial stresses has to be taken into account in order to analyse the severity of each contact.

## **7.3 Recommendation and further work**

---

### **7.3.1 Fretting tests**

In the tests carried out with 90° crossing angles, it was reported the two wear behaviours presented in these type of tests which leads to a variable coefficient of wear with respect to the sliding distance and contact pressure. With the aim to characterize this effect in

crossing angles close to those one presented in wire ropes, fretting wear tests with different crossing angles but under different number of cycles should be carried out. In the case of using small crossing angles, further repeatability tests have to be introduced, due to the dispersion that can be obtained in both the test and the measurement of the wear scar. Moreover a study of the wear debris layer has to be carried out in order to understand better the two wear mechanism behaviour.

In both the 90° crossing angle tests and different crossing angle test was shown the influence of the contact pressure in the wear behaviour. Taking into account that the wire ropes are composed by different diameters thin steel wires, it is proposed to do fretting wear tests with different diameters. According to the results obtained in this thesis it is assumed that in the smaller diameter wires which leads in higher contact pressures should be obtained higher coefficients of wear.

From all this tests it is proposed to develop a global wear law which could predict the wear coefficient corresponding to the operational geometrical conditions presented in wire rope systems.

Future works could be focused on fretting wear test with a more exhaustive crack pack identification under different loads and strokes conditions. These tests are indispensable to improve the FE tool developed in this thesis for predicting the effect of fretting wear in the fatigue life reduction of these components. Taking into account this phenomenon the fretting fatigue tests proposed by Wang et al. [149] could be carried out in order to developed a more robust FE wear crack nucleation and propagation methodology for thin steel wires. These tests were done in more realistic conditions, close to those presented in wire rope systems, but with wider diameters wires in comparison with the analysed ones in this work. For this reason, it should be taken into account the greater complexity for the tests with thin wires.

### **7.3.2 Fretting wear modelling**

As has been reported in this thesis the coefficient of wear depends on stroke and contact pressure. Moreover it is shown the variable coefficient of wear appeared with respect the number of cycles due to the two wear behaviours presented in this test. To solve this problem the specific coefficient of wear which represent the mean of the variable coefficient of wear for each test conditions has been used satisfactorily in this work. Nevertheless the implementation of a global wear model in the FEM wear simulation methodology that include all variables that have influence in the coefficient of wear, could give a better understanding of the wear severity under the different operational an geometrical variables.

On the other hand the development of a local wear coefficient which depends on contact pressure and sliding distance is a great approach that should be addressed in future works. Around this aspect Argatov et al. [157] in the framework of the Archard Kragelsky model, has developed a model which takes into account the dependence of the wear rate on the contact pressure for the 90° crossed cylinder tests carried out in this thesis. In future works, it should be implemented this model in the FEM approach proposed in this thesis, in order to see the validity of this model. One of the disadvantages of this model is the sensitivity that could present the different approaches developed in this thesis for the optimization the wear modelling. Nevertheless the implementation of this type of models could be very important in order to see the effect of wear of the fatigue life reduction of these components.

The simulation of wear debris layers is another approach that could be addressed in future works as reported by Ding [135]. Nevertheless it is presumed that the modelling of the effect the debris layers in the 3D models developed in this thesis will increase the computational time drastically with the complexity that requires the characterization of these layers in thin steel wires.

### **7.3.3 Fretting wear-fatigue modelling**

The fretting wear frictionally induced crack initiation is the last aspect that has been addressed in this thesis in terms of FE modelling. Nevertheless there is further work to do in order to characterize correctly the fretting induced fatigue life reduction in the wire rope systems.

Future work will be focused in the characterization of the fatigue behaviour of thin steel wires with the complexity associate to the very small diameter. This is because the fatigue properties of the wires are related to different parameters: such as the interlamellar spacing of the pearlitic obtained by the cold-drawn process, the diameter of the wire or the size of the inner defects. Moreover the statistical models [155] which relate the wire defects with the fatigue life of the wire can also be introduced in combination with the multiaxial fatigue models.

The combined FE wear model and SWT critical plane damage methodology proposed in this thesis has given conservative results. In order to improve this methodology it is proposed to introduce the volume averaging techniques [56], [68] or the Ruiz parameters in the SWT critical approach [59], [63] to improve both the life and the crack location predictions. Moreover other multiaxial models as reported by Navarro et al. [64] can be implemented in order to improve the life predictions.

The combination of the crack propagation model with the initiation model is another aspect that has to be addressed in future work in order to explain better the effect of crack propagation or arrest due to the wear effect. Around this aspect Madge et al. [62] proposed a FE approach which combined both the initiation and crack propagation model with the wear model for 2D problems. In order to extend this approach to the 3D problems it is proposed to use the X-FEM approach. Recently Giner et al. [158] presented an efficient procedure to predict fatigue lives in fretting fatigue problems, based on a combined initiation–propagation approach in which the extended finite element method (X-FEM) is used. The main advantage of X-FEM is that while in the traditional FE modelling the crack tip singularity should be modelled with more refined elements and collapsed nodes, with X-FEM is not necessary to generate a mesh that conforms to the crack boundaries. This is because of the X-FEM methodology uses enrichment nodes surrounding the crack tip. Therefore only a single mesh such as those ones proposed in this thesis for the stress concentration factor calculation, could be used for any crack length and orientation propagation, reducing both the computational time and the creation of new FE models.



---

# REFERENCES

---

- [1] Orona lifts Company. *Orona references, Comercial, Centro comercial parque principado*. 2012, available from: [www.orona.es](http://www.orona.es)
- [2] Mobilift cranes Company. *Rental, Cranes*. 2012, available from: [www.mobiliftoman.com](http://www.mobiliftoman.com)
- [3] Doppelmayr. *Products, Funiculars*. 2012, available from: [www.doppelmayr.com](http://www.doppelmayr.com)
- [4] M. A.Urchequi. *Estudio del daño generado por fretting en hilos metálicos de cables de ascensores*. Arrasate-Mondragón: Mondragon Unibertsitatea, 2007.
- [5] M. Molkow, W. Scheunemann. Wire rope for elevator suspension. *Elevator World*, 2003, Vol. 51, No. 5, pp. 100-117
- [6] K. Feyrer. *Wire Ropes: Tension, Endurance, Reliability*, Springer, Germany, 2007.
- [7] Inem elevators. *Products, Lift components, Gearless motors*. 2012, available from: <http://www.imem.com>
- [8] K.K. Schrems. Wear related fatigue in a wire rope failure, *Journal of Testing & Evaluation*, 1994, Vol. 22, pp. 490-499.
- [9] R.B. Waterhouse. Fretting in steel ropes and cable – A review, *ASTM Special Technical Publication*, 2002, Vol. 1425, pp.3-14.
- [10] M.A. Urchequi, W.Tato, X.Gómez, Wear evolution in a stranded rope subjected to cyclic bending, *Journal of Materials Engineering and Performance*, 2007, Vol. 17, pp. 550-560.
- [11] “Reglas de seguridad para la construcción e instalación de ascensores – Parte 1: Ascensores eléctricos”, UNE-EN 81-1, 2001-176., pp. 12
- [12] H. Hertz. Über die Berührung fester elastischer körper (On the contact of solids). *J. reine und angewandte Mathematik*, 1882, Vol. 92, pp. 156-171.
- [13] K. L. Johnson. *Contact Mechanics*. Cambridge University Press, Cambridge, 1985.
- [14] B. Bushan. *Modern Tribology Handbook*. CRC Press LLC, Florida, 2000.
- [15] C. Cattaneo. Sul contatto di due corpi elastici: distribuzione locale degli sforzi, *Rendiconti dell'Accademia nazionale dei Lincei*, 1938, Vol. 27, No. 6., pp. 342-348, 434-436, 474-478.
- [16] R. D. Mindlin. Compliance of elastic bodies in contact. *Journal of applied mechanics*, 1949, Vol. 16, pp. 259-268.
- [17] K. L. Johnson. Surface interaction between elastically loaded bodies under tangential forces. *Proceedings of Royal society A*, 1955, Vol. 230, pp. 531.
- [18] R. B. Waterhouse. Fretting wear. *ASM handbook*, Vol. 18, Friction, Lubricant, and Wear technology, ASM International Handbook Committee, 1992, pp. 449-481.
- [19] S. J. Shaffer and W. A. Glaeser. Fretting fatigue. *ASM Handbook*, Vol. 19, Fatigue and fracture, ASM International Handbook Committee, 1996, pp. 801-803.
- [20] G. W. Stachowiak, A. W. Batchelor. *Engineering Tribology*. Tribology Series, Vol. 24, Elsevier Science: Amsterdam, Netherlands, 1993.

- [21] Y. Berthier, L. Vincent, M. Gedet. Fretting fatigue and fretting wear. *Tribology international*, 1989, Vol. 22, pp. 235-242.
- [22] M. Kuno, R. B. Waterhouse. The effect of oscillatory direction on fretting wear under crossed cylinder contact conditions, *Eurotrib 89, Proceeding of the 5<sup>th</sup> International Congress on Tribology*, 1989, Helsinki, Vol. 3, pp. 30-35.
- [23] J. M. Dobromirski. Variables in the fretting process: are there 50 of them?, *Standardization of fretting fatigue tests methods and equipment*, ASTM STP 1159 (American Society for Testing of Materials), Philadelphia, 1992.
- [24] O. Vingsbo, S. Söderberg. On fretting maps, *Wear*, 1988, Vol. 126, pp. 131-147.
- [25] Z. R. Zhou, K. Nakazawa, M. H. Zhu, N. Maruyama, Ph. Kapsa, L. Vincent. Progress in fretting maps, *Tribology International*, 2006, Vol. 39, pp. 1068-1073.
- [26] L. Vincent, J. Berthier, M. Godet. Testing methods in fretting fatigue: a critical appraisal, *ASTM*, 1992, vol. 1159, pp. 317-330.
- [27] S. Fouvry, Ph. Kapsa, L. Vincent. An elastic-plastic shakedown analysis of fretting wear, *Wear*, 2001, Vol. 247, pp. 41-54.
- [28] S. Fouvry, Ph. Kapsa, L. Vincent. Analysis of sliding behaviour for fretting loading: determination of transition criteria, *Wear*, 1995, Vol. 185, pp. 35-46.
- [29] S. Heredia, S. Fouvry. Introduction of a new sliding regime criterion to quantify partial, mixed and gross slip fretting regimes: Correlation with wear and cracking processes. *Wear*, 2010, Vol. 269, pp. 512-524.
- [30] N. Ohmae, T. Tsukizoe. The effect of slip amplitude on fretting, *Wear*, 1974, Vol. 27, pp. 281-294.
- [31] M. J. Lewis, P. B. Didsbury. The rubbing fretting behaviour of mild steel in air at room temperature: the effects of load, frequency, slip amplitude and test duration, *Treatise on Material Science and Technology*, New York: Academic Press, New York, 1979.
- [32] L. Toth. The investigation of the steady state of steel fretting, *Wear*, 1972, Vol. 20, pp. 277-283.
- [33] J. Warburton. The fretting of mild steel in air, *Wear*, 1989, Vol. 131, pp. 365-386.
- [34] G. X. Chen, Z. R. Zhou. Study on transition between fretting and reciprocating sliding wear, *Wear*, 2001, Vol. 250, pp. 665-672.
- [35] S. Fouvry. *Etude quantitative des dégradations en fretting*. Ecole Central de Lyon, France, 1997.
- [36] M. Varenberg, I. Etsion, G. Halperin. Slip index: a new unified approach to fretting, *Tribology Letters*, 2004, Vol. 17, No. 3, pp. 569-573.
- [37] D. Klaffke. Towards a tribological reference test-fretting test?, *Tribo Test*, 2006, Vol. 12, pp. 133-147.
- [38] D. Klaffke. Fretting wear of ceramic, *Tribology International*, 1989, Vol. 22, pp. 89-101.
- [39] J. Warburton, R. Bradford. The progressive wear of tubes: The volumes of the intersections of cylinders with each other and with flats, *Wear*, 1986, Vol. 113, pp. 331-352.
- [40] S. Fouvry, T. Liskiewicz, Ph. Kapsa, S. Hannel, E. Sauger. An energy description of wear mechanisms and its applications to oscillating sliding contacts, *Wear*, 2003, Vol. 255, pp. 287-298.
- [41] T. Liskiewicz, S. Fouvry. Development of friction energy capacity approach to predict the surface coating endurance under complex oscillating sliding conditions, *Tribology International*, 2005, Vol. 38, No. 1, pp. 69-79.
- [42] A. Ramalho, J. C. Miranda. The relationship between wear and dissipated energy in sliding systems, *Wear*, 2006, Vol. 260, pp. 361-367.
- [43] S. Fouvry, C. Paulin, T. Liskiewicz. Application of an energy wear approach to quantify fretting contact durability: Introduction of a wear energy capacity concept, *Tribology International*, 2007, Vol. 40, N° 10-12, pp. 1428-1440.
- [44] K.N. Smith, P. Watson, T.H. Topper, A stress-strain function for the fatigue of metals, *Journal of Materials*, 1970, Vol. 15, pp. 767-778.

- [45] A. Fatemi, D. F. Socie. A Critical Plane Approach to Multiaxial Fatigue Damage Including Out-of-Phase Loading. *Journal of Fatigue and Fracture of Engineering Materials and Structures*, 1988, Vol. 11, No. 3, pp. 149-165.
- [46] D. L. McDiarmid. A shear stress based critical-plane criterion of multiaxial fatigue failure for design and life prediction. *Journal of Fatigue and Fracture of Engineering Materials and Structures*, 1994, Vol. 17, pp. 1475-1484.
- [47] L. Fellows, D. Nowell, D. Hills. On the initiation of fretting fatigue cracks. *Wear*, 1997, Vol. 205, pp. 120-129.
- [48] K. Dang Van. Macromicro approach in high-cycle multiaxial fatigue. Advances in D.L. McDowell and R. Ellis (eds.), *Multiaxial Fatigue, ASTM STP 1191*, ASTM, Philadelphia, PA, 1993, pp. 120-130.
- [49] D. F. Socie, G. B. Marquis. Multiaxial fatigue. SAE Int, 2000.
- [50] B. Crossland. Effect of large hydrostatic pressures on the torsional fatigue strength of an alloy steel. In: Proceedings of the international conference on fatigue of metals. London: Institution of mechanical Engineers; 1956, pp. 138-149.
- [51] D. Socie, Multiaxial fatigue damage models. *Journal of Engineering Materials and Technology*, 1987, Vol. 109, pp. 293-298.
- [52] C. Ruiz, P.H.B. Boddington, K.C. Chen. An investigation of fatigue and fretting in dovetail joint, *Experimental Mechanics*, 1984, Vol. 24, pp. 208-217.
- [53] M.P. Szolwinski, T.N. Farris, Mechanics of fretting fatigue crack formation. *Wear*, 1996, Vol. 198, pp. 93-107.
- [54] Christopher D. Lykins, Shankar Mall, Vinod Jain. An evaluation of parameters for predicting fretting fatigue crack initiation, *International Journal of Fatigue*, 2000, Vol. 22, pp. 703-716.
- [55] Christopher D. Lykins, Shankar Mall, Vinod K. Jain. Combined experimental-numerical investigation of fretting fatigue crack initiation, *International Journal of Fatigue*, 2001, Vol. 23, pp. 703-711
- [56] J. A. Araújo, D. Nowell. The effect of rapidly varying contact stress fields on fretting fatigue. *International Journal of Fatigue*, 2002, Vol. 24, pp. 763-775
- [57] O. Jin, S. Mall. Effects of slip on fretting behaviour: experiments and analyses, *Wear*, 2004, Vol. 256, pp. 671-684. □
- [58] W. S. Sum, E.J. Williams, S.B. Leen. Finite element, critical-plane, fatigue life prediction of simple and complex contact configurations, *International Journal of Fatigue*, 2005, Vol. 27, pp. 403-416.
- [59] J. Ding, W. S. Sum, R. Sabesan, S. B. Leen, I. R. McColl, E. J. Williams. Fretting fatigue predictions in a complex couplings. *International Journal of Fatigue*, 2007, Vol. 29, pp. 1229-1244.
- [60] J.J. Madge, S. B. Leen, P.H. Shipway. The critical role of fretting wear in the analysis of fretting fatigue, *Wear*, 2007, Vol. 263, pp. 542-551.
- [61] J.J. Madge, S.B. Leen, I.R. McColl, P.H. Shipway. Contact-evolution based prediction of fretting fatigue life: Effect of slip amplitude, *Wear*, 2007, Vol. 262, pp. 1159-1170.
- [62] J. J. Madge, S. B. Leen, P. H. Shipway, A combined wear and crack nucleation-propagation methodology for fretting fatigue prediction, *International journal of fatigue*, 2008, Vol. 30, pp. 1509-1528.
- [63] J. Ding, D. Houghton, E. J. Williams, S. B. Leen. Simple parameters to predict effect of surface damage on fretting fatigue, *International Journal of Fatigue*, 2011, Vol. 33, pp. 332-342.
- [64] C. Navarro, S. Muñoz, J. Domínguez. On the use of multiaxial fatigue criteria for fretting fatigue life assessment. *International Journal of Fatigue*, 2008, Vol. 30, pp. 32-44.
- [65] C. Navarro, J. Vázquez, J. Domínguez. A general model to estimate life in notches and fretting fatigue, *Engineering Fracture Mechanics*, 2011, Vol. 78, pp. 1590-1601.
- [66] M. Buciumeanu, I. Crudu, L. Palaghian, A.S. Miranda, F.S. Silva. Influence of wear damage on the fretting fatigue life prediction of an Al7175 alloy, *International Journal of Fatigue*, 2009, Vol. 31, pp. 1278-1285.

- [67] S. Fouvry, Ph. Kapsa, L. Vincent, K. Dang Van. Theoretical analysis of fatigue cracking under dry friction for fretting loading conditions, *Wear*, 1996, Vol. 195, pp. 21-34.
- [68] S. Fouvry, P. Duo, Ph. Prruchaut. A quantitative approach of Ti-6Al-4V fretting damage: friction, wear and crack nucleation, *Wear*, 2004, Vol. 257, pp. 916-929.
- [69] V. Fridrici, S. Fouvry, P. Kapsa, P. Perruchaut. Prediction of cracking in Ti-6Al-4V alloy under fretting-wear: use of the SWT criterion, *Wear*, 2005, Vol. 259, pp. 300-308.
- [70] H. Proudhon, S. Fouvry, J. Y. Buffière. A fretting crack initiation prediction taking into account the surface roughness and the crack nucleation process volume, *Wear*, 2005, Vol. 27, pp. 569-579.
- [71] H. Proudhon, S. Fouvry, G.R. Yantio. Determination and prediction of the fretting crack initiation: introduction of the (P, Q, N) representation and definition of a variable process volume, *International Journal of fatigue*, 2006, Vol. 28, pp. 707-713.
- [72] S. Muñoz, H. Proudhon, J. Domínguez, S. Fouvry. Prediction of the crack extension under fretting wear loading conditions, *International journal of fatigue*, 2006, Vol. 28, pp. 1769-1779.
- [73] A. L. Mohd Tobi, J. Ding, G. Bandak, S. B. Leen, P. H. Shipway, A study on the interaction between fretting wear and cyclic plasticity for Ti-6Al-4V, *Wear*, 2009, Vol. 267, pp. 270-282.
- [74] T. Zhang, P.E. McHugh, S.B. Leen. Computational study on the effect of contact geometry on fretting behaviour, *Wear*, 2011, Vol. 271, pp. 1462-1480.
- [75] B.R. Pearson, P. A. Brook, R. B. Waterhouse. Fretting in aqueous media, particularly of roping steels in seawater, *Wear*, 1985, Vol. 106, No. 1-3, pp. 225-260.
- [76] A.W. Batchelor, G.W. Stachowick. Extending the life of wire rope by development of improved wire coatings and sheave materials, *Mechanical Engineering Transactions – Institution of Engineers, Australia*, 1992, Vol. 17, No. 3, pp. 161-169.
- [77] R.B. Waterhouse, I.R. McColl, S.J. Harris, M. Tsujikawa. Fretting wear of a high-strength heavily work-hardened eutectoid steel, *Wear*, 1994, Vol. 175, pp. 51-57.
- [78] I.R. McColl, S.J. Harris, R.B. Waterhouse, Lubricated fretting wear of high strength eutectoid steel rope wire, *Wear*, 1995, Vol. 185, pp. 203-212.
- [79] D.K. Zhang, S.R. Ge, Y.H. Qiang. Research on the fatigue and fracture behavior due to the fretting wear of steel wire in hoisting rope, *Wear*, 2003, Vol. 255, pp. 1233-1237.
- [80] Y. Shen, D.K. Zhang, S.R. Ge. Effect of fretting amplitudes on fretting wear behavior of steel wires in coal mines, *Mining Science and Technology*, 2010, Vol. 20, pp. 803-808.
- [81] D.K. Zhang, Y. Shen, X. Linmin, S.R. Ge. Fretting wear behaviors of steel wires in coal mine under different corrosive mediums, *Wear*, 2011, Vol. 271, pp. 866-874.
- [82] M.A. Urchegui, M. Hartelt, R. Wäsche and X. Gómez. Laboratory fretting tests with thin wire specimens, *Tribo Test*, 2007, Vol. 13, N° 2, pp 67-81.
- [83] M.A. Urchegui, M. Hartelt, R. Wäsche and X. Gómez. Analysis of different strategies to reduce fretting wear in thin steel roping wires, *Tribo Test*, 2008, Vol. 14, pp. 43-57.
- [84] V. Périer, L. Dieng, L. Gaillet, S. Fouvry. Influence of an aqueous environment on the fretting behaviour of steel wires used in civil engineering cables, *Wear*, 2011, Vol. 271, pp. 1585–1593.
- [85] C. H. Meng. *Wear modelling: Evaluation and categorization of wear models*, The University of Michigan, Michigan, 1994.
- [86] F. T. Barwell. Wear of metals, *Wear*, 1958, Vol. 1, N° 4, pp. 317–332.
- [87] S. K. Rhee. Wear equation for polymers sliding against metal surfaces, *Wear*, 1970, Vol. 16, N° 6, pp. 431-445.
- [88] J. F. Archard. Elastic deformation and the laws of friction, *Proc. R. Soc. London*, 1957, Vol. 243, pp. 190-205.
- [89] T. F. J. Quin. Oxidational wear, *Wear*, 1971, Vol. 18, pp. 413-419.
- [90] NAM P. SUH. The delamination theory of wear, *Wear*, 1973, Vol. 25, pp. 111-124.
- [91] H. Mohrbacher, J. P. Celis, J. R. Roos. Laboratory testing of displacement and load induced fretting, *Tribology International*, 1995, Vol. 28, pp. 269-278.
- [92] S. Fouvry, P. Kapsa, H. Zahouani, L. Vincent. Wear analysis in fretting of hard coatings through a dissipated energy concept, 1997, *Wear*, Vol. 203-204, pp. 393-493.

- [93] L.A. Galin. Contact problems of the theory of elasticity in the presence of wear, *J. Appl. Math. Mech.*, 1976, Vol. 40, pp. 931–936.
- [94] L.A. Galin, I.G. Goryacheva, Axisymmetric contact problem of the theory of elasticity in the presence of wear, *J. Appl. Math. Mech.*, 1977, Vol. 41, pp. 826–831.
- [95] P. Podra, S. Andersson. Wear simulation with the Winkler surface model, *Wear*, 1997, Vol. 207, pp. 79-85.
- [96] I. Goryacheva. *Contact Mechanics in Tribology*, Kluwer Academic Publishers, Dordrecht, 1998.
- [97] J. Jiang, R.D. Arnell. On the running-in behaviour of diamond-like carbon coatings under the ball-on-disk contact geometry, *Wear*, 1998, Vol. 217, pp. 190–199.
- [98] D. J. Dickrell, W.G. Sawyer. Evolution of wear in a two-dimensional bushing. *Tribology Transactions*, 2004, Vol. 47, pp. 257-262.
- [99] V. Hegadekatte. *Modeling and simulation of dry sliding wear for micro-machine applications*. Universität Karlsruhe, Karlsruhe, 2006.
- [100] I. Argatov, W. Tato. Asymptotic modeling of reciprocating sliding wear – Comparison with finite-element simulations, *European Journal of Mechanics and Solids*, 2012, Vol. 34, pp. 1–11.
- [101] L. Johanson. Numerical simulation of contact pressure evolution in fretting, *Journal Tribology*, 1994, Vol. 116, pp. 247-254.
- [102] P. Podra, S. Andersson. Simulating sliding wear with finite element method, *Tribology International*, 1999, Vol. 32, No. 2, pp. 71-81.
- [103] M. Oqvist. Numerical simulation of mild wear using updated geometry with different step size approaches, *Wear*, 2001, Vol. 249, pp. 6-11.
- [104] I. R. McColl, J. Ding, S. B. Leen. Finite element simulation and experimental validation of Fretting wear, *Wear*, 2004, Vol. 256, pp. 1114-1127.
- [105] N. H. Kim, D. Won, D. Burris, B. Holtkamp, G. R. Gessel, P. Swanson, W. G. Sawyer, Finite element analysis and experiments of metal/metal wear in oscillatory contacts, *Wear*, 2005, Vol. 258, No. 11-12, pp. 1787-1793.
- [106] V. Hegadekatte, N. Huber, O. Kraft. Finite element based simulation of dry sliding wear, *Modelling and simulation in materials science and engineering*, 2005, Vol. 13, pp. 57-75.
- [107] J. Ding, I. R. McColl, S. B. Shipway. The application of fretting wear modelling to a spline couplings, *Wear*, 2007, Vol. 262. pp. 1205-1216.
- [108] J. Ding, I.R. McColl, S.B. Leen, P.H. Shipway, A finite element based approach to simulating the effects of debris on fretting wear, *Wear*, 2007. Vol. 263, pp. 481-491.
- [109] V. Hegadekatte, S. Kurzenhäuser, N. Huber, O. Kraft. A predictive scheme for wear in tribometers, *Tribology international*, 2008, Vol. 41, pp. 1020-1031.
- [110] A.L. Mohd Tobi, J. Ding, S. Pearson, S. B. Leen, P. H. Shipway. The effect of gross sliding fretting wear on stress distributions in thin W-DLC coating systems. *Tribology International*, 2010, Vol. 43, pp. 1917–1932.
- [111] G. K. Sfantos, M. H. Aliabadi. Wear simulation using an incremental sliding Boundary Element Method, *Wear*, 2006, Vol. 260, pp. 1119-1128.
- [112] J. A. Gonzalez, R. Abascal. Efficient stress evaluation of stationary viscoelastic rolling contact problems using the boundary element method: Application to viscoelastic coatings, *Engineering Analysis with Boundary Elements*, 2006, Vol. 30, No. 6, pp. 426-434.
- [113] L. Rodriguez-Tembleque, R. Abascal, M.H. Aliabadi. A boundary elements formulation for general 3D wear simulation. In *8th World Congress on Computational Mechanics and 5th European Congress on Computational Methods in Applied Sciences and Engineering*, Venice, Jun 30 - Jul 5 2008.
- [114] L. Rodriguez-Tembleque, R. Abascal, M.H. Aliabadi. A Boundary elements formulation for 3D fretting-wear problems. *Engineering Analysis with Boundary Elements*, 2011, Vol. 35, pp. 935–943
- [115] S. S. Iyer, P L. Ko. Finite element modelling of plastic deformation, crack growth and wear particle formation for sliding wear of power plant components, *Proceedings of the 1996 ASME Pressure Vessels and Piping Conference*, Montreal, Jul. 21-26 1996.

- [116] P. L. Ko, S. S. Iyer, H. Vaughan, M. Gadala. Finite element modelling of crack growth and wear particle formation in sliding contact, *Wear*, 2001, Vol. 251, pp. 1265-1278.
- [117] Q. Li, J. Loughran, Z. Peng, J. Osborne. A Fracture Based Model for Wear Debris Formation, *Key Engineering Materials*, 2006, Vol. 324-325, pp. 1157-1160.
- [118] V. L. Popov, S. G. Psakhie. Numerical simulation methods in tribology, *Tribology International*, 2007, Vol. 40, pp. 916-923.
- [119] H. Kloss, R. Wäsche. Analytical approach for wear prediction of metallic and ceramic materials in tribological applications, *Wear*, 2009, Vol. 266, pp. 476-481.
- [120] S. Miyamoto, H. Sakai, T. Shiraishi, S. Morishita. A flow modeling of lubricating greases under shear deformation by cellular automata, *Proceedings of the 7th international conference on Cellular Automata for Research and Industry*, France, Sep. 20-23, 2006.
- [121] W. Österle, A.I. Dmitriev, H. Kloß. Possible impacts of third body nano structure on friction performance during dry sliding determined by computer simulation based on the method of movable cellular automata, *Tribology International*, 2012, Vol. 48, pp. 128-136.
- [122] C. Y. Lee, Y. S. Chai, J. W. Bae. Theoretical analysis for studying the fretting wear problem of steam generator tubes in a nuclear power plant, *Nuclear engineering and technology*, 2005, Vol. 37, No. 2, pp. 201-206.
- [123] Y. S. Chai, C. Y. Lee, J. W. Bae, S. Y. Lee, J. K. Hwang, Finite element analysis of fretting wear problems in consideration of frictional contact, *Key Engineering Materials*, 2005, Vol. 297-300, pp. 1406-1411.
- [124] J. Ding, S.B. Leen, I.R. McColl. The effect of slip regime on fretting wear-induced stress evolution, *International Journal of Fatigue*, 2004, Vol. 26, pp. 521-531.
- [125] C. Mary, S. Fouvry, Numerical prediction of fretting contact durability using energy wear approach: Optimisation of finite-element model, *Wear*, 2007, Vol. 263, pp. 444-450.
- [126] C. Paulin, S. Fouvry, C. Meunier. Finite element modelling of fretting wear surface evolution: application to a Ti-6Al-4V contact, *Wear*, 2008, Vol. 264, No. 1-2, pp. 26-36.
- [127] R. Wäsche, M. Hartelt. Wear testing with crossed cylinders – comparison of methods, Proc. 16<sup>th</sup> Intern. Colloquium on Tribology, (ed. W. J. Bartz), Technische Akademie Esslingen, Ostfildern, Jan. 15.-17. 2008.
- [128] D. Klaffke. On the influence of test parameters on friction and wear of ceramics in oscillating sliding contacts, *TriboTest*, 1995, Vol. 1, pp. 311-320.
- [129] S. Fouvry. Shakedown analysis and fretting wear response under gross slip condition, *Wear*, 2001, Vol. 251, pp. 1320-1331.
- [130] H. Kato, K. Komai. Tribofilm formation and mild wear by tribo-sintering of nanometer-sized oxide particles on rubbing steel surfaces, *Wear*, 2007, Vol. 262, pp. 36-41.
- [131] J. R. Gomes, A. Ramalho, M. C. Gaspar, S. F. Carvalho. Reciprocating wear tests of Al-Si/SiCp composites: A study of the effect of stroke length, *Wear*, 2005, Vol. 259, pp. 545-552.
- [132] S. Fouvry, T. Liskiewicz, C. Paulin. A global-local wear approach to quantify the contact endurance under reciprocating-fretting sliding conditions, *Wear*, 2007, Vol. 263, pp. 518-531.
- [133] F.P. Bowden, D. Tabor, *Friction and Lubrication of Solids*, Vol. I, Oxford University Press, London, 1964.
- [134] Abaqus User's Manual, Version 6.9, Hibbit, Karlsson & Sorensen, Inc., USA, 2009.
- [135] J. Ding. *Modelling of fretting wear*. Nottingham: University of Nottingham, 2003.
- [136] H. Czichos, S. Becker, J. Lexow. International multilaboratory sliding wear tests with ceramics and steel, *Wear*, 1989, Vol. 135, pp. 171-191.
- [137] B. Kanavalli. *Application of user defined subroutine UMESHMOTION in Abaqus to simulate dry rolling/sliding wear*. Master thesis, Stockholm, Sweden: Royal Institute of Technology (KTH), 2006.
- [138] H. Akima. A method of bivariate interpolation and smooth surface fitting for values given at irregularly distributed points. *Journal ACM Transactions on Mathematical Software*, Vol. 4, pp. 148-164, 1978.
- [139] F. David. Watson. *Contouring: A guide to the analysis and display of spacial data*. Pergamon, 1994.

- [140] MINITAB User's Guide 2: Data Analysis and Quality Tools, Minitab Inc., USA, 2010.
- [141] Costello GA. *Theory of wire rope*. 2nd ed. New York: Springer-Verlag, 1997.
- [142] D. Walter. Pilkey. *Peterson's Stress concentration Factors*, Jon Wiley, New York, 1997.
- [143] J. Llorca, V. Sánchez-Gálvez. Fatigue limit and fatigue life prediction in high strength cold drawn eutectoid steel wires. *Fatigue of engineering materials and structures*, Vol. 12, pp. 31 – 45, 1985.
- [144] S. Beretta, M. Boniardi. Fatigue strength and surface quality of eutectoid steel wires. *International Journal of Fatigue*, Vol. 21, pp. 329-335, 1999.
- [145] J. Petit, C. Sarrazin-Baudoux, F. Lorenzi. Fatigue crack propagation in thin wires of ultra high strength steels. *Procedia Engineering*, Vol.2, pp. 2317-2326, 2010.
- [146] Kasper Lambrighs, Ignace Verpoest, Bert Verlinden, Martine Wevers. Influence of the load ratio on the threshold intensity factor range for heavily drawn steel wires. *Engineering Failure Analysis*, Vol. 18, pp. 694-699, 2011.
- [147] E. Navaei Alvar, J. Aghazadeh Mohandesi. Fatigue damage accumulation in cold-drawn steel wire under variable loading. *Materials and design*, Vol. 31, pp. 2018 – 2024, 2010.
- [148] Roberto Brighenti, Andrea Carpinteri, Sabrina Vantadori. Influence of residual stresses on fatigue crack propagation in pearlitic cold-drawn steel wires. *Materials Science Forum*, Vol. 681, pp. 229 – 235, 2011.
- [149] D.G. Wang, D.K. Zhang DK, S. R. Effect of displacement amplitude on fretting fatigue behavior of hoisting rope wires in low cycle fatigue. *Tribology International*, Vol. 52, pp. 178-189, 2012.
- [150] J. Das, S.M. Sivakumar. An evaluation of multiaxial fatigue life assesment methods for engineering components. *International Journal of Pressure Vessels and Piping*, Vol. 76, pp. 741-746, 1999.
- [151] L. Del Llano-Vizcaya, C. Rubio-González, G. Mesmacque, T. Cervantes-Hernández. Multiaxial fatigue and failure análisis of helical compression Springs. *Engineering Failure analysis*, Vol. 13, pp. 1303-1313, 2006.
- [152] SS. Manson. Fatigue: a complex subject-some simple approximations. *Experimental mechanics*, Vol. 5, pp. 193-226, 1965.
- [153] U. Muralidharan, SS. Manson. Modified universal slopes equation for estimation of fatigue characteristics. *ASME Journal of Engineering Materials and Technology*, Vol. 110, pp. 55–58, 1988.
- [154] M.A. Meggiolaro, J. T. P. Castro. Statistical evaluation of strain-life fatigue crack initiation predictions. *International Journal of Fatigue*, Vol. 26, pp. 463-476, 2004.
- [155] S. Beretta, S. Matteazzi. Short crack propagation in eutectoid steel wires. *International Journal of Fatigue*, Vol. 18, pp. 451-456, 1996.
- [156] I. Verpoest, E. Aernoudt, A. Deruyttere, M. De Bondt. The fatigue threshold, surface condition and fatigue limit of steel wire. *International Journal of Fatigue*, Vol. 7, pp. 199-214, 1985.
- [157] I.I. Argatov, X. Gómez, W. Tato, M.A. Urchegui. Wear evolution in a stranded rope under cyclic bending: Implications to fatigue life estimation. *Wear*, Vol. 271, pp. 2857-2867, 2011.
- [158] E. Giner, C. Navarro, M. Sabsabi, M. Tur, J. Dominguez, F.J. Fuenmayor. Fretting fatigue life prediction using the extended finite element method. *International Journal of Mechanical Sciences*, Vol. 53, pp. 217-225, 2011.